Investigating the potential of emerging porous organic-based photocatalysts for CO_2 reduction

by

Giulia E. M. Schukraft

A Thesis submitted in fulfilment of the requirements for the degree of Doctor of Philosophy and the Diploma of Imperial College London

Chemical Engineering Department

Materials Department

Imperial College London

June 2022

To my father Jurgen and grandfather Ugo, who have inspired me throughout my life to pursue passionate and rigorous research, for their thoughtful suggestions and continuous interest in my experiments, and lastly, for their unwavering support throughout all of my endeavours.

Declaration of authorship

I hereby declare that this thesis is my own work and any work performed by others has been appropriately acknowledged and referenced in the forthcoming text.

Copy right declaration

The copyright of this thesis rests with the author. Unless otherwise indicated, its contents are licensed under a Creative Commons Attribution 4.0 International Licence (CC BY).

Under this licence, you may copy and redistribute the material in any medium or format for both commercial and non-commercial purposes. You may also create and distribute modified versions of the work. This is on the condition that you credit the author.

When reusing or sharing this work, ensure you make the licence terms clear to others by naming the licence and linking to the licence text. Where a work has been adapted, you should indicate that the work has been changed and describe those changes.

Please seek permission from the copyright holder for uses of this work that are not included in this licence or permitted under UK Copyright Law.

Abstract

The conversion of CO_2 to synthetic fuels via photocatalysis represents a unique opportunity for sustainable energy production, addressing two of the most pressing problems of our time, namely climate change and the global energy crisis. In order to overcome the current constraints regarding performance for industrial applications, more efficient photocatalysts must be developed. In this thesis, I investigate the potential of emerging porous organic-based photocatalysts for CO_2 photoreduction in the gas phase. The first part of my thesis focuses on better understanding the factors which govern charge transfer across semiconductor/metal-organic framework (MOF) heterojunction interfaces. By measuring the electronic structure of the individual heterojunction components and taking into account band bending, I built a band model of the heterojunction interface, which helped rationalize the photocatalytic enhancements and losses observed in MOF-based heterojunctions. This model highlights the importance of considering band bending when constructing MOF-based heterojunctions, an aspect that is not commonly investigated. The second part of my thesis focuses on investigating for the first time the ability of hypercrosslinked polymers (HCPs) to photoreduce CO_2. I show that HCPs are promising visible-light active photocatalysts for the conversion of CO_2 to CO. The leading HCP of this study outperforms TiO_2 P25 by a factor of 7.5 when using only visible light and sacrificial H_2O, without using additional sacrificial agents or co-catalysts. Lastly, the final part of my thesis focused on investigating the CO_2 photoreduction mechanism, as well as the CO_2 and H_2O adsorption process on a triazine-biphenyl HCP. This was achieved by coupling in-situ diffuse reflectance infrared Fourier transform spectroscopy (DRIFTS), modulation excitation experiments, density functional theory (DFT) calculations, and advanced processing techniques. I found that CO_2 and H_2O adsorb on the same HCP sites albeit with different adsorption strengths. The primary amines of the triazines were identified as favouring strong CO_2 binding interactions. No intermediate species were found under transient light irradiation. However, I observed partial CO_2 and H_2O desorption and a redistribution of interactions between the CO_2/H_2O molecules that remain adsorbed at the HCP adsorption sites. Overall, this thesis presents new opportunities for the use and rational design of emerging porous organic-based photocatalysts for CO_2 reduction.

Publications

1 - G. E. M. Schukraft, I. Itskou, R. T. Woodward, B. Van Der Linden, C. Petit, A. Urakawa, "A combined DFT and in-situ DRIFT spectroscopy study on CO_2 and H_2O adsorption on a hypercosslinked polymer", under review.

2 - G. E. M. Schukraft, B. Moss, G. Kafizas, C. Petit, "Effect of Band Bending in Photoactive MOF-Based Heterojunctions". *ACS Appl. Mater. Interfaces*, 2022, 14, 17, 19342-19352.

3 - G. E. M. Schukraft, R. T. Woodward, S. Kumar, M. Sachs, S. Eslava, C. Petit, "Hypercrosslinked polymers as a photocatalytic platform for visible-light-driven CO_2 photoreduction using H_2O", *ChemSusChem*, 2021, 14, 7, 1720-1727.

4 - G. E. M. Schukraft, C. Petit, "Green Synthesis and Engineering Applications of Metal-Organic Frameworks", in *Sustainable Nanoscale Engineering*, Elsevier, 2020, 139-162. Eds. Gyorgy Szekely and Andrew Livingston.

5 - Z. Ye, **G. E. M. Schukraft**, A. L´Hermitte, Y. Xiong, E. Brillas, C. Petit, I. Sires, "Mechanism and stability of an Fe-based 2D MOF during the photoelectron-Fenton treatment of organic micropollutants under UVA and visible light irradiation", *Water research*, 2020, 184, 115986.

6 - M. Taddei, **G. E. M. Schukraft**, M. E. A. Warwick, D. Tiana, M. J McPherson, D. I. R. Jones, C. Petit, "Band gap modulation in zirconium-based metal-organic frameworks by defect engineering", *J. Mater. Chem A*, 2019, 7, 41, 23781-23786.

Acknowledgements

First and foremost, I would like to thank Professor Camille Petit for her guidance throughout this incredible and challenging journey that was my PhD. She consistently encouraged me to pursue independence in my scientific decision making and as a result I had the unique opportunity to self-select my PhD topic and pursue it through to completion. Camille also supported me when I suggested expanding my research beyond the Imperial College lab, and as a result I undertook a four-month research project in the Netherlands, focused on a completely new subject on in-situ infrared spectroscopy. Her mentorship has made me a better and more rigorous independent researcher, and for that I thank her immensely.

I also thank my family for their support throughout my PhD, especially my parents, who motivated me during the challenging times and have always surrounded me with their love. I am thankful for my teammates who facilitated my day to day work and made it a pleasure to come into the lab each day. I would like to thank my husband for always believing in me and for transmitting his positive energy to me, regardless of the situation.

I also would like to acknowledge EPSRC for the funding through the Centre of Doctoral Training in Advanced Characterisation of Materials (CDT-ACM), which gave me the opportunity to undertake this PhD.

Finally, I would like to thank my collaborators Dr Benjamin Moss, Dr Andreas Kafizas, Ms Ioanna Itskou, Dr Michael Sachs, Dr Gwihlerm Kerherve, Dr Mahmoud Ardakani and Ms Patricia Carry from Imperial College London, Prof Atsushi Urukawa from TU Delft, Dr Robert Woodward from the University of Vienna and Dr Marco Taddei from the University of Pisa, for their scientific inputs and for carrying out experiments for this thesis.

.

Abbreviations

Abbreviation	Description	Abbreviation	Description
ATR-FTIR	Attenuated total reflectance Fourier transform infrared	HOMO	Highest-occupied molecular orbital
ATR-IRS	Attenuated total reflectance infrared spectroscopy	LMCT	Ligand-to-metal charge transfer
AQY	Apparent quantum yield	LUMO	Lowest-unoccupied molecular orbital
BET	Brunauer-Emmett-Teller	MCR	Multivariate curve resolution
CB	Conduction band	MOFs	Metal-organic frameworks
COFs	Covalent organic frameworks	NHE	Normal hydrogen electrode
CMPs	Conjugated microporous polymers	NAP-XPS	Near-ambient pressure X-ray photoelectron spectroscopy
CNNS	Graphitic carbon nitride nanosheets	PAFs	Porous aromatic frameworks
DFT	Density functional theory	PIMPs	Polymers of intrinsic microporosity
DMF	*N*,*N*-Dimethylformamide	POPs	Porous organic polymers
DRIFTS	Diffuse reflectance infrared Fourier transform spectroscopy	QE	Quantum efficiency
DR-UV/Vis	Diffuse reflectance UV-Vis spectroscopy	SE	Secondary electrons
E_g	Band gap	SEM	Scanning electron microscopy
E_F	Fermi level energy	ssNMR	Solid-state nuclear magnetic resonance
E_{vac}	Vacuum level energy	TCD	Thermal conductivity detector
EPR	Electron paramagnetic resonance	TCSPC	Time-correlated single photon counting
EXAFS	Extended X-ray absorption fine structure spectroscopy	TEM	Transmission electron microscopy
FID	Flame ionization detector	TGA	Thermogravimetric analysis
GC	Gas chromatography	XANES	X-ray absorption near edge structure spectroscopy
g-C_3N_4	Graphitic carbon nitride	XAS	X-ray absorption spectroscopy
HCPs	Hypercrosslinked polymers	XPS	X-ray photoelectron spectroscopy
HPLC	High-performace liquid chromatography	XRD	X-ray diffraction
2-Hmin	2-methylimidazole	WF	Work function

Table of content

Declaration of authorship 2
Copy right declaration 2
Abstract 3
Publications 4
Acknowledgements 5
Abbreviations 6
Table of content 7
List of Figures 10
List of Tables 16
Chapter 1 17
1.1 Thesis outline 17
1.2 Background 17
1.3 Personal motivations 18
Chapter 2 19
2.1 Photocatalysis 19
2.1.1 Fundamental of photocatalysis 19
2.1.1.1 Electronic structure of a semiconductor 19
2.1.1.2 Photocatalytic process 20
2.1.1.3 Photocatalysts requirements 21
2.1.1.4 Photocatalytic metrics 23
2.1.2 Photocatalytic CO_2 reduction 24
2.1.2.1 Motivation for CO_2 photoreduction 24
2.1.2.2 CO_2 photoreduction mechanism 25
2.1.2.3 Thermodynamic considerations 25
2.1.2.4 Kinetics considerations 28
2.1.2.5 Liquid vs gas phase 29
2.1.2.6 The economic importance of CO_2 photoreduction products 29
2.1.2.7 Investigate CO_2 photoreduction mechanisms and adsorption processes 30
2.1.3 Alternative approaches to CO_2 reduction routes 36
2.2 Traditional photocatalysts 38
2.2.1 TiO_2 and derivatives 38
2.2.2 Non-titanium metal oxides 41
2.2.3 Metal sulfides and selenides 41
2.3 Emerging classes of organic-based photocatalysts 42
2.3.1 Graphitic carbon nitride 42
2.3.2 Metal-organic frameworks 44
2.3.3 Covalent organic frameworks 47

2.3.4 Amorphous porous polymers 49
2.3.4.1 Conjugated microporous polymers 49
2.3.4.2 Hypercrosslinked polymers 51
2.4 Semiconductor/semiconductor heterojunctions 53
2.4.1 Fundamental of heterojunctions 53
2.4.2 Semiconductor/metal oxide heterojunctions 54
2.4.3 Semiconductor/organic-based semiconductor heterojunctions 55
2.4.4 Semiconductor/MOF heterojunctions 57
2.5 Conclusions and knowledge gaps from the literature 60
2.6 Research objectives 61
Chapter 3 **62**
3.1 Characterisation of photocatalysts 62
3.1.1 Structural and chemical properties 62
3.1.1.1 Powder X-ray diffraction 62
3.1.1.2 Scanning electron microscopy 63
3.1.1.3 Thermogravimetric analysis 64
3.1.1.4 Solid-state nuclear magnetic resonance spectroscopy 64
3.1.1.5 Inductive plasma optical emission spectroscopy 65
3.1.1.6 CHNS-O elemental analysis 65
3.1.1.7 X-ray photoelectron spectroscopy 66
3.1.1.8 Attenuated total reflectance Fourier transform infrared spectroscopy 67
3.1.1.9 Density functional theory 68
3.1.1.10 Transmission electron microscopy 68
3.1.2 Gas sorption and textural properties 69
3.1.2.1 Nitrogen gas adsorption 69
3.1.2.2 H_2, CO_2 and water vapour adsorption 71
3.1.3 Photochemical properties 71
3.1.3.1 Diffuse reflectance ultraviolet-visible spectrometry 71
3.1.3.2 Diffuse reflectance infrared Fourier transform spectroscopy 72
3.1.3.3 Multivariate curve resolution analysis 74
3.1.3.4 Valence band XPS and work function measurements 75
3.1.3.5 Time-correlated single photon counting 77
3.1.4 Gas phase CO_2 photoreduction experiments 78
3.1.4.1 Photocatalytic testing 78
3.1.4.2 CO_2 photoreduction product quantification 81
3.1.4.3 Photocatalytic control tests 82
3.1.4.4 Reported photocatalytic metrics 82
Chapter 4 **86**
4.1 Introduction 86
4.2 Material synthesis 87
4.3 Results and discussion 91
4.3.1 Characterisation of CNNS/Co-ZIF-L heterojunctions 91

4.3.2 CO_2 photoreduction activity and band bending diagram of CNNS/Co-ZIF-L 94
4.3.3 The importance of band bending and band alignment to understand electron flow in MOF-based heterojunctions 97
4.3.4 Screening of CNNS/MOF-based heterojunctions based on their band bending diagram 99
4.3.5 Characterisation of CNNS/Ti-MIL-125-NH_2 heterojunction 105
4.4 Conclusion 110
Chapter 5 **111**
5.1 Introduction 111
5.2 Material synthesis 112
5.3 Results and discussion 113
5.3.1 Hypercrosslinked polymer synthesis and characterisation 113
5.3.2 CO_2 photoreduction activity of hypercrosslinked polymers 116
5.4 Conclusion 121
Chapter 6 **123**
6.1 Introduction 123
6.2 Material Synthesis 124
6.3 Results and discussion 125
6.3.1 Hypercrosslinked polymer characterisation 125
6.3.2 Vibrational analysis during H_2O adsorption 138
6.3.3 Vibrational band analysis in the presence of CO_2 and H_2O under irradiation 142
6.4 Conclusion 145
Chapter 7 **147**
7.1 Findings and achievements 147
7.2 Future plans 149
References 151
Appendix 1 170
Appendix 2 198
Appendix 3 222
Rights and permissions 238

List of Figures

Figure 2.1 Schematic illustration of the electronic structure of a semiconductor. 20

Figure 2.2 Schematic illustration of a typical photocatalytic process occurring in a semiconductor. 21

Figure 2.3 Schematic illustration of the band edge positions of commonly used semiconductors with respect to the thermodynamic potentials of CO_2 reduction to the most commonly formed C_{1+} products. H^+/H_2 and O_2/H_2O reduction potentials are also shown as H_2 and H_2O are often used as the sacrificial agents during CO_2 photoreduction. 22

Figure 2.4 Market price of selected products that can be produced from CO_2 reduction, as a function of the energy content. Reproduced with permission from the American Chemical Society.[20] 30

Figure 2.5 Summary of the main strategies used to improve the photocatalytic efficiency of TiO_2 and its derivatives. 38

Figure 2.6 The surface properties of polymeric g-C_3N_4.[60] Reproduced with permission from the Royal Society of Chemistry. 43

Figure 2.7 Illustration of the MOF design strategy. 44

Figure 2.8 Schematic illustration of an indirect excitation of a MOF crystal. 45

Figure 2.9 Schematic illustration of the CO_2 photoreduction process over Ti/Zr-UiO-66-NH_2.[78] Reproduced with permission from the Royal Society of Chemistry. 46

Figure 2.10 Schematic illustration of (a) the HOMO-LUMO transition of a π-conjugated systems and (b) the HOMO-LUMO transition of a molecular orbital.[80] Reproduced with permission from Elsevier. 47

Figure 2.11 Schematic representation of the incorporation of Re inside the COF skeleton.[83] Reproduced with permission from the Royal Society of Chemistry. 48

Figure 2.12 (a) reaction scheme of the synthesis of CMPs and (b) photographic images of the synthesised CMPs with their corresponding UV-Vis absorption spectra (left) and their photoluminescence spectra (right). [86] Adapted with permission from the American Chemical Society. 50

Figure 2.13 Schematic illustration of the three most commonly investigated heterojunctions. 53

Figure 3.1 Schematic of the X-ray diffraction principle, explaining Bragg's equation. 63

Figure 3.2 Schematic illustration of the sampling configuration of ATR-FTIR. 67

Figure 3.3 Schematic representation of Equation 16 using time-resolved data, where D represents the obtained data (sample spectrum measured at different times), and S and C represent the pure spectra and the concentration time profile of the pure spectra, respectively.[154] Adapted with permission from Elsevier. 74

Figure 3.4 Schematic illustration of the different analytical methods needed to determine the band diagram of a semiconductor using XPS.[155] Reproduced with permission from ChemRxiv. 76

Figure 3.5 Schematic illustration of the timing diagram of a time-correlated single photon coupling histogram.[156] Adapted with permission from Elsevier. 77

Figure 3.6 Photocatalytic gas-solid reactor setup used to evaluate photocatalytic CO_2 reduction: (1) CO_2 cylinder, (2) H_2 generator, (3) mass flow controllers, (4) non return valves, (5) H_2O saturator, (6) photoreactor, (7) Xe arc lamp, (8) pressure transducer, (9) gas chromatograph, (10) vacuum pump.[131] Reproduced with permission from John Wiley and Sons. 79

Figure 3.7 Photographs of the photoreactor system: (a) open photoreactor with photocatalyst mounted onto a metallic disc, (b) closed photoreactor and (c) photoreactor illuminated with a 300 W Xe lamp.79

Figure 3.8 Emission spectra of the Xenon arc lamp used during photocatalytic measurements (300W, LOT Quantum Design). 80

Figure 4.2 Chemical and structural characterisation of the parent materials and CNNS-1/ZIF-L-X heterojunctions (where X refers to the weight percent of MOF used): (a) PXRD patterns; (b) ATR- FTIR spectra; (c) N_2 sorption isotherms at -196 °C; (d - f) TEM images. 92

Figure 4.3 (a) CO_2 sorption isotherms at 25 °C, (b) UV-Vis absorption spectra of CNNS-1, Co-ZIF-L and CNNS-1/ZIF-L-22, (c) CO photocatalytic production rates of CNNS-1, Co-ZIF-L and CNNS-1/ZIF-L-X heterojunctions (note: X corresponds to the weight percent of MOF used). 94

Figure 4.4 Band diagram between two distinct n-type semiconductors a) before and b) after contact. 96

Figure 4.5 Work function measurements of: (a) CNNS-1 and (b) Co-ZIF-L; measured at the secondary cut-off, which represents the low kinetic region of the XPS spectra, where the kinetic energy of the detected photo-electrons is equal to zero, and (c) band bending diagram of CNNS-1/Co-ZIF-L heterojunction before and after contact. The delta symbol used in figure c) represents the difference between the fermi levels of both heterojunction components. 97

Figure 4.6 High resolution XPS of Co-ZIF-L and CNNS-1/ZIF-L-22 Co 2*p* and O 1*s* core level spectra showing an identical shift towards lower binding energies upon heterojunction formation. Consequently, the Co 2*p* - O 1*s* peak separation (Δ) is invariant upon heterojunction formation. 98

Figure 4.7 Structural representation of a) the pores and b) metal cluster of Ti-MIL-125-$NH_{2..}$ Adapted with permission from Elsevier.[179] 100

Figure 4.8 SEM images of (a) Co-ZIF-67 NS, (b) CoNi-ZIF-67 NS, (c) Ni-ZIF-67 NS, and (d) Ti-MIL-125-NH_2, and their corresponding (e) PXRD patterns and (f) UV-Vis absorbance spectra. 102

Figure 4.9 Band bending diagram of CNNS-1/Co-ZIF-67 NS, CNNS-1/CoNi-ZIF-67 NS, CNNS-1/Ni-ZIF-67 NS and CNNS-1/Ti-MIL-125-NH_2 heterojunctions (a) before and (b) after contact. 104

Figure 4.10 Work function measurements of: (a) CNNS-2 and (b) Ti-MIL-125-NH_2; (c) band bending diagram of CNNS-2/Ti-MIL-125 heterojunction before and after contact. 106

Figure 4.11 Ti-MIL-125-NH_2 and CNNS-2/MIL-25 O^{2-} (oxide) and Ti 2*p* 3/2 components of the O 1*s* and Ti 2*p* spectrum showing an identical shift towards lower binding energies upon heterojunction formation. Consequently, the O^{2-} - Ti 2*p* 3/2 peak separation (Δ) is invariant upon heterojunction formation. This observation can be explained by Equations A1.1 - A1.2 in Figure A1.11. 107

Figure 4.12 (a) UV-Vis absorption spectra of CNNS-2, Ti-MIL-125-NH_2 and CNNS-2/MIL-25, (b) photocatalytic CO evolution rate of CNNS-2, Ti-MIL-125-NH_2 and CNNS-2/MIL-25 heterojunction under UV-Vis irradiation, (c) CO evolution rates after repeated photocatalytic measurements and (d) kinetic study of CO_2 photoreduction using CNNS-2/MIL-25. 109

Figure 5.1 (a) Reaction scheme for the production of HCP-3 by Friedel-Crafts alkylation, (b) representative chemical structures of HCP repeat units, (c) N_2 adsorption isotherms at -196 °C, filled symbols represent adsorption and empty symbols represent desorption, (d) CO_2 uptake at 1 bar and 25 °C for HCPs in both 'dry' and 'wet' states, i.e. HCPs exposed to a humid atmosphere before measurement, (e) pore size distributions of HCPs, calculated using the density functional theory (DFT) method. 114

Figure 5.2 (a) UV-Vis absorption coefficient spectra with absorption onsets indicated, (b) photoluminescence decay kinetics probed at 700 nm following excitation at 282 nm, along with the instrument response function (IRF) probed at the excitation wavelength, (c) band structures based on the X-ray photoelectron spectroscopy (XPS) and DR-UV/Vis analyses, (d) photocatalytic production rates using sacrificial H_2 in UV-Vis, (e) photocatalytic production rates using sacrificial H_2O in both UV-Vis and visible light alone, (f) HCP-3 recyclability test over 5 cycles of 3 h irradiation using UV-Vis light and sacrificial H_2O. 117

Figure 5.3 (a) H_2 and (b) H_2O adsorption isotherms at 25 °C. Filled symbols represent adsorption and empty symbols represent desorption. The inset in (a) shows the H_2 isotherms with a smaller y-axis for clarity. 120

Figure 6.1 Overview of the chemical, structural and optoelectronic features of the triazine-biphenyl HCP sample: (a) synthesis reaction scheme (inset shows a photograph of the polymer), (b) atomic composition based on CHNS-O analysis, (c) solid-state ^{13}C NMR spectra, (d) N_2 sorption isotherm at -196 °C (filled symbols = adsorption; empty symbols = desorption) and (e) UV-Vis absorption coefficient spectrum with absorption onset. 126

Figure 6.2 (a) CO_2 and (b) H_2O sorption isotherms at 25 °C and 50 °C of the studied triazine-biphenyl HCP. Filled symbols = adsorption; empty symbols = desorption. 127

Figure 6.3. Vibrational analysis and band assignment for the triazine-biphenyl HCP sample: (a) simulated infrared spectra of one and six triazine molecules, experimental ATR infrared spectrum of an 80 nM triazine monomer solution and triazine monomer powder. (b) Simulated infrared spectrum of one biphenyl monomer molecule and experimental ATR infrared spectrum of the biphenyl monomer powder. (c) Comparison between the ATR infrared spectra of the triazine and biphenyl monomer with that of the

triazine-biphenyl HCP. (d) Comparison between the ATR-IR and DRIFT spectra of the HCP and the simulated one. 130

Figure 6.4 Representation of the spectral components obtained upon processing the difference spectrum using MCR. (a) The represented difference spectrum corresponds to the average of the difference spectra acquired under a CO_2 atmosphere at 50 °C, and (b) the represented difference spectrum corresponds to the average of the difference spectra acquired under 133

Figure 6.5 Representation of the origin of positive and negative bands in a difference spectrum. Panel (a) illustrates the type of difference spectrum obtained upon a red shift of the vibrational bands of a material compared to its background spectrum. Panel (b) illustrates the type of difference spectrum obtained upon a blue shift of the vibrational bands of a material compared to its background spectrum. 134

Figure 6.6 DRIFTS study of CO_2 adsorption on HCP. Left panels of (a) and (b): comparison between the DRIFT infrared spectrum of the triazine-biphenyl HCP sample with the positive (a) and negative (b) spectral components obtained for CO_2 adsorption measurements at 50 °C, 100 °C and 150 °C after performing MCR analysis. The right panels of (a) and (b) represent the component concentration profiles obtained by MCR, which illustrate the contribution of the spectral component to the overall spectra over time. (c) Comparison between the ATR infrared spectrum of the triazine monomer with the positive spectral components obtained for CO_2 adsorption measurements at 150 °C after MCR analysis. (d) Illustration of the CO_2 adsorption sites in triazine-biphenyl HCP. 136

Figure 6.7 DRIFTS study of H_2O adsorption on HCP. (a) Schematic illustration of the spectral components obtained after processing the difference spectrum using MCR. The difference spectrum corresponds to the average of the difference spectrum acquired under a H_2O atmosphere at 50 °C. Left panels of (b), (c) and (d): comparison between the DRIFT spectrum of the triazine-biphenyl HCP sample with: water vapour (b), the positive (c) and negative (d) spectral components obtained for H_2O adsorption measurements at 50 °C and 100 °C after performing MCR analysis. Right panels of (b), (c) and (d): component concentration profiles obtained by MCR. (e) Illustration of the H_2O adsorption sites in HCP. 140

Figure 6.8 MCR components extracted from DRIFTS measurements during CO_2 and H_2O co-adsorption HCP under intermittent light irradiation. (a) Comparison between the DRIFT spectrum of the triazine-biphenyl HCP sample with that of water vapour (A), and the positive (B, C, D, E) spectral components obtained under a CO_2/H_2O atmosphere and transient UV-Vis irradiation at 50 °C. (b) Component concentration profiles were obtained by MCR. 143

Figure 6.9 Schematic illustration of the impact of light irradiation upon CO_2 and H_2O interactions with the HCP. It highlights the changes in the number of interactions between the HCP and the substrates. The latter is relative to the number of interactions detected under light off. 144

List of Tables

Table 2.1 CO_2, H_2O and H_2 reduction potential vs NHE at pH=0. 26

Table 2.2 Gibbs free energy of CO_2 reduction when using H_2 or H_2O as reducing agent. 27

Table 2.3 Examples of studies that used in-situ ATR-IRS and/or DRIFTS to study CO_2 photoreduction. 34

Table 2.4 Strengths and weaknesses of in-situ XPS, XAS, EPR, and FTIR characterisation techniques. 35

Table 2.5 Strengths and weaknesses of electrochemical, thermal, biochemical and photocatalytic approaches to convert CO_2. 37

Table 2.6 Summary of the strengths and weaknesses of 'traditional' photocatalysts, i.e. TiO_2, non-titanium metal oxides, metal sulfides and metal selenides, including their product selectivity, overall efficiency, and most studied reaction phase for CO_2 photoreduction. 40

Table 2.7 Summary of the strengths and weaknesses of emerging classes of organic-based porous photocatalysts, i.e. g-C_3N_4, MOFs, COFs, CMPs and HCPs, including their product selectivity, overall efficiency, and most studied reaction phase for CO_2 photoreduction. 52

Table 2.8 Examples of semiconductor/metal oxide-based photocatalysts developed for CO_2 photoreduction. 55

Table 2.9 Examples of g-C_3N_4 and COFs-based heterojunctions for CO_2 photoreduction. 57

Table 2.10 Examples of MOF-based heterojunctions developed for CO_2 photoreduction. 59

Chapter 1

Introduction

1.1 Thesis outline

The content of this thesis follows a sequential structure that guides the reader through a series of chapters with details depicting each stage of this research and a summary of the conclusion that was reached at each stage. Chapter 1 outlines the scientific and personal motivations for undertaking this specific research project. Chapter 2 presents the theory and the background research surrounding my investigations into photocatalytic CO_2 conversion. As a result of Chapter 2, I defined my research objectives which are provided at the end of the chapter. Chapter 3 describes the techniques and methods used to collect the results necessary to conduct the research. Chapters 4, 5 and 6 present and discuss the results obtained. Finally, Chapter 7 provides the conclusion of the thesis.

1.2 Background

Addressing climate change and the global energy crisis is a matter of urgency. To drastically reduce our reliance on fossil fuels, we must reshape our energy portfolio and increase the proportion of renewables. In this regard, the use of sunlight to produce fuels and value-added chemicals presents a unique opportunity to address this need. Each day, the sun provides more than 10,000 times the global energy demand and could hence be used to build a sustainable chemical industry while addressing the energy crisis.[1] Solar fuel production can be achieved by producing H_2 from H_2O, and C_1 and C_{1+} chemicals from CO_2 via photochemical, thermochemical, and electrochemical processes. However, in order to minimize the energy required for conversion and render these processes viable, a catalyst is required. This thesis focuses on developing catalysts for CO_2 photoconversion, a photochemical route towards solar fuel production.

To date, numerous metal oxides and metal selenides have been investigated as catalysts for CO_2 photoreduction, however, their activity remains too low for industrial applications and their lack of structural diversity represents a major obstacle towards improving their photocatalytic performance. Thus, research in this field focuses on exploring and developing new classes of photocatalysts with a high degree of versatility such as metal-organic frameworks (MOFs) and porous organic polymers (POPs). This thesis aims to investigate the potential of emerging porous carbon-based photocatalysts for CO_2 photoreduction to value-added chemicals. Specifically, I explored and designed new MOF-based heterojunctions and hypercrosslinked polymers (HCPs) for CO_2 photoreduction in the gas phase.

1.3 Personal motivations

Since witnessing my first lecture on MOFs given by Prof K. C. Stylianou during my Master's degree at École Polytechnique Fédérale de Lausanne, I have been fascinated by this emerging class of materials. Their crystalline structure combined with their high degree of versatility presents a vast opportunity for structural and functional exploration. It was evident that part of my PhD would involve working with MOFs to gain a better understanding of this field. Investigating MOFs for photocatalytic applications allowed me to contribute to cutting-edge research on the topic while simultaneously addressing the pressing environmental and energy production challenges that we face today.

Also, during my Master program, I had the opportunity to work with polymer hybrid MOFs, which developed my interest for amorphous polymers. I therefore decided to dedicate the second half of my PhD to investigating amorphous porous polymers for photocatalytic purposes. This class of materials has only recently been introduced for photocatalysis, therefore it represented a unique opportunity to pursue a subject I am passionate about while contributing to new scientific research in an emerging field.

Overall, the combination of these topics provided the foundation for this thesis and have been the source of motivation for both my academic work throughout this PhD and ultimately a guide for my future professional endeavours.

Chapter 2

Literature review

As this project aims to investigate new porous organic-based photocatalysts for CO_2 photoreduction, this literature review begins with an overview of the fundamentals of photocatalysis and CO_2 photoreduction. Subsequently, the literature review focuses on the main trends adopted in the design of traditional photocatalysts for CO_2 photoreduction. This section also provides insights into the key remaining challenges faced by traditional photocatalysts, which prompted the development of new classes of photoactive materials. In addition, an in-depth review of the main strategies used in the design of emerging organic-based photocatalysts for CO_2 photoreduction is provided. The latter includes advances made in the field of metal-organic frameworks (MOFs), covalent organic frameworks (COFs) and amorphous porous organic polymers. Finally, the literature review outlines the different strategies used to enhance the photoreduction activity of traditional and emerging organic-based photocatalysts via heterojunction formation.

2.1 Photocatalysis

2.1.1 Fundamental of photocatalysis

Photocatalysis refers to the use of a photocatalyst that absorbs light and uses this energy to promote a chemical reaction. The photocatalyst is typically a semiconductor. Hence, before further exploring the core concept of photocatalysis, I will briefly summarise some important characteristics of the electronic structure of a semiconductor.

2.1.1.1 Electronic structure of a semiconductor

Semiconductor materials display of a band gap (E_g) defined as the energy difference between the valence band (VB) and the conduction band (CB) (Figure 2.1).[2, 3] The energy of the VB represents the highest energy occupied by electrons at absolute zero temperature, while the energy of the CB represents the lowest energy of vacant states.[2] The magnitude of E_g defines the energy needed to promote an electron from the VB to the CB; the larger the band gap, the more energy is required. The

vacuum level (E_{vac}) corresponds to the energy of an electron at rest (i.e. with zero kinetic energy with respect to the sample surface) just outside the semiconductor surface.[2, 3] The Fermi level energy (E_F) is defined as a hypothetical energy level that has a 50% probability of being occupied by an electron at any given time.[4] The position of the Fermi level with respect to the VB and the CB can be used to determine the electrical properties of a semiconductor.[2] The last important concept to be defined is the work function (W_F) of a semiconductor, which represents the energy needed to remove an electron from the Fermi level to the E_{Vac}.[3]

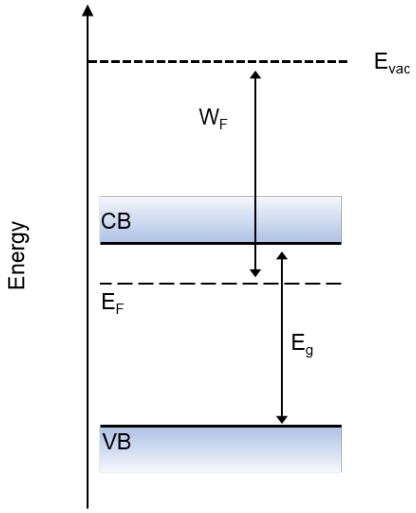


Figure 2.1 Schematic illustration of the electronic structure of a semiconductor.

2.1.1.2 Photocatalytic process

As Figure 2.2 illustrates, upon light irradiation of a semiconductor, photons are absorbed, exciting electrons from the VB to the CB and generating a positive charge, i.e. a hole, in the VB. The photogenerated electrons and holes are often referred to as charge carriers. This process only occurs if the incoming photons carry equal or higher energies than the E_g of the semiconductor. Once irradiated, the photogenerated charge carriers migrate to the photocatalyst surface where the photoexcited electrons will reduce adsorbed molecules, while the holes will act as oxidative species. At any time, electron-hole recombination can occur at the surface and within the bulk of the photocatalyst. Such phenomenon inhibits photocatalysis as the number of available photogenerated charge carriers decreases over time.

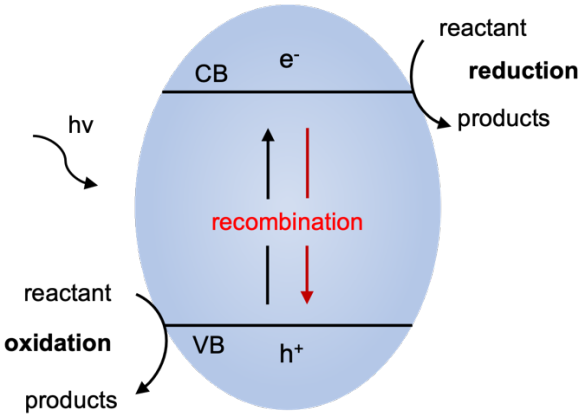


Figure 2.2 Schematic illustration of a typical photocatalytic process occurring in a semiconductor.

2.1.1.3 Photocatalysts requirements

When selecting a photocatalyst for a specific application, one needs to consider several parameters. First, one needs to evaluate its band edge positions, which determine if the photocatalyst will be able to catalyse a specific reaction. The CB potential should be more negative than that of the reduction reaction, while the VB potential should be more positive than that of the oxidation reaction.[5] For instance, to reduce CO_2 to CO using H_2 as proton source, the CB and the VB must be respectively located above -0.12 V and below 0 V vs normal hydrogen electrode (NHE) at pH=0 (Figure 2.3).[6]

Second, one must consider the light absorption properties of the photocatalyst. As 43% of the solar energy is in the visible range (400 - 750 nm) and only 4% in the UV range (10 - 400 nm), visible-light photocatalysts are needed to efficiently use the sunlight. Consequently, small band gap photoresponsive materials are preferred as they absorb visible light, leading to higher charge carriers formation and correspondingly to higher photocatalytic activity. However, when minimizing the band gap one needs to beware of the band edge positions of the photocatalyst.

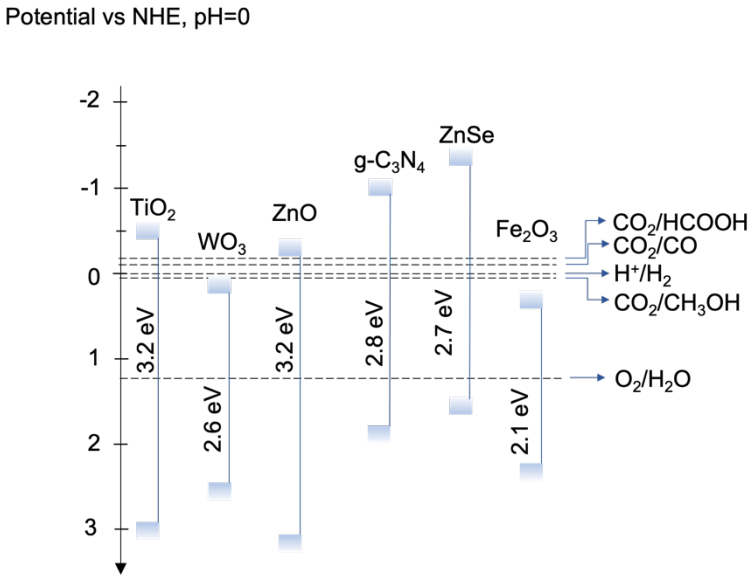


Figure 2.3 Schematic illustration of the band edge positions of commonly used semiconductors with respect to the thermodynamic potentials of CO_2 reduction to the most commonly formed C_{1+} products. H^+/H_2 and O_2/H_2O reduction potentials are also shown as H_2 and H_2O are often used as the sacrificial agents during CO_2 photoreduction.

Third, one needs to consider charge dynamics. Charge recombination is a competing and undesirable process that can take place within picoseconds while the desired photocatalytic process usually takes place in the order of nanoseconds.[7] Thus, to effectively transfer charges from the photocatalyst to the adsorbed species, the photocatalyst should display charge carrier lifetimes in the range of nanoseconds. The higher the charge carrier lifetime, the better.

Fourth, a photocatalyst should be porous enough to allow good substrate diffusion and adsorption. Finally, the chosen photocatalyst should exhibit selective substrate affinities to favour adsorption of the desired substrate over undesired ones. Lack of substrate selectivity often leads to the formation of undesired products and lowers the production rate of the target product.

Fulfilling all these requirements is not an easy task and developing photocatalysts with all desired characteristics represents the major challenge in the field.

2.1.1.4 Photocatalytic metrics

Reporting and comparing the photoactivity of distinct photocatalysts is complex and often confusing in the current literature as it is set-up dependent. The number and energy of photons reaching the catalyst surface depend on the light source, the type of reactor and the photocatalyst preparation/deposition.[8] Thus, one cannot directly compare the observed photoactivity of distinct photocatalysts when measured in different set-ups. However, various metrics are available to report the photocatalytic activity and facilitate comparison.

First, a normalized yield can be calculated. The latter is defined as the ratio of the photocatalyst activity to the activity of a reference photocatalysts measured under the same experimental conditions.[8] To compare the normalized yield of distinct photocatalysts, the reference catalyst needs to be identical. To date, owing to its wide commercial use and its well-studied photoactivity, Degussa TiO_2 P25 is commonly used as the reference material. Despite the simplicity of this approach, it assumes that the activity of both the photocatalyst and the reference material are equally affected by the experimental conditions, which may not always be true. For example, in the UV region where TiO_2 P25 is mostly active, experimental condition changes that do not affect the UV region might not affect the photoactivity of TiO_2 P25 in the same manner as that of the studied photocatalyst. Nonetheless, comparing normalized yields remains an effective and simple method.

The Apparent quantum yield (AQY) is another commonly used metric. From an engineering point of view, it is important to quantify the number of products produced per incident photons, i.e. input vs output. The AQY is defined as the number of reacted electrons divided by the number of incident photons reaching the catalyst's surface at a given wavelength (Equation 1):[9-11]

$$\mathrm{AQY}(\lambda)(\%) = \frac{\text{number of reacted electrons}}{I\,(\lambda)} x100 \qquad (1)$$

where: $\mathrm{AQY}(\lambda)$ is the apparent quantum yield, and $I\,(\lambda)$ is the number of incident photons reaching the catalyst surface at a given wavelength.

The AQY is commonly measured at 420 nm and consequently requires monochromatic light. Hence, this metric does not take into account that the number of reacted electrons depends on the number of photoexcited electrons, which in turn depends on the excitation wavelength.

Another commonly used metric is quantum efficiency (QE). From a mechanistic point of view, it is of interest to quantify the amount of product formed per absorbed photons. The QE is defined as the amount of product formed divided by the total absorbed photon flux (Equation 2).[9, 11]

$$\mathrm{QE} = \frac{\text{rate of reactant consumed or product formed}}{q_p} \quad (2)$$

where: QE is the quantum efficiency and q_p is the absorbed photon flux.

Finally, from a practical point of view, it is important to report the photocatalytic conversion rate. For industrial applications, the ultimate requirement is to achieve conversion rates in the range of $mol.g^{-1}.h^{-1}$.

In summary, different metrics are reported in different studies making comparison throughout literature difficult. To facilitate comparison across literature and to better evaluate the efficiency of a photocatalyst, it is recommended to report several photocatalytic metrics whenever possible. However, other factors such as temperature and pressure can impact substrate diffusion and the adsorption/desorption process, thereby affecting the photoactivity. Such factors are not considered in the aforementioned metrics. Thus, when reporting photocatalytic activities, it is important to specify in detail all relevant experimental conditions. Doing so enables one to decide whether the comparison between distinct photocatalysts is substantiative. I refer the reader to Qureshi et al. and Melchionna et al. for a more comprehensive discussion of the topic.[9, 11]

2.1.2 Photocatalytic CO_2 reduction

2.1.2.1 Motivation for CO_2 photoreduction

Combining CO_2 reduction with photocatalysis to transform CO_2 into value-added chemicals and synthetic fuels represents a unique opportunity to mitigate climate change and address the energy crisis. The cheap and abundant feedstock of both sunlight and CO_2 makes CO_2 photoreduction highly attractive. Photocatalytic CO_2 reduction has shown great promise towards carbon-based fuel production, however, it still faces numerous challenges.

2.1.2.2 CO_2 photoreduction mechanism

CO_2 reduction is a multi-electron transfer process that can be decomposed into 4 steps:

1. CO_2 adsorption
2. CO_2 activation
3. Product formation (C=O dissociation, new bond formation)
4. Product desorption

The first step involves adsorption of CO_2 and the reductants. This step initiates the photocatalytic process by creating a contact between the substrate and the photocatalytic site. Adsorption is dependent on the surface chemistry, porosity and the pore structure of the photocatalyst, which determine substrate diffusion and the number of available adsorption sites. In this regard, multimodal pores will facilitate diffusion, while high surface area and functional groups can enhance CO_2 adsorption.[12] The subsequent steps involve CO_2 activation and product formation. CO_2 activation refers to lowering the C=O dissociation energy to facilitate the formation of intermediate species. CO_2 activation can be promoted by increasing the affinity/interaction of CO_2 with the photocatalyst adsorption sites by modifying the functional groups of the photocatalyst surface. Finally, the last steps of CO_2 photoconversion is product desorption. For the latter to occur, the affinity of CO_2 with the photocatalyst should not be too strong; therefore, one needs to find a balance between CO_2 activation and product desorption.

2.1.2.3 Thermodynamic considerations

When performing CO_2 photoreduction, one must consider the system's thermodynamics to understand the energy required by the process and how it can be minimized.

Gibbs free energy

The energy required to convert CO_2 can be approximated by the Nernst equation and will depend on both the reduction and oxidation reactions (Equations 3 and 4).

$$\Delta G = -nFE_{cell} \quad (3)$$

$$E_{cell} = E_{cathode} - E_{anode} \quad (4)$$

where:

ΔG: Gibbs free energy (J.mol^{-1}); n: number of electrons transferred in the reaction; F: Faraday constant (96 500 C.mol^{-1}); E_{cell}: potential of the cell (J.C^{-1}); $E_{cathode}$: potential of the cathode (J.C^{-1}); E_{anode}: potential of the anode (J.C^{-1}).

As Table 2.1 illustrates, by targeting a specific product, one can minimize the energy input needed. For example, from a thermodynamic perspective, CH_4 production is easier to achieve than CO production (reactions 3 and 6 of Table 2.1).[13]

Table 2.1 CO_2, H_2O and H_2 reduction potential vs NHE at pH=0.

Number	Reactions	Reduction potential vs NHE at pH=0 (V)
1	$CO_2 + e^- \rightarrow CO_2^-$	-1.90
2	$CO_2 + 2H^+ + 2e^- \rightarrow HCOOH$	-0.2
3	$CO_2 + 2H^+ + 2e^- \rightarrow CO + H_2O$	-0.12
4	$CO_2 + 4H^+ + 2e^- \rightarrow HCHO + H_2O$	-0.07
5	$CO_2 + 6H^+ + 6e^- \rightarrow CH_3OH + H_2O$	0.04
6	$CO_2 + 8H^+ + 8e^- \rightarrow CH_4 + H_2O$	0.18
7	$O_2 + 4H^+ + 4e^- \rightarrow 2H_2O$	1.23
8	$H^+ + 2e^- \rightarrow H_2$	0

However, to assess the overall energy required to convert CO_2, one needs to consider the full reaction. The choice of the reducing agent will also impact the required energy input. For instance, using H_2 as reducing agent over H_2O is thermodynamically more favourable (reactions 7 and 8 of Tables 2.1). To convert CO_2 to CO using H_2 as the reducing agent requires 22.6 kJ.mol^{-1} compared to 513 kJ.mol^{-1} when using H_2O (Table 2.2).

Table 2.2 Gibbs free energy of CO_2 reduction when using H_2 or H_2O as reducing agent.

Number	Reactions	ΔrG (kJ.mol^{-1})
1	$CO_2 + H_2 \rightarrow CO + H_2O$	22.6
2	$CO_2 + H_2O \rightarrow CO + O_2 + H_2O$	513

Another important thermodynamic factor to take into account when performing CO_2 photoreduction is the band edge positions of the photocatalyst.[13] For the reduction and oxidation reactions to occur, the CB potential should be more negative than that of the reduction reaction, and the VB potential should be more positive than that of the oxidation reaction. The reduction potentials tabulated in Table 2.1 are for liquid systems and thus are not necessarily well-suited to assess the capability of a photocatalyst to reduce/oxidize substrates in the gas phase. However, reduction potentials in the gas phase cannot be measured and therefore, one has to use the liquid phase values even if they are only indicative.

Product selectivity

Thermodynamics can also be used to understand product selectivity. From a thermodynamic perspective, product selectivity is influenced by the reduction and oxidation potentials of the formed product. As mentioned above, CO_2 photo-conversion to CH_4 and CH_3OH is thermodynamically more favourable than CO_2 conversion to CO. The former products require a potential of 0.04 and 0.18 V, respectively, compared to -0.12 V for the latter. In addition, the reaction selectivity is influenced by the values of CB and CV of the photocatalysts. For instance, if the photocatalyst does not display the required reduction potential to reduce CO_2 to CO, CO cannot form, while other products might.

Overall, the thermodynamic analysis of CO_2 photoreduction informs on the required input energy and how to minimize it, as well as how to control product selectivity. However, such analysis only takes into account the initial and final conditions of the process and does not give information about the speed at which the reaction proceeds, i.e. the rate of the reaction. Thus, when studying CO_2 photoreduction, one should also take into account the reaction kinetics.

2.1.2.4 Kinetics considerations

Diffusion, adsorption, reaction and desorption

To assess the overall kinetics of a reaction, one needs to look at the kinetics of each elementary step.[14] For CO_2 photoreduction, we have four key steps:

1. Diffusion of reactants from the bulk phase to the catalytic sites
2. Adsorption of the reactants onto the catalytic sites
3. Reaction
4. Desorption of products from the surface.

The first two elementary steps depend on temperature, pressure, gas phase composition, as well as photocatalyst morphology and porosity. To increase diffusion rates, one can reduce the crystal size and select photocatalysts displaying larger pores such as mesopores (2 - 50 nm) and macropores (> 50 nm). However, catalysts displaying larger pores often exhibit reduced thermal stability and chemical activity.[15] Thus, selecting photocatalysts displaying a combination of micro-, meso- and even macro-pores is considered the most promising strategy to favour faster diffusion rates while retaining the photocatalytic activity.[15] The third and fourth elementary steps, which involve the reaction and product desorption, can be tuned by tailoring the affinity/interaction of the reactants/products with the photocatalyst adsorption sites. One needs to find a balance between reactant activation and product desorption.

Product selectivity

Kinetics can also influence product selectivity. While thermodynamic selectivity determines which product will be predominantly produced based on the energy required, kinetic selectivity determines which product will be favoured based on the conversion rate.[16] As Table 2.1 shows, CO_2 conversion often requires a transfer of two or more electrons. The more electrons required, the more kinetically challenging the reaction will be. As H_2 evolution is a two-electron transfer process (reaction 8 table 2.1), it represents a kinetically more favourable reaction compared to CO_2 conversion and thus competes with CO_2 reduction. In some cases, H_2 evolution can be inhibited by enhancing CO_2 activation, which can be achieved by increasing the strength of CO_2 adsorption. As explored by Yu et al., the presence of amino groups can suppress H_2 evolution and favour CO_2 reduction to CO. Yet, despite the numerous

effort undertaken to suppress H_2 evolution, selective reduction of CO_2 over H_2 evolution still remains a key challenge in the field.[17]

Kinetics also impacts carbonaceous product selectivity. For instance, from a kinetic point of view, CH_4 is more difficult to produce than CO as CO_2 conversion to CH_4 requires eight electrons while CO_2 conversion to CO requires only two. Controlling kinetic selectivity remains a challenging task as it often relates to the type of intermediate formed which is influenced by various factors such as the physicochemical properties of the photocatalyst and the reaction phase (liquid vs gas phase).[16]

2.1.2.5 Liquid vs gas phase

To yield high CO_2 photoconversion, the reducing agent, CO_2, photons, and the photocatalyst need to be in contact. Therefore, the reaction medium needs to be carefully chosen.[18] Until 2000, CO_2 photoreduction was mostly carried out in liquid-phase reactors.[19] However, such reactors suffer from limited CO_2 mass transfer from the gas phase to the catalyst surface, poor light utilisation, difficult catalyst dispersion, complex product separation and problematic scale-up. More recently, the use of gas-phase reactors has become popular as they facilitate CO_2 adsorption/activation on the photocatalyst and enable to tune the CO_2 to reducing agent ratio towards optimal activity. In addition, as above mentioned, one needs to consider that the reaction medium influences product selectivity. In gas-phase reactions, CO_2 is reduced to the lowest oxidation state of carbon, driving the reaction selectivity towards CO and CH_4 production. For instance, in the gas phase g-C_3N_4 and TiO_2 produce CO, however, in the liquid phase products with carbons in intermediate oxidation states are favoured, promoting formic acid, methanol, and formaldehyde production.[18]

In summary, gas phase media are advantageous for CO_2 photoreduction; however, depending on the desired final product, one might nevertheless have to choose a liquid phase medium.

2.1.2.6 The economic importance of CO_2 photoreduction products

As mentioned in the above sections, in order to control product selectivity one has to take into account thermodynamics, kinetics, and the phase of the reaction (i.e liquid vs gas). As Figure 2.4 shows, the different products produced by CO_2 photoreduction have distinct techno-economic perspectives. Ethylene and ethanol represent good compromises between profitable niche markets and impactful

mass markets for CO_2 reduction, however, in photocatalysis their production rates are often limited by slow kinetics.[20] Of major interest is also pure CO, which is widely used for the production of methanol and liquid hydrocarbon fuels via the Fisher-Tropsch process. Its favourable kinetic makes it one of the most attractive CO_2 photoreduction products.

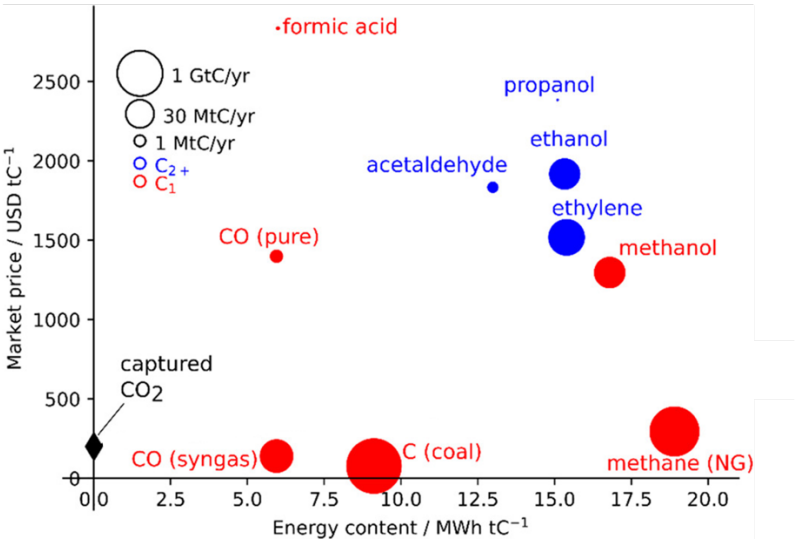


Figure 2.4 Market price of selected products that can be produced from CO_2 reduction, as a function of the energy content. Reproduced with permission from the American Chemical Society.[20]

2.1.2.7 Investigate CO_2 photoreduction mechanisms and adsorption processes

Available in-situ characterisation techniques

Given the complexity of CO_2 photoreduction, photocatalysts are commonly developed using a trial-and-error approach. Yet, gaining a better understanding of what happens at the molecular level is of high importance to design efficient photocatalysts.[21] Monitoring in real-time the active adsorption site, the reaction intermediates, and product formation in a controlled atmosphere (in-situ) or under experimental conditions (operando) is essential to establishing the relationship between the photocatalyst activity/selectivity and its structure.[21, 22] Both in-situ and operando characterisation techniques are currently used to investigate CO_2 photoreduction. The most common ones are reviewed below, with a particular emphasis on in-situ Fourier transform infrared (FTIR) spectroscopy.

Near-ambient pressure X-ray photoelectron spectroscopy (NAP-XPS) is a powerful in-situ characterisation technique. Upon X-ray irradiation, XPS probes the kinetic energy of the photoelectrons emitted by the sample, which is related to the chemical environment of the atoms it contains (for more details see Section 3.1.1.7).[23] For each element, time-resolved in-situ NAP-XPS can detect changes in coordination environment and oxidation state. In-situ NAP-XPS is also used to detect reaction intermediates and track the photocatalyst composition throughout the experiment.[24, 25] For instance, Tashibi et al. explored the influence of Pt on the product selectivity of TiO_2 for gas-phase CO_2 photoreduction.[26] Under light irradiation, using in-situ NAP-XPS, carbonate species and single-site CO molecules were detected on Pt sites. Once irradiation stopped, the adsorbed CO molecules did not desorb, which favoured total CO reduction to CH_4 and explained the high product selectivity of Pt/TiO_2 towards CH_4 production. When using in-situ NAP-XPS, one must monitor sample degradation during analysis and keep in mind that this technique can only be used to study gas-solid systems.

X-ray absorption spectroscopy (XAS) has also been reported as an in-situ characterisation technique for catalytic reactions.[25] XAS is a synchrotron-based technique that measures the X-ray beam attenuation at defined wavelengths. XAS can be divided into two types: X-ray absorption near edge structure (XANES) and extended X-ray absorption fine structure (EXAFS). For a given element, XANES probes the region up to 100 eV above the absorption edge, while EXAFS probes the region from 100 eV up to 2000 eV.[27] The absorption edge of a chemical element is defined as a steep increase in X-ray absorption. The latter occurs when the incident photon's energy corresponds to the minimum energy required to excite an electron to an excited state. XANES looks at the absorption spectra obtained when exciting electrons from core orbitals to unoccupied valence orbitals, probing the oxidation state, covalency and the coordination geometry of an element.[23] EXAFS analyses the energy absorbed caused by the scattering of ionized electrons. It gives information on the distance, the number, and the type of neighbouring atoms of a given element.[27] During CO_2 photoreduction, in-situ XANES and EXAFS can monitor in real-time the above-mentioned properties for all the elements present in the photocatalyst. For example, Yuang et al. investigated the dynamic chemical composition of a Cu/TiO_2 photocatalyst during gas-phase CO_2 photoreduction with water vapour as a reducing agent.[28] Using in-situ XANES, under light irradiation, Cu(II) was found to gradually reduce to Cu(I) and finally to Cu(0). Compared to the initial composition, the final Cu(I)/Cu(0) mixture was found to promote CH_4 production

and favour higher photoactivity compared to the Cu(II)/TiO_2. This study highlights the importance of monitoring the chemical composition of a photocatalyst under operando conditions as it determines the true link between catalyst structure and the photoactivity. While certainly a very powerful technique, in-situ XAS requires access to a synchrotron facility.

Another commonly used in-situ characterisation technique is in-situ electron paramagnetic resonance (EPR) spectroscopy.[25] This technique probes molecules that contain unpaired electrons. When exposing an electron to a magnetic field, its spin vector aligns either parallel or antiparallel to the magnetic field, creating two distinct spin states. The energy difference between these two spin states is referred to as transition energy. Upon microwave irradiation, absorption of the incoming wave occurs when its energy is equal to the transition energy. However, when electrons are paired, their spins are required to be antiparallel and therefore cannot flip in a magnetic field; consequently, no EPR signal will be detected. Thus, by monitoring in-situ EPR one can detect in real-time the formation of a radical intermediate. In addition, as the EPR signal depends on the environment of the unpaired electron, in-situ EPR can identify the radical intermediate. For CO_2 photoconversion, in-situ EPR is used to detect reduced intermediate species such as $CO_2^{\bullet-}$, as well as oxidized intermediate species.[29] This was for instance demonstrated by Wang et. al. using BiOBr/NiO for CO_2 photoreduction with water vapour as the reducing agent.[30] Under light irradiation, $^{\bullet}OH$ radicals were detected, which demonstrated the strong oxidation power of BiOBr/NiO, and therefore confirmed the valence band potential obtained by Mott-Schottky experiments. Overall, in-situ EPR is a very sensitive technique to identify intermediate spices, however, its scope is limited to the detection of unpaired electrons.

Last but not least, in-situ infrared spectroscopy is a powerful characterisation technique commonly used to identify adsorbed intermediate species.[21] Infrared spectroscopy is based on light absorption by chemical bonds and gives information on the type of functional groups present in a sample. Different detection modes can be used. Attenuated total reflectance infrared spectroscopy (ATR-IRS) probes the portion of light internally reflected, while diffuse reflectance infrared Fourier transform spectroscopy (DRIFTS) probes the diffuse reflection. More information on the operating modes of ATR-IRS and DRIFTS can be found in Sections 3.1.1.6 and 3.1.3.2, respectively. Overall, both ATR-IRS and DRIFTS can be used for in-situ characterisation. ATR-IRS is preferred to study solid-liquid interactions as the liquid can easily penetrate through the sample and enter in contact with the ATR crystal, while DRIFTS

is preferred to study solid-gas interactions as it allows to easily put a gas into contact with the sample's surface. In-situ FTIR spectroscopy techniques are often used to investigate catalytic reactions owing to their fast data acquisition and high surface sensitivity. Both ATR-IRS and DRIFTS have been used to gain a better understanding of gas diffusion, CO_2 adsorption, CO_2 activation, intermediates formation and product selectivity, all of which can be used to optimise CO_2 photoreduction.[31-34] Table 2.3 summarises the findings derived from using in-situ ATR-IRS and DRIFTS to study CO_2 photoreduction.

Table 2.3 Examples of studies that used in-situ ATR-IRS and/or DRIFTS to study CO_2 photoreduction.

Photocatalyst	Technique	Reaction phase	Findings	Ref.
Cu_3SnS_4	ATR-IRS	gas	*Understanding CO_2 activation and reduction mechanism:* Bicarbonate species were detected, suggesting an interaction between surface hydroxyl groups and CO_2. Surface exposed Cu^+ and Cu^{2+} were found to also contribute to CO_2 adsorption. Based on the detected intermediate, a reaction pathway towards CH_4 production was hypothesised.	31
Zn vacancies rich ZnS (V_{Zn}-rich ZnS)	ATR-IRS	liquid	*Understanding product selectivity:* Compared to ZnS which exhibits high H_2 selectivity, V_{Zn}-rich ZnS is selective towards formic acid production due to the formation of bidentate carbonate followed by its transformation to monodentate and bidentate formate intermediates.	32
Tetraethylene pentamine film	ATR-IRS and DRIFTS	gas	*Study of CO_2 mass transfer:* For a thin tetraethylenepentamine film, CO_2 transfers quickly into the bulk. Whereas, when increasing the film thickness, CO_2 diffusion into the bulk is slowed down by the surface formation of interconnected networks of ammonium-carbamate ion pairs.	34
Pt/TiO_2 and Co/TiO_2	DRIFTS	gas	*Understanding product selectivity:* Co/TiO_2 is more selective towards CO production, while Pt/TiO_2 exhibits higher H_2 selectivity due to the fast formate decomposition by Pt.	35
TiO_2@ $ZnIn_2S_4$	DRIFTS	liquid	*Understanding the reaction mechanism:* without irradiation, under a CO_2 and H_2O atmosphere, carbonate species are detected. Subsequently, under irradiation, new carboxylate, formic acid, and methoxy group bands are observed. Based on the detected intermediate species a CO_2 photoreduction mechanism towards CH_3OH and CH_4 production is proposed.	36
Oxygen depleted $Cu(I)/TiO_{2-x}$	DRIFTS	gas	*Understanding CO_2 activation and reaction mechanism:* CO_2 was found to interact with Ti^{3+} to form carboxylate species. The presence of surface Cu^+ and oxygen vacancies favours dissociation of the carboxylate C-O bond. Upon C-O dissociation, the oxygen vacancies are filled and CO is found to interact with Cu^+. By flushing the catalyst with He, the catalyst was regenerated with CO desorption.	37

To summarise, numerous in-situ characterisation techniques are available to investigate CO_2 photoreduction and CO_2 adsorption. Depending on the main purpose of the study, one might select one in-situ characterisation technique over another. As Table 2.4 shows, each characterisation technique has different advantages and limitations. It should be noted that in-situ characterisation techniques can be complementary to each other and therefore multiple in-situ characterisation techniques are often coupled together. To investigate CO_2 photoreduction, coupling in-situ EPR with in-situ FTIR spectroscopy is becoming increasingly popular.

Table 2.4 Strengths and weaknesses of in-situ XPS, XAS, EPR, and FTIR characterisation techniques.

Technique	Strengths	Weaknesses
In-situ XPS	• Straightforward quantification	• Possible sample degradation • For gas-solid systems only • Requires specific instrumentation
In-situ XAS	• Straightforward quantification • Sensitive to oxidation state and the local coordination of the elements • For liquid-solid and gas-solid systems	• Difficult to use on complex systems • Possible sample degradation • Requires access to a synchrotron facility • Requires specific instrumentation
In-situ EPR	• Very sensitive method to detect intermediate species	• Detects only unpaired electrons • For liquid-solid systems only • Requires specific instrumentation
In-situ ATR-IR In-situ DRIFTS	• High surface sensitivity, makes it easy to identify adsorbates • Little sample preparation • Fast acquisition	• Mostly surface-sensitive • Difficult quantification • Requires specific instrumentation

Monitoring active sites and species

Active adsorption sites and active intermediate species are at the core of photocatalysis. Determining the active sites and the active species is key to understanding the activity and product selectivity of a photocatalyst. During CO_2 photoconversion, often various species are formed at the catalyst surface but not all species necessarily participate in the catalytic process. To understand a catalytic mechanism, one needs to differentiate between active and spectator species. This distinction can be done via modulation excitation techniques, which use an external stimulus to perturb the system at a defined

and constant frequency.[21] The chosen stimulus needs to influence the catalytic reaction. For instance, one can change temperature, pH or light flux. Upon perturbation of the system, the reaction parameters linked to that stimulus will be affected and will change at the same periodic frequency as the stimulus. It should be noted that the affected parameter usually displays a phase delayed response to that of the stimulus. To study CO_2 photoreduction, changes in the light flux is the stimulus of choice. Thus, when coupling modulation excitation experiments with time-resolved in-situ characterisation techniques, one can differentiate between spectator and photocatalytic changes.

Another key challenge when analysing in-situ and operando data are overlapping signals/bands, which make accurate data interpretation very challenging.[21] Coupling in-situ techniques and modulation excitation experiments with advanced data processing methods allows to resolve overlapping bands based on the phase delay response of each species driven by the stimulus. A powerful data processing method that detangles overlapping signals is multivariate curve resolution (MCR).[38, 39] How to couple modulation excitation experiments with MCR is further discussed in Chapter 7.

Overall, numerous efforts have been made to develop tools to determine the nature of active sites and active intermediate species. In particular, combining in-situ or operando measurements with modulation excitation experiments and advanced data processing is a very powerful approach, yet not often reported due to the complex implementation of advanced data processing techniques.

2.1.3 Alternative approaches to CO_2 reduction routes

CO_2 conversion to value-added chemicals and fuels can be achieved by electrochemical, thermal, photocatalytic, and biochemical methods.[40] Each of these methods presents different advantages and limitations as briefly summarised below and in Table 2.5.

Electrochemical methods use electrical energy to reduce CO_2.[41] A CO_2 electrolyser is made of a cathode and an anode. By applying a current to the system CO_2 reduction occurs at the cathode while water is oxidized at the anode. To promote faster conversion rates a catalyst can be deposited on both electrodes. Electrochemical methods are promising technologies for CO_2 reduction owing to the mild operation conditions, the relatively easy scale-up, and the possibility to couple it with renewable energy to yield a zero net carbon emission process.[41] One of the main challenges that researchers in the field

face are low product selectivity, complex product separation, and limited CO_2 mass transfer from the gas phase to the catalyst surface.[42]

Thermal methods refer to the use of heat to overcome the thermodynamic barrier of CO_2 conversion.[43] The main advantages of thermal methods are their high conversion rates and their ability to be coupled with renewable energies. However, CO_2 conversion requires high temperatures. Therefore, research in this area is focused on developing catalysts to lower the required thermal input via CO_2 activation.

Biochemical CO_2 conversion refers to the use of an enzyme or microbial catalyst to convert CO_2. Such methods have received increased interest as one of their main advantages is high product selectivity and high conversion efficiency. Enzymatic reactions have shown to convert CO_2 into CO, methanol and other hydrocarbons with very high selectivity; however, the high cost and the need for specific bioreactors limit their real-world application.[44] Research here focuses on engineering micro-organisms to alter the conversion pathways towards higher catalytic rates.

Table 2.5 Strengths and weaknesses of electrochemical, thermal, biochemical and photocatalytic approaches to convert CO_2.

Approaches	Strengths	Weaknesses
Electrochemical	• Easy scale-up • Can be coupled with renewable energies • Stable long-term operation • Usually performed at low pressure and temperature	• Requires electric energy • Expensive technology • High operation cost
Thermal	• Can be coupled with renewable energies • High yield	• Requires high temperatures • Low catalyst stability
Biochemical	• High selectivity • Requires low pressure and temperature • Impurity tolerance	• Low yield • High cost • Specific environment required
Photocatalytic	• Economically feasible • Environmentally friendly • Usually performed at low pressure and temperature	• Low product selectivity • Low yield • Low catalyst stability

2.2 Traditional photocatalysts

'Traditional' semiconductors such as metal oxides, sulfides and selenides have attracted much attention as CO_2 photoreduction catalysts owing to their appropriate band edge position and their ability to photogenerate charges under light irradiation. Yet, these semiconductors suffer from fast electron-hole recombination rates, poor light absorption and restricted CO_2 adsorption, which limit their catalytic activity. Three main strategies have been developed to enhance the CO_2 photoreduction activity of traditional photocatalysts: 1) enhance visible light absorption to intensify photocharge carrier generation, 2) increase CO_2 adsorption/activation, and 3) reduce charge recombination. This section focuses on the main advances made in the development of TiO_2, non-titanium metal oxides, metal sulfides and metal selenides photocatalysts.

2.2.1 TiO_2 and derivatives

TiO_2 is one of the most investigated photocatalysts for CO_2 photoreduction owing to its chemical stability, non-toxicity, and low cost. TiO_2 possess three major phases: rutile, anatase and brookite which display band gaps of 2.98, 3.1 and 3.3 eV, respectively, with their VB and CB located between around 2.9 and -0.15 V vs NHE at pH=0.[45] However, TiO_2 suffers from poor light absorption, fast electron-hole recombination rates, limited CO_2 adsorption and low product selectivity. To provide some perspective, TiO_2 anatase has a charge recombination rate of ~30 ps, a light absorption onset at ~410 nm and a CO_2 uptake capacity of 0.062 mmol.g^{-1}.[46, 47] To enhance the photoreduction activity of TiO_2 numerous strategies have been developed (Figure 2.5)

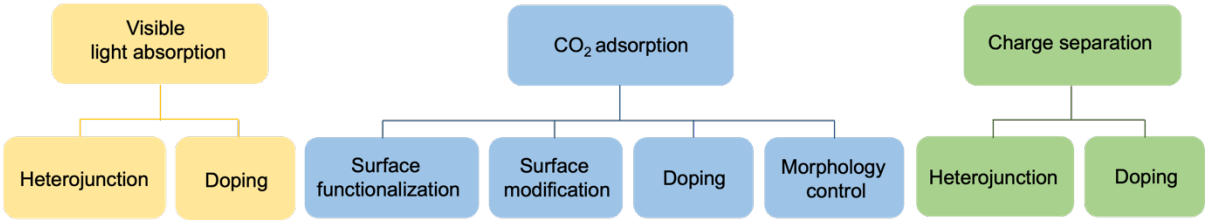


Figure 2.5 Summary of the main strategies used to improve the photocatalytic efficiency of TiO_2 and its derivatives.

To increase the visible light response, both metal and non-metal doping have been applied. Metal-doping introduces impurity's energy levels below the CB, while non-metal-doping introduces impurity's energy levels above the VB, narrowing the TiO_2 band gap and thus enhancing TiO_2 visible light absorption capacity.[48] Enhanced light-harvesting can also be achieved by forming a heterojunction between TiO_2 and a visible active semiconductor, where a heterojunction is defined as an intimate contact between two materials.[49]

To reduce TiO_2 fast charge recombination, doping and heterojunction formation have been successfully implemented.[50] Doping with impurities creates levels in the band gap which can trap electrons and reduce the recombination rate, while heterojunctions promote spatial separation of the photogenerated charges. The fundamentals of semiconductor/semiconductor heterojunctions will be discussed in more detail in Section 2.4.2.

Regarding CO_2 adsorption and CO_2 activation, both can be boosted by surface functionalization and modification. The former consists in functionalizing the TiO_2 surface with basic groups such as amine and hydroxyl groups to favour CO_2 adsorption, while the latter consists in modifying the TiO_2 surface to create defects. For instance, creating oxygen defects promotes the formation of defective Ti^{3+} surface sites which can act as adsorption sites and thus increase CO_2 uptake.[51]

In summary, improving TiO_2 photoreduction activity has been extensively explored; in addition, the research on TiO_2 focuses on understanding fundamental aspects such as product selectivity and reaction mechanisms (some examples have been presented in Section 2.1.2.7). To date, TiO_2 and its derivatives are being used for both liquid and gas-phase CO_2 photoreduction. In the gas phase, the main products are CO and CH_4, while in the liquid phase, CH_3OH and HCOOH production have been widely reported. Depending on the reaction conditions and the type of catalyst, the activity of TiO_2 and its derivatives range between 2 and 1000 $\mu mol.g^{-1}.h^{-1}$ displaying an AQY between 0.014 and 1.5%, and a QE between 0.007 and 5.7%.[48, 49] A summary of the product selectivity and overall photocatalytic efficiency of titanium oxides can be found in Table 2.6. One should note that most studies do not report the AQY nor the QE. Even when these are reported, the testing conditions and reactor set-ups often differ, which greatly complicates the comparison of the photocatalyst performance. Table 2.6 shows studies where either the AQY and/or QE are reported.

Table 2.6 Summary of the strengths and weaknesses of 'traditional' photocatalysts, i.e. TiO_2, non-titanium metal oxides, metal sulfides and metal selenides, including their product selectivity, overall efficiency, and most studied reaction phase for CO_2 photoreduction.

Photocatalysts	Strengths	Weaknesses	Reaction phase	Product formed	Reported activity ($\mu mol.g^{-1}.h^{-1}$)	AQY & QE (%)
TiO_2	• High reactivity • Good thermal stability • Abundance, low cost • Non-toxic	• Not visible active • Fast charge recombination • Relatively poor reduction power	Liquid and gas phase	Gas phase: CO and CH_4. Liquid phase: CH_3OH and HCOOH	2-1000	0.014 to 1.5 (420 nm) & 0.007 to 5.7[48, 49]
Non-titanium metal oxides	• High reactivity • High absorption efficiency • Low cost (production cost of ZnO is up to 75% lower than that of TiO_2) • Non-toxic	• Not visible active • Instability under acidic pH • Fast charge recombination	Mainly liquid-phase but the number of gas-phase studies is steadily increasing	Gas phase: CO and CH_4. Liquid phase: CH_3OH and HCOOH	0.5-600	0.03 to 5 (350 nm) [52, 53]
Metal sulfides and selenides	• Strong reduction ability • Visible light absorption • Ease of production • Good thermal stability	• Undergo photocorrosion • Fast charge recombination • Insufficient visible absorption	Liquid and gas phase	Gas phase: CO and CH_4. Liquid phase: CH_3OH and HCOOH	0.1-3000	0.3 to 1.92 (420 nm) [54, 55]

2.2.2 Non-titanium metal oxides

Numerous non-titanium metal oxides have been developed for CO_2 photoreduction, including ZnO, Ga_2O_3, WO_3, Ta_2O_3, and Cu_2O.[56] Most metal oxides exhibit large band gaps. For instance, ZnO, Ga_2O_3 and WO_3 display band gaps of 3.4, 4.6, and 3.0 eV, thereby benefitting from large overpotentials for CO_2 photoreduction,[56] but at the same time limiting their light absorption capacity. Like most photocatalysts, metal oxides suffer from fast electron-hole recombination rates and low CO_2 adsorption. To improve light absorption, CO_2 adsorption and reduce charge recombination, numerous strategies like those described for TiO_2 have been employed, i.e. surface functionalization, heterojunction formation as well as metal and non-metal doping.[56] Some metal oxides such as Cu_2O, Bi_2WO_6 and $ZnGa_2O_3$ possess narrower band gaps and are thus active under visible light, however, their activity remains still too low and engineering strategies such as metal doping and heterojunction formation are in addition required to improve their activity. A summary of the product selectivity and overall photocatalytic efficiency of non-titanium oxides can also be found in Table 2.6.

2.2.3 Metal sulfides and selenides

Compared to metal oxides, metal sulfides and metal selenides display more negative reduction potentials and therefore a higher overpotential to reduce CO_2.[57] In addition, their narrow band gaps allow them to utilise visible light to generate charges. For CO_2 photoreduction, the most investigated metal sulfides are CdS ($E_g = 2.4\ eV$) and Bi_2S_3 ($E_g = 1.7\ eV$), while the most investigated metal selenides are CdSe ($E_g = 1.7\ eV$) and ZnSe ($E_g = 2.7\ eV$).[57] The catalytic efficiency of these catalysts remains limited by high charge recombination rates and photocorrosion. Photocorrosion is caused by the photogenerated holes which oxidise the sulfide or selenide ions which lead to photocatalyst degradation.[55] To suppress photocorrosion, different strategies such as heterojunction formation and the addition of a hole sacrificial agent have been tested, while to lower charge recombination, metal doping and heterojunction formation have been implemented.[58] A summary of the product selectivity and overall photocatalytic efficiency of metal sulfides and selenides can be found in Table 2.6.

2.3 Emerging classes of organic-based photocatalysts

As discussed in Section 2.2, 'traditional' semiconductors have received much attention as photocatalysts, however, their photoactivity remains too low for large scale applications and their poor structural/chemical tunability limit their design towards increased photoactivity. Such limitations have prompted the development of readily tunable visible-light active materials such as organic-based photocatalysts. However, the number of published studies on organic-based photocatalysts remains considerably smaller than the number of published studies on TiO_2 and other metal oxides. Based on SciFinder, the number of published articles on traditional photocatalysts for CO_2 photoreduction, when using TiO_2, CdS and metal oxides as keywords, is around 162,000, while for organic-based photocatalysts, when using g-C_3N_4, MOFs and COFs as keywords, the number of published papers is around 50,000. In the context of CO_2 photoreduction, this new class of materials is just emerging. The following section focuses on the main advances made in the development of graphitic carbon nitride (g-C_3N_4), MOFs, COFs, and amorphous porous polymers as photocatalysts.

2.3.1 Graphitic carbon nitride

g-C_3N_4 is a layered metal-free polymeric material made of triazine units, which is typically synthesised via a one-step thermal process using nitrogen-rich precursors such as melamine (Figure 2.6).[59] Owing to its moderate band gap (2.7 eV), which results in visible light absorption, and its relatively high reduction potential (-0.9 V vs NHE at pH=0), g-C_3N_4 can photoreduce CO_2. Its metal-free nature and low cost represent additional advantages. However, g-C_3N_4 still suffers from limited visible light absorption capacity beyond 460 nm, limited CO_2 adsorption and fast electron-hole recombination rates.[59] To overcome these shortcomings, numerous efforts have been undertaken.

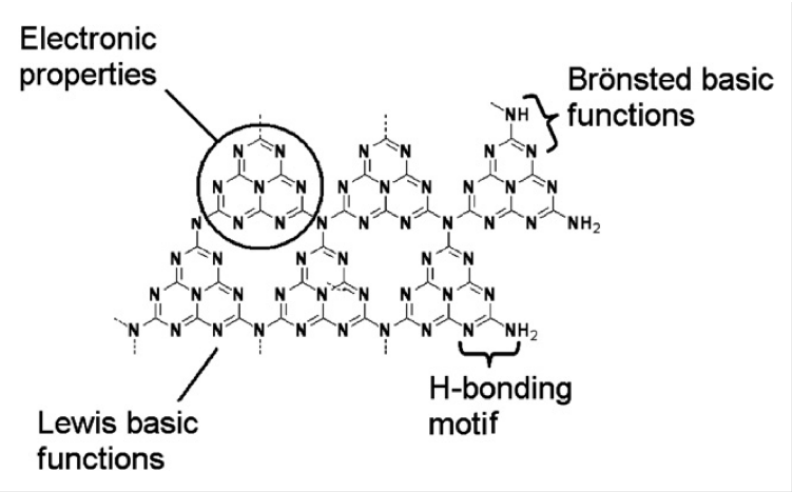


Figure 2.6 The surface properties of polymeric g-C_3N_4.[60] Reproduced with permission from the Royal Society of Chemistry.

One of the most common strategies to enhance g-C_3N_4 activity is exfoliation. The higher surface-to-volume ratio of g-C_3N_4 nanosheets (CNNS) enhances active site exposure and limits bulk recombination. [61-63]

To increase the CNNS visible light response, nitrogen defects can be introduced by heating the sample under an H_2 atmosphere.[64] As investigated by Li et al., N-defects promote the formation of mid-gap states below the CB of CNNS, narrowing the band gap and thus extending the visible light absorption from 420 to 510 nm.[64] Doping is another approach. For instance, as investigated by Wang et al. via DFT calculations, the VB of S-doped CNNS gives a lower reduction potential than that of pure CNNS, which shifts the light absorption onset from 440 to 510 nm.[65]

To enhance CNNS CO_2 adsorption, surface modifications have been developed. As Figure 2.6 illustrates, unmodified CNNS already displays surface defects on its termination edges created by uncompleted polycondensation. These defects favour the formation of primary and secondary amino groups that act as basic sites to adsorb and activate CO_2. Thus, by increasing the number of defects via surface modification, one can enhance CO_2 adsorption/activation.[66]

Regarding charge separation, it can be improved by doping and heterojunction formation. As for traditional photocatalysts, metal and non-metal doping promote the formation of mid-gap states, which can trap the photogenerated electrons to support charge separation. However, when introducing mid-

gap states, one needs to be careful that they respect the minimum required potential to reduce CO_2.[67] Section 2.4.3 will discuss in more detail semiconductor/g-C_3N_4 heterojunctions.

In summary, defect engineering, doping and heterojunction formation have all successfully been implemented to improve g-C_3N_4 and CNNS CO_2 photoreduction activity. In general, the activity of pure g-C_3N_4 and CNNS is lower than that of most metal oxides. Upon modification, the activity of g-C_3N_4 and CNNS can increase leading to much higher production rates. Table 2.7 summarises the product selectivity and overall photocatalytic efficiency of g-C_3N_4 and CNNS.

2.3.2 Metal-organic frameworks

MOFs are a class of porous materials formed by metal ions or metal clusters that are linked together by organic molecules, referred to as ligands or linkers (Figure 2.7).[68] Given their organic and inorganic hybrid nature, MOFs display a remarkable and unique versatility. The ability to change the ligand and the metal provides a structural and chemical diversity beyond that of any other inorganic material. In theory, one can design a MOF that displays the desired CO_2 affinity, pore size, surface area, light absorption capacity, and band edge position.[69]

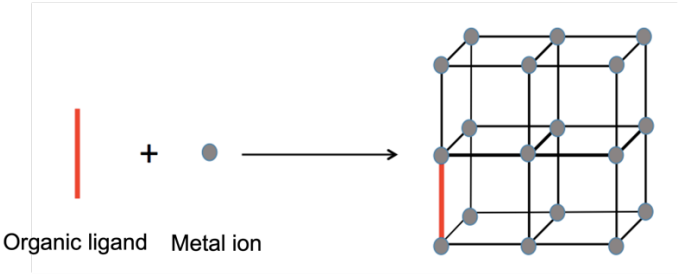


Figure 2.7 Illustration of the MOF design strategy.

Numerous MOFs have been investigated for photocatalytic CO_2 reduction. The most studied ones are Zr-UiO-66-NH_2 and Ti-MIL-125-NH_2, owing to their high metal coordination numbers and strong metal-ligand bonds, which makes them water stable,[70] and Co-ZIF-67 which displays good light absorption capacity in the UV, visible and IR regions.[71]

Upon light irradiation of a MOF, the electrons of the metal cluster are directly or indirectly photoexcited.[72] In the first case, the metal cluster directly absorbs the incoming photons generating photocharges, while

in the second case, the ligand first absorbs the photons to generate photoexcited electrons, which are then transferred to the metal cluster, where adsorbed CO_2 is reduced. To enable efficient ligand-to-metal charge transfer (LMCT), the lowest-unoccupied molecular orbital (LUMO) of the ligand needs to overlap with the highest-occupied molecular orbital (HOMO) of the metal (Figure 2.8). However, most MOFs display poor orbital overlap, thus upon indirect excitation of the metal cluster, poor charge transfer occurs, limiting the photocatalytic efficiency. Despite this drawback, indirect excitation is preferred over direct excitation, as it allows to increase electron-hole separation and hence reduces charge recombination. Different techniques have been implemented to improve the LMCT process, suppress charge recombination, boost light harvesting, and enhance CO_2 adsorption/activation.

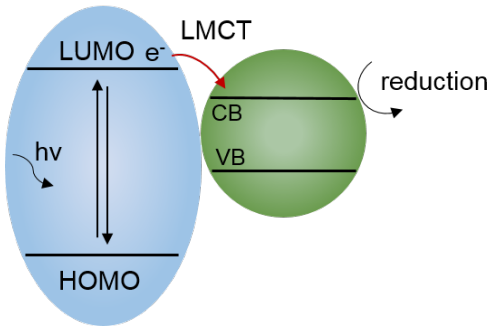


Figure 2.8 Schematic illustration of an indirect excitation of a MOF crystal.

Enhanced light-harvesting can easily be achieved by ligand functionalization, e.g. addition of amino groups to the ligand. The nitrogen atom can donate electrons to the aromatic ligand, which results in a shift of the HOMO orbital to higher energy.[73,74] This narrows the band gap and thus enhances light absorption. As investigated by Hendon et al., upon amino functionalization the band gap of Ti-MIL-125 gets reduced from 3.6 to 2.6 eV, which corresponds to a shift of the light absorption onset from 345 to 475 nm.[74] The higher the electron density of the linker, the narrower the band gap.[75] Another commonly used strategy to enhance light harvesting is through integrating ligands with extended conjugation. A common example is the use of porphyrins as ligands. To this end, Xu et al. synthesised a Zr-based porphyrin MOF named PCN-222, where the porphyrins act as chromophores.[76] However, despite being a promising technique, porphyrin ligands are costly.

Improving CO_2 adsorption is also of importance to yield high CO_2 conversion rates. Introducing basic functional groups such as amino groups via linker functionalization boosts CO_2 adsorption and

activation. CO_2 adsorption/activation can also be enhanced by increasing the number of accessible active sites via morphology control. For instance, the 2D version of Co-ZIF-67, referred to as Co-ZIF-L, exhibits a leaf-like morphology with enhanced CO_2 adsorption capacities compared to the 3D counterpart Co-ZIF-67.[77]

Finally, as for most semiconductors, photoexcited charges are short-lived in MOFs, which can be improved via ligand functionalization. Introducing electron-donating functional groups such as amino groups promote a better overlap of the LUMO and HOMO orbitals of the ligand and the metal, and therefore favour better LMCT.[73] Charge migration can also be achieved by constructing bimetallic MOFs, which enables electron transfer between the metal ions, often referred to as metal-to-metal charge transfer.[78] As illustrated by Figure 2.9, the doped metal can act as a mediator to separate charges, favouring longer charge carrier lifetimes. Finally, heterojunction formation has also shown great promise towards spatial charge separation and is discussed in more detail in Section 2.4.4.

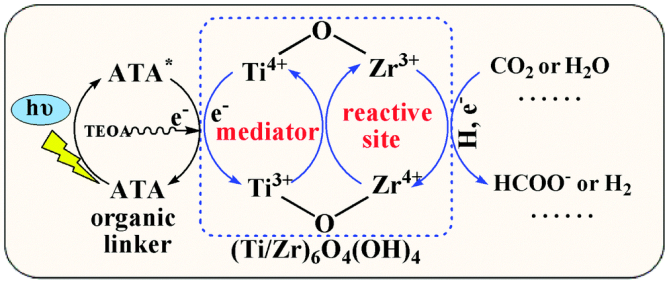


Figure 2.9 Schematic illustration of the CO_2 photoreduction process over Ti/Zr-UiO-66-NH_2.[78] Reproduced with permission from the Royal Society of Chemistry.

To summarise, the photocatalytic activity of MOFs has been successfully improved via ligand functionalization, morphology control, and metal substitution. In general, the catalytic performance of unmodified MOFs is lower than that of metal oxides. Upon modification, the activity of MOFs can be increased leading to much higher production rates, with Ru-, Re-, and porphyrin based-MOFs being the most active MOFs. Table 2.7 summarises the product selectivity and overall photocatalytic efficiency of modified and unmodified MOFs.

2.3.3 Covalent organic frameworks

COFs are a class of porous organic polymers formed by light elements such as C, N, O and B that are linked together through covalent bonds.[79] Owing to the presence of covalent bonds, COFs display high thermal and chemical stability. Depending on the chosen organic building block, COFs can also display high crystallinity. In addition, the presence of π-conjugated electronic networks favours visible light absorption owing to the lower energy required to excite an electron from a π to a π* orbital (Figure 2.10a). To increase their CO_2 photoreduction activity, various strategies relying on enhanced light absorption, charge transfer/separation and CO_2 adsorption/activation have been employed.

Light absorption can be tuned by choosing different organic building blocks to increase the degree of conjugations. As Figure 2.10b illustrates, conjugation promotes the formation of molecular orbitals that display a smaller energy difference between the LUMO and HOMO orbitals.[80] Thus, COFs with extended conjugated systems display narrower band gaps leading to wider light absorption.[81] Introduction of extended π-conjugated systems such as porphyrins, and imidazole groups have shown great promise to enhance light absorption. Depending on the chosen building blocks COFs can display band gaps between 1.2 and 2.9 eV.[81]

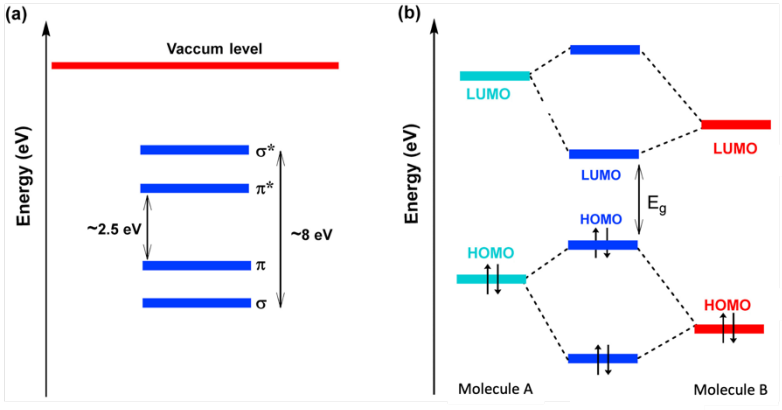


Figure 2.10 Schematic illustration of (a) the HOMO-LUMO transition of a π-conjugated systems and (b) the HOMO-LUMO transition of a molecular orbital.[80] Reproduced with permission from Elsevier.

Enhanced CO_2 adsorption and activation can be achieved by choosing organic building blocks with specific functional groups. For instance, as investigated by Li et al., the presence of azine groups

induces stronger CO_2 interactions.[82] Metalation techniques have also been used to enhance the number of active catalytic sites. As Figure 2.11 illustrates, metal sites such as Re- and Ru-complexes can be grafted onto the COF.[83]

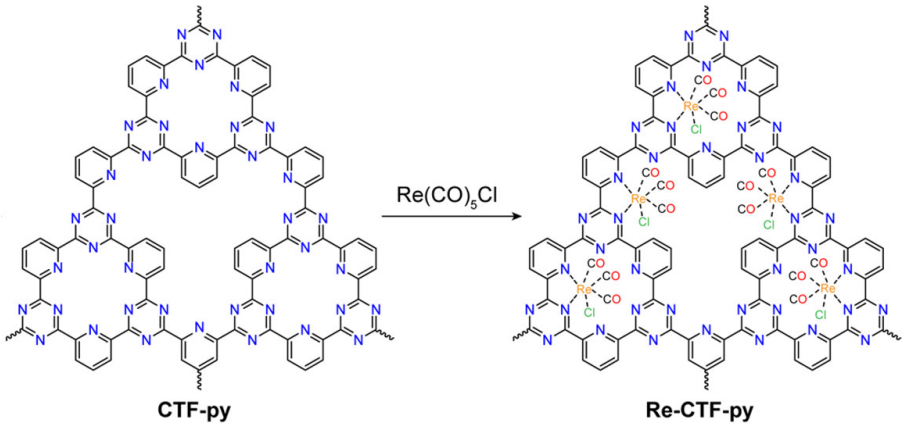


Figure 2.11 Schematic representation of the incorporation of Re inside the COF skeleton.[83] Reproduced with permission from the Royal Society of Chemistry.

Enhanced charge separation can be achieved by integrating electron donor and electron acceptor moieties in the COF skeleton. Lei et al. reported a carbazole/triazine-based COF, where the HOMO and the LUMO orbitals are located on the electron donor, i.e. carbazole, and the electron acceptor components, i.e. triazine, respectively.[84] As the authors demonstrate, the spatial separation between the HOMO and LUMO orbitals facilitates electron-hole separation. Another commonly used method to promote charge separation is the formation of semiconductor/COF heterojunctions, which is discussed in more detail in Section 2.4.3.

In summary, the photocatalytic performance of unmodified COFs is lower than that of metal oxides. To improve their photoactivity metal-doping, heterojunction formation and incorporation of electron donor and acceptor moieties are required. Table 2.7 summarises the product selectivity and overall photocatalytic efficiency of modified and unmodified COFs.

2.3.4 Amorphous porous polymers

Over time, research interest has shifted from developing traditional photocatalysts to developing tunable crystalline structures such as MOFs and COFs. For many years, crystallinity was considered a required physicochemical property to yield high photocatalytic activity owing to its ability to influence charge conduction and enable faster electron transfer from the CB to the reactant. Thus, for a long time, amorphous materials were not seen as viable photocatalysts owing to their poor charge conduction. Although crystallinity does facilitate charge migration, charge conduction may not be as critical for amorphous porous materials due to the short distance between the reactant and the active sites where the charges are generated. Hence, in recent years the use of amorphous porous organic polymers (POPs) as photocatalysts has rapidly grown.[79]

Amorphous POPs can be classified into four main categories. Conjugated microporous polymers (CMPs), porous aromatic frameworks (PAFs), polymers of intrinsic microporosity (PIMs) and hypercrosslinked polymers (HCPs). For CO_2 photoreduction the most investigated ones are CMPs and HCPs, thus the following sections will focus on the advances made for these two classes of materials.

2.3.4.1 Conjugated microporous polymers

CMPs are a class of amorphous polymeric materials formed by alternating single and double covalent bonds.[85] The presence of extended π-conjugation through the entire structure enables visible light absorption. Due to the chemical structure of the monomers used, CMPs also display intrinsic and permanent porosity. In addition, their high chemical stability, relatively low cost, and ability to tune their physicochemical properties through the judicious selection of monomers, make them highly attractive for this application. The most prominent study illustrating the main advantage of CMPs over traditional photocatalysts was published by Sprick et al.[86] By simply varying the monomer's composition, the authors tuned the optical gap of pyrene-based CMPs (Figure 2.12). The synthesised CMPs displayed band gaps ranging from 1.9 to 2.95 eV, which corresponds to light absorption onsets ranging from 680 to 420 nm, opening new research avenues for the development of photoactive CMPs.

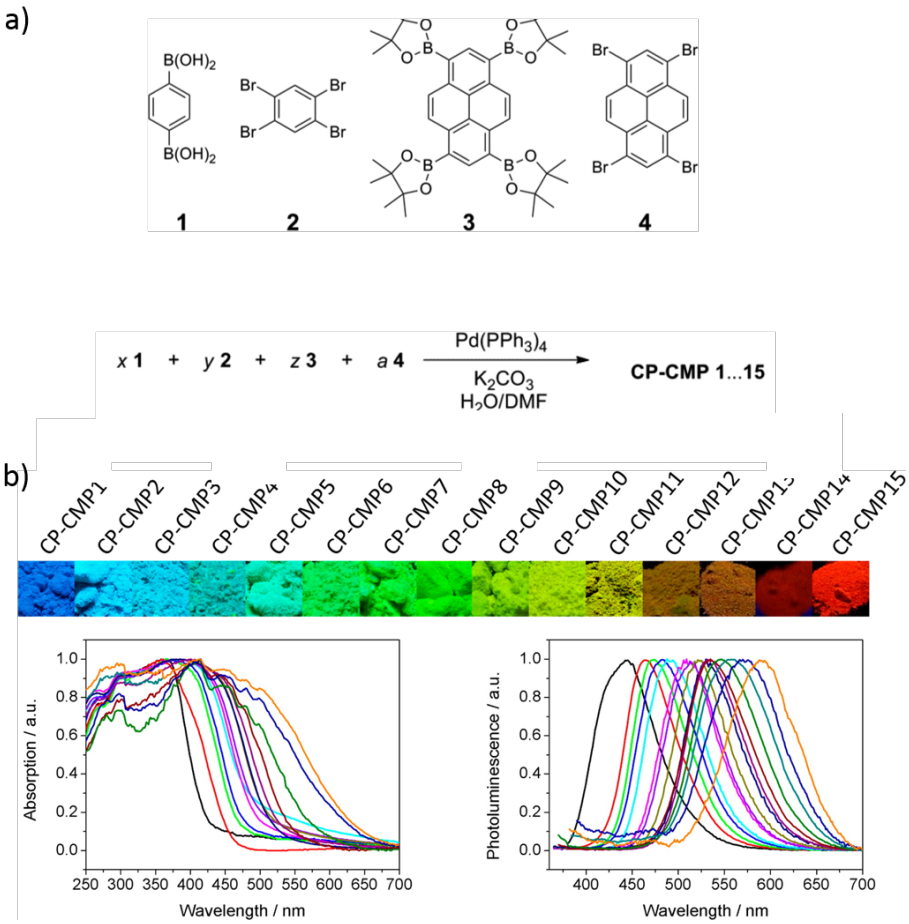


Figure 2.12 (a) reaction scheme of the synthesis of CMPs and (b) photographic images of the synthesised CMPs with their corresponding UV-Vis absorption spectra (left) and their photoluminescence spectra (right). [86] Adapted with permission from the American Chemical Society.

Up to now, CMPs have been predominantly used for photocatalytic H_2 evolution while their use for CO_2 photoreduction remains quasi unexplored. To improve the CO_2 photoreduction activity of CMPs, similar strategies to those used to improve COFs photoactivity have been implemented.

Enhanced charge separation can be achieved by incorporating electron donor and electron acceptor moieties in the CMPs backbone to spatially separate the HOMO and LUMO orbitals of the metal and that of the ligand.[87] The light absorption can be tailored by optimising the π-conjugation system,[88] while CO_2 adsorption and activation can be improved by grafting Re- and Ru-complexes onto the CMP skeleton.[89]

Overall, CMPs have been used for CO_2 photoreduction and have shown promising results as metal-free photocatalysts. Table 2.7 summarises the product selectivity and overall photocatalytic efficiency of CMPs.

2.3.4.2 Hypercrosslinked polymers

HCPs are densely crosslinked amorphous polymers constituted of organic building blocks.[79] HCPs exhibit a unique chemical and structural diversity as non-functional aromatic compounds (i.e. without specifically polymerisable groups) can be 'knitted' together using an external crosslinker. Moreover, owing to the mild reaction conditions and the use of inexpensive monomers, HCPs are relatively low-cost materials. The increasing scientific interest around HCPs is also explained by their simple and scalable synthesis process.

Up to date, HCPs have been primarily developed for gas adsorption/separation. For instance, HCPs have shown great promise for CO_2 capture. As investigated by Dawson et al., increasing the concentration of amino moieties in the HCP structure improves CO_2 adsorption capacities and favours selective CO_2 adsorption over N_2.[90] By optimising the surface area, the pore size and the CO_2 affinity, HCPs can display a CO_2 uptake capacity of up to 2.8 $mmol.g^{-1}$ at 1 bar at 25 °C .[91] For comparison, the benchmark CO_2 adsorbent zeolite 13X has a CO_2 uptake capacity of ~4 $mmol.g^{-1}$ at 1 bar and 25 °C.

Apart from CO_2 capture, HCPs have also been used for catalytic transformations. The use of HCPs to assist photocatalysis, in particular for CO_2 photoreaction, is just emerging. Wang et al. investigated an HCP-TiO_2-graphene catalyst for CO_2 photoreduction, where the HCP component appeared to facilitate CO_2 adsorption and diffusion.[92] However, the authors did not discuss the photoreduction ability of the HCP alone. Owing to their promising physiochemical properties, it would be of interest to investigate the CO_2 photoreduction activity of HCPs.

Table 2.7 Summary of the strengths and weaknesses of emerging classes of organic-based porous photocatalysts, i.e. g-C_3N_4, MOFs, COFs, CMPs and HCPs, including their product selectivity, overall efficiency, and most studied reaction phase for CO_2 photoreduction.

Photo-catalysts	Strengths	Weaknesses	Reaction phase	Product formed	Reported activity ($\mu mol.g^{-1}.h^{-1}$)	AQY & QE (%)
g-C_3N_4	• Simple, scalable, and low-cost synthesis • Hydrothermal stability • Excellent electron mobility generated by extended π-conjugation	• Limited versatility • Limited porosity	Mainly liquid-phase but the number of gas-phase studies is steadily increasing	Gas phase: CO and CH_4. Liquid phase: CH_3OH and HCOOH	2 - 500	0.09 to 3.4%.[54, 93] (420 nm)
MOFs	• High versatility • High porosity	• Most MOFs display poor water stability • Costly synthesis and often difficult to scale up	Mainly liquid-phase but the number of gas-phase studies is steadily increasing	Gas phase: CO and CH_4. Liquid phase: CH_3OH and HCOOH	2 - 2800	0.2×10^{-2} to 7%.[94] (475 nm)
COFs	• Hydrothermal stability • High versatility • High porosity • Excellent electron mobility generated by extended π-conjugation	• Requires specific polymerisable monomeric units	Mainly liquid-phase but the number of gas-phase studies is steadily increasing	Gas phase: CO and CH_4. Liquid phase: CH_3OH and HCOOH	0.3 - 1400	$0\ 5.10^{-3}$ to 1.2%.[95, 96] (420 nm)
CMPs	• Simple and scalable synthesis • Hydrothermal stability • High porosity • Excellent electron mobility generated by extended π-conjugation	• No crystallinity, making it more difficult to characterise	Liquid and gas phase	Independently of the reaction phase, most studies investigate CO_2 photoreduction to CO	0.3 - 100	Up to 3.4% (400 nm).[97]
HCPs	• Simple and scalable synthesis • Hydrothermal stability • High porosity	• No crystallinity, making it more difficult to characterise	The photoreduction activity of HCPs has never been investigated	-	-	-

2.4 Semiconductor/semiconductor heterojunctions

2.4.1 Fundamental of heterojunctions

A heterojunction is defined as an intimate contact between two distinct materials. When the materials display complementary band gaps, the interface can induce spatial electron-hole separation and improve light absorption. To date, heterojunction formation is one of the most effective methods to enhance the activity of a photocatalyst. Three types of heterojunctions are commonly explored: Type I, Type II and Z-scheme (Figure 2.13).[98, 99]

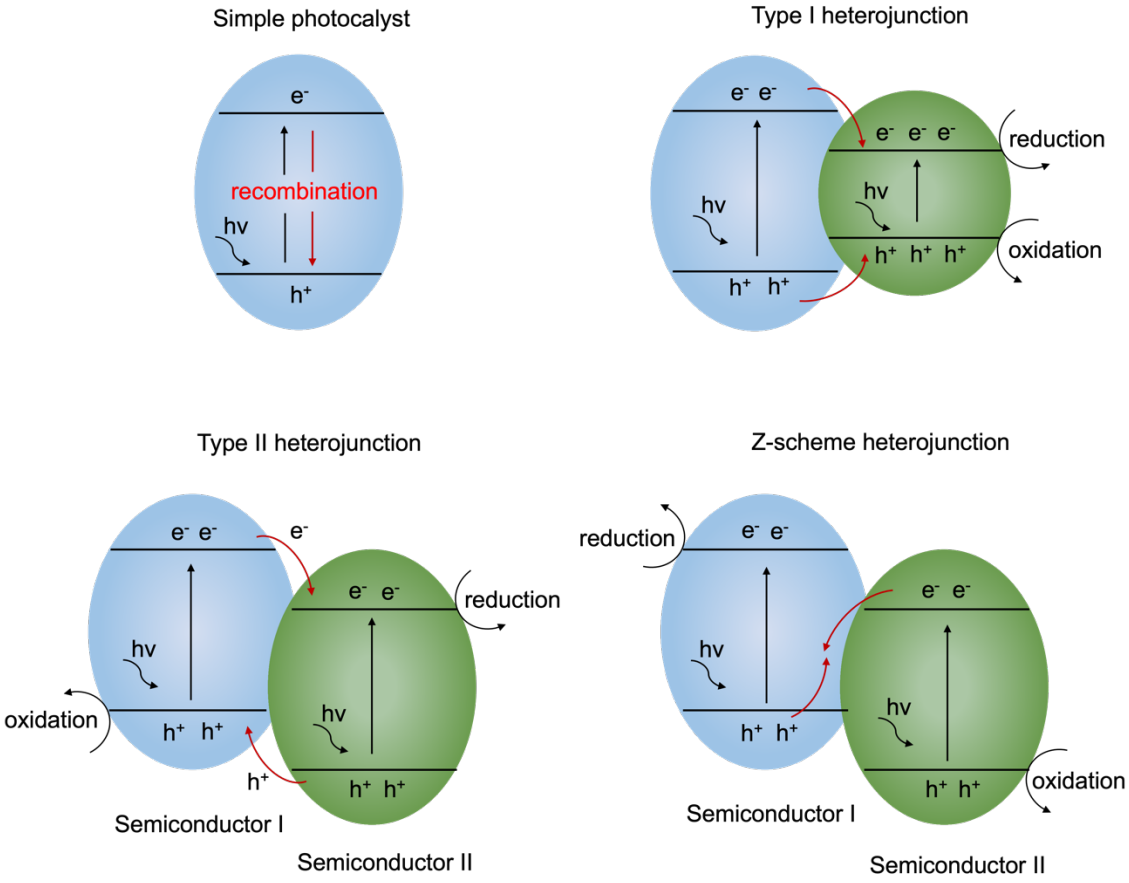


Figure 2.13 Schematic illustration of the three most commonly investigated heterojunctions.

As Figure 2.13 illustrates, upon irradiation of a Type I heterojunction, the photogenerated charge carriers accumulate on the same semiconductor, thus Type I heterojunction does not favour spatial charge separation. For Type II heterojunctions, the CB and the VB are correctly positioned to promote efficient charge separation. Upon light irradiation, the photogenerated electrons migrate to

semiconductor II, while the holes migrate to semiconductor I. However, during charge migration, the reduction and oxidation potentials of the photogenerated electrons and holes are reduced. For Z-scheme heterojunctions, the photogenerated charges are spatially separated while retaining their reducing and oxidizing potentials.

As shown by the different heterojunction types, when adequate band gap overlap is achieved, heterojunction formation can reduce charge recombination and enhance light absorption. However, when designing a heterojunction, one needs to keep in mind that the CB and the VB of the semiconductors should respectively exhibit more negative and more positive potentials than those of the targeted reduction and oxidation reactions. Therefore, when developing a new heterojunction, adequate band gap overlap and band edge positioning are key.

2.4.2 Semiconductor/metal oxide heterojunctions

Coupling metal oxides with other semiconductors is an efficient strategy to enhance CO_2 photoreduction as it allows to combine the ability of metal oxides to generate charges while providing an interface across which charges can be separated.[100-105] When developing a hetereojunction, one must consider the contact between both heterojunction components. As explored by Qin et al. the loading of CuO in a CuO/TiO_2 heterojunction can considerably affect the photoreduction activity.[105] A loading of 1% CuO yields the highest activity. Above 1% loading, CuO was found to agglomerate reducing intimate contact with TiO_2, while below 1%, CuO concentration was too low to promote efficient charge separation.

To date, numerous studies have investigated semiconductor/metal oxide heterojunctions. For instance, Beig et al., coupled TiO_2 with CdS achieving a 3-fold activity increase compared to pure TiO_2 owing to effective charge migration and enhanced light absorption.[104] Table 2.8 reports papers that have investigated semiconductor/metal oxide heterojunctions for CO_2 photoreduction. Studies that coupled metal oxides with organic-based semiconductors and MOFs are discussed in Sections 2.4.3 and 2.4.4, respectively.

Table 2.8 Examples of semiconductor/metal oxide-based photocatalysts developed for CO_2 photoreduction.

Photocatalyst	Reaction phase	Product	Yield	Comments	Ref.
CuO_2/TiO_2[a]	gas	CO	× 4 compared to pure CuO_2	Enhance charge separation, protects CuO_2 from photocorrosion	103
CuO/TiO_2[a]	liquid	$HCOOCH_3$	× 4 compared to pure TiO_2	Effect of CuO loading on the heterojunction photoactivity	105
CdS/TiO_2[a]	gas	CO CH_4	× 3 compared to pure TiO_2	Enhance visible light absorption	104
CdS/ZnO	liquid	CO CH_4	× 4 compared to pure CdS	Visible light absorption, charge separation	102
Cds/WO3	gas	CH_4	× 10 compared to pure CdS	Z-scheme, efficient charge separation	101
CuO/ZnO	liquid	CH_3OH	× 2.5 compared to pure ZnO	Charge separation	100

[a] The authors used TiO_2 anatase

2.4.3 Semiconductor/organic-based semiconductor heterojunctions

Combining the unique physicochemical properties of organic-based photocatalysts, i.e. visible light absorption, tunable band gap, and CO_2 affinity, while enhancing charge separation represents a unique opportunity to promote CO_2 photoreduction. This section focuses on the advances made in the development of heterojunctions based on g-C_3N_4 and COFs.

Organic-based photocatalysts such as g-C_3N_4 and COFs have been coupled with numerous metal oxides including WO_3, TiO_2 and ZnO.[106] To optimise such heterojunctions for high photoconversion rates, different strategies have been investigated: 1) optimise charge separation, 2) enhance light-harvesting and 3) improve CO_2 adsorption.

Like for semiconductor/metal oxides heterojunctions, the contact between both components is crucial to yield effective charge separation. The interfacial contact area can be tuned by controlling the morphology of the heterojunction components. Crake et al. reported a CNNS/TiO_2 with TiO_2 displaying

nanosheets or bipyramidal morphologies.[49] When using TiO_2 nanosheets, CNNS/TiO_2 showed higher photocatalytic performance than with bipyramidal TiO_2 owing to long-lived charges, which were not observed when using bipyramidal TiO_2. The enhanced charge lifetime was attributed to better charge separation resulting from a better contact between CNNS and 2D TiO_2 nanosheet than with bipyramidal TiO_2. It is well established that 2D materials are highly beneficial for CO_2 photoreduction.[107] Compared to 3D materials, their high surface area and higher surface-to-volume atom ratio result in more accessible active sites and high substrate adsorption. In addition, when coupling 2D materials with other 2D semiconductors, the 2D-2D interface promotes superior electron-hole transfer across the heterojunction due to superior interfacial contact. Moreover, owing to the low thickness of each semiconductor, the distance of charge transport to reach the interface is considerably reduced leading to faster charge separation. However, engineering 2D-2D heterojunctions remains complicated and the number of available 2D materials is limited.

Regarding enhanced light absorption, CNNS and COFs have been coupled with other visible-light-active semiconductors such as CdS and Fe_2O_3.[108, 109] As explored by Vu et al., when coupling CNNS with CdS, CO production was enhanced 10-fold compared to the activity of pure CNNS.[109] The latter was attributed to a light absorption onset shift from 480 to 570 nm and efficient charge separation.

To improve CO_2 adsorption, CNNS and COF have been coupled with porous materials such as MOFs, which will be discussed in Section 2.4.4.

In summary, efforts have been made to develop organic-based heterojunctions (Table 2.9). Research in the field focuses on improving charge separation while enhancing light absorption and CO_2 adsorption. To date, g-C_3N_4-based heterojunctions are the most explored ones. However, the number of COF-based heterojunctions is steadily increasing. Over time, more advanced composites have been explored such as tertiary composites. However, thus far, the photoactivity of organic-based heterojunctions still remains too low. To support the development of efficient heterojunctions, further research efforts are needed to understand and control the key parameters influencing charge transfer across the heterojunction interface.

Table 2.9 Examples of g-C_3N_4 and COFs-based heterojunctions for CO_2 photoreduction.

Photocatalyst	Reaction phase	Product	Yield	Comments	Ref.
g-C_3N_4/WO_3	liquid	CH_3OH	× 2.4 compared to pure g-C_3N_4	Z-scheme	110
g-C_3N_4/ZnO	gas	CO CH_4	× 5 and × 8 compared to pure g-C_3N_4 and TiO_2 P25, respectively	Type II	111
CNNS/TiO_2[a]	gas	CO	× 10 and × 2 compared to pure g-C_3N_4 and TiO_2 P25	Type II, 2D-2D heterojunction	49
CNNS/rGO NS	gas	CH_4	× 5.4 compared to pure CNNS	2D-2D heterojunction	112
CNNS/MnO_2	gas	CO	× 5 compared to pure CNNS	Z-scheme 2D-2D heterojunction	113
CNNS/COF	liquid	CO	× 5.4 compared to pure CNNS	Z-scheme 2D-2D heterojunction	33
COF/TiO_2[a]	gas	CO	× 5 compared to the pure COF	Z-scheme	108
COF/SnS_2	liquid	CO CH4	× 7.2 compared to the pure COF	Z-scheme	114

[a] The authors used TiO_2 anatase

2.4.4 Semiconductor/MOF heterojunctions

Similarly, as for semiconductor/organic-based heterojunction, semiconductor/MOF heterojunctions combine the ability to design a MOF with the desired physicochemical properties and the ability to provide a charge migration path.[99, 115] Numerous semiconductor/MOF-based heterojunctions have been developed to improve the CO_2 photoreduction ability of promising semiconductors by: 1) favouring electron-hole migration/separation, 2) improving light-harvesting, and 3) increasing the number of available active sites to enhance CO_2 adsorption/activation.

As shown by various studies, MOF-based heterojunctions can inhibit charge recombination by promoting charge migration.[46] However, efficient charge transfer across the heterojunction interface is key to yield effective charge separation. The latter can be optimised by favouring intimate interactions between the heterojunction components. As studied by Hong et al.,"nano-scale mixing" by in-situ growth

of MOF crystals in the presence of CNNS, promotes greater photoactivity compared to physically mixed CNNS/MOF heterojunctions.[116] Wang et al. also demonstrated that in-situ synthesis of a CNNS/Zr-UiO-66-NH_2 heterojunction favours the formation of NHx-Zr-O bonds, which accelerated charge migration through the interface, leading to a 2-fold activity increase.[117] Charge separation can also be optimised by coupling 2D MOFs with other 2D materials. Mu et al. reported a 2D-2D Ni-MOF/rGO structure with a 7-fold activity increase compared to pure rGO.[118] This increase was attributed to the intimate contact of the 2D-2D heterojunction and the enriched electron density at the isolated Ni sites which promoted higher CO_2 adsorption. Interestingly, other 2D MOFs have been coupled with other semiconductors, however, most reports focus on the effect of morphology on CO_2 adsorption, rather than understanding the effect of using 2D MOFs on the heterojunction interface.

MOF-based heterojunctions have also been developed to enhance the light-harvesting capacity of promising photocatalysts. For instance, owing to its broad light absorption in the UV, visible and IR regions, Co-ZIF-67 has been coupled with various semiconductors such as CdS and TiO_2.[119, 120]

Regarding CO_2 adsorption/activation, the CO_2 uptake capacity of promising semiconductors has been successfully enhanced by coupling them with MOFs. When judiciously selecting the MOF, MOF-based heterojunctions can promote selective and high CO_2 adsorption near the active sites. This can be done by choosing a highly porous MOF and by linker functionalization, e.g. addition of amino groups to the linker.[77]

As Table 2.10 illustrates, efforts have been undertaken to develop MOF-based heterojunctions. Until recently most studies have been based on a trial-and-error approach, however, research is slowly shifting towards understanding the fundamentals behind charge recombination and CO_2 activation via state-of-the-art characterisation techniques and computational calculations.

Table 2.10 Examples of MOF-based heterojunctions developed for CO_2 photoreduction.

Photocatalyst	Reaction phase	Product	Yield	Comments	Ref.
CNNS/Co-ZIF-9 physically mixed	liquid	CO	× 2 compared to pure CNNS (0.9%)	Integration of an imidazolate-based linker in the MOF to enhance CO_2 activation	121
g-C_3N_4/ Zr-UiO-66-NH_2	liquid	CO CH_4	× 2 compared to pure g-C_3N_4	Formation of chemical bond: NHx–Zr–O to increase charge separation	117
CNNS/BIF-20 (boron imidazole framework)	liquid	CO CH_4	× 10 compared to pure CNNS	Suppression of electron-hole recombination through B-H bond migration (proved by modelling)	122
CNNS/ Fe-MIL-101-NH_2	gas	CO	× 7 compared to the pure CNNS	Amino groups favour visible light absorption and higher CO_2 adsorption.	123
TiO_2[a]/ Cu-HKUST-1	gas	CH_4	× 5 compared to pure TiO_2	Prove for the first time that MOF-based heterojunction can separate charges	124
TiO_2/Mg-CPO-27	gas	CO CH_4	× 2 compared to pure TiO_2	Uncoordinated Mg^{2+} sites enable superior CO_2 uptake	125
TiO_2[a]/Co-ZIF-9	gas	CO CH_4	× 2 compared to pure TiO_2	Shift the light absorption from the UV to the visible light region by choosing a visible photoactive MOF	126
TiO_2[a]/ Zr-UiO-66- NH_2	gas	CO	× 2 compared to pure TiO_2	Shift the absorption light range from the UV to the visible light region by linker functionalization, enhance charge lifetime	46
TiO_2[a]/ Ti-MIL-125-NH_2	gas	CH_4	× 1.7 compared to pure TiO_2	Type II heterojunction to enhance charge separation	127
$Ru(bpy)_3$/Co-ZIF-67	liquid	CO	nanosheets perform × 1.3 better than octahedron MOFs	Effect of MOF morphology in MOF-based heterojunctions	77
CdS/Co-ZIF-67	liquid	CO	× 1.7 compared to pure CdS	Enhance light absorption, improved CO_2 uptake and charge separation by forming a Type II heterojunction	119
Bi_2S_3@Ti-MIL-125-NH_2	liquid	CO CH_4	× 1.9 compared to pure Bi_2S_3	Covalent S-H bond between both components	86

[a] The authors used TiO_2 anatase

2.5 Conclusions and knowledge gaps from the literature

As demonstrated by the literature review, the design of efficient photocatalysts remains a priority in the context of CO_2 photoconversion. Research in the field focuses on two distinct strategies: 1) improving the photoreduction activity of existing photocatalysts and 2) developing new photocatalysts.

Regarding the first strategy, heterojunction formation has shown promising results owing to its ability to reduce charge recombination while taking advantage of the physicochemical properties of both heterojunction components. Exciting advancements have been made by coupling promising photocatalysts such as TiO_2, CNNS and CdS with a wide variety of materials. Of particular interest are semiconductor/MOF-based heterojunctions. To date, the field of MOF-based heterojunctions is growing rapidly and has achieved significantly enhanced CO_2 photoreduction activity. However, a better understanding of the factors which govern charge transfer across the heterojunction interface is required. Most studies acknowledge the importance of interface contact for charge separation by distinguishing between simple physically mixed and in-situ heterojunctions. However, the factors which affect electron flow across the heterojunction interface are very rarely studied. Gaining a better understanding of the latter would support the rational development of effective MOF-based heterojunctions.

Regarding the development of new CO_2 photoreduction catalysts, porous organic-based materials have been identified as promising candidates with MOFs and COFs being the most investigated ones. Given the recent and rapid development of porous organic-based materials for CO_2 photoreduction, numerous questions remain to be answered: How do the chemical, structural and optoelectronic properties of porous organic-based photocatalysts influence CO_2 photoreduction? What are the typical products generated? What is the extent (if any) of degradation? How does CO_2 adsorb at the surface of porous organic-based photocatalysts? Answering these questions is essential to rationally develop efficient porous organic-based photocatalysts. In addition, despite their intriguing physicochemical properties, numerous porous organic-based materials such as HCPs have not yet been investigated for CO_2 photoreduction. Investigating the potential of such photocatalysts may enable the development of highly versatile catalysts and open new opportunities in terms of photocatalysts design.

2.6 Research objectives

The overall goal of this project is to investigate the potential of organic-based photocatalysts for the photocatalytic reduction of CO_2 in the gas phase. Based on the literature review and the knowledge gaps, three research objectives have been defined.

Objective 1 — To gain a better understanding of MOF-based heterojunction interfaces.

Here, I aim to better understand the factors which affect electron flow across the semiconductor/MOF interface. Achieving this would lead to rationally improving electron transfer across MOF-based heterojunctions and decrease charge recombination to yield higher activity. To address this objective, I designed a CNNS/MOF heterojunction and created a band model that describes the heterojunction interface.

Objective 2 — To explore HCPs as new photocatalysts for CO_2 photoreduction.

HCPs represent a promising class of materials for CO_2 photoreduction owing to their good CO_2 uptake capacities and high tunability. This objective proposes that HCPs would be able to photoreduce CO_2 and sets out to test this hypothesis. I synthesised, characterised, and tested three distinct HCPs for CO_2 photoreduction. I chose the chemistries of the HCPs to investigate the role of amino rich functional groups on the HCPs activity and their CO_2 uptake capacity. In addition, I investigated the robustness of the HCPs under photocatalytic reduction and the effect of using different reducing agents on their photoactivity, i.e. H_2 vs H_2O.

Objective 3 – To determine HCPs CO_2 photoreduction mechanism, as well as the CO_2 and H_2O adsorption processes.

As seen in the literature review, the use of amorphous porous polymers for CO_2 photoreduction is steadily increasing. However, little is known of the CO_2 photoreduction mechanisms, and the CO_2/H_2O adsorption process on amorphous porous polymers. Gaining a better understanding of these mechanisms is key to the rational design of improved adsorbents and photocatalysts. To address this objective, I synthesised and characterised a triazine-based HCP. The CO_2 photoreduction mechanism and the CO_2/H_2O adsorption sites were investigated by coupling in-situ DRIFTS with modulation excitation experiments, DFT calculations, and advanced data processing techniques.

Chapter 3

Methods

3.1 Characterisation of photocatalysts

In this chapter, the characterisation techniques and the photoreactor set-up used for this thesis are described along with the fundamental principles of the techniques used therein.

3.1.1 Structural and chemical properties

3.1.1.1 Powder X-ray diffraction

Powder X-ray diffraction (XRD) is a non-destructive characterisation technique used to probe the crystal structure of a material.[128] Upon X-ray irradiation, the electrons of the atoms present in the sample diffract the X-rays in specific directions with defined angles. Each set of crystalline planes will act as a diffraction grating. For each angle, when Bragg's law is satisfied, constructive interference occurs and will lead to the formation of a peak in the XRD pattern (Equation 5). The obtained XRD pattern, which represents the intensity of the diffracted X-ray for each angle, is unique to the material and can be used to identify or confirm the successful synthesis of a material.

$$n\lambda = 2d\mathrm{Sin}(\theta) \qquad (5)$$

where:

n: an integer; λ: the wavelength of the incident radiation (nm); d: the relative distance between two planes of atoms (nm); θ: the angle between the incident beam and the diffraction plane (°) (Figure 3.1).

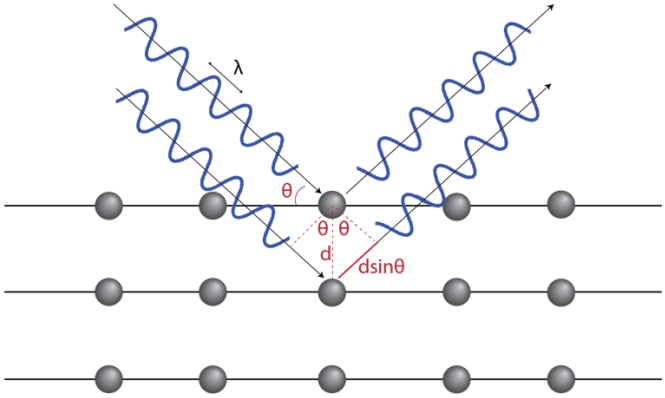


Figure 3.1 Schematic of the X-ray diffraction principle, explaining Bragg's equation.

Powder XRD measurements were recorded at room temperature on a BRUKER 2D PHASE diffractometer operating at 30 kV and 10 mA with monochromated Cu Kα radiation (λ = 0.15418 nm), following the same methods as previously described.[129] Prior to analysis, the samples were finely grounded, when necessary, and placed onto a diffraction plate.

3.1.1.2 Scanning electron microscopy

Scanning electron microscopy (SEM) is a characterisation technique that uses the signal generated by a sample upon exposure to a focused electron beam.[130] Upon sample exposure, various types of signals are produced. Of particular interest are secondary electrons (SE), which are ejected from their orbitals upon interaction with the primary electron beam. Due to their low energy (< 50 eV) only SE emitted close to the surface can reach the detector. Thus, by rasterizing the surface of the sample with a finely focused electron beam, one can obtain a high-resolution image of the sample's surface topology. When SEM analysis is conducted on an insulating sample, a very thin metallic layer can be deposited on the surface of the material to avoid charging of the sample.

SEM images were taken using a high-resolution Leo Gemini 1525 microscope in secondary electron mode, following the same methods as previously described.[46, 129, 131] Specifically, before analysis, the samples were ground, deposited on carbon tape, and coated with 20 nm of chromium to reduce charging.

3.1.1.3 Thermogravimetric analysis

Thermogravimetric analysis (TGA) monitors the weight change of a sample upon applying a certain temperature profile (i.e. heating, isothermal or cooling).[132] The obtained TG curve which represents the sample mass as a function of the temperature can be used to determine the sample composition, purity and thermal stability.

Thermal analyses were performed using a Netzsch TG209 F1 Libra thermogravimetric analyser. At least 10 mg of sample was heated from room temperature to 900 °C at a rate of 10 °C.min^{-1} under either a flow of air or N_2 (flow rate 100 mL.min^{-1}), following the same methods as previously described.[46, 49, 129] An initial isothermal step of 1 h was included at 120 °C to ensure the removal of adsorbates before heating was continued. The purity of the gases used was > 99.99% for both N_2 and air.

3.1.1.4 Solid-state nuclear magnetic resonance spectroscopy

Solid-state nuclear magnetic resonance (ssNMR) spectroscopy is a characterisation technique that uses a magnetic field to determine the composition of a sample.[133] When placing a sample in a magnetic field, the nuclei with a non-zero nuclear spin, i.e. possessing a finite magnetic moment, will align either parallel or antiparallel to the applied magnetic field. The energy difference between these two nuclear spin states is referred to as transition energy and depends on the magnetic field at the nucleus. The electrons around the nucleus will create a small magnetic field opposite to the applied magnetic field, which reduces the effective magnetic field strength at the position of the nucleus. The transition energy will therefore depend on the electron density around the nuclei and thus its chemical environment. The greater the electron density, the smaller the transition energy will be. Upon irradiation, absorption of the incoming wavelength occurs when the wavelength energy is equal to the transition energy. After absorption, a transition back to the original spin state will emit a signal at the same frequency as the one absorbed, which is often referred to as the resonance frequency. By comparing the difference between the resonance frequency of a nucleus in the analysed sample to that of a standard, one can calculate a chemical shift, which is characteristic for the chemical environment. Only nuclei with an odd number of protons or neutrons will have a finite spin and thus an NMR signal. To date, ^{1}H, ^{13}C, and ^{15}N are the isotopes most commonly used with NMR. For instance, by performing ^{13}C ssNMR spectroscopy one can determine the chemical environment of the ^{13}C atoms present in a sample. Given the low

concentration of isotopes in a sample, the NMR signal is often enhanced by performing solid-state cross-polarization magic angle spinning NMR.[133]

For Chapter 5, solid-state cross-polarization magic angle spinning ^{13}C NMR analysis was conducted by Dr Hanspeter Kählig at the University of Vienna, while for Chapter 6 experiments were conducted by Dr Xu Yingqi at Imperial College London. Both sets of experiments were performed on a Bruker 600MHz AVANCE III HD spectrometer. Around 20 mg of sample was packed into a 3.2 mm zirconia rotor, following the same method as previously described.[129] The spinning was set at 14 kHz with a relaxation delay of 4 s. A total of 2028 scans were collected.

3.1.1.5 Inductive plasma optical emission spectroscopy

Inductive plasma optical emission spectroscopy (ICP-OES) is a characterisation technique that uses argon plasma for the detection and quantification of chemical elements.[134] A nebulized sample is introduced into a high-temperature argon plasma, where the sample is degraded and its individual atomic constituents are excited via collisions with the energetic plasma ions and electrons. Upon relaxation to the ground state, photons are emitted from the sample atoms with wavelengths characteristic of the individual chemical elements. As the amount of light emitted at each wavelength is proportional to the number of emitters present in the sample, ICP-EOS is able to quantify the concentration of the detected elements.

ICP-EOS measurements were conducted to determine the Fe content of the HCP samples. These analyses were performed by MEDAC Ltd. Prior to analysis 25 mg of sample was digested using sulfuric and perchloric acid.

3.1.1.6 CHNS-O elemental analysis

CHNS-O elemental analysis is a method relying on combustion which quantifies the amount of carbon, hydrogen, sulfur and oxygen present in a sample. The combustion gases are analysed and quantified by gas chromatography to determine the ratio of elements present in the sample. While C, H, N, and S can be determined using the aforementioned method, the oxygen ratio can be determined separately using pyrolysis.

Elemental analysis was carried out on a Eurovector EA 3000 CHNS-O Elemental Analyser by Dr Mag Johannes Theiner from the University of Vienna. A micro-Sartorius, ME 5 OCE balance was used to weigh around 0.5 mg of sample, following the same methods as previously described.[129] To ensure accuracy, duplicate tests were performed. High purity helium (> 99.999%) was used as a carrier gas.

3.1.1.7 X-ray photoelectron spectroscopy

X-ray photoelectron spectroscopy (XPS) is a spectroscopy technique that uses X-rays to characterise the surface of a material.[135] This technique employs X-rays as an irradiation source to knock out electrons from their orbitals. As Equation 6 shows, the kinetic energy of the ejected electrons is related to the energy of the light source, the binding energy and the work function of the spectrometer. By plotting the rate of emission, i.e. the intensity, vs the binding energy, one can determine the composition, oxidation state, and chemical bonds present in the sample (Equation 6). To compensate for the electrons lost in the sample and avoid charging of the sample, an electron flood gun is often used during such measurements.

$$E_{K\,measured} = h\nu - E_{binding} - \phi_{spectrometer} \qquad (6)$$

where:

$E_{K\,measured}$: the measured kinetic energy of the photoelectron ($m^2.kg.s^{-2}$); h: Planck's constant (6.626 x 10^{34} $m^2.kg.s^{-1}$); ν: wave frequency of the incoming X-ray beam (s^{-1}); $E_{binding}$: binding energy of the photoelectron ($m^2.kg.s^{-2}$).; and $\phi_{spectrometer}$: the work function of the spectrometer ($m^2.kg.s^{-2}$).

XPS measurements were performed on a Thermo Scientific K-Alpha+ X-ray photoelectron spectrometer equipped with an MXR3 Al Kα monochromatic X-ray source (hv = 1486.6 eV) following the same procedure as reported before.[129, 136, 137] Specifically, samples were ground and mounted on the XPS holder using a conductive carbon tape. The X-ray gun power was set to 72 W (6 mA and 12 kV). Survey scans were acquired using 200 eV pass energy, 0.5 eV step size, and 100 ms (50 ms x 2 scans) dwell times. All high-resolution spectra were acquired using 20 eV pass energy and 0.1 eV step size. Data analysis was performed using the Thermo Avantage data analysis program. All the samples

were referenced against the C–C peak of adventitious carbon in the C 1*s* spectrum at a binding energy of 284.8 eV.

For Chapter 4, deconvolution of the core level spectra of the MOFs, CNNS and CNNS/MOF heterojunctions were performed by our collaborator Dr Benjamin Moss from Imperial College London. The core levels associated to CNNS were deconvoluted using a melon model.[138]

3.1.1.8 Attenuated total reflectance Fourier transform infrared spectroscopy

Attenuated total reflectance Fourier transform infrared (ATR-FTIR) spectroscopy is a characterisation technique that determines the radiation wavelengths absorbed by a sample.[21] In ATR-FTIR, the IR beam is directed onto an optically dense crystal to create an evanescent wave that extends beyond the crystal surface onto the sample with a penetration depth of ~ 0.5 to 2 μm (Figure 3.2).[139]

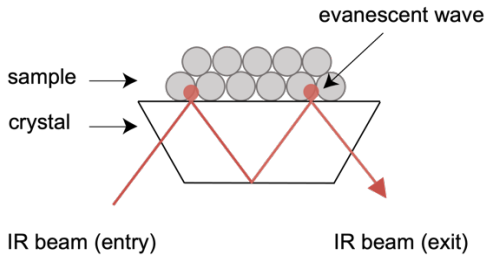


Figure 3.2 Schematic illustration of the sampling configuration of ATR-FTIR.

Upon IR exposure, the wavelengths of light having the same frequency as the atomic bonds present in the sample will be absorbed. By plotting the absorbance against the radiation wavenumber, one can determine which functional groups are present in the sample.

For Chapters 4 and 5, ATR-FTIR spectroscopy was performed in the range of 1000 - 4000 cm^{-1} on finely ground samples using a PerkinElmer Spectrum 100 FT-IR spectrometer equipped with an ATR accessory.[129, 140] A total of 16 scans were collected. For Chapter 6, ATR-FTIR measurements were performed in the range of 900 - 4000 cm^{-1} on finely ground samples using a Thermo Nicolet instrument equipped with a liquid N_2 MCT detector. A total of 220 scans were collected.

3.1.1.9 Density functional theory

Density functional theory (DFT) is a quantum mechanical model that can be used to predict a variety of molecular properties such as molecular vibrations.[140] DFT was used to simulate the vibrational frequency spectrum of triazine and biphenyl molecules, which were then compared to the experimental infrared spectra for vibrational analysis (see Chapter 6 for more detail). The premise of DFT is to describe a molecular system using the electron density distribution, which simplifies the Schrödinger equation and allows to solve it for more complex systems. To determine the vibrational frequencies present in a molecule, one first needs to use DFT to minimize the molecule energy (i.e. optimise the molecule geometry), which can then be used to determine the vibration frequency of each atom.

All DFT calculations were performed with B3PW91 functional using the software Gaussian 09. For the geometry optimisation and calculation of the infrared spectra of one triazine and one biphenyl molecule, the 6-311G(2d,2p) basis set was used. For the calculation of the six triazines molecular cluster, an initial geometry optimization was performed using the PM3 semiempirical method followed by the DFT calculation with the 3-21 basis set. The output file was then further optimised using the 6-311G(2d,2p) basis set. To compare the simulated infrared spectra with the experimental ones, an empirically determined scaling factor of 0.973 was used for the triazine molecules, while a scaling factor of 0.970 was used for the biphenyl molecules. DFT calculations were performed with the assistance of Prof Atsushi Urukawa from TU Delft.

3.1.1.10 Transmission electron microscopy

Transmission electron microscopy (TEM) is an electron microscopy technique in which a focused beam of electrons is transmitted through a sample.[141] Scattering within the sample reduces the number of electrons reaching the detector. By rasterizing the sample surface with the electron beam and measuring the intensity of the transmitted electron beam, one can obtain an image of the exposed sample. TEM is a high-resolution microscopy technique reaching atomic resolution.

TEM measurements were conducted with the help of Dr Mahmoud Ardakani from Imperial College London. TEM images were taken by a JEOL 2100Plus instrument at an acceleration voltage of 200 kV following the same procedure as reported before.[131] Before analysis, the samples were dispersed into ethanol and drop-casted on a carbon-coated copper grid (holey carbon film, 300 mesh).

3.1.2 Gas sorption and textural properties

3.1.2.1 Nitrogen gas adsorption

This volumetric method measures the pressure change caused by adsorption between the adsorbent sample chamber and a storage vessel.[142] The collected adsorption isotherm, which represents the amount of gas adsorbed vs partial pressure, can be used to estimate the surface area of the sample. As Equation 7 illustrates, by applying the Brunauer-Emmett-Teller (BET) theory one can plot $\frac{P}{n(P_o-P)}$ vs $(\frac{P}{P_o})$ to determine the monolayer capacity (m_n) and the BET constant C from the intercept $(\frac{1}{m_n C})$ and the slope $(\frac{C-1}{m_n C})$.[143, 144]

$$\frac{P}{n(P_o - P)} = \frac{1}{m_n C} + \frac{C-1}{m_n C}\left(\frac{P}{P_o}\right) \quad (7)$$

where:

P: equilibrium pressure (Pa); P_o: saturation pressure (Pa); n: adsorption capacity (mol.g^{-1}); m_n: monolayer capacity (mol.g^{-1}); C: BET constant related to the enthalpy of monolayer adsorption.

The BET surface area can then be calculated using Equation 8.

$$S_{BET} = m_n . L . \sigma \quad (8)$$

where:

m_n: monolayer capacity (mol.g^{-1}); L: Avogadro's constant (6.022 x 10^{23} mol^{-1}); σ: average area occupied by each molecule on the monolayer ($\sigma(N_2)$ = 0.162 nm^2).

The total pore volume can also be determined from the N_2 adsorption isotherms using Equation 9.

$$V_{tot} = \frac{PV_{ads}V_m}{RT} \quad (9)$$

where:

V_{tot}: total pore volume ($m^3.g^{-1}$); P: pressure (Pa); V_{ads}: volume of N_2 adsorbed at P/Po = 0.97, (derived from the sorption isotherm, $m^3.g^{-1}$); V_m: liquid nitrogen molar volume (34.7 $m^3.mol^{-1}$); R: ideal gas constant (8.314 $Pa.m^3.mol^{-1}.K^{-1}$); T: temperature (K).

The micropore and mesopore volumes can be calculated using different models.[145] Using the Dubinin-Radushkevich model, the absorption capacity from the micropores (n_{mic}) can be determined from the intercept of the linear range of the plot $\log(n)$ vs $(\log\left(\frac{P}{P_o}\right))^2$, which can be used to determine the micropore and mesopore volume (Equation 10 -12).

$$\log(n) = \log(n_{mic}) - D\left(\log\left(\frac{P}{P_o}\right)\right)^2 \quad (10)$$

$$V_{micro} = \frac{n_{mic}M}{\rho} \quad (11)$$

$$V_{meso} = V_{total} - V_{micro} \quad (12)$$

where:

n: adsorption capacity at P ($mol.g^{-1}$); n_{mic}: adsorption capacity from the micropores ($mol.g^{-1}$); D: empirical constant; P: equilibrium pressure (derived from isotherm, Pa); P_o: saturation pressure (derived from isotherm, Pa); M: adsorbate molar mass ($kg.mol^{-1}$); ρ: adsorbate density ($kg.m^{-3}$); V_{meso}: mesopore volume ($m^3.g^{-1}$); V_{micro}: micropore volume ($m^3.g^{-1}$).

Finally, the pore size distribution can be estimated by fitting the isotherm with a specific model such as DFT.

Nitrogen isotherms were measured using a porosity analyser (Micromeritics 3Flex) at -196 °C following the same procedure as reported before.[129] Specifically, prior to measurement, all samples were degassed overnight at 120 °C at around 0.2 mbar pressure. Samples underwent a further degassing step at 120 °C in-situ on the porosity analyser for 4 h, this time at around 0.003 mbar. Surface areas were calculated using the Brunauer−Emmett−Teller (BET) method (Equations 7 - 8).[144] The total volume of pores (V_{tot}) was calculated from the volume of N_2 adsorbed at P/P_0 = 0.97 (Equation 9). The

micropore volume (V_{micro}) was determined using the Dubinin−Radushkevich and the DeBoer t-plot methods in Chapters 5 and 6, respectively.[145, 146] The pore size distribution was derived from the adsorption isotherms by using the built-in software from Micromeritics and selecting the DFT model for carbon slit shape pores (N_2@77 on Carbon Slit Pores by NLDFT).

3.1.2.2 H_2, CO_2 and water vapour adsorption

Similar to porosity analysis, a volumetric gas analyser was used to collect sorption isotherms for H_2, CO_2 and water vapour. These isotherms were collected at 25 °C using a Micromeritics 3Flex instrument, equipped with a liquid container in the case of H_2O. The samples were degassed overnight at 120 °C at around 0.2 mbar pressure and again in-situ on the porosity analyser for 4 h down to around 0.003 mbar. Research grade (99.999%) CO_2 and H_2 (99.9995%, Peak Scientific PH200 hydrogen generator) were used for CO_2 and H_2 isotherms. For H_2O isotherms, miliQ water with a resistance > 18.2 micro-ohms was purified by four freeze pump thraw cycles. Water isotherms were collected up to a relative pressure of 0.8 to avoid condensation. For "wet" CO_2 uptake, i.e. investigating CO_2 uptake on H_2O pre-exposed samples, the samples were exposed to humid air (> 99% humidity) by placing them in a sealed vessel containing liquid water and a hygrometer for at least 48 h at room temperature. The samples were not in contact with the liquid water during this process. After removal, "wet" CO_2 adsorption isotherms were performed at 25 °C up to 1 bar, skipping all prior degassing steps. The first pressure CO_2 adsorption point was collected at around 10 mbar (~2 orders of magnitude higher than a standard 'dry' measurement) to minimise water desorption.

3.1.3 Photochemical properties

3.1.3.1 Diffuse reflectance ultraviolet-visible spectrometry

Diffuse reflectance ultraviolet-visible (DR-UV/Vis) spectrometry is a characterisation technique that determines the spectral characteristic of an opaque sample by measuring its diffuse reflectance.[147] Upon UV-Vis light irradiation, two types of reflection can occur: specular reflection, where the angle of reflection is equal to the incident angle, and diffuse reflectance, where the angle of reflection is independent of the incident angle.[148] The latter includes reflection, refraction and diffraction.[148] Owing to the intimate interaction with the sample, diffuse reflectance is subject to modifications by the absorption bands of the material. An absorption coefficient can be calculated by applying the Kubelka-

Munk function (Equation 13). By plotting the absorption coefficient vs wavelength, one can gain information about the light absorption properties of the sample.[149,150, 151] In addition, by plotting $(\alpha h\upsilon)^{1/n}$ against $h\nu$, the band gap of the sample can be determined. Such a plot is often referred as Tauc plot. As Equation 14 shows, a Tauc plot can only be used when the nature of the band gap transition is known.

$$\alpha = \frac{(1 - R_\infty)^2}{2R_\infty} \tag{13}$$

$$(\alpha h\upsilon)^{1/n} = B(h\nu - E_g) \tag{14}$$

where:

α: absorption coefficient; R_∞: relative reflectance measured by the equipment; h: Plancks constant (6.626 x 10^{34} $m^2.kg.s^{-1}$); ν: radiation frequency (s^{-1}); B: a proportional constant; E_g: band gap (eV); n: equal to 0.5 or 2 for direct or indirect band gap transitions, respectively.

DR-UV/Vis spectra were obtained using a Shimadzu UV-2600 spectrometer equipped with an integrating sphere. The absorption spectra were derived using the Kubelka–Munk function (Equations 13 and 14). To determine the band gap of Ti-MIL-125-NH_2 and Co-ZIF-L (direct semiconductors), a value of n = 0.5 was used, while for CNNS (indirect semiconductor), a value of n = 2 was used.

3.1.3.2 Diffuse reflectance infrared Fourier transform spectroscopy

Diffuse reflectance infrared Fourier transform spectroscopy (DRIFTS) is a characterisation technique that measures the portion of light reflected by the surface of a sample by probing the diffuse reflectance.[21] Similar to DR-UV/Vis, the diffuse reflectance is subject to modifications caused by the light absorption properties of the sample. Using the Kubelka-Munk equation one can calculate the absorption coefficient of the sample, which can then be plotted as a function of the wavelengths to gain information on the functional groups present at the sample's surface. Because the IR beam is directed directly onto the sample surface, in-situ DRIFTS can be used to probe gas-solid interactions.

In-situ DRIFTS measurements were performed on a Nicolet 8700 Thermo scientific FTIR instrument equipped with a liquid N_2 cooled MCT detector. A Praying Mantis optical accessory from Harrick was

used. The optical accessory included a high temperature and low-pressure Harrick cell and a series of optical mirrors to collect the refracted IR beam. The in-situ cell has three windows: two IR transparent windows made of BaF_2, and one window made of fused silica for UV-Vis irradiation. A thermocouple was used to control the temperature inside the cell. Prior to the analysis, a few milligrams of sample were loaded into the cell and heated at 150 °C for 18 h under He flow (30 $mL.min^{-1}$). When needed, the temperature was then lowered to 50 °C or 100 °C.

CO_2 adsorption measurements were performed by alternatively passing CO_2 and He through the set-up. At first, the cell was flushed with a CO_2/He flow of 6.6 $mL.min^{-1}$ with a 2:1 ratio for 50 min and then the atmosphere was switched to a He flow of 30 $mL.min^{-1}$ for another 50 min. Two CO_2/He - He cycles were performed. Prior to passing any CO_2 through the DRIFTS cell, a DRIFT spectrum of the HCP was acquired under a He atmosphere and used as background spectrum for the subsequent experiments.

For H_2O adsorption measurements, water-saturated He and dry He were alternately passed through the DRIFTS cell. The cell was flushed initially with a water-saturated He stream of 6.6 $mL.min^{-1}$ for 50 min and then switched to a He flow of 30 $mL.min^{-1}$ for 50 min. Two water-saturated He - He cycles were performed. Prior to passing any water vapour through the DRIFTS cell, a DRIFT spectrum of the HCP was acquired under a He atmosphere and used as background spectrum for the subsequent experiments.

For transient irradiation experiments, a SwiftCure PLU-10 lamp equipped with an optical fibre and a high-pressure Hg lamp (250 W) was used. The sample was exposed to a CO_2/water-saturated He atmosphere (1.5 vol/vol ratio) for 1 h without light irradiation. The UV-Vis lamp was then turned on for 3 h and only afterwards transient irradiation was undertaken for an additional 3 h. During transient irradiation, the light was turned on and off every 5 min. For all DRIFTS measurements, scans were collected every 12 s. Spectra were recorded in single beam mode. For isotopic DRIFTS measurements, a similar procedure was used. The sample was exposed to a water-saturated $^{13}CO_2$ atmosphere instead of a water-saturated $^{12}CO_2$ atmosphere and then irradiated with the UV-Vis light.

3.1.3.3 Multivariate curve resolution analysis

Multivariate curve resolution (MCR) represents a family of methods that can solve the mixture analysis problem, i.e. resolve complex mixtures evolving in time into individual pure components and their corresponding time-dependent concentration.[152] As represented by Equation 15, MCR describes the data set (D) as the sum of the pure components ($\mathrm{D_i}$) contributing to the signal and a component E, which represents the deviation unexplained by the model. $\mathrm{D_i}$ can further be expressed as a function of the concentration profile C_i and the pure spectra S_i^T (Equation 16 and Figure 3.3).[152, 153]

$$\mathrm{D} = \sum_{\mathrm{i}} \mathrm{D_i} + \mathrm{E} \tag{15}$$

$$\mathrm{D} = \sum_{\mathrm{i}} \mathrm{C_i S_i^T} + \mathrm{E} \tag{16}$$

where:

D: the obtained data set; $\mathrm{D_i}$: pure components; E: the error unexplained by the model; $\mathrm{C_i}$: concentration profile; $\mathrm{S_i^T}$: pure spectra.

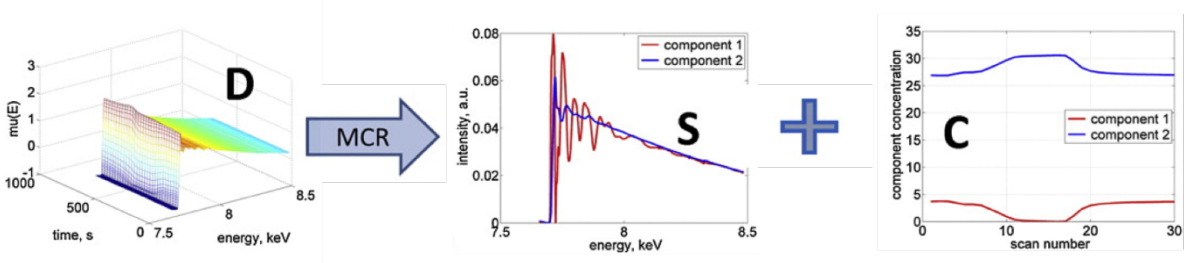


Figure 3.3 Schematic representation of Equation 16 using time-resolved data, where D represents the obtained data (sample spectrum measured at different times), and S and C represent the pure spectra and the concentration time profile of the pure spectra, respectively.[154] Adapted with permission from Elsevier.

To resolve the mixture problem, iterative methods are used. To start with, one has to estimate the number of different pure components. The program then makes a preliminary fit to the data and returns an initial estimation of the concentration profile and the corresponding spectra for the chosen number

of components. Before the next iteration, constraints can be applied to the parameters, the most common of which (and the only one used in this thesis) is to require the spectral features to display non-negative intensities. Spectra and concentration profiles are then further optimised and iterated until the convergence criterion is reached. The significance and importance of the applied constraints will be further discussed in Chapter 7.

It should be noted that the output of an MCR analysis depends crucially on the number of estimated pure components. Thus the analysis should be repeated while changing the number of estimated pure components, and only the most meaningful results should be taken into account. To accept or reject a given fit output, one has to judge if the resulting spectra can be identified with known and expected spectral features (e.g. from water vapour or plausible intermediate species).

The data obtained by time-resolved DRIFTS in Chapter 7 were processed by MCR analysis. This approach allowed identification of the vibrational bands involved in CO_2 or H_2O adsorption, as well as the corresponding concentration profiles. When performing MCR, the number of components was changed between 4 and 12; the results retained for the final fit were 6 and 7 for CO_2 and H_2O adsorption measurements, respectively (results were almost invariant for small variations around these numbers). For transient irradiation measurements, the number of components was varied between 4 and 15 and set to 10 for the final analysis. A non-negativity constraint and a convergence criterion of 0.1 were also applied.

3.1.3.4 Valence band XPS and work function measurements

XPS can be used to collect VB and work function spectra.[2, 3] As Figure 3.4 illustrates, VB XPS measurements determine the distance between the E_F and the VB offset, while work function measurements determine the distance between E_F and the vacuum level. By coupling the above measurements with DR-UV/Vis spectroscopy the band diagram of a semiconductor can be determined relative to the vacuum. To convert CB, VB and E_F from the absolute energy scale (relative to vacuum) into the redox potential scale (relative to SHE), a shift of +4.44 is required, as 4.44 eV on the former corresponds to 0.00 V on the latter, at 25 °C.

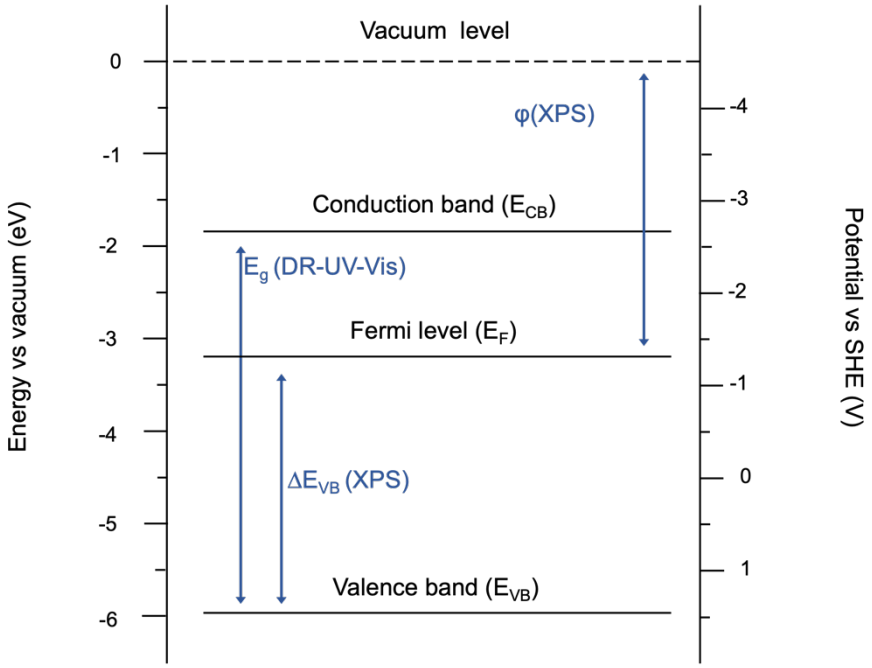


Figure 3.4 Schematic illustration of the different analytical methods needed to determine the band diagram of a semiconductor using XPS.[155] Reproduced with permission from ChemRxiv.

Valence band spectra were collected on a Thermo Scientific K-Alpha+ X-ray photoelectron spectrometer equipped with an MXR3 Al Kα monochromatic X-ray source (hv = 1486.6 eV), in the valence band region of the survey spectra (between 20 and -3 eV) using 15 eV pass energy and 0.05 eV step size, following the same procedure as reported before.[129, 137] To account for potential variations across the surface of the material, valence band spectra were measured at four different locations and the average was taken.

The work function of the photocatalysts were determined by measuring the secondary electron cut-off in the low kinetic energy region. The sample holder contained a clean gold standard sample, which was used as reference material to ensure correct calibration. A sample bias of -29.47 V was applied to the sample. The cut-off spectra were obtained using a pass energy of 10 eV. To account for potential variations across the surface of the material, the work function was measured at three different locations except if indicated otherwise, and the average was taken.

3.1.3.5 Time-correlated single photon counting

Time-correlated single photon counting (TCSPC) is a well-established technique to measure the decay of fluorescence over time (Figure 3.5).[156] In a typical experiment the sample is periodically excited with an ultrafast laser pulse. Single photon events are detected and their arrival time is correlated to the laser pulse, used as time reference signal.[157] The resulting histogram represents the time decay of fluorescence. This technique helps characterise and compare fluorescence electron recombination rates of different materials.

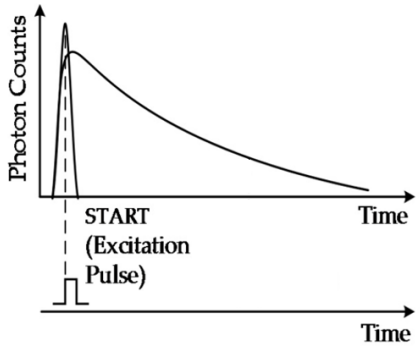


Figure 3.5 Schematic illustration of the timing diagram of a time-correlated single photon coupling histogram.[156] Adapted with permission from Elsevier.

TCSPC experiments were carried out by our collaborator Dr Michael Sachs from Imperial College London using a commercial TCSPC setup (Horiba DeltaFlex) equipped with a pulsed LED excitation source (Horiba NanoLED series) and a fast rise-time photomultiplier detector (Horiba PPD-650). The instrument response function (IRF) was measured at the wavelength of the excitation source (475 nm). During all other measurements, a suitable long-pass filter was inserted between the sample and the detector to block off scattered excitation light.

3.1.4 Gas phase CO_2 photoreduction experiments

3.1.4.1 Photocatalytic testing

A gas-solid photoreactor was assembled by a previous lab member as presented in Figure 3.6.[131] The experiments were conducted using the same procedures as outlined previously.[46, 49, 129, 131, 137, 158] Specifically, the photocatalyst was deposited on a stainless-steel plate with a fixed area of 9.6 cm^2 (Figure 3.7). To do so, 20 mg of the ground photocatalyst was dispersed in 1.2 mL of deionized water or ethanol, sonicated for 30 s and drop cast onto the sample holder. CO_2 (grade 5, > 99.999%, BOC) and H_2 (99.9995%, Peak Scientific PH200 hydrogen generator) were flowed at controlled rates using mass flow controllers (Omega Engineering, 0 - 50 $mL.min^{-1}$). For experiments using H_2 as sacrificial agent, the photoreactor (35 cm^3) was vacuumed and replenished with a gas mixture of CO_2 and H_2 (1.5 vol/vol ratio) six times. The same gas mixture of CO_2 and H_2 was subsequently passed over the catalyst bed in the photoreactor for 15 residence times before it was sealed at 1.25 bar and irradiated for 5 h (Chapter 4) or 3 h (Chapter 5). For experiments using water as sacrificial agent, a CO_2 and N_2 gas mixture (1.5 vol/vol ratio) was flowed through a H_2O bubbler to saturate the stream. The photoreactor was vacuumed and replenished with a gas mixture of CO_2, N_2 and H_2O vapour at least six times prior to measurement. Photocatalytic tests were conducted at ambient temperature. A xenon arc lamp (300 W, λ > 325 nm, LOT Quantum Design) equipped with a water filter was used as irradiation source. The distance from the lamp to the sample was set to 9.5 cm resulting in a broadband irradiance at the sample surface of 1830 $W.m^{-2}$. The lamp emission spectrum is shown in Figure 3.8. For visible light measurements a long pass UV filter (λ < 400 nm, LOT Quantum Design) was used.

As illustrated by Figure 3.9, evolved gases were analysed by gas chromatography (GC) with gas sampling valves connected directly to the photoreactor. The GC (Agilent Technologies, 7890B) was equipped with a HayeSep (Agilent J&W 6 foot, 1/8 inch, 2mm, HayeSep Q Column 80/100 SST) and a molecular sieve (Agilent J&W 6 foot, 1/8 inch, 2 mm, MolSieve 5A, 60/80) packed columns. A thermal conductivity detector (TCD) and a flame ionisation detector (FID) were used as detectors. For recyclability tests, the aforementioned process was repeated after each irradiation cycle without opening the photoreactor. The photocatalytic CO_2 reduction tests were repeated three times for each material under the same reaction conditions, unless stated otherwise.

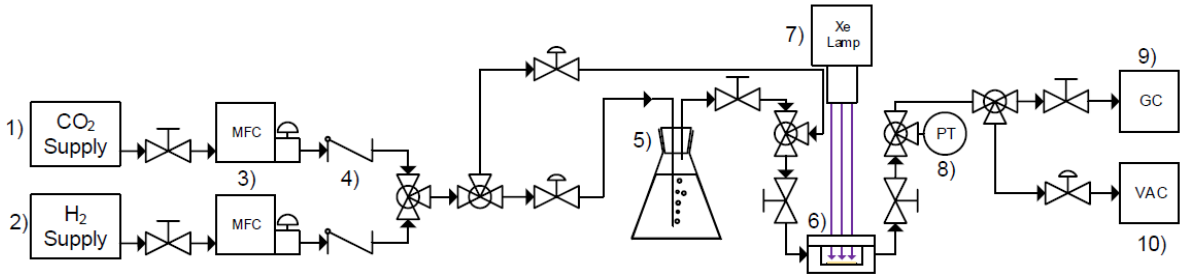


Figure 3.6 Photocatalytic gas-solid reactor setup used to evaluate photocatalytic CO_2 reduction: (1) CO_2 cylinder, (2) H_2 generator, (3) mass flow controllers, (4) non return valves, (5) H_2O saturator, (6) photoreactor, (7) Xe arc lamp, (8) pressure transducer, (9) gas chromatograph, (10) vacuum pump.[131] Reproduced with permission from John Wiley and Sons.

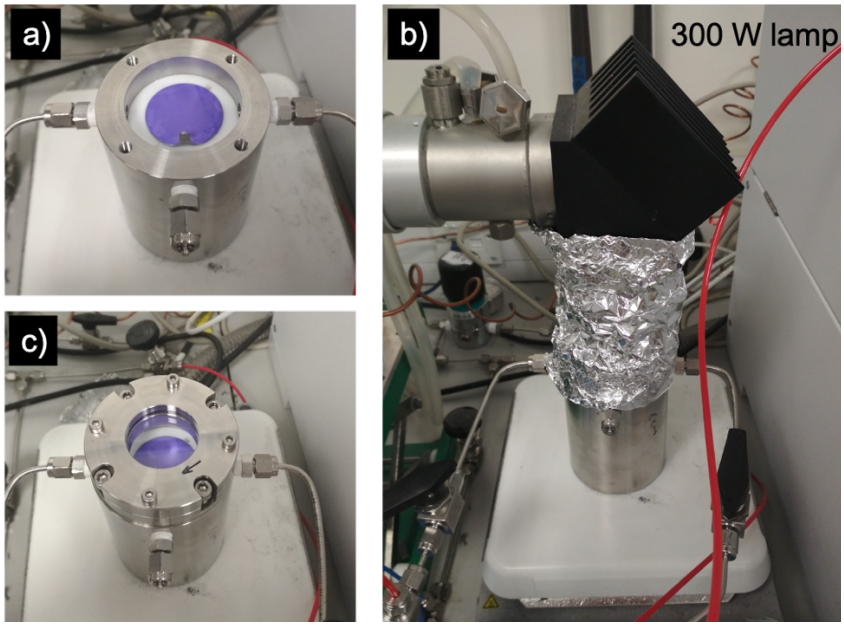


Figure 3.7 Photographs of the photoreactor system: (a) open photoreactor with photocatalyst mounted onto a metallic disc, (b) closed photoreactor and (c) photoreactor illuminated with a 300 W Xe lamp.

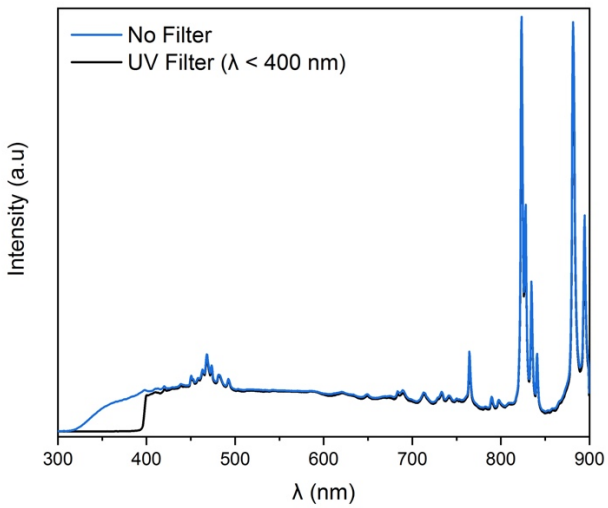


Figure 3.8 Emission spectra of the Xenon arc lamp used during photocatalytic measurements (300W, LOT Quantum Design).

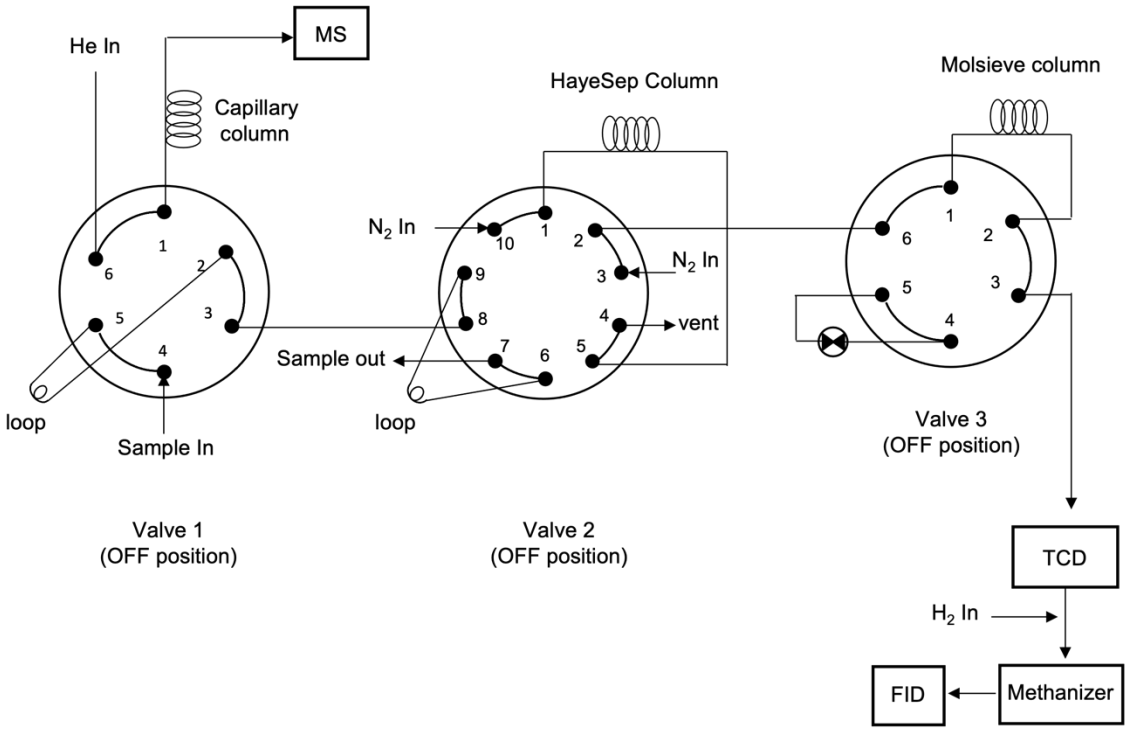


Figure 3.9 Diagram of the GC configuration used to analyse the CO_2 photoreduction products, showing the types of columns used, the detectors, and the configuration of the gas valves.

3.1.4.2 CO_2 photoreduction product quantification

The total amount of gas produced was calculated using the ideal gas law assuming a molar volume of 24.7 L.mol^{-1} at 25 °C (Equation 17). The GC provides the concentration of each gas present in the photoreactor, which was converted to moles using Equation 18, and further converted to µmol.h^{-1}.g^{-1} to determine the evolution rate of each detected gas.

$$n_{tot} = \frac{V_{tot}}{V_m} \quad (17)$$

$$n_x = C_x n_{tot} \quad (18)$$

where:

n_{tot}: total number of moles present in the photoreactor (mol); V_m: gas molar volume (L.mol^{-1}); V_{tot}: photoreactor volume (L); n_x: moles of gas x (mol); C_x: concentration of gas x determined by the GC (vol%).

H_2O_2 was detected using a colourimetric peroxide test stick from Sigma Aldrich, following the same methods as previously described.[129] 20 mg of sample was dispersed into 12 mL of H_2O. The photoreactor was vacuumed 3 times and backfilled with Research grade (99.999%) CO_2 for 1 h to reach the adsorption/desorption equilibrium of CO_2 on the catalyst surface. The photoreactor was then irradiated for 3 h under UV-Vis light. After irradiation, the photocatalyst was filtered and removed from the solution. A peroxide test stick was then dipped 1 s into the aqueous solution. In presence of H_2O_2 a colour change from white to blue should be observed.

Formic acid and methanol were quantified by Ms Patricia Carry using high-performance liquid chromatography (HPLC). After 3 h of UV-Vis irradiation, the sample was dispersed in 2 mL of water for 10 min. After immersion, the sample was filtered and removed from the aqueous solution. 20 µl of the filtrate was then analysed by HPLC (instrument: Shimadzu Prominence 20A, column: SUPELCOGEL C-610H, 30 cm x 7.8 cm with Supelguard 610H, mobile phase: 0.1% (v/v) phosphoric acid, flow rate: 0.6 mL.min^{-1}, temperature: 30 °C, sample volume: 20 µl, run time: 23 min).

3.1.4.3 Photocatalytic control tests

To ascertain the photocatalytic nature of the evolved gases the following control experiments were performed:

1- Catalytic test under an inert atmosphere (N_2/H_2 or N_2/H_2O)

2- Test without catalyst

3- Catalytic test without light

4- Catalytic test with isotopic labelling using $^{13}CO_2$

The first two control tests determine the amount of evolved gases not generated from catalysis, which could result from degradation of the material or from any residual contamination. The third test determines if the evolved gases are indeed the results of light irradiation and thus photocatalysis, while isotopic labelling confirms if the evolved gases arise from the catalytic conversion of CO_2.

The procedure used for the catalytic tests under an inert atmosphere is identical to the one performed when using CO_2, except that CO_2 was replaced with N_2 (grade 5, > 99.999%). For the control experiments 2 and 3, the procedure is identical to the one performed when using CO_2, except that in the first case no sample is drop-casted on the stainless-steel plate, while for the second case the sample is not irradiated. For isotopic tracing, the experiments were performed with $^{13}CO_2$ (BOC, > 98% atom $^{13}CO_2$ compared to $^{12}CO_2$, > 99%). The reactor was flushed with He for 1 h before injecting 15 mL of $^{13}CO_2$. After irradiation, the evolved gases were analysed by a mass spectrometer (Shimadzu MS) equipped with a Q-bond and a MolSieve column with gas sampling valves connected directly to the photoreactor.

3.1.4.4 Reported photocatalytic metrics

To compare the photoactivity of the investigated materials to the literature, the photoactivity of TiO_2 P25 was measured and can be used to calculate the normalized activity. In addition, the QE of the leading material of each study is reported. Below is a step-by-step overview on how the quantum efficiency for CO production from CO_2 was calculated (Equations 19 - 32).[137]

The quantum efficiency at a given wavelength λ is defined as:

$$\mathrm{QE} = \frac{\mathrm{N_e}}{\mathrm{N_p}} = \frac{\text{no. of reacted electrons}}{\text{no. of absorbed photons}} \text{ x100} \tag{19}$$

Based on the stoichiometry of the CO evolution redox reaction Equation 19 can be expressed as:

$$\mathrm{QE} = \frac{2\mathrm{N_{CO}}}{\mathrm{N_p}} = \frac{(2)(\text{no. of evolved CO molecules})}{\text{no. of absorbed photons}} \text{ x100} \tag{20}$$

For a polychromatic light source, we must consider the total number of absorbed photons across the wavelength range (200 - 900 nm for UV-Vis and 400 - 900 nm for visible irradiation) and the corresponding total moles of CO evolved during the irradiation time, thus:

$$\mathrm{QE} = \frac{2\mathrm{N_{CO\ (total)}}}{\mathrm{N_p}} = \frac{(2)(\text{ total no. of evolved CO molecules})}{\text{total no. of absorbed photons}} \text{ x100} \tag{21}$$

The number of photons absorbed by the photocatalyst at a given wavelength λ is given by:

$$\mathrm{N_{P,absorbed}} = \frac{(\mathrm{P_{abs}})(\lambda)(\mathrm{t})}{(\mathrm{hc})} \tag{22}$$

where λ denotes the wavelength, P denotes the power of the irradiation source, t denotes the irradiation time, h denotes Planck's constant and c the speed of light.

Equation 22 can be expressed as:

$$\mathrm{N_{P,absorbed}} = \frac{[\mathrm{I_{abs}}(\lambda)](\mathrm{S})(\lambda)(\mathrm{t})}{(\mathrm{hc})} \tag{23}$$

where $[\mathrm{I_{abs}}(\lambda)]$ denotes the intensity of the irradiation absorbed at a specific wavelength, S denotes the irradiation area, t denotes the irradiation time, h denotes Planck's constant and c the speed of light.

To determine the number of photons absorbed by the photocatalyst at a given wavelength λ, we need to consider the absorbance (Abs) of the material at that wavelength and apply the Beer-Lambert law:

$$\mathrm{Abs}(\lambda) = -\log\left[\frac{\mathrm{I_F}(\lambda)}{\mathrm{I_I}(\lambda)}\right] \tag{24}$$

where $\mathrm{I_I}(\lambda)$ denotes the intensity emitted from the irradiation source at a given wavelength λ and $\mathrm{I_F}(\lambda)$ denotes the intensity after passing through the photocatalyst at the same wavelength λ.

The intensity of irradiation absorbed by the photocatalyst at a given wavelength λ is given by:

$$\mathrm{I_{abs}}(\lambda) = \mathrm{I_I}(\lambda) - \mathrm{I_F}(\lambda) \tag{25}$$

which, using Equation 24, can be written as:

$$\mathrm{I_{abs}}(\lambda) = \mathrm{I_I}(\lambda) - \mathrm{I_I}(\lambda)10^{-\mathrm{Abs}(\lambda)} = \mathrm{I_I}(\lambda)\left[1 - 10^{-\mathrm{Abs}(\lambda)}\right] \tag{26}$$

Substituting Equation 26 into Equation 23 gives Equation 27:

$$\mathrm{N_{P,absorbed}} = \frac{\mathrm{I_I}(\lambda)\left[1 - 10^{-\mathrm{Abs}(\lambda)}\right](\mathrm{S})(\lambda)(\mathrm{t})}{(\mathrm{hc})} \tag{27}$$

The total number of photons absorbed by the photocatalyst across the entire wavelength range of the irradiation source is then given by Equations 28 and 29:

$$\mathrm{N_{P,absorbed\ (total)}} = \sum_{\lambda_{\mathrm{start}}}^{\lambda_{\mathrm{end}}} \frac{\mathrm{I_I}(\lambda)\left[1 - 10^{-\mathrm{Abs}(\lambda)}\right](\mathrm{S})(\lambda)(\mathrm{t})}{(\mathrm{hc})} \tag{28}$$

$$\mathrm{N_{P,absorbed\ (total)}} = \frac{(\mathrm{S})(\mathrm{t})}{(\mathrm{hc})} \sum_{\lambda_{\mathrm{start}}}^{\lambda_{\mathrm{end}}} \mathrm{I_I}(\lambda)\left[1 - 10^{-\mathrm{Abs}(\lambda)}\right](\lambda) \tag{29}$$

The total number of evolved CO molecules during a given reaction cycle can be written as:

$$\mathrm{N_{CO(total)}} = (\mathrm{N_a})(\mathrm{n_{CO,total}}) \tag{30}$$

where $\mathrm{N_a}$ denotes Avagadro's constant and $\mathrm{n_{CO,total}}$ denotes the total moles of CO evolved during the irradiation time.

Combining Equations 30 and 29 into Equation 21 results in a final expression for the quantum efficiency of CO evolution, which is further illustrated in the below equation:

$$QE_{CO} = \frac{(2)\,N_{CO\,(total)}}{N_P} = \frac{(2)(N_a)(n_{CO,total})}{\frac{(S)(t)}{(hc)}\sum_{\lambda_{start}}^{\lambda_{end}} I_I(\lambda)[1-10^{-abs(\lambda)}](\lambda)}\ x100 \quad (31)$$

Dimensional analysis of Equation 31:

$$QE_{CO} = \left|\frac{1}{mol}\right| \left|\frac{mol}{1}\right| \left|\frac{1}{m^2}\right| \left|\frac{1}{s}\right| \left|\frac{m^2.kg}{s}\right| \left|\frac{m}{s}\right| \left|\frac{1}{m}\right| \left|\frac{m^2}{W}\right| \left|\frac{W.s^3}{kg.m^2}\right| = (-) \quad (32)$$

Chapter 4

Effect of band-bending in photoactive MOF-based heterojunctions

This chapter is adapted from the manuscript published in *ACS Appl. Mater. Interfaces* (Schukraft et al. *ACS Appl. Mater. Interfaces* 2022, 14, 17, 19342-19352).[140] Dr Benjamin Moss and Dr Andreas Kafizas from Imperial College London contributed to this study with their scientific inputs. In addition, X-ray photoelectron spectroscopy (XPS) deconvolution spectra were performed by Dr Benjamin Moss.

4.1 Introduction

As explored in Sections 2.2 and 2.3, in the context of CO_2 conversion into value-added chemicals, the design of efficient photocatalysts remains a priority.[159, 160] Several semiconductors such as TiO_2, ZnO, CdS, and graphitic carbon nitride (g-C_3N_4) have been extensively studied for photocatalytic CO_2 conversion.[106, 161-167] However, challenges such as fast electron-hole recombination and poor utilization of the solar spectrum limit their efficiency. The formation of heterojunctions may help address some of these shortcomings. In fact, heterojunctions provide an interface across which charge carriers may become separated and, if materials with complementary band gaps are chosen, increase the proportion of the solar spectrum which can be harvested.[168]

Compared to conventional semiconductor heterojunctions, semiconductor/metal-organic framework (MOF) heterojunctions provide unique advantages. The high tunability of MOFs enables tailored structural, optoelectronic and surface properties beyond those of many inorganic materials. In theory, one can select a MOF to display desirable physicochemical properties (e.g. CO_2 affinity, pore sizes, surface area, light absorption) and build a MOF-based heterojunction with enhanced activity compared to its individual components.[5, 99, 126, 169-172] As highlighted in Section 2.4.4, to date numerous semiconductor/MOFs heterojunctions have been developed and investigated as catalysts for CO_2

photoconversion.[5, 99, 159] It is well established that the morphological, structural and chemical features of the heterojunction interface can influence the electron flow across the interface.[77, 126, 131, 173] Thus, controlling and understanding this interface is necessary for the design of efficient heterojunctions. For instance, the band bending, caused by an offset in Fermi levels between two heterojunction components, can affect electron/hole flow across the heterojunction under illumination. However, until now, this concept has only rarely been studied in MOF-based heterojunctions.[174, 175]

This chapter investigates the importance of considering interfacial band bending when building photoactive semiconductor/MOF heterojunctions. I show how to construct a simple band model that can predict the positive or negative impact of band bending on the photoreduction activity. For this study, I used graphitic carbon nitride nanosheets (CNNS), as the semiconductor representative, and selected different MOFs, including Co-ZIF-L and Ti-MIL-125-NH_2 as the MOF counterpart. All chosen MOFs displayed a 2D morphology to promote a 2D-2D contact between the MOF and CNNS, which should promote a high surface contact and favour charge separation. Moreover, MOFs were selected owing to their visible light absorption and their ability to catalyse CO_2 photoreduction.[127, 176] Overall, this chapter furthers our understanding of MOF-based heterojunction interfaces, while exploring new CNNS/MOF-based heterojunctions to improve CNNS CO_2 photoreduction activity.

4.2 Material synthesis

$Co(NO_3)_2.6H_2O$ (98%), $Ni(NO_3)_2.6H_2O$ (98%), 2-methylimidazole (2-Hmin, 99%), titanium isopropoxide (97%), melamine (99%), 2-amino-1,4-benzenedicarboxylic acid (99%), TiO_2 P25 (> 99.5%, 21 nm primary particle size), ethanol (98%), methanol (99.8%), and N,N-dimethylformamide (99%) were purchased from Sigma-Aldrich. All reagents were used as received. All gases were purchased from BOC.

Graphitic carbon nitride nanosheets (CNNS-1 and CNNS-2):

Bulk g-C_3N_4 was synthesised by heating melamine in a muffle furnace to 560 °C at a 5 °C.min^{-1} ramp under static air and maintaining the temperature for 4 h. CNNS were obtained by liquid exfoliation of the prepared g-C_3N_4. 500 mg (5.4 mmol) of bulk g-C_3N_4 was ultrasonicated (Elma, Elmasonic P H 30) into 150 mL of a 75:25 water/ethanol mixture. Two batches of CNNS were prepared and are referred

to as CNNS-1 and CNNS-2. For CNNS-1, after 8 h of sonication, the graphitic nanosheets in the supernatant were collected by centrifugation at 1000 rpm for 4 min. For CNNS-2, after 5 h of sonication, the graphitic nanosheets in the supernatant were collected by centrifugation at 1000 rpm for 2 min. The final products were dried at 110 °C overnight in air.

Co-ZIF-L:

The synthesis approach was adapted from Ref.[177]. 0.625 g (2.1 mmol) of $Co(NO_3)_2.6H_2O$ and 1.3 g (15.8 mmol) of 2-Hmin were respectively dissolved in 40 mL of deionized water. The metal-containing solution was then rapidly added to the 2-Hmin solution under magnetic stirring. After 30 min of stirring, the reaction was left idle for 4 h. The final product was centrifuged, washed with ethanol and dried at 110 °C overnight in air.

Co-ZIF-67 NS:

The synthesis approach was adapted from Ref.[178]. 1.092 g (3.7 mmol) of $Co(NO_3)_2.6H_2O$ and 1.23 g (14.9 mmol) of 2-Hmin were respectively dissolved in 30 mL of methanol. The metal-containing solution was then rapidly added to the 2-Hmin solution under magnetic stirring and ultrasonicated for 20 min. The mixture was centrifuged for 10 min at 5100 rpm and the collected Co-ZIF-67 particles were diluted in 30 mL of methanol. The solution was then rapidly added to a 30 mL methanol solution containing 1.092 g (3.7 mmol) of $Co(NO_3)_2.6H_2O$, transferred to a 100 mL autoclave, and heated at 120 °C for 1 h. After natural cooling to room temperature, the obtained yellow product was washed with methanol and dried at 110 °C overnight in air.

CoNi-ZIF-67 NS and Ni-ZIF-67 NS:

A similar procedure to Co-ZIF-67 NS was used. For CoNi-ZIF-67 NS, the metallic solution contained 0.546 mg (1.9 mmol) of $Co(NO_3)_2.6H_2O$ and 0.546 mg (1.9 mmol) of $Ni(NO_3)_2.6H_2O$. After centrifugation, the collected CoNi-ZIF-67 particles were diluted in 30 mL of methanol and rapidly added to a 30 mL methanol solution containing 0.546 mg (1.8mmol) of $Co(NO_3)_2.6H_2O$ and 0.546 mg (1.8mmol) of $Ni(NO_3)_2.6H_2O$. For Ni-ZIF-67 NS, the metallic solution contained 1.098 g (3.8 mmol) of $Ni(NO_3)_2.6H_2O$. After centrifugation, the collected Ni-ZIF-67 particles were diluted in 30 mL of methanol and rapidly added to a 30 mL methanol solution containing 1.098 g (3.8 mmol) of $Ni(NO_3)_2.6H_2O$.

Ti-MIL-125-NH_2:

The synthesis approach was adapted from Ref.[179]. 180.4 mg (0.1 mmol) of 2-amino-1,4-benzenedicarboxylic acid was mixed with 4.15 mL of DMF and 4.15 mL of methanol. 0.148 mL (0.8 mmol) of titanium isopropoxide was then added dropwise under magnetic stirring and sonicated for 5 min. The solution was then transferred to a 25 mL autoclave and heated to 150 °C for 16 h. After natural cooling to room temperature, the obtained yellow product was washed with DMF and methanol and dried at 150 °C overnight under vacuum.

CNNS-1/Co-ZIF-L heterojunctions:

A hydrothermal in-situ synthesis was used to synthesise Co-ZIF-L in the presence of preformed CNNS to obtain CNNS/Co-ZIF-L heterojunctions. The desired quantity of CNNS-1 was ultrasonicated in presence of 125 mg (0.4 mmol) of $Co(NO_3)_2.6H_2O$ in 8 mL of deionized water for 30 min. 260 mg (3.1 mmol) of 2-Hmim was dissolved into 8 mL of deionized water. Once the sonication was complete, the $Co(NO_3)_2$ solution was added to the 2-Hmim solution under vigorous stirring. After 30 min of stirring, the reaction was left idle for 4 h. The solution was centrifuged, and the supernatant removed. The final product was dried at 60 °C overnight in air. The obtained heterojunctions are referred to as CNNS-1/ZIF-L-X, where X represents the weight percent of MOF in the sample as determined by thermogravimetric analysis (TGA). As Figure 4.1 shows, the char yield of CNNS at 900 °C is 0 %, while Co-ZIF-L char yield is 48.57%. Using the equation illustrated in Table 4.1, one can determine the weight percent of MOF in a heterojunction.

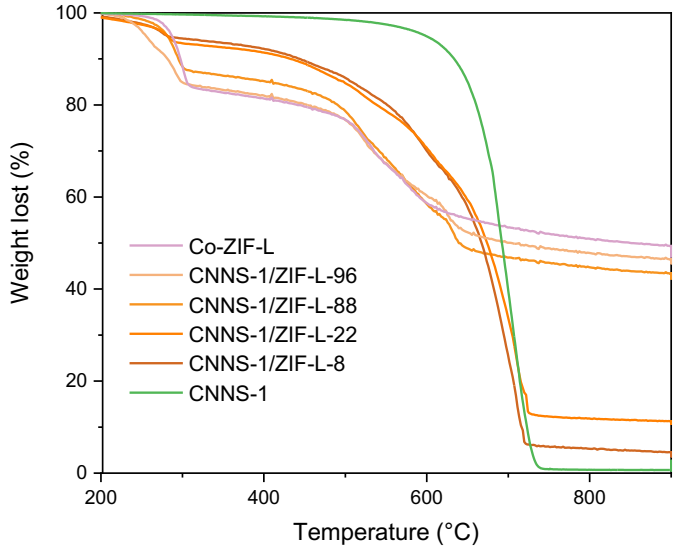


Figure 4.1 Thermogravimetric analyses of CNNS-1, Co-ZIF-L and CNNS-1/ZIF-L-X heterojunctions under N_2 atmosphere.

Table 4.1 Composition of the samples as derived by the thermogravimetric analysis of CNNS-1, Co-ZIF-L and CNNS-1/ZIF-L-X heterojunctions. The numbers in parenthesis correspond to approximations to the nearest unit.

Samples	**Final mass (% mass)**	**Mass loss[a] (% mass)**	**$X_{CNNS\text{-}1}$[b] (% mass)**	**$X_{Co\text{-}ZIF\text{-}L}$[c] (% mass)**
Co-ZIF-L	48.57		0	100
CNNS-1/ZIF-L-96	46.78	1.79	3.68 (4)	96
CNNS-1/ZIF-L-88	42.76	5.81	11.96 (12)	88
CNNS-1/ZIF-L-22	10.79	37.78	77.78 (78)	22
CNNS-1/ZIF-L-8	3.68	44.71	92.42 (92)	8
CNNS-1	0.02		100	0

[a] $\text{Mass loss} = \text{Co-ZIF-L}_{\text{Final mass}} - \text{CNNS-1/ZIF-L-X}_{\text{Final mass}}$

[b] Calculated: $X_{CNNS-1} = \frac{\Delta \text{mass loss}}{\text{Co-ZIF-L}_{\text{Final mass}}}$

[c] $X_{Co-ZIF-L} = 1 - X_{CNNS-1}$

CNNS-2/Ti-MIL-125-NH_2 heterojunction:

A similar procedure to CNNS-1/Co-ZIF-L heterojunctions was used here. 432 mg (4.7 mmol) of CNNS-2 was sonicated in the presence of 180 mg (2.2 mmol) of 2-amino-1,4-benzenedicarboxylic acid in 4.15 mL of DMF and 4.15 mL of methanol for 30 min. 0.148 mL (0.8 mmol) of titanium isopropoxide was then added dropwise under magnetic stirring. The solution was sonicated for 5 min and then transferred to a 25 mL autoclave and heated to 150 °C for 16 h. After cooling to room temperature, the obtained yellow product was washed with DMF and methanol and dried at 150 °C overnight. The obtained heterojunction is referred to as CNNS-2/MIL-25, where the number 25 represents the weight percent of MOF in the sample as determined by TGA (Figure A1.2 and Table A1.2).

4.3 Results and discussion

4.3.1 Characterisation of CNNS/Co-ZIF-L heterojunctions

I chose Co-ZIF-L as the MOF counterpart to gain a better understanding of MOF-based heterojunction interfaces and improve CNNS CO_2 photoreduction activity. The 2D morphology of Co-ZIF-L, its unique light absorption in the UV, visible and IR regions, and its ability to catalyse CO_2 photoreduction make it an excellent candidate (Figure 4.1 and A1.3).

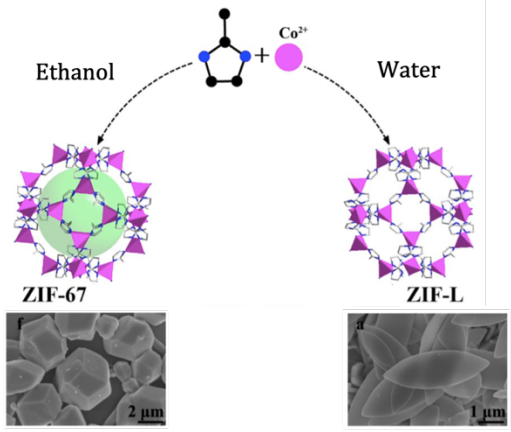


Figure 4.1 Structural representation and SEM images of Co-ZIF-67 and its 2D counterpart Co-ZIF-L. Adapted with permission from CrystEngComm.[177]

Using a one pot solvothermal approach, I synthesised four different CNNS/Co-ZIF-L heterojunctions, named CNNS-1/ZIF-L-X where X represents the weight percent of MOF in the sample (X = 8, 22, 88 and 96 wt% as determined by thermogravimetric analysis, Figure 4.1 and Table 4.1). A variety of characterisation techniques confirmed the successful incorporation of both CNNS-1 and Co-ZIF-L in the heterojunctions (Figure 4.2).

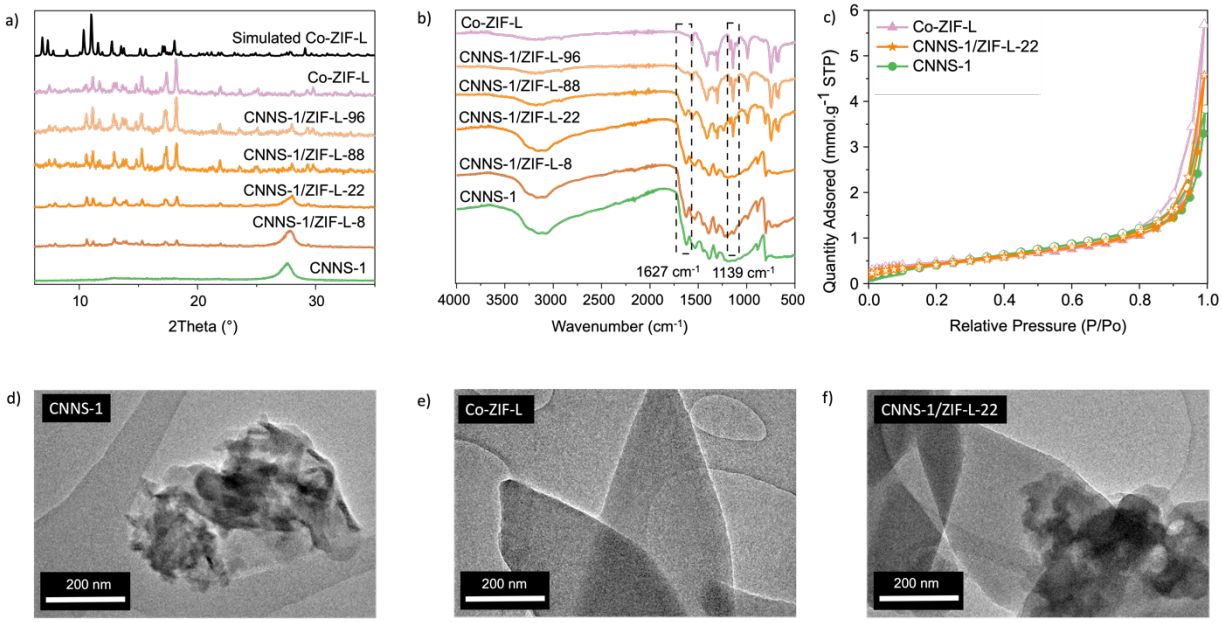


Figure 4.1 Chemical and structural characterisation of the parent materials and CNNS-1/ZIF-L-X heterojunctions (where X refers to the weight percent of MOF used): (a) PXRD patterns; (b) ATR-FTIR spectra; (c) N_2 sorption isotherms at -196 °C; (d - f) TEM images.

Figure 4.2a shows the X-ray diffraction patterns (XRD) of CNNS-1/ZIF-L-X exhibiting a combination of CNNS-1 and Co-ZIF-L patterns. Samples with a high MOF content show a high level of crystallinity with similar patterns to that of the pure MOF, while heterojunctions with a high CNNS-1 content exhibit the broad (002) peak of carbon nitride, corresponding to the spacing between stacked sheets.[180] Similarly, attenuated total reflectance Fourier transform infrared (ATR-FTIR) spectra display bands from both CNNS-1 and Co-ZIF-L (Figure 4.2b). The band at 2800 - 3500 cm^{-1} corresponds to the stretching vibration of the N–H bond from the residual $-NH_x$ group of CNNS-1, the bands at 1627 and 1312 cm^{-1} correspond to C=N and C-N stretching modes respectively, while the band at 804 cm^{-1} corresponds to the out-of-plane C–N bending of CNNS-1.[181, 182] The vibrational band at 1139 cm^{-1} is characteristic of

the in-plane bending modes from the imidazole group present in Co-ZIF-L.[183] Transmission electron microscopy (TEM) of CNNS-1 reveals an agglomerate of CNNS-1 nanosheets forming clusters of ~0.5 μm, while Co-ZIF-L displays a leaf-like morphology and a particle size of ~2 μm. In addition, TEM images of CNNS-1/ZIF-L-22 display both Co-ZIF-L and CNNS-1 particles and show direct growth and contact between CNNS-1 and Co-ZIF-L, bringing further evidence of heterojunction formation (Figures 4.2d - f). Finally, XRD, FTIR, XPS and TEM suggest that the structure of Co-ZIF-L and CNNS-1 did not change after heterojunction formation.

Having confirmed the formation and composition of the heterojunctions, I next evaluated features that influenced their CO_2 photoreduction properties, namely porosity, CO_2 sorption and light absorption. CNNS-1 displays a surface area and a CO_2 uptake at 25 °C and 1 bar of 33 $m^2.g^{-1}$ and 0.15 $mmol.g^{-1}$, respectively (Figures 4.2c, 4.3a and Table A1.3). The values for Co-ZIF-L are 41 $m^2.g^{-1}$ and 1.28 $mmol.g^{-1}$ (Figures 4.2c, 4.3a and Table A1.3). As expected, considering the lower MOF content of CNNS-1/ZIF-L-22, the heterojunction displays a surface area of 37 $m^2.g^{-1}$ with a CO_2 uptake of 0.27 $mmol.g^{-1}$. Overall, compared to pure CNNS-1, the heterojunction formation favours higher CO_2 uptakes due to the presence of Co-ZIF-L. The Tauc plots show that both CNNS-1 and Co-ZIF-L absorb UV and visible light with respective band gaps of 2.73 and 1.95 eV (Figure A1.4). As Figure 4.3b shows, CNNS-1/ZIF-L-22 exhibits the absorption features of both Co-ZIF-L and CNNS-1.

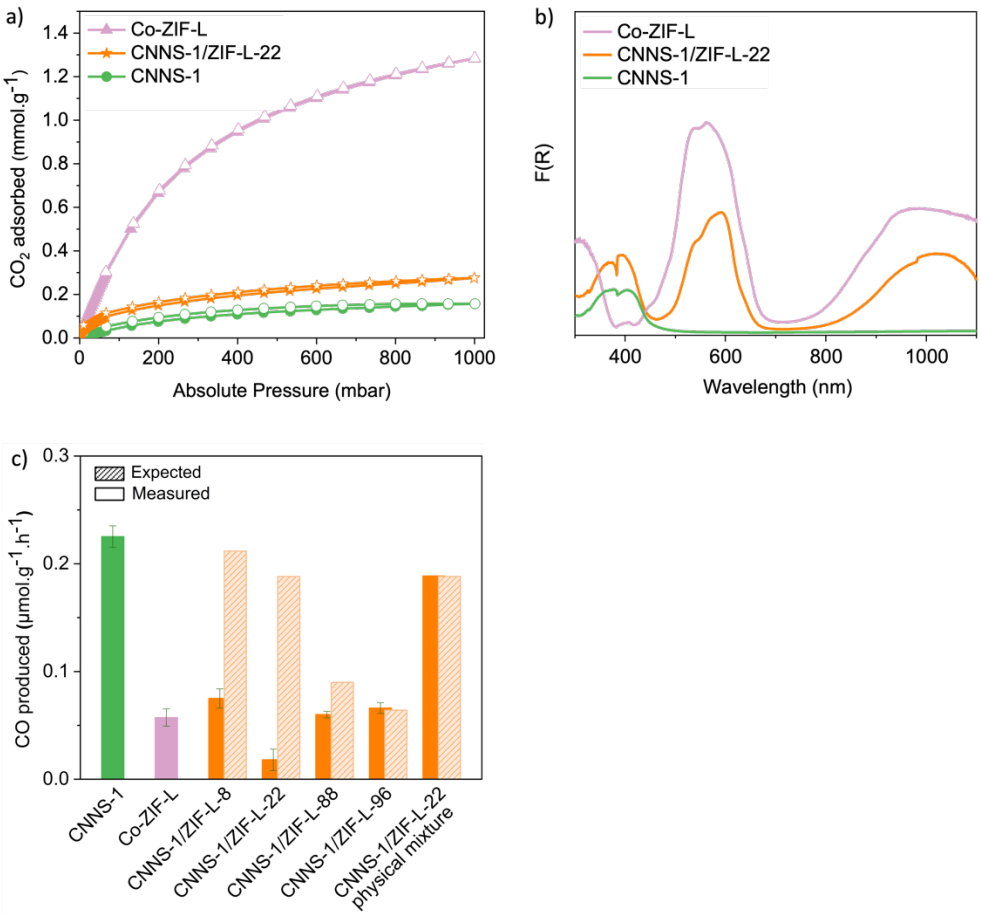


Figure 4.2 (a) CO_2 sorption isotherms at 25 °C, (b) UV-Vis absorption spectra of CNNS-1, Co-ZIF-L and CNNS-1/ZIF-L-22, (c) CO photocatalytic production rates of CNNS-1, Co-ZIF-L and CNNS-1/ZIF-L-X heterojunctions (note: X corresponds to the weight percent of MOF used).

4.3.2 CO_2 photoreduction activity and band bending diagram of CNNS/Co-ZIF-L

CO_2 photoreduction tests were carried out at ambient temperature in a heterogeneous gas-solid photoreactor under UV-Vis irradiation (Xe arc lamp, 300 W, Figure 3.8, Section 3.1.4.1), without the addition of a co-catalyst or photosensitizer. H_2 was used as the sacrificial proton and electron source. All samples photoreduced CO_2 with a 100% gaseous selectivity towards CO.

To determine the effect of heterojunction formation on the CO_2 photoreduction activity, I calculated an expected photoactivity based on the composition of the heterojunction components. In the absence of

interaction, it is reasonable to expect the heterojunction activity to be proportional to the sum of the activities of the base materials. For example, for CNNS-1/ZIF-L-22, composed of 22 wt% MOF and 78 wt% CNNS-1 (see Table 4.1 and Table A1.4), the expected activity is the sum of Co-ZIF-L photoactivity, multiplied by 0.22, and CNNS-1 photoactivity, multiplied by 0.78. I then compared these activity values to the activity actually measured for the heterojunctions (Figure 4.3c and Table A1.4). Surprisingly, the formation of a CNNS-1/ZIF-L heterojunction negatively impacts the photoreduction activity in most cases. As Figure 4.3c shows, for CNNS-1/ZIF-L-96 the activity remains unimproved, while for CNNS-1/ZIF-L-8, -22, and -88, the amount of CO produced decreases upon heterojunction formation. For heterojunctions with a high MOF content the activity resembles the one of the physical mixture, whereas, for the others, the heterojunction formation reduces the activity. Such observation corroborates that the intimate contact between CNNS-1 and Co-ZIF-L negatively impacts the photoreduction activity. Such behaviour is most noticeable for CNNS-1/ZIF-L-22 where CO production is 0.018 ± 0.01 $\mu mol \cdot g^{-1} \cdot h^{-1}$ compared to 0.188 $\mu mol \cdot g^{-1} \cdot h^{-1}$ for the expected value. To further study the effects of CNNS-1/ZIF-L-22 heterojunction formation on the photoactivity, I prepared and tested a physical mixture containing the same composition as the latter (Table A1.4). As Figure 4.3c shows, the activity of the physically mixed sample is equal to the expected value (0.189 vs 0.188 $\mu mol.g^{-1}.h^{-1}$, respectively), whereas a 10-fold decrease in the activity is observed between the physical mixture and the in-situ synthesised heterojunction. Given that both components have some degree of inherent activity for CO_2 reduction, these results show that the intimate contact between CNNS-1 and Co-ZIF-L upon heterojunction formation negatively impacts the CO_2 photoreduction activity.

In the literature, numerous reports show an enhanced CO_2 photoreduction activity in MOF-based heterojunctions.[5, 46, 94, 117, 123, 169, 184-188] However, studies do not commonly focus on investigating and understanding the origin of photocatalytic losses in MOF-based heterojunctions, I tackled the problem by investigating how electrons flow across the heterojunction.

I first resolved the electronic structure of CNNS-1 and Co-ZIF-L using the method explained in Section 3.1.3.4 (Figure 4.5, Figures A1.4 - A1.6). While doing so is common in the literature for MOF-based heterojunctions, the obtained electronic structures do not usually consider the effects of band bending and band alignment.[189]

Heterojunction systems are better described by band bending diagrams.[190, 191] This concept is widespread in the photoelectrochemisty literature but much less so in MOF photocatalysis studies.[189, 192-196] Band bending occurs when two semiconductors with distinct work functions, i.e. different Fermi levels, are put into contact. Upon contact, electrons transfer from one semiconductor to the other until equilibrium is reached, i.e. both Fermi levels are aligned (Figure 4.4). This spontaneous electron diffusion favours the formation of negative and positive charges at the interface, generating an internal electric field. This electric field results in upward or downward band bending. Band bending upon heterojunction formation can thus affect how charge carriers flow across the heterojunction, thereby influencing electron-hole recombination/separation. While electronic structures for MOF-based heterojunctions tend to neglect band bending and band alignment, considering these effects enables one to better describe the photocatalytic process occurring at a heterojunction interface.

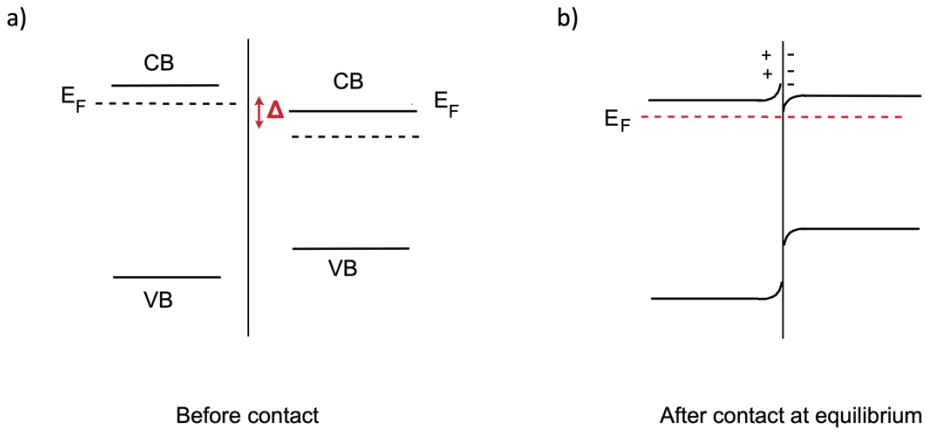


Figure 4.3 Band diagram between two distinct n-type semiconductors a) before and b) after contact.

This concept appears in the recently introduced step-scheme (S-scheme) MOF-based heterojunction, however, it is usually not considered in other (i.e. non S-scheme) MOF-based heterounctions.[174, 175] To understand the electron flow in our system, I determined the band alignment using X-ray photoelectron spectroscopy (XPS), and used this information to produce a band bending diagram for the CNNS-1/Co-ZIF-L heterojunctions (Figure 4.5c and Figures A1.7 - A1.11). The implications of my findings are discussed below.

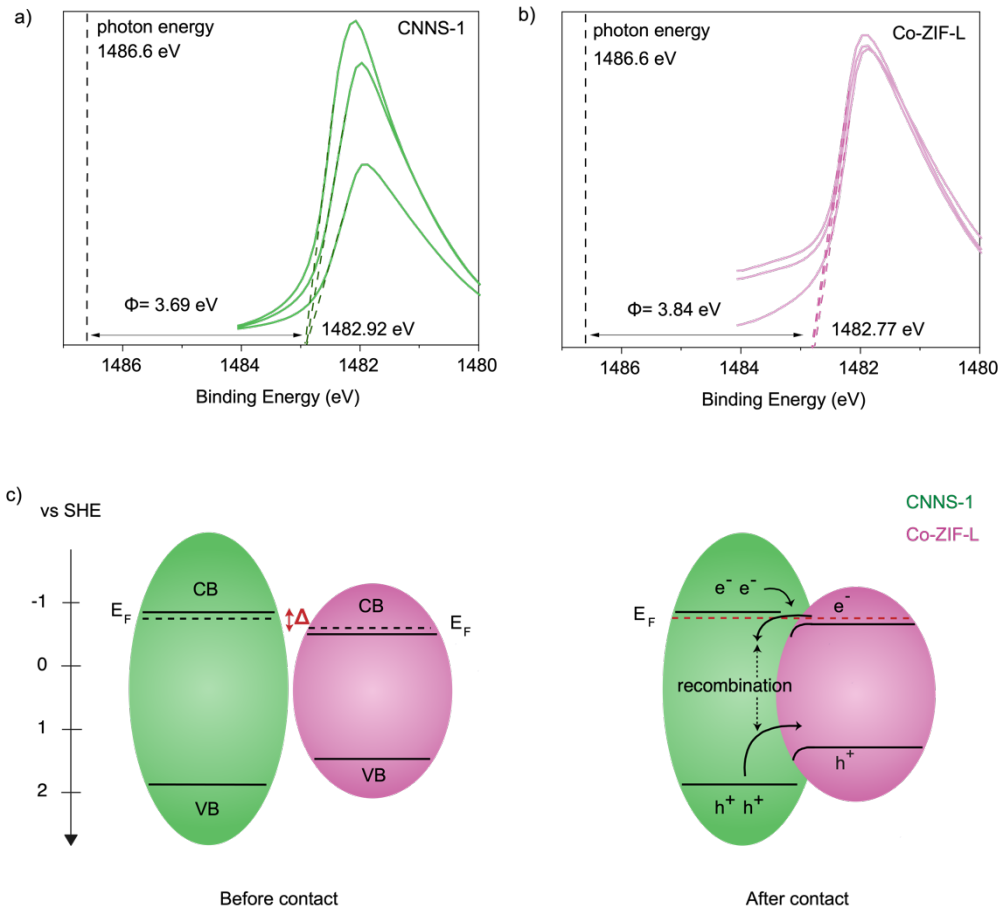


Figure 4.4 Work function measurements of: (a) CNNS-1 and (b) Co-ZIF-L; measured at the secondary cut-off, which represents the low kinetic region of the XPS spectra, where the kinetic energy of the detected photo-electrons is equal to zero, and (c) band bending diagram of CNNS-1/Co-ZIF-L heterojunction before and after contact. The delta symbol used in figure c) represents the difference between the fermi levels of both heterojunction components.

4.3.3 The importance of band bending and band alignment to understand electron flow in MOF-based heterojunctions

Using XPS, I investigated the surface chemical states of CNNS-1, Co-ZIF-L and CNNS-1/ZIF-L-22 (Figures A1.7 - A1.9). The main C 1*s* peak of CNNS-1 at 288 eV corresponds to sp^2 bonded carbons (N=C-N), while the N 1*s* core level display four deconvoluted peaks at 398.6, 399.3, 400.2 and 401.2 eV characteristic of the heptazine ring, heptazine core, $-NH_2$ and -NH groups, respectively.[197, 198] Regarding Co-ZIF-L, the deconvoluted Co 2*p* spectrum shows eight different binding energies at 781.8

784.1, 797.2, and 799.4 eV attributed to Co^{3+} 2 $p_{3/2}$, Co^{2+} 2 $p_{3/2}$, Co^{3+} 2$p_{1/2}$, Co^{2+} 2$p_{1/2}$ respectively, along with the satellite peaks at 786.9, 789.7, 802.7, and 805.0 eV.[199] The main C 1*s* peaks correspond to C-C (284.8 eV), C-CH_3 (285.0 eV), N-C-C-N (285.6 eV) and C-N-C (286.6 eV) bonds, while the peaks at 398.9 and 400.6 eV in the N 1*s* spectrum relate to the sp^2 and sp^3 nitrogen of the imidazole linker.[199]

Interestingly, when comparing CNNS-1/ZIF-L-22 to Co-ZIF-L spectra, a 0.8 eV shift to higher binding energy is observed in the Co 2*p* and O 1*s* core levels associated to Co-ZIF-L (Figure 4.6 and Figures A1.10 - A1.11). This shift is unlikely the result of identical chemical shifts for both Co 2*p* and O 1*s* core levels. Instead, I attribute these changes to a Fermi level shift.[192, 200, 201] Since the Fermi level of a material is defined at 0 eV in XPS, a constant shift of all Co-ZIF-L core line peaks towards higher binding energy suggests an upward shift in the Fermi level position upon heterojunction formation.[131, 200, 201]

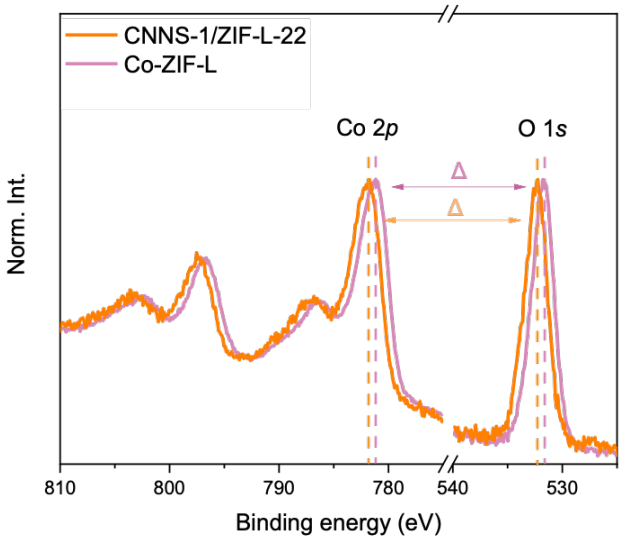


Figure 4.5 High resolution XPS of Co-ZIF-L and CNNS-1/ZIF-L-22 Co 2*p* and O 1*s* core level spectra showing an identical shift towards lower binding energies upon heterojunction formation. Consequently, the Co 2*p* - O 1*s* peak separation (Δ) is invariant upon heterojunction formation.

As defined by Equations A1.1 and A1.2 in Figure A1.11, the difference in binding energy between two peaks is independent of the position of the Fermi level. Figure 4.6 shows that, indeed, the separation of the Co 2*p* and O 1*s* peaks remains constant in Co-ZIF-L and CNNS-1/ZIF-L-22, further suggesting it corresponds to a Fermi level shift.

I did not observe any significant shift in the core level associated to CNNS-1 indicating the absence of a Fermi level shift and, thus, no band bending is occurring on CNNS-1. I foresee that the potential drop, generated by interfacial charge transfer, may mainly distribute across the MOF. Hence, upon heterojunction formation, electrons transfer from CNNS-1 to Co-ZIF-L until the Fermi levels align. This upward shift is consistent with the sign of the work function difference between CNNS-1 and Co-ZIF-L (i.e. 3.69 eV vs 3.84 eV respectively, Figures 4.5a and 4.5b). Overall, upon heterojunction formation, one can interpret the change in the position of the Fermi level to be equal to the potential drop in the heterojunction upon equilibration of the two materials forming the junction. In semiconductor-based heterojunctions, the change in chemical potential upon heterojunction formation can be used to probe band bending. An upward shift of the Fermi level upon interface contact suggests downwards band bending and vice versa. Based on these observations, and using band gap, valence band and work function measurements, I built the band bending diagram shown in Figure 4.5c.

According to Figure 4.5c, after heterojunction formation, a Type I straddling gap is formed. Under illumination, the photogenerated electrons of CNNS-1 are predicted to migrate to the conduction band of Co-ZIF-L. The straddling junction combined with downward band bending will likely cause electrons to accumulate in Co-ZIF-L at the heterojunction interface with CNNS-1. This could hinder electrons from flowing to the surface of Co-ZIF-L, where they can reduce CO_2. In addition, such accumulation of electrons at the heterojunction interface may reduce their mobility and increase the likelihood of recombination with the photogenerated holes that also accumulate in Co-ZIF-L. It should be noted that the band bending diagram agrees with the observed photocatalytic results, suggesting a decrease of available photogenerated charges upon heterojunction formation.

4.3.4 Screening of CNNS/MOF-based heterojunctions based on their band bending diagram

Based on the above findings, I investigated the potential of other MOFs to build a CNNS/MOF heterojunction with a more favourable band bending diagram. I chose Co-ZIF-67 NS, CoNi-ZIF-67 NS, Ni-ZIF-67 NS and Ti-MIL-125-NH_2 owing to their visible light absorption and their 2D morphology. More specifically, Co-ZIF-67 NS was chosen owing to its strong visible light absorption between 350 and 550 nm, its 2D morphology and the similarity of its composition with Co-ZIF-L.[202] In fact, as investigated by

Li et al., Co-ZIF-67 and ZIF-67 are both constituted of the same metal and ligand, i.e. Co and 2-methylimidazole, while displaying different monomer to metal ratios.[203] This difference was thought to help maintain the unique light absorption properties of Co-ZIF-L while varying its band edge position. To further alter Co-ZIF-67 NS band edge position to yield a Type II heterojunction upon contact with CNNS-1, CoNi-ZIF-67 NS and Ni-ZIF-67 NS were also investigated. As explored by Dong et al., substituting Co atoms with Ni atoms upshifts the conduction band towards a more negative reduction potential, which should facilitate the formation of a Type II heterojunction when coupled with CNNS-1.[204] Finally, Ti-MIL-125-NH_2 was chosen owing to its appropriate band edge position. Ti-MIL-125-NH_2 has been repeatedly used for CO_2 photoconversion and its band edge position are located at ~2.1 V and ~ -0.6 V vs NHE at pH = 0, which should favour the formation of a Type II heterojunction upon contact with CNNS-1 (Table A1.5).[205, 206] Figure 4.7 illustrates the structure of Ti-MIL-125-NH_2.

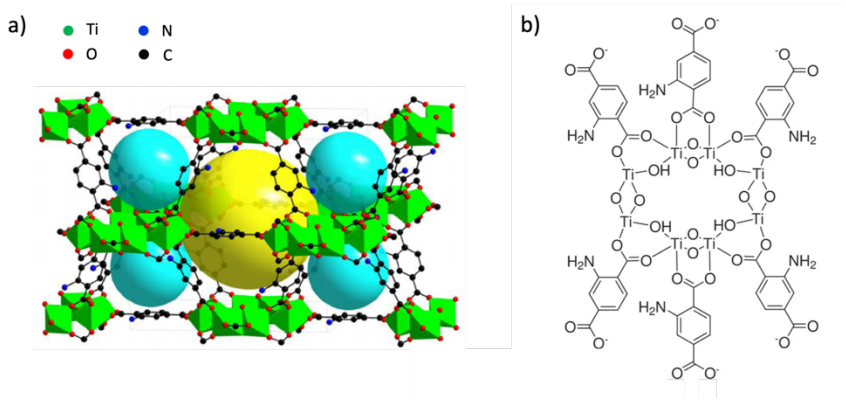


Figure 4.6 Structural representation of a) the pores and b) metal cluster of Ti-MIL-125-NH_2.. Adapted with permission from Elsevier.[179]

Having identified the alternative MOFs, I synthesised and characterised them using a variety of techniques. As Figures 4.8a - d illustrate, scanning electron microscopy (SEM) images confirms the 2D nature of the MOFs. Co-ZIF-67 NS, CoNi-ZIF-67 NS and Ni-ZIF-67 NS display ultrathin nanosheets, while Ti-MIL-125-NH_2 displays thicker plate like particles. XRD patterns of Co-ZIF-67 NS, CoNi-ZIF-67 NS and Ni-ZIF-67 NS exhibit broad (002) and (222) peaks, in agreement with what is reported in the literature (Figure 4.8e).[178, 202] The observed XRD patterns are expected owing to the 2D morphology of the samples. The (002) peak dominates as, when the sample dries, the nanosheets tend to orientate parallel to the drying surface, leading to preferential diffraction of the (002) crystal plane.[207] Compared

to Co-ZIF-67 NS, the XRD patterns of CoNi-ZIF-67 NS and Ni-ZIF-67 NS display broader peak shapes, which could be the result of the presence of thinner nanosheets.[207] Regarding Ti-MIL-125-NH_2, its XRD pattern shows similar patterns to those of the simulated MOF, confirming its successful synthesis.

To investigate the composition of the aforementioned MOFs, I performed XPS analysis (Figures A1.12 - A1.15). For ZIF-67 NS based MOFs, the deconvoluted C 1*s* spectrum shows three deconvoluted peaks corresponding to C-CH_3 (~285.1 eV), N-C-C-N (~286 eV) and C-N-C (~286.9 eV) bonds while the peaks at 399.1 and 400.8 eV in the N 1*s* spectrum relate to the sp^2 and sp^3 nitrogen of the imidazole linker.[208] The deconvoluted Co 2*p* spectra of Co-ZIF-67 NS and CoNi-ZIF-67 NS show eight different binding energies at ~781.4, ~783.7, ~796.8, and ~799.0 eV attributed to Co^{3+} 2 $p_{3/2,}$ Co^{2+} 2 $p_{3/2}$, Co^{3+} $2p_{1/2}$, and Co^{2+} $2p_{1/2}$ respectively, along with the satellite peaks at ~786.7, ~789.5, ~802.5, and ~805.3 eV.[199] The deconvoluted Ni 2*p* spectra of CoNi-ZIF-67 NS and Ni-ZIF-67 NS show eight different binding energies at ~855.5, ~857.6, ~872.5, and ~873.9 eV attributed to Ni^{3+} 2 $p_{3/2,}$ Ni^{2+} 2 $p_{3/2}$, Ni^{3+} $2p_{1/2}$, and Ni^{2+} $2p_{1/2}$ respectively, along with their satellite peaks at ~863.2, ~865.2, ~879.9, and ~881.5 eV, respectively.[209] Based on the elemental composition determined from XPS data, CoNi-ZIF-67 NS contains 7.5 at% of Co and 0.5 at% of Ni, which corresponds to a 15:1 Co to Ni metal ratio. For Ti-MIL-125-NH_2, deconvolution of the C 1*s* spectrum shows four different binding energies at 298.9, 286.8, 285.2 and 284.8 eV, attributed to C=O, C-N, C=C and C-C, respectively (Figure A1.15).[210] Ti 2*p* displays two binding energy peaks at 458.9 and 464.6 eV, attributed to Ti $2p_{3/2}$ and Ti $2p_{1/2}$ of Ti^{IV}, respectively,[211] while the O 1*s* spectrum shows two peaks at 532.7 and 531.2 eV corresponding to C=O and titanium oxo clusters.[127]

To assess the light absorption properties of the MOFs, diffuse reflectance ultraviolet-visible (DR-UV/Vis) measurements were performed. The absorbance spectra of Co-ZIF-67 NS and Ti-MIL-125-NH_2 are similar to those reported in the literature.[127, 202] However, for CoNi-ZIF-67 NS and Ni-ZIF-67 NS their absorbance spectra were not found in the literature. Overall, the absorbance spectra and their derived Tauc plots show that Co-ZIF-67 NS, CoNi-ZIF-67 NS, Ni-ZIF-67 NS and Ti-MIL-125-NH_2 absorb both UV and visible light with respective band gaps of 1.75, 1.82, 3.57 and 2.93 eV (Figure 4.8f and Figure A1.16). Ni-ZIF-67 NS Tauc plot indicates the presence of mid-gap states with the smallest distance between the valence band and the mid-gap states being of 2.3 eV.

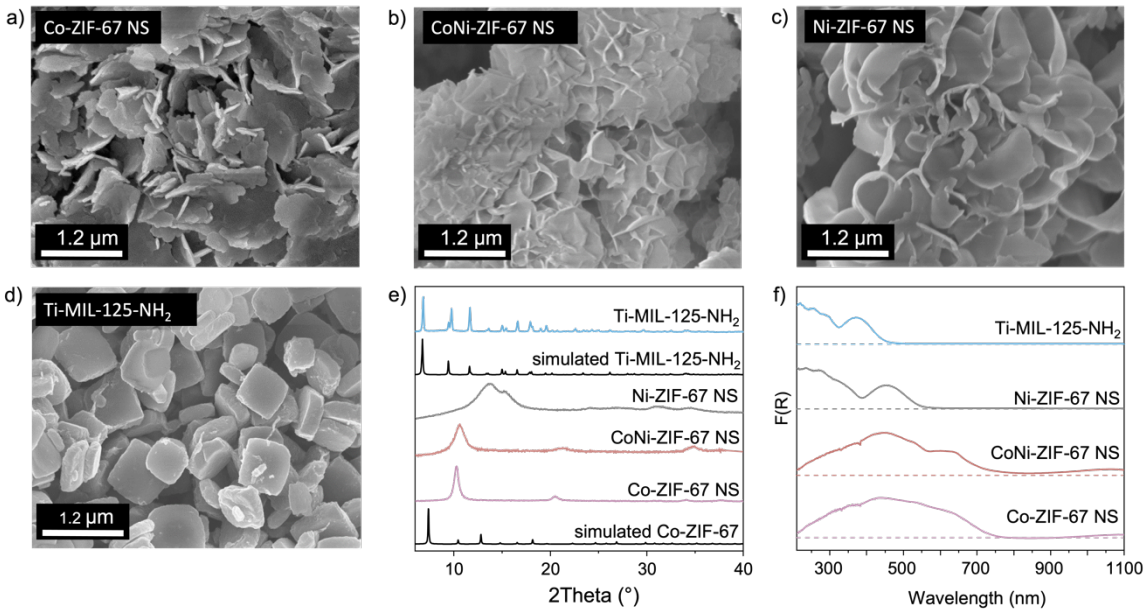


Figure 4.7 SEM images of (a) Co-ZIF-67 NS, (b) CoNi-ZIF-67 NS, (c) Ni-ZIF-67 NS, and (d) Ti-MIL-125-NH_2, and their corresponding (e) PXRD patterns and (f) UV-Vis absorbance spectra.

When developing a heterojunction, one should establish the band bending diagram at an early stage of the research. To do so, I performed limited characterisation of the samples using selected techniques (i.e. XRD, SEM, UV-Vis and XPS) and proceeded with building the band bending diagram of the heterojunctions (namely: CNNS-1/Co-ZIF-67 NS, CNNS-1/CoNi-ZIF-67 NS, CNNS-1/Ni-ZIF-67 NS and CNNS-1/Ti-MIL-125-NH_2). I performed valence band and work function measurements on all the MOFs. Based on the obtained band bending diagrams, only the most promising heterojunction was synthesised, characterised and tested for CO_2 photoreduction.

The conduction band of Co-ZIF-67 NS, CoNi-ZIF-67 NS, Ni-ZIF-67 NS and Ti-MIL-125-NH_2 were located at -0.55, -0.65, -1.94 and -0.64 V vs NHE at pH=0, respectively, while their valence band were located at 1.20, 1.19, 1.15 and 2.28 V vs NHE at pH=0, respectively (Figure A1.16 - A1.17, Table A1.5). The work functions of the aforementioned MOFs were determined to be at 3.63, 3.62, 3.77 and 3.63 eV, respectively (Figure A1.18). Based on these results, I constructed the band bending diagram shown in Figure 4.9. As Figure 4.9b illustrates, CNNS-1/ Co-ZIF-67 NS and CNNS-1/CoNi-ZIF-67 NS favour the formation of a Type I straddling gap, which will not promote effective charge separation across the

interface as both electrons and holes migrate to the MOF. Regarding the electronic structure of CoNi-ZIF-67 NS and Ni-ZIF-67 NS, the presence of Ni atoms gradually upshifts the conduction band position and impacts the Fermi level position, which leads to the formation of a type II heterojunction upon formation of CNNS-1/Ni-ZIF-67 NS. As Figure 4.9b illustrates, after contact and under illumination, photogenerated electrons migrate to CNNS-1, while holes migrate to Ni-ZIF-67 NS. In such heterojunction, charges should be spatially separated, and heterojunction formation should favour higher photoactivity compared to the physical mixture of the heterojunction components. However, in CNNS-1/Ni-ZIF-67 NS, CO_2 photoreduction will take place on CNNS-1 and will not take advantage of CO_2 activation on the MOF surface which is inherently better than that of CNNS-1, owing to the inorganic nature of MOFs. Regarding CNNS-1/Ti-MIL-125-NH_2, the band bending diagram indicates the formation of a Type II heterojunction, where electrons migrate to Ti-MIL-125-NH_2 and holes migrate to CNNS-1. In contrast to CNNS-1/Ni-ZIF-67 NS, CNNS-1/Ti-MIL-125-NH_2 should promote CO_2 photoreduction on the MOF and take advantage of its strong activation sites.

Based on the band bending diagrams, CNNS-1/Ti-MIL-125-NH_2 appears to be the most promising heterojunction, which should promote charge transfer across the heterojunction interface and improve CNNS photoactivity. I therefore decided to synthesise, characterise and test CNNS/Ti-MIL-125-NH_2 heterojunctions for CO_2 photoreduction.

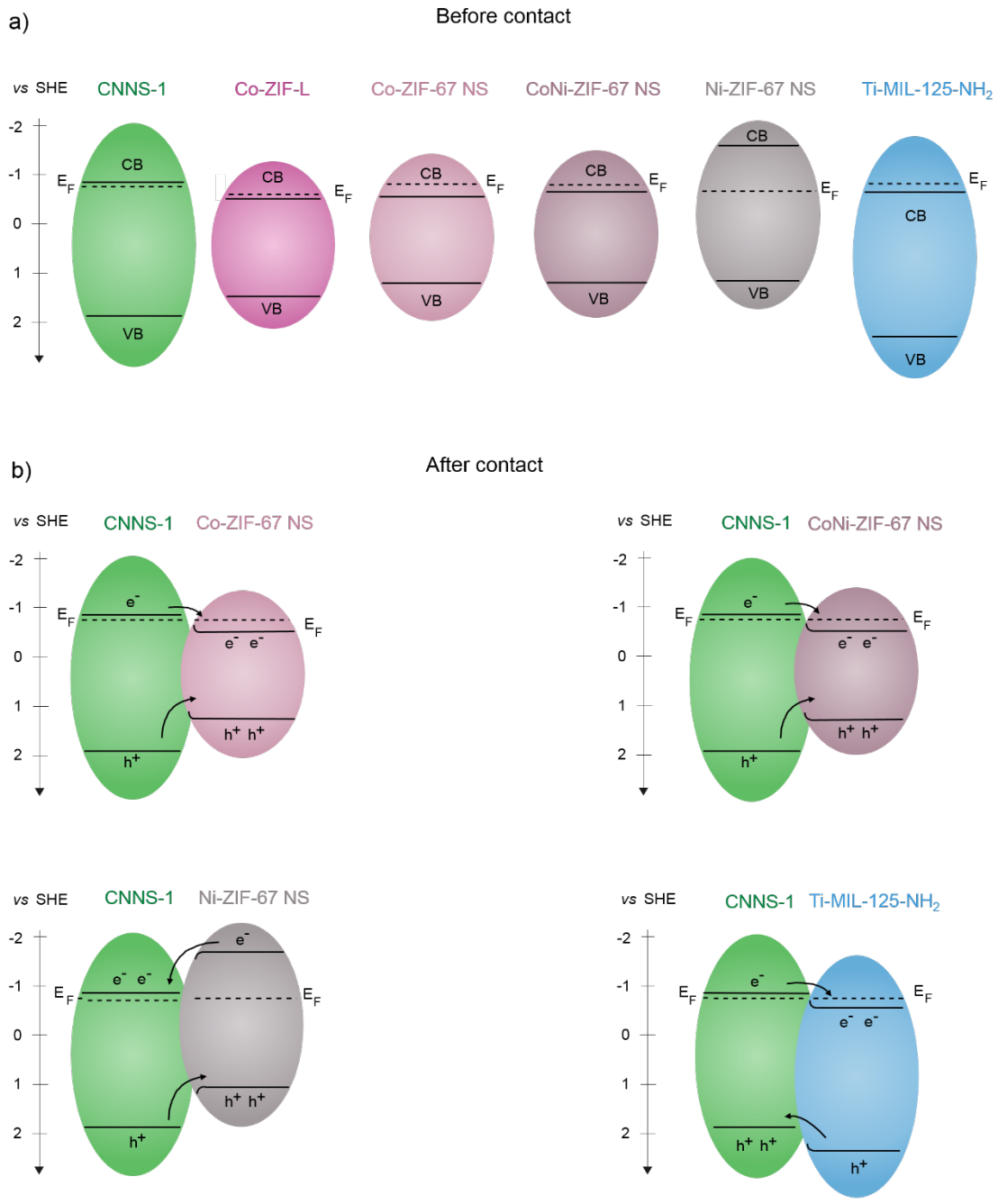


Figure 4.8 Band bending diagram of CNNS-1/Co-ZIF-67 NS, CNNS-1/CoNi-ZIF-67 NS, CNNS-1/Ni-ZIF-67 NS and CNNS-1/Ti-MIL-125-NH_2 heterojunctions (a) before and (b) after contact.

4.3.5 Characterisation of CNNS/Ti-MIL-125-NH_2 heterojunction

The synthesised CNNS/Ti-MIL-125-NH_2 heterojunction is named CNNS-2/MIL-25, where the number 25 represents the weight percent of MOF in the sample as determined by thermogravimetric analysis (Figure A1.2 and Table A1.2). For CNNS/Ti-MIL-125-NH_2 heterojunction synthesis, I used another batch of CNNS, namely CNNS-2. Both CNNS-1 and CNNS-2 exhibit comparable physicochemical properties with similar band edge position and band gaps (i.e. 2.73 and 2.75 eV, respectively, Figures A1.4, A1.5, A1.19 and Table A1.5). In a similar manner to CNNS-1/Co-ZIF-L, PXRD, ATR-FTIR, TEM, UV-Vis absorption, N_2 adsorption isotherms at -196 °C and CO_2 adsorption isotherms at 25 °C measurements confirmed the successful formation of a CNNS-2/Ti-MIL-125 heterojunction (A1.20 - A1.22 and Table A1.6).

I then conducted DR-UV/Vis analyses, core level XPS analyses, valence band and work function measurements on CNNS-2, to determine the band bending diagram of CNNS-2/MIL-25 heterojunction. One should note that the aforementioned measurements were already undertaken for Ti-MIL-125-NH_2 in the previous section. Overall, both CNNS-2 and Ti-MIL-125-NH_2 absorb UV and visible light with respective band gaps of 2.75 eV and 2.93 eV (Figures 4.7a, 4.9a and Figure A1.19). The conduction band and valence bands of CNNS-2 and Ti-MIL-125-NH_2 were located at -0.64 V, 2.28 V and -0.4 V, 2.53 V vs NHE at pH= 0, respectively, in agreement with values reported in the literature (Figures 4.7c, A1.23 - A1.24 and Table A1.5).[205, 212, 213] The work functions of CNNS-2 and Ti-MIL-125-NH_2 were determined to be 3.75 eV and 3.63 eV, respectively (Figures 4.10a and b).

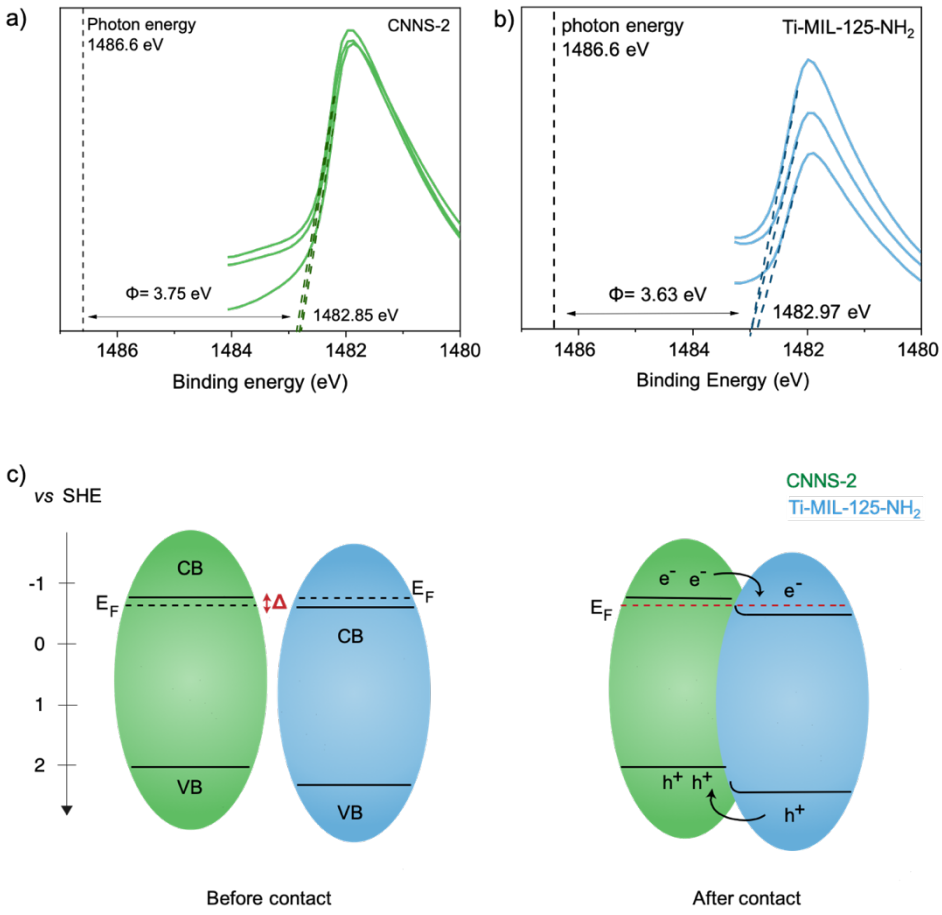


Figure 4.9 Work function measurements of: (a) CNNS-2 and (b) Ti-MIL-125-NH_2; (c) band bending diagram of CNNS-2/Ti-MIL-125 heterojunction before and after contact.

High resolution XPS shows C 1*s*, N 1*s* core levels of CNNS-2 and Ti 2*p*, C 1*s*, N 1*s* and O 1*s* core levels of Ti-MIL-125-NH_2 in line with reported literature (Figures A1.25 and A1.26).[49, 181, 210] As mentioned in the above section, deconvolution of the C 1*s* spectrum of Ti-MIL-125-NH_2 shows four different binding energies at 298.9, 286.8, 285.2 and 284.8 eV, attributed to C=O, C-N, C=C and C-C, respectively.[72] Ti 2*p* displays two binding energy peaks at 458.9 and 464.6 eV, attributed to Ti $2p_{3/2}$ and Ti $2p_{1/2}$ of Ti^{IV}, respectively.[73] For the oxygen environment, two peaks were observed at 532.7 and 531.2 eV corresponding to C=O and titanium oxo clusters.[72]

Compared to Ti-MIL-125-NH_2, the spectra of CNNS-2/MIL-25 exhibit a shift towards lower binding energy in the Ti 2*p* and O 1*s* core levels associated to Ti-MIL-125-NH_2 (Figures 4.11 and A1.27). Additionally, as Figure 4.11 illustrates, one can see a constant separation of these two core levels in

Ti-MIL-125-NH_2 and CNNS-2/MIL-25, suggesting that the observed shift corresponds to a Fermi level shift. Similarly to CNNS-1/Co-ZIF-L, I did not observe any significant shift in the core level associated to CNNS-2, suggesting that no band bending is occurring on CNNS-2. I foresee that the potential drop generated by interfacial charge transfer may mainly distribute across the MOF. In addition, this downward shift is consistent with the sign of the work function difference between CNNS-2 and Ti-MIL-125-NH_2 (i.e. 3.75 vs 3.63 eV respectively, Figures 4.10a and 4.10b). Upon heterojunction formation, electrons will transfer from Ti-MIL-125-NH_2 to CNNS-2 until Ti-MIL-125-NH_2 Fermi level aligns with that of CNNS-2.

Based on these results and using band gap, valence band and work function measurements, I constructed the band bending diagram shown in Figure 4.10c. After contact and under illumination, photogenerated electrons migrate to Ti-MIL-125-NH_2, while holes migrate to CNNS-2. In this Type II heterojunction, charges should be spatially separated, and heterojunction formation should favour higher photoactivity.

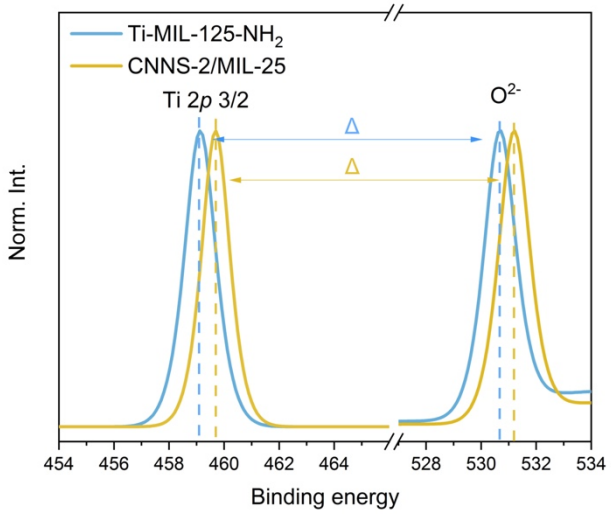


Figure 4.10 Ti-MIL-125-NH_2 and CNNS-2/MIL-25 O^{2-} (oxide) and Ti 2*p* 3/2 components of the O 1*s* and Ti 2*p* spectrum showing an identical shift towards lower binding energies upon heterojunction formation. Consequently, the O^{2-} - Ti 2*p* 3/2 peak separation (Δ) is invariant upon heterojunction formation. This observation can be explained by Equations A1.1 - A1.2 in Figure A1.11.

To verify this hypothesis, CO_2 photoreduction tests were performed on CNNS-2, Ti-MIL-125-NH_2 and CNNS-2/MIL-25. The photocatalytic CO_2 reduction tests were repeated 3 times for each material under the same reaction conditions. To determine the effect of heterojunction formation on the CO_2 photoreduction activity, I calculated an expected photoactivity based on the contribution of the heterojunction components as defined for CNNS-1/ZIF-L-X (Figure 4.12b and Table A1.7). In addition, I prepared and tested a physical mixture containing the same composition of CNNS-2/MIL-25. All samples photoreduced CO_2 with a 100% gaseous selectivity towards CO. As Figure 4.12b shows, CNNS-2 produces 0.23 ± 0.009 $\mu mol \cdot g^{-1} \cdot h^{-1}$ of CO, while Ti-MIL-125-NH_2 produces 0.68 ± 0.031 $\mu mol.g^{-1}.h^{-1}$. After heterojunction formation, the CNNS-2/MIL-25 heterojunction shows a 1.8-fold photocatalytic improvement compared to the physical mixture and the expected photoactivity (i.e. 0.60 ± 0.025 $\mu mol.g^{-1}.h^{-1}$ vs 0.35 and 0.34 $\mu mol.g^{-1}.h^{-1}$, respectively). These results highlight the positive impact of an intimate contact between CNNS-2 and Ti-MIL-125-NH_2 upon heterojunction formation that leads to enhanced photoactivity. Based on the band bending diagram, one can attribute this increase of activity to an enhanced electron/hole separation made possible by the formation of a Type II staggered gap heterojunction. The band bending found in this heterojunction results in a thermodynamic driving force that drives charge carrier separation, with photogenerated electrons and holes flowing into Ti-MIL-125-NH_2 and CNNS-2, respectively.

Finally, the performance of CNNS-2/MIL-25 was compared to the benchmark heterojunction TiO_2 P25, composed of ~80% anatase and ~20 % rutile TiO_2, which showed a remarkably higher activity (i.e. three times higher).

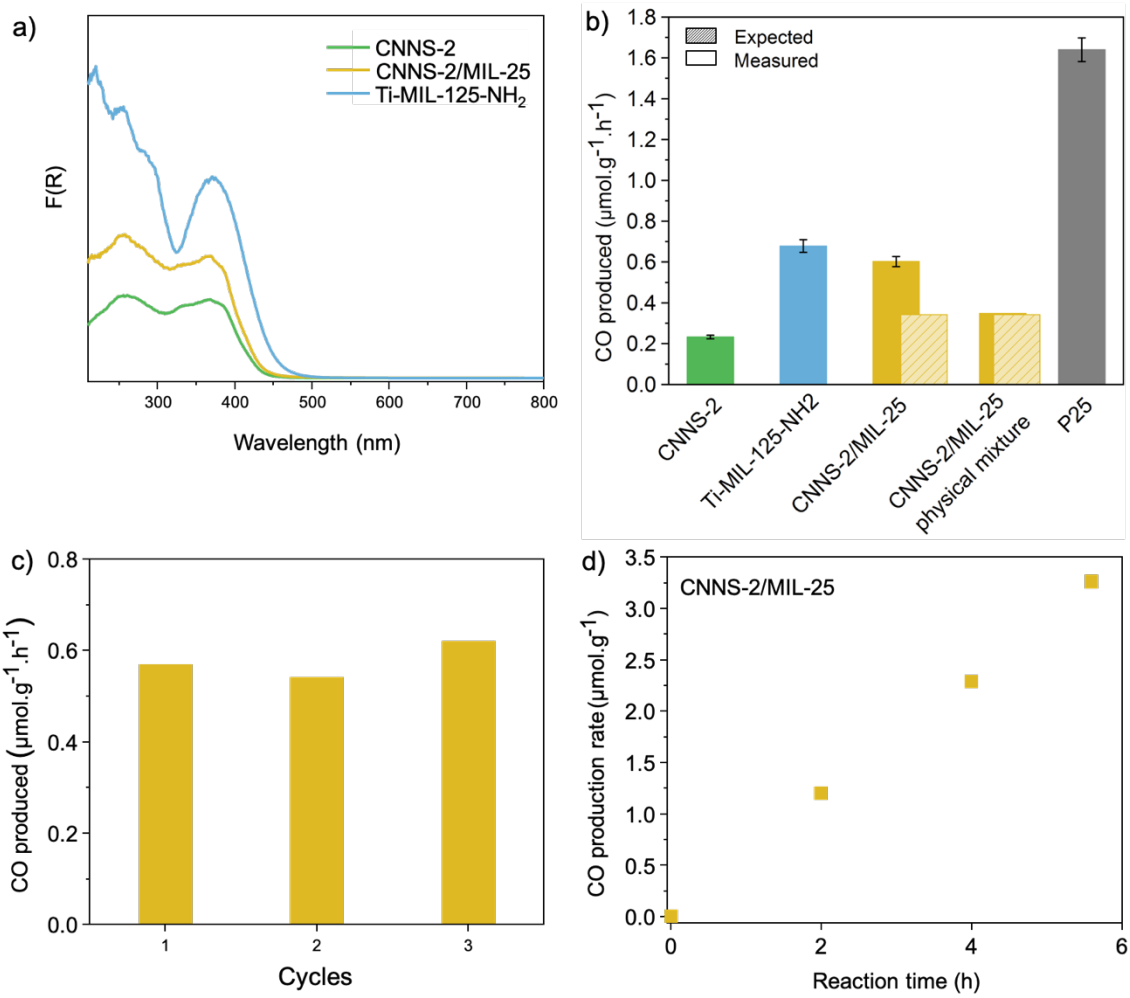


Figure 4.11 (a) UV-Vis absorption spectra of CNNS-2, Ti-MIL-125-NH_2 and CNNS-2/MIL-25, (b) photocatalytic CO evolution rate of CNNS-2, Ti-MIL-125-NH_2 and CNNS-2/MIL-25 heterojunction under UV-Vis irradiation, (c) CO evolution rates after repeated photocatalytic measurements and (d) kinetic study of CO_2 photoreduction using CNNS-2/MIL-25.

To verify the photocatalytic production of CO from CO_2, I conducted a series of control experiments (Table A1.8). In the absence of CO_2 (i.e. N_2/H_2 environment), the activity decreased by 73%. Additionally, I performed isotopic labelled $^{13}CO_2$ measurement. As shown in Figure A1.28, after light irradiation, a ^{13}CO peak (m/z = 29) is observed, confirming the photocatalytic origin of the detected CO. Kinetic studies point to a linear production of CO during 5 h and 40 min of irradiation (Figure 4.12d). In addition, recyclability tests indicate no decline in the photocatalytic performance over 3 cycles (Figure 4.9c). Yet, to assess CNNS-2/MIL-25 photocatalytic stability, one needs to perform post-reaction

characterisations. To do so, I collected XRD spectra, high resolution XPS, N_2 and CO_2 adsorption isotherms before and after photocatalytic testing. As Figures A1.29 to A1.30 show, adsorption isotherms and high resolution XPS spectra of C 1*s*, N 1*s*, O 1*s* and Ti 2*p* core levels did not change significantly pointing to a relatively high photocatalytic stability.

Having confirmed the photocatalytic nature of CNNS-2/MIL-25, one can conclude that contrary to CNNS-1/Co-ZIF-L heterojunction, for which band bending appears to inhibit the photoactivity compared to the physical mixture, band bending effects in CNNS-2/Ti-MIL-125-NH_2 enhance photoactivity by favouring a Type II heterojunction which more efficiently separates photogenerated charge.

4.4 Conclusion

In this chapter, I highlight the importance of interfacial band bending when developing semiconductor/MOF-based heterojunctions. Depending on the heterojunction components, band bending effects can inhibit or enhance CO_2 photoreduction activity. Using the examples of CNNS/Co-ZIF-L and CNNS/Ti-MIL-125-NH_2 heterojunctions for CO_2 photoreduction, I show how to construct a simple band model that can predict the impact of band bending on the photoreduction activity. Since taking into account band bending enables to better describe the heterojunction interface, one should establish a band bending diagram at an early stage of the research. Investigating the effects of band bending becomes particularly important when the heterojunction involves two semiconductors with distinct work functions. These findings helped to develop a Type II CNNS/Ti-MIL-125-NH_2 heterojunction with favourable band bending. This heterojunction shows selective CO_2 photoreduction to CO with a 1.8-fold photocatalytic improvement compared to the physical mixture. Overall, this study enables to better understand the factors which affect electron flow across the semiconductor/MOF interface, while presenting new opportunities on how to further decrease charge recombination and improve electron transfer across MOF-based heterojunctions.

Chapter 5

Hypercrosslinked polymers as a photocatalytic platform for CO_2 photoreduction

The results presented in this chapter were published in *ChemSusChem* (Schukraft et al. *ChemSusChem* 2021, 14, 7, 1720 - 1727).[129] This work was conducted in collaboration with Dr Robert Woodward, a postdoctoral researcher in Prof Camille Petit's group. Dr Robert Woodward synthesised the investigated hypercrosslinked polymers (HCPs) and assisted with porosity and vapour adsorption measurements. Solid-state cross-polarization magic angle spinning ^{13}C NMR (ssNMR), elemental analysis, time-resolved fluorescence and high-performance liquid chromatography (HPLC) analysis were performed by Dr Hanspeter Kählig (University of Vienna), Dr Mag Johannes Theiner (University of Vienna), Dr Michael Sachs (Imperial College London), and Ms Patricia Carry (Imperial College London), respectively.

5.1 Introduction

As explored in the literature review, the need for visible light-active photocatalysts has prompted research towards materials with improved efficiency compared to traditional photocatalysts. Of particular interest are porous organic polymers.[214-218] Their structural versatility enables photochemical tunability and, ultimately, optimisation of the photocatalytic performance. Various porous polymers such as covalent organic frameworks (COFs) and conjugated microporous polymers (CMPs) have demonstrated promising results towards CO_2 photoconversion.[79, 81, 87] However, their synthesis generally requires the use of rare-earth metals, or specifically polymerisable monomeric units, presenting implementation barriers due to relatively high-costs and poor sustainability.[79, 81, 87]

Hypercrosslinked polymers (HCPs) represent a class of materials with excellent tunability and relatively low cost.[219, 220] Non-functional aromatic compounds (i.e. without specifically polymerisable groups) can be 'knitted' together using an external crosslinker, providing substantial scope for the design of HCPs. HCPs are being developed for many different applications such as gas separation and storage,[221, 222] and catalysis,[223] however the ability of HCPs alone to catalyse solar fuel production, remains unknown.

In this chapter, I present the first use of HCPs as photocatalysts for CO_2 reduction. As the choice of the reducing agent can affect the photoreduction activity, I also investigated the influence of the reducing agent on the HCP's photoactivity (i.e. H_2 vs H_2O). Additionally, this work aims to evaluate the robustness of HCPs under photocatalytic conditions. Finally, this study attempts to determine how the chemical, structural, and optoelectronic properties of HCPs influence CO_2 photoreduction.

5.2 Material synthesis

TiO_2 P25 (> 99.5%, 21 nm primary particle size), benzene (99%), dimethoxymethane (99%), 2,4-diamino-6-phenyl-1,3,5-triazine (97%), aniline (99.5%), 1,2-dichloroethane (99%), N,N-dimethylformamide (99%), methanol (99.8 %), chloroform (99%) and iron(III) chloride (98%) were purchased from Sigma-Aldrich. 4,4'-bis(methoxymethyl)biphenyl (96%) was purchased from Tokyo Chemical Industry (TCI) UK. All reagents were used as received. All gases were purchased from BOC.

HCP-1:

20 mL of anhydrous 1,2-dichloroethane was added to 0.78 g (10 mmol) of benzene and 2.28 g (30 mmol) of dimethoxyethane under N_2, before the solution was purged with N_2 for at least a further 30 min. After purging, 4.87 g (30 mmol) of iron(III) chloride was quickly added to the solution and the mixture was heated to 80 °C for a further 24 h, during which the reaction was kept under an inert atmosphere. The resulting solid was allowed to cool before it was filtrated using a Büchner funnel and washed with methanol until the filtrate was almost colourless. The polymer was then further washed by Soxhlet extraction in methanol for 24 h. Finally, the polymer was dried in a vacuum oven overnight at 100 °C. The reaction yield was 84% based on a hypothetical polycondensation of 100%.

HCP-2:

The overall procedure remained the same as HCP-1 with 20 mL of 1,2-dichloroethane added to 0.28 g (3 mmol) of aniline and 1.45 g (6 mmol) of 4,4'-bis(methoxymethyl)biphenyl before 0.98 g (6 mmol) of iron(III) chloride was added. The reaction yield was 66% based on a hypothetical polycondensation of 100%.

HCP-3:

The overall procedure remained the same as HCP-1 with 20 mL of 1,2-dichloroethane added to 0.37 g (2 mmol) of 2,4-diamino-6-phenyl-1,3,5-triazine and 0.97 g (4 mmol) of 4,4'-bis(methoxymethyl)biphenyl before 0.65 g (4 mmol) of iron(III) chloride was added. In addition to methanol, HCP-3 was also washed in chloroform by Soxhlet extraction, to ensure the removal of unreacted 2,4-diamino-6-phenyl-1,3,5-triazine. The reaction yield was 91% based on a hypothetical polycondensation of 100%.

5.3 Results and discussion

5.3.1 Hypercrosslinked polymer synthesis and characterisation

I synthesised three HCPs of varied chemical structure, HCP-1, HCP-2, and HCP-3 via a Friedel-Crafts alkylation reaction using external crosslinkers to 'knit' together aromatic monomers. A general reaction scheme and representative HCP structures are shown in Figures 5.1a and b. HCP-1, one of the most widely-studied HCPs in recent years, was produced via the crosslinking of benzene using an aliphatic dimethoxymethane external crosslinker.[224] HCP-2 is comprised of aniline crosslinked using 4,4-bis(methoxymethane)biphenyl, as the analogous polymer produced using dimethoxymethane was non-porous.[225] HCP-3 consists of 2,4-diamino-6-phenyl-1,3,5-triazine crosslinked using 4,4-bis(methoxymethane)biphenyl. I chose the chemistries of HCP-2 and HCP-3 to try to improve the CO_2 adsorption selectivity via the inclusion of amino groups. Photographic images of the networks (Figure A2.1) reveal a colour gradient from dark to light brown from HCP-1 to HCP-3.

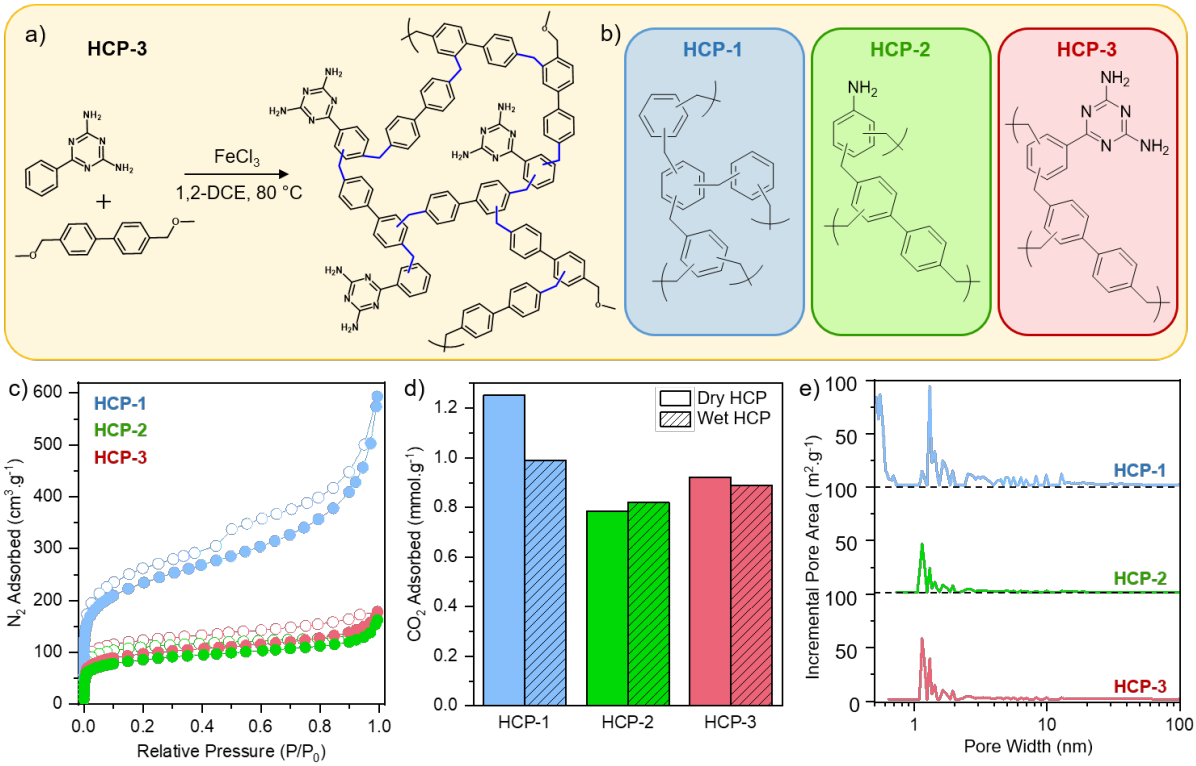


Figure 5.1 (a) Reaction scheme for the production of HCP-3 by Friedel-Crafts alkylation, (b) representative chemical structures of HCP repeat units, (c) N_2 adsorption isotherms at -196 °C, filled symbols represent adsorption and empty symbols represent desorption, (d) CO_2 uptake at 1 bar and 25 °C for HCPs in both 'dry' and 'wet' states, i.e. HCPs exposed to a humid atmosphere before measurement, (e) pore size distributions of HCPs, calculated using the density functional theory (DFT) method.

The aromatic monomers were successfully incorporated into the networks, as confirmed using a variety of characterisation techniques. Solid-state cross-polarization magic angle spinning ^{13}C NMR (ssNMR) (Figure A2.2) of all polymers showed signals at around 139 and 129 ppm corresponding to quaternary aromatic carbons (C_{Ar}) and aromatic C_{Ar}-H. Signals at ~36 ppm are assigned to newly formed methylene bridges, while weak signals at ~54 ppm and ~74 ppm correspond to unreacted methyl ethers, O-CH_3 and C_{AR}-C-O, respectively. The signal at 74 ppm is absent in HCP-3, however, a new signal at ~102 ppm emerges, suggesting this signal may be shifted downfield in this case. For HCP-3 the signal at 166 ppm is assigned to triazine carbons and in HCP-2 the C-NH_2 signal is expected at ~146 ppm and is therefore likely eclipsed by the substituted aromatic peak. Attenuated total reflectance Fourier transform

infrared (ATR-FTIR) spectra showed distinct stretches for primary amines in HCP-2 and HCP-3, and the triazine tertiary amines in HCP-3 (Figure A2.3). HCP-2 and HCP-3 contain 1.3 and 7.1 at% N, respectively, as determined via elemental analysis (Table A2.1), which may explain the lack of a signal in ssNMR for C-NH_2 in HCP-2. These values correspond to final polymer compositions of roughly 1:4 and 1:3 monomer to crosslinker ratios for HCP-2 and HCP-3, respectively. Scanning electron microscopy images revealed HCP-1 and HCP-3 as agglomerated spherical particles, whereas HCP-2 shows a more fibrous structure (Figure A2.4). Thermogravimetric analysis demonstrated the high thermal stability of all HCPs, with decomposition temperatures of > 300 °C in both N_2 and air (Figures A2.5 - A2.6). Char yields in N_2 at 900 °C were > 60% in all HCPs, while complete degradation was observed in air at > 550 °C. Powder X-ray diffraction confirmed the amorphous nature of all HCP networks (Figure A2.7).

Having confirmed the formation and composition of the HCPs, I next evaluated features that influenced their CO_2 photoreduction properties, namely porosity and CO_2 sorption. To assess the porous nature of the networks I performed N_2 sorption measurements at -196 °C. HCP-1, HCP-2, and HCP-3 exhibited BET surface areas of 951, 311, and 357 $m^2.g^{-1}$, respectively (Figure 5.1c and Table A2.2). All HCPs displayed type IV isotherms,[226] with significant microporosity, as indicated by the steep N_2 uptake at low relative pressures, as well as meso/macroporosity. The micropore volume was highest in HCP-1 (0.46 $cm^3.g^{-1}$), dropping to 0.13 and 0.16 $cm^3.g^{-1}$ for HCP-2 and HCP-3, respectively, reflecting trends seen in the polymer's BET surface areas. Figure 5.1e highlights a multimodal pore size distribution for all networks, predominantly concentrated in the micropore region.

To assess the CO_2 uptake ability of HCPs, I collected adsorption isotherms at 25 °C up to 1 bar (full isotherms are shown in Figure A2.8). Although the HCPs followed the expected trend, i.e. higher surface area polymers adsorbed more CO_2, the CO_2 capacities did not reflect the large differences in surface areas (Table A2.2). The presence of the amino groups in HCP-2 and HCP-3, which are known to impart CO_2 selectivity to hypercrosslinked polymers,[90] increased uptake density per unit of surface area due to stronger interactions with CO_2.[227] In addition, since I used sacrificial water vapour for CO_2 photoreduction (see below) and the presence of adsorbed H_2O is shown to impede CO_2 uptake in polar HCPs, due to competitive adsorption,[228] I investigated the effect of H_2O and CO_2 co-adsorption. To mimic the conditions of the photoreduction experiments, I exposed the samples to humid air (> 99%

humidity) for at least 48 h before collecting CO_2 adsorption isotherms at 25 °C up to 1 bar. Crucially, samples were not degassed prior to CO_2 adsorption measurements to avoid removing adsorbed H_2O (details in Section 3.1.2.2). The CO_2 sorption capacities at 1 bar are given in Figure 5.1d. The full isotherms of both degassed, “dry”, and humidity-exposed, “wet”, HCPs are shown in Figure A2.8. Wet HCP-1 showed a 21% decrease in CO_2 capacity in comparison to its dry equivalent, while the amine-containing HCP-2 and HCP-3 showed a negligible difference in CO_2 uptake between the wet and dry networks. These uptake capacities demonstrate that CO_2 can still adsorb in the presence of H_2O. To further investigate the impact of water vapour, I measured the catalytic ability of “wet” HCPs (i.e. pre-exposed to humidity) in a pure CO_2 stream. The HCPs still displayed CO_2 photoreduction activity (Table A2.3), albeit decreased, which indicates that CO_2 could still adsorb onto the materials and react. One should note that during the ‘normal’ photoreduction experiments, I did not expose HCPs to water vapour prior to CO_2 reduction, but rather a stream of CO_2 containing water vapour.

5.3.2 CO_2 photoreduction activity of hypercrosslinked polymers

To evaluate the potential of HCPs for CO_2 photoreduction, I investigated their optoelectronic properties using diffuse reflectance ultraviolet-visible spectroscopy (DR-UV/Vis). The UV-Vis spectra show that all HCPs absorb light in both the UV and visible range, with estimated optical gaps of 3.56, 3.54 and 3.19 eV for HCP-1, HCP-2 and HCP-3, respectively (Figure 5.2a). All three HCPs exhibited photoluminescence as shown in Figure A2.9. I probed their photoluminescence lifetimes at 700 nm using time-correlated single photon counting (TCSPC) upon 282 nm excitation. The time at which the photoluminescence signal has decayed to half its initial amplitude (half-life time) was 1.9 ns, 2.2 ns, and 3.2 ns for HCP-1, HCP-2, and HCP-3, respectively, which demonstrates that HCP-3 has a substantially longer excited state lifetime than HCP-1 or HCP-2. I estimated the HCP’s valence band (VB) and conduction band (CB) positions by complementing our DR-UV/Vis data with VB and work function measurements, as explained in Section 3.1.3.4. For all HCPs, the CB is located above the reduction potential of CO_2/CO and the VB below the oxidation potential of both H^+/H_2 and O_2/H_2O (Figure 5.2c). Hence, the band diagrams point towards a sufficient thermodynamic driving force to enable the reduction of CO_2 to CO using either H_2 or H_2O vapour as a sacrificial agent. Overall, the light absorption properties of HCPs, as well as their CO_2 adsorption capacities, make them *a priori* attractive candidates for CO_2 photoreduction.

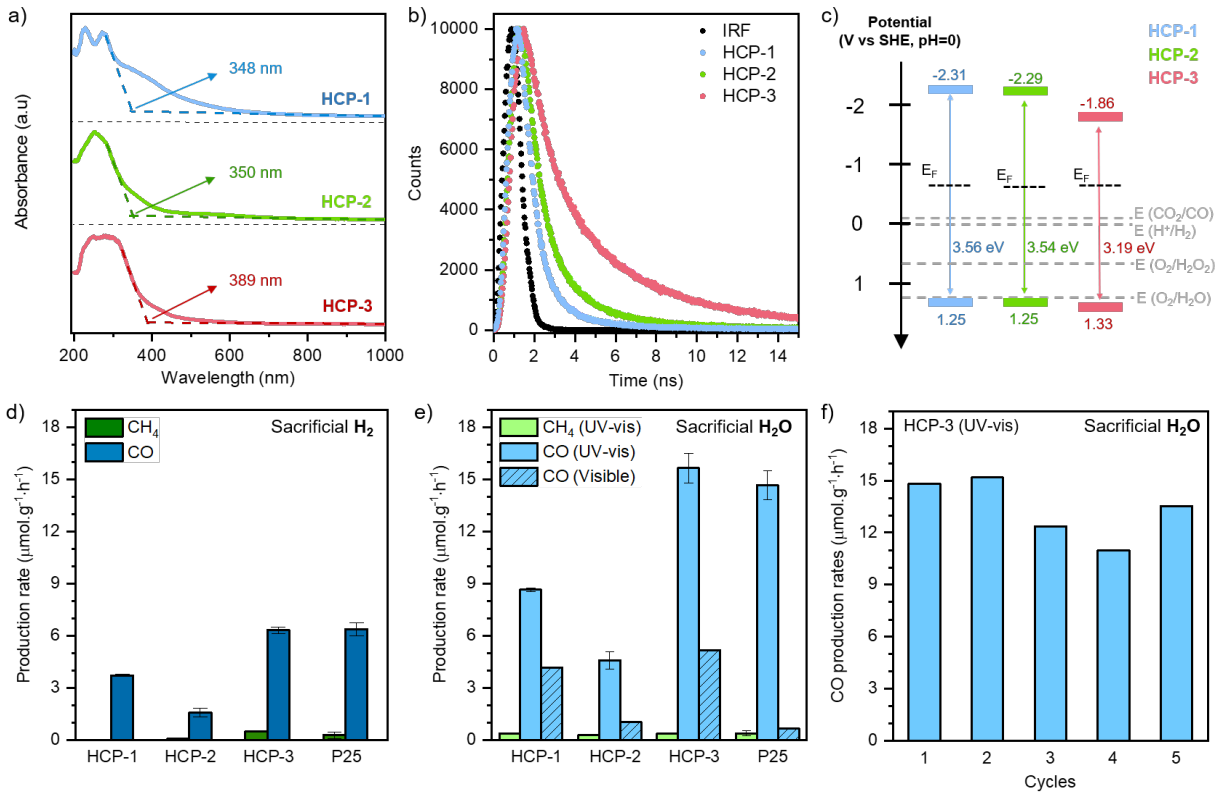


Figure 5.2 (a) UV-Vis absorption coefficient spectra with absorption onsets indicated, (b) photoluminescence decay kinetics probed at 700 nm following excitation at 282 nm, along with the instrument response function (IRF) probed at the excitation wavelength, (c) band structures based on the X-ray photoelectron spectroscopy (XPS) and DR-UV/Vis analyses, (d) photocatalytic production rates using sacrificial H_2 in UV-Vis, (e) photocatalytic production rates using sacrificial H_2O in both UV-Vis and visible light alone, (f) HCP-3 recyclability test over 5 cycles of 3 h irradiation using UV-Vis light and sacrificial H_2O.

After establishing their CO_2 adsorption ability and desirable optoelectronic properties, I tested HCPs for photocatalytic CO_2 reduction. Tests were conducted in a heterogeneous gas-solid photoreactor at ambient temperature, using either H_2 or H_2O as a sacrificial agent under UV-Vis or visible irradiation alone (Xe arc lamp, 300 W, Figure 3.7, Section 3.1.4.1). A gas-phase reactor was chosen to combine CO_2 adsorption and CO_2 conversion, avoiding limitations owing to poor CO_2 solubility in water (Figure 3.6, Section 3.1.4.1). No co-catalyst or photosensitiser was required, but some residual iron is present from the HCP synthesis and may play a role in the overall photocatalytic activity (Table A2.1) as shown

with Pd for other organic materials in the context of H_2 evolution.[229, 230] However, HCP-3, the most efficient photocatalyst, has the lowest Fe content (31 ppm), suggesting that residual Fe does not play a major role in the photoactivity. In each experimental set, I compared the HCP performance to that of the benchmark TiO_2 P25.

For all HCPs, after 3 h of irradiation, the primary carbonaceous product observed was CO, with a gaseous product selectivity of up to 93% and 98% using sacrificial H_2 or H_2O, respectively (Figures 5.2d and 5.2e, and Table A2.3 - A2.5). Trace CH_4 was also detected, representing the only other gaseous carbonaceous product detected. Gaseous product selectivity is simply the ratio between CO and the sum of all carbonaceous products detected (i.e. CO and CH_4). Quantum efficiencies were calculated for HCP-3 in both UV-Vis and visible light alone and compared to a selection of competitive organic photocatalysts for gaseous CO_2 reduction (Table A2.5 and A2.6). This is intended to provide some perspective rather than a direct comparison.

To investigate the production of less volatile compounds remaining on the polymer surface, I washed HCP-3 with water post-irradiation and analysed the resulting solution using HPLC. Low concentrations of methanol and formic acid were detected (Figures A2.12 - A2.13), the build-up of which at the surface could lead to decreased catalyst activity with time. Interestingly, when using H_2O as sacrificial agent, I did not detect O_2. Instead, I observed H_2O_2 after photocatalysis (Figure A2.14). The formation of H_2O_2 may originate from two possible routes. Either H_2O is first oxidised to O_2 and is then reduced to H_2O_2 on the surface of the catalyst, resulting in a lack of detectable O_2, as reported in a different study.[231] Alternatively, H_2O is directly oxidised to H_2O_2.

Regardless of the sacrificial agent, HCP-2 exhibited the lowest CO production rate, while HCP-3 displayed the highest. The photocatalytic performance of HCP-3 was comparable to that of TiO_2 P25 under UV-Vis light and was up to 7.5x better when irradiated with only visible light (Figure 5.2e, Table A2.3). I observed photocatalytic activity for all HCPs under visible light alone, a significant finding for organic materials requiring no doping or co-catalyst. The decrease in activity under visible light compared to UV-Vis irradiation is rationalised using their UV-Vis absorption spectra (Figure 5.2a). As HCP-1 is the network that shows the highest light absorption in the visible region, its photoactivity is the least affected by the absence of UV light. Activity in the visible range is promising for the future of HCP

photocatalysts in real-world applications as visible light comprises a large portion of the sun's output reaching the Earth's surface. Targeted network modifications might allow further optimisation of this visible light activity.

The high photocatalytic activity of HCP-3 likely arises from the presence of triazine groups. Lee et al. reported stronger electrostatic CO_2 interactions in triazines when compared to benzene and amino groups, as are present in HCP-1 and HCP-2, respectively.[232] Triazine groups may also offer an additional delocalisation of the electrons, favouring lower electron-hole recombination.[233, 234] Time-resolved photoluminescence showed that HCP-3 displayed the slowest electron-hole recombination rate (Figure 5.2b), leaving more time for charges to migrate to the surface of the photocatalyst for CO_2 photoconversion. To gain further insights on the key parameters influencing CO_2 adsorption and photoconversion, a systematic HCPs screening is required.

Interestingly, CO_2 photoreduction performance of HCPs improved by up to 2.5x when replacing H_2 with sacrificial H_2O (Figures 5.2d and e). From a thermodynamic standpoint, such behaviour is intriguing as H_2O oxidation requires a higher driving force than H_2 oxidation. I hypothesised that the increased photoactivity in the presence of H_2O is due to HCPs displaying significantly improved adsorption capacities for H_2O when compared to H_2. This leads to an increased availability of the sacrificial agent at the photoactive sites on the HCPs' surface, improving photoreduction rates. To investigate this hypothesis, I collected pure H_2 and H_2O adsorption isotherms for all HCPs (Figure 5.3). From the pure adsorption isotherms, under operating conditions (atmospheric pressure, 25 °C) HCPs adsorbed < 0.1 $mmol.g^{-1}$ of H_2, in comparison to between 2 and 9.4 $mmol.g^{-1}$ for H_2O, an increase of 2 orders of magnitude. HCP-1 adsorbed the highest amount of H_2O despite a lack of amino functionality, however, elemental analysis revealed it contained significant residual oxygen from incomplete crosslinking reactions (11.4 wt.% compared to 4.1 and 3.6 wt.% for HCP-2 and HCP-3, respectively), likely increasing its H_2O adsorption ability. Adding to this effect, the high porosity and microporosity will also contribute to the water uptake of the HCPs, thereby explaining the trend in water sorption. A higher concentration of sacrificial agent at the HCP's surface should favour high CO_2 photoreduction rates, explaining the increase of photoactivity when using H_2O as reducing agent.

To further investigate the importance of H_2O adsorption on the photoactivity, I decreased the humidity inside the photoreactor by decreasing the temperature of the water vapour saturator to ~1 °C. At 1 °C, the partial pressure of H_2O at saturation is reduced (6.6 mbar), thereby dramatically reducing the concentration of H_2O introduced into the system. After sealing the reactor, I conducted CO_2 photoreduction measurements at 25 °C, under atmospheric pressure. The decreased humidity of the stream resulted in a 38% decrease in activity for HCP-3 (Figure A2.15). Indeed, H_2O uptake in this network is reduced to around 0.4 $mmol.g^{-1}$ at 6.6 mbar, as estimated from the pure water sorption isotherm (Figure 5.3b). This further corroborates the importance of the adsorption of the sacrificial agents to the photocatalyst surface. Nonetheless, further mechanistic studies are required to further understand H_2O adsorption and the structure-property relationship for these materials.

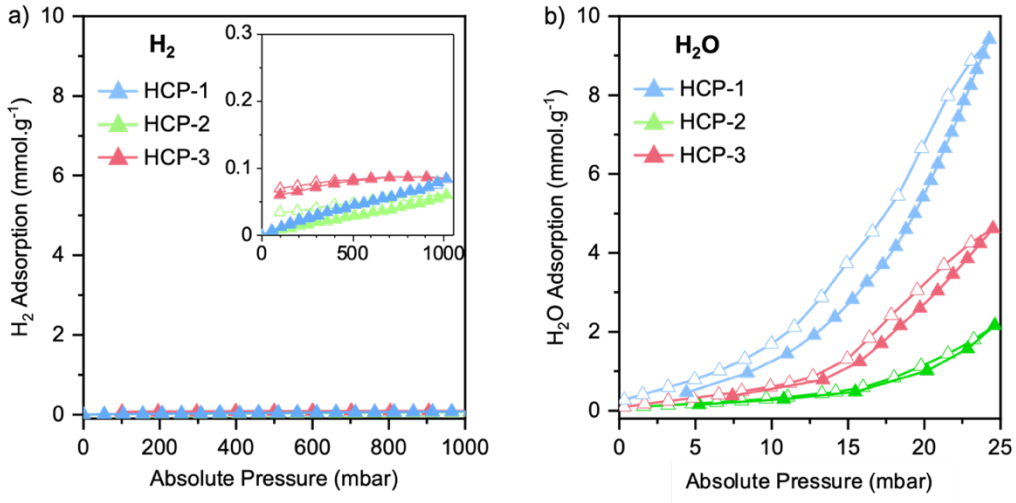


Figure 5.3 (a) H_2 and (b) H_2O adsorption isotherms at 25 °C. Filled symbols represent adsorption and empty symbols represent desorption. The inset in (a) shows the H_2 isotherms with a smaller y-axis for clarity.

I further examined the photocatalytic properties under UV-Vis irradiation of HCP-3, the most active photocatalyst of this study. Kinetic studies point to a relatively linear production of CO up to 3 h of irradiation, which decreases slightly after 6 h (Figure A2.16). Recyclability tests were also performed. As Figure 5.2f shows, after 5 cycles the photoactivity decreased by 9%, which may be due to the formation of surface products (e.g. methanol and formic acid) or mild degradation of the polymer.

To assess the possible degradation, I collected XPS spectra of all polymers before and after irradiation. Deconvolution of C 1*s*, N 1*s* and O 1*s* spectra for all HCPs showed that the amount of sp^3 aliphatic crosslinker and the amount of partially crosslinked C-O slightly decreased after irradiation (Figures A2.17 - A2.19). Elemental analysis showed minimal change in the bulk polymer composition after the irradiation process (Table A2.1). SsNMR spectra were also collected for all networks after the photoreduction process (Figure A2.2), which also showed no major structural change to bulk composition. I then further probed the structural and chemical stability of HCP-3 by collecting N_2, CO_2, and H_2O sorption isotherms and FTIR spectra, all of which showed no significant alteration, except for a change in the shape of the N_2 isotherm (Figures A2.20 - A2.21 and Table A2.2). The slight degradation of the polymer seen in XPS measurements post-irradiation may arise from the formation of H_2O_2 which decomposes into hydroxyl radicals under UV-Vis irradiation and lead to structural changes.

To verify the evolution of CO from CO_2 conversion over HCPs photocatalysts, I conducted a series of control experiments, i.e.: in an inert atmosphere (N_2/H_2 or N_2/H_2O), without catalyst, without light, and isotopic labelling of $^{13}CO_2$ (control experiments details are outlined in Table A2.3). In the absence of CO_2, the activity decreased by 77% to 88% depending on the atmosphere (N_2/H_2O vs N_2/H_2), which suggests degradation. I attribute the trace CO detected under inert atmosphere to the degradation of some carbon sp^3 aliphatic crosslinkers and residual oxygen-containing functional groups of the HCP crosslinkers. To verify the photocatalytic production of CO from CO_2, I conducted isotopic labelled $^{13}CO_2$ tests using H_2O as a sacrificial agent under UV-Vis light irradiation. I observe a ^{13}CO peak (m/z= 29) after light irradiation, confirming the ability of HCPs to photoconvert CO_2 to CO (Figure A2.22). No $^{13}CH_4$ was observed, likely due to the good selectivity of the HCP towards CO, as shown in Figures 5.2d and e.

5.4 Conclusion

In this chapter, I report HCPs for the first time as photocatalysts for the conversion of CO_2 into value-added chemicals. Under visible light irradiation, HCPs show promising photoactivity using only H_2O as sacrificial agent, without the requirement of any co-catalyst or photosensitiser. In fact, they significantly outperform the benchmark material TiO_2 P25. The photoactivity of HCPs notably increased when using H_2O as sacrificial agent compared to tests performed using H_2. This was attributed to the superior H_2O

adsorption capacities, which favoured a higher concentration of the sacrificial agent near the photoactive sites. In addition, by choosing the chemistries of the HCPs, I attempted to investigate the effect of amino groups on their CO_2 adsorption and photoactivity. The presence of amino groups was found to favour higher CO_2 uptakes. However, to gain a comprehensive understanding of the relationship between the HCPs' structure and their photoactivity, further studies are required. Finally, this study also evaluated the robustness of HCPs under photocatalytic conditions. After photocatalytic testing, I observed degradation of the polymer, which was hypothesised to come from the decomposition of sp^3 aliphatic crosslinkers and partially crosslinked methoxy groups. This decomposition may have been derived from the formation of H_2O_2 which decomposed into hydroxyl radicals under UV-Vis irradiation.

Chapter 6

Mechanisms of CO_2 and H_2O adsorption on a hypercrosslinked polymer studied using DFT and in-situ DRIFT spectroscopy

This chapter is adapted from a manuscript that has been submitted for publication. Solid-state cross-polarization magic angle spinning ^{13}C NMR (ssNMR) and elemental analysis were performed by Dr Xu Yingqi (Imperial College London) and Dr Mag Johannes Theiner (University of Vienna), respectively. The polymer under study was synthesised in a joint effort with Ms Ioanna Itskou (Imperial College London). Prof Atsushi Urukawa (TU Delft) and Dr Robert Woodward (University of Vienna) participated in this study with their scientific inputs. Specifically, Prof Atsushi Urukawa taught me how to analyse diffuse reflectance Fourier transform infrared spectroscopy (DRIFTS) data using multivariate curve resolution (MCR) analysis.

6.1 Introduction

To build on the findings of Chapter 5 and tailor the physicochemical properties of hypercrosslinked polymers (HCPs) towards improved CO_2 photoconversion rates, one needs to further understand the relationship between the adsorption/photoconversion mechanisms and the underlying HCP structure. As demonstrated on other materials such as zeolites,[235, 236] non-porous linear polymers,[34] alumina,[237, 238] TiO_2[239,35] and other metal oxides,[240] in-situ infrared spectroscopy can provide useful insights into adsorption and photoconversion mechanisms. As in both processes CO_2 and H_2O adsorptions represent critical steps that one could a priori control to optimise gas adsorption and CO_2 conversion, it would be of interest to study these mechanisms. The use of IR to study CO_2 adsorption mechanisms

on HCPs, while attractive, is not without challenges. For instance, the organic nature of HCPs means that many of the relevant IR absorption bands of the polymers and CO_2 may overlap.

Herein, I investigate CO_2 and H_2O adsorption on a triazine-biphenyl HCP by combining density functional theory (DFT), in-situ diffuse reflectance Fourier transform infrared spectroscopy (DRIFTS), and multivariate curve resolution (MCR). The HCP under study is comparable to HCP-3, the highest performing catalyst in the CO_2 photoreduction study as explored in Chapter 5.[129] The presence of triazine groups enabled me to investigate the role of a nitrogen-rich functional group on CO_2 and H_2O adsorption. I first assigned the HCP vibrational bands, and then identified the HCP vibrational fingerprints involved in intermolecular interactions with CO_2 and H_2O. Given the CO_2 photoreduction ability of HCPs, I also investigated CO_2 and H_2O adsorption under transient light irradiation.

6.2 Material Synthesis

2,4-Diamino-6-phenyl-1,3,5-traizine (97%), triflic acid (99%), 1,2-dichloroethane (99%), chloroform (99%) and methanol (99.8%) were purchased from Sigma-Aldrich, while 4,4-bis(methoxymethyl)biphenyl (96%) was purchased from TCI chemicals. $^{12}CO_2$ (grade 4.0, > 99.99 %), N_2 (grade 5.0, > 99.999 %) and He (grade 5.0, > 99.999 %) were purchased from Linde Gas Benelux. $^{13}CO_2$ (99.0 at% ^{13}C) was purchased from Sigma-Aldrich. All reagents were used as received.

Triazine-biphenyl HCP:

1.2 g (4.9 mmol) of 4,4-bis(methoxymethyl)biphenyl and 0.46 g (2.4 mmol) of 2,4-diamino-6-phenyl-1,3,5-traizine were dissolved in 18 mL of 1,2-dichloroethane. 0.98 mL (11 mmol) of triflic acid was then added dropwise while stirring. The mixture was kept under stirring at 90 °C for an additional 18 h. The resulting polymer was recovered and washed via Soxhlet extraction with 150 mL methanol for 24 h, followed by 150 mL of chloroform for 48 h. The polymer was then dried under vacuum at 150 °C and finely ground.

6.3 Results and discussion

6.3.1 Hypercrosslinked polymer characterisation

I synthesised a triazine-biphenyl HCP via the crosslinking of 4,4-bis(methoxymethyl)biphenyl and 2,4-diamino-6-phenyl-1,3,5-triazine, subsequently referred to as biphenyl and triazine monomers, respectively. Triflic acid was used as the polymerization catalyst. Figure 6.1a illustrates the reaction scheme and the structure of the studied HCP. The photographic and scanning electron images of the polymer reveal a light brown material constituted of agglomerated particles of around 40 nm in diameter (Figures 6.1a and A3.1).

I confirmed the synthesis of the HCP using several characterisation techniques. As Figure 6.1c shows, the solid-state cross-polarization magic angle spinning ^{13}C NMR (ssNMR) signal at 139 and 129 ppm correspond to the quaternary aromatic carbons and the aromatic C_{AR}-H carbons, respectively.[241] The signal at 37 ppm is assigned to the newly formed methylene bridges generated by crosslinking,[241] and that at 190 ppm to the carbons of the triazine ring.[242] Incorporation of the triazine monomer is further confirmed by the atomic composition calculated from the elemental analysis (Figure 6.1b, Table A3.1 and Equation A3.1). The studied triazine-biphenyl HCP contains 0.62 at% of N, corresponding to a 1:31 triazine to biphenyl monomer ratio. One can attribute the disparity between the 1:3 triazine to biphenyl monomer feed ratio and the one obtained to the poor solubility of triazine in 1,2-dichloroethane. The existence of 1.1 at% of O suggests the presence of methoxy groups arising from partially crosslinked biphenyl molecules. X-ray photoelectron spectroscopy (XPS) analyses corroborate the above observations (Figure A3.2). The C 1*s* peaks at 284.5, and 285 eV correspond to the sp^2 aromatic carbons and the newly formed aliphatic methyl bridges, respectively.[243] The peak at 286.9 eV corresponds to the carbon of the methoxy group of partially crosslinked biphenyl molecules.[243] The N 1*s* core level displays two deconvoluted peaks at 398.5 and 399.8 eV characteristic of the triazine ring, and one deconvoluted peak at 401.3 eV characteristic of $-NH_2$ groups.[244]

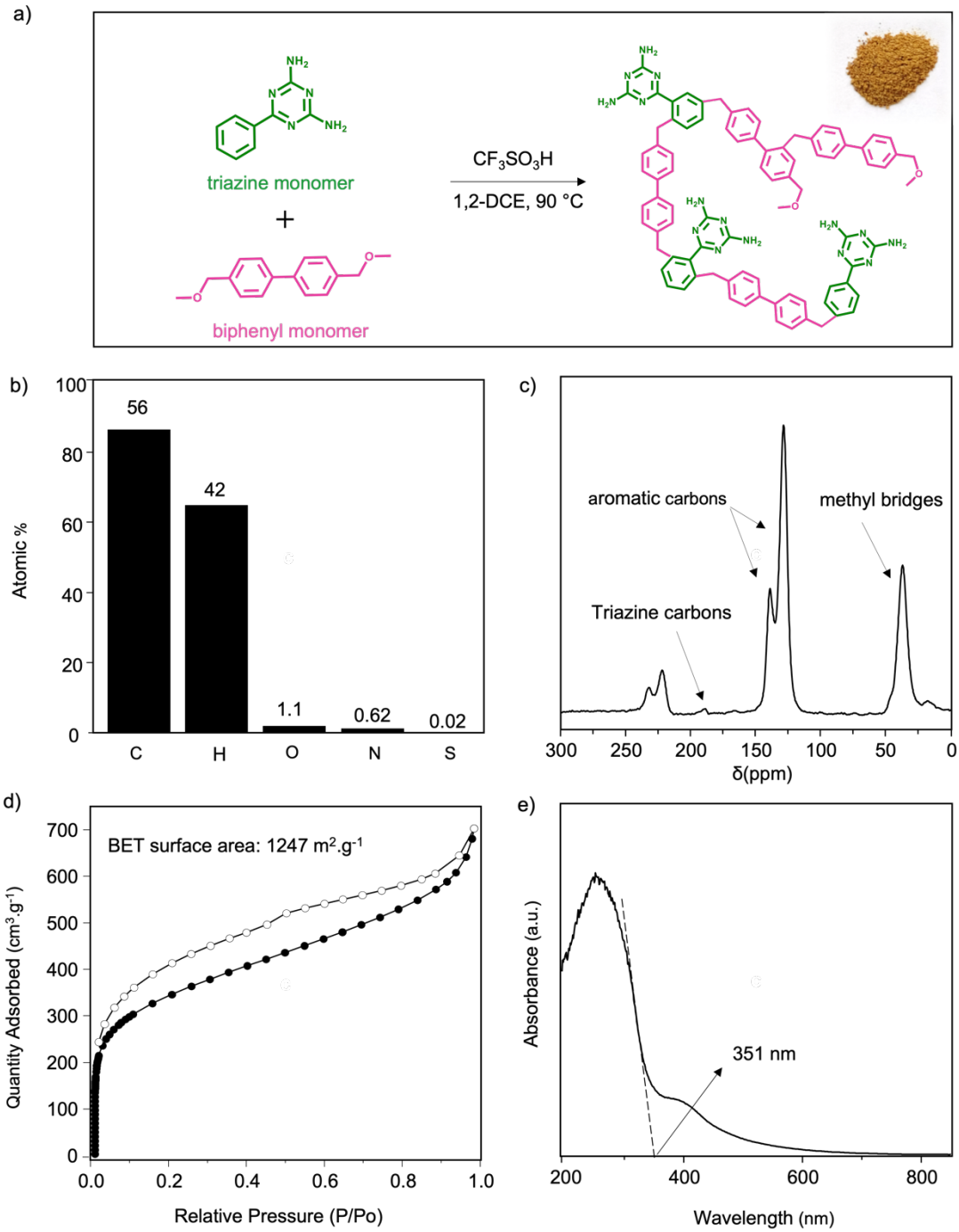


Figure 6.1 Overview of the chemical, structural and optoelectronic features of the triazine-biphenyl HCP sample: (a) synthesis reaction scheme (inset shows a photograph of the polymer), (b) atomic composition based on CHNS-O analysis, (c) solid-state ^{13}C NMR spectra, (d) N_2 sorption isotherm at -196 °C (filled symbols = adsorption; empty symbols = desorption) and (e) UV-Vis absorption coefficient spectrum with absorption onset.

Next, I evaluated the textural properties of HCP via N_2 sorption at -196 °C (Table A3.2, S_{BET} = 1247 $m^2.g^{-1}$, V_{tot} = 0.978 $cm^3.g^{-1}$, V_{meso} = 0.842 $cm^3.g^{-1}$, V_{mic} = 0.136 $cm^3.g^{-1}$). The HCP exhibits a type IV sorption isotherm, indicative of mesopores (Figure 6.1d), and a multimodal pore size distribution with a predominance of micropores and mesopores in the 0.5 - 0.7 nm and 1 - 4 nm regions, respectively (Figure A3.3). Powder X-ray diffraction confirmed the amorphous nature of the HCP network (Figure A3.4). I assessed the thermal stability of the HCP via thermogravimetric analysis, and confirmed thermal stability up to 250 °C in both N_2 and air (Figure A3.5). Finally, diffuse reflectance ultraviolet-visible spectroscopy measurements (DR-UV/Vis) show that the triazine-biphenyl HCP adsorbs light in both the UV and visible regions of the spectrum with an absorption offset at 351 nm (Figure 6.1e).

3.2. Hypercrosslinked polymer sorption properties

Having evaluated the chemical, structural and light absorption properties of the triazine-biphenyl HCP, I next investigated the sorption at 25 °C and 50 °C of CO_2 and H_2O, two species present in the CO_2 capture and CO_2 photoreduction processes (Figure 6.2). The former temperature facilitates comparison with published literature while the latter corresponds to the temperature at which I performed CO_2 photoreduction measurements.

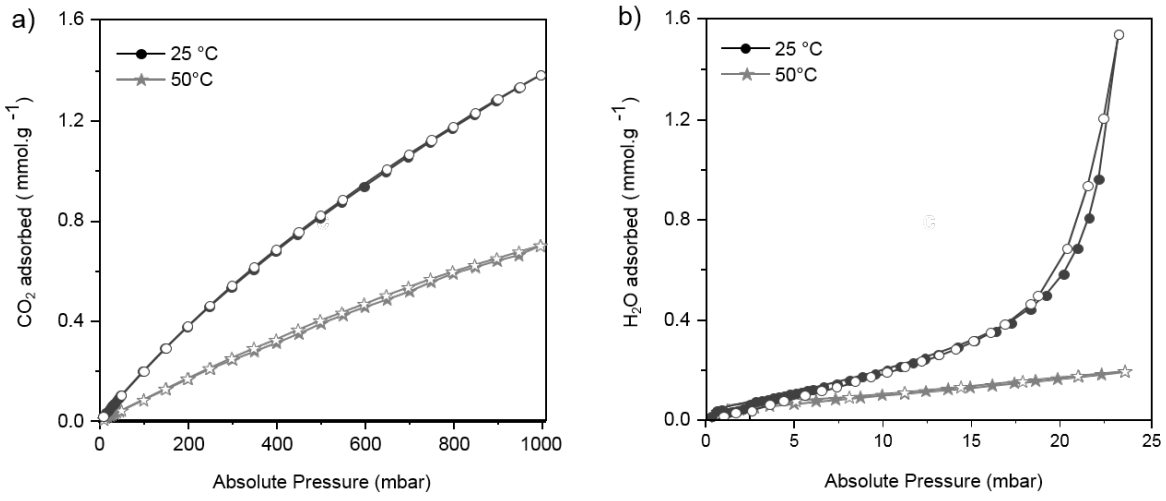


Figure 6.2 (a) CO_2 and (b) H_2O sorption isotherms at 25 °C and 50 °C of the studied triazine-biphenyl HCP. Filled symbols = adsorption; empty symbols = desorption.

As Figure 6.2a shows, the HCP sample displays CO_2 uptake capacities at 1 bar and at 25 and 50 °C of 1.38 mmol.g^{-1} and 0.70 mmol.g^{-1}, respectively. To provide some perspective, zeolite 13X, a benchmark CO_2 adsorbent, exhibits a CO_2 uptake capacity of ~4 mmol.g^{-1} at 1 bar and 25 °C.[245] Compared to other HCPs, the studied HCP displays relatively similar adsorption capacities (Table A3.3). Depending on the monomer used, the HCP's CO_2 uptake capacity can reach up to 2.8 mmol.g^{-1} at 25 °C and 1 bar.[246]

Regarding H_2O sorption, at 23 mbar and at 25 and 50 °C, the studied HCP displays a low H_2O uptake capacity of 1.5 and 0.17 mmol.g^{-1}, respectively (Figure 6.2b, to be compared to 16.7 mmol.g^{-1} at 25 °C and 23 mbar for zeolite 13X).[247] Despite a higher surface area, the HCP studied here adsorbs considerably less H_2O compared to a previously investigated benzene-based hypercrosslinked polymer (HCP-1, Chapter 5), which displayed a surface of 951 m^2.g^{-1} and a H_2O uptake capacity of 9.4 mmol.g^{-1}.[129] The relatively low H_2O uptake capacities of the triazine-biphenyl HCP likely result from the low oxygen content, i.e. 1.1 at% O compared to 11.38 at% O for the benzene-based HCP.

3.3. Vibrational analysis and band assignment

Having evaluated the sorption properties of HCP, I next explored how CO_2 and H_2O adsorb on the HCP surface using infrared spectroscopy. To identify the HCP vibrational fingerprints involved in intermolecular interactions with CO_2 and H_2O, one must assign the HCP's vibrational bands. In theory, one could use the computed infrared spectra of a single triazine and biphenyl molecule and compare them with the measured infrared spectrum of the HCP. However, owing to the complex interactions between monomer molecules after polymerization, the experimental HCP infrared spectrum will differ from the simulated ones. Hence, to achieve a precise band assignment, I must understand how intermolecular interactions impact the infrared spectrum of a triazine molecule and that of a biphenyl molecule, i.e. band shifts, band broadening and appearance of new vibrational bands.

I evaluated the effect of triazine intermolecular interactions on its infrared spectrum by gradually increasing the number of triazine interactions in the computer simulations. This was carried out by computing the infrared spectra of one and six triazine molecules. Given the increasing computing cost, I studied the effect of more intermolecular interactions experimentally by collecting the attenuated total reflectance infrared (ATR-IR) spectrum of an 80 nM triazine solution and that of crystallized triazine

powder. I focused the initial vibrational analysis on the spectral region ranging from 1800 to 1000 cm^{-1} where interactions with the substrate dominate. I discuss the vibrational analysis of other spectral regions below.

As Figure 6.3a and Table A3.4 show, triazine intermolecular interactions generate prominent spectral changes. An increase in intermolecular interactions, specifically in the number of their configurations, gives rise to band broadening. Among the measured spectra, the triazine powder infrared spectrum displays the broadest band shapes resulting from an increased number of dipole-dipole interactions between the amino groups present in the triazine monomer. When increasing the number of intermolecular interactions, various band shifts can be observed. Bands 1, 2, and 5 of Figure 6.3a, which correspond to NH_2 stretching vibrations coupled with C-NH_2, C-C and C-N vibrations, according to the normal mode analysis (Table A3.4), respectively, gradually shifted towards higher wavenumbers. Additionally, one can observe the appearance of new vibrational bands (bands 3 and 4) that correspond to N-H vibrations coupled with N-C=N vibrations. Overall, as Figure 6.3a shows, by gradually capturing the spectral implications of triazine intermolecular interactions, I achieve a precise assignment of the triazine powder vibrational bands. As triazine powder is used as precursor for the HCP synthesis, the spectral features generated by strong intermolecular interaction will likely be present in the infrared spectrum of the HCP. A detailed assignment of the triazine powder vibrational bands can be found in Table A3.4.

To investigate the effect of the biphenyl intermolecular interactions on the IR spectral features, I followed a similar approach. The absence of strong polar groups in the biphenyl molecule and therefore, the lack of strong dipole-dipole intermolecular interactions, facilitated the assignment process. As Figure 6.3b shows, the simulated infrared spectrum of a single biphenyl molecule agrees well with the measured infrared spectrum of the biphenyl powder. The vibrational band at 1088 cm^{-1} (band 3, Figure 6.3b and Table A3.5) corresponds to the stretching vibration of the methoxy group. Two new vibrational bands are observed at 1718 and 1697 cm^{-1} (bands 1 and 2, Figure 6.3b). As both vibrational bands do not correspond to any of the ones present in the computed infrared spectra of a single biphenyl molecule, they likely originate from biphenyl intermolecular interactions. The broad band tailing and their location at around 1700 cm^{-1} point to C=O bond vibrations. I assign these two vibrational bands to the interaction

of an aromatic carbon with an oxygen atom of a methoxy group present in another biphenyl molecule. A detailed assignment of the biphenyl powder vibrational bands can be found in Table A3.5.

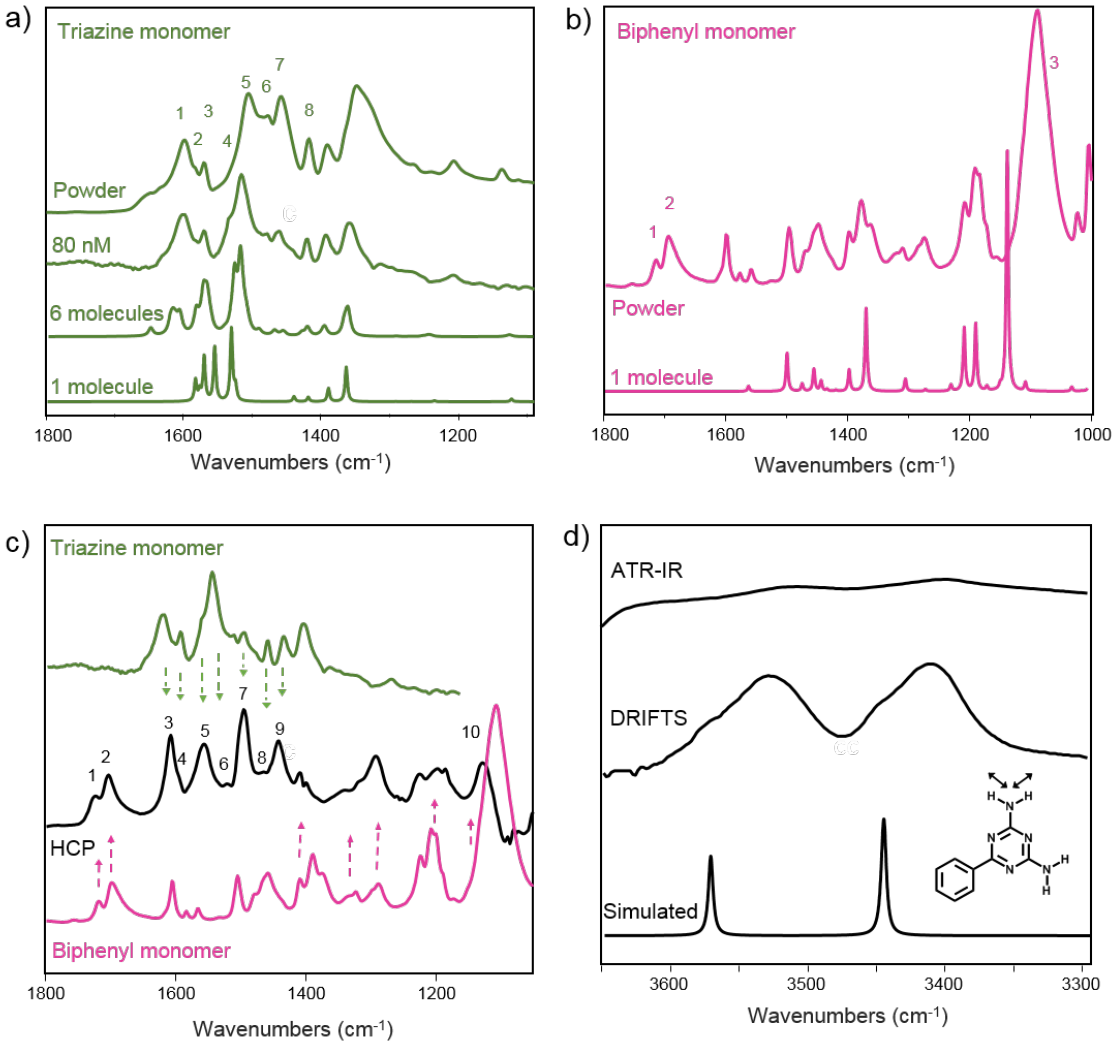


Figure 6.3. Vibrational analysis and band assignment for the triazine-biphenyl HCP sample: (a) simulated infrared spectra of one and six triazine molecules, experimental ATR infrared spectrum of an 80 nM triazine monomer solution and triazine monomer powder. (b) Simulated infrared spectrum of one biphenyl monomer molecule and experimental ATR infrared spectrum of the biphenyl monomer powder. (c) Comparison between the ATR infrared spectra of the triazine and biphenyl monomer with that of the triazine-biphenyl HCP. (d) Comparison between the ATR-IR and DRIFT spectra of the HCP and the simulated one.

The band assignment of the triazine and biphenyl powder, and the spectral implications of intramolecular interaction being confirmed, a precise analysis of the triazine-biphenyl HCP vibrational bands is now possible. As Figure 6.3c shows, HCP exhibits characteristic vibrational bands of both triazine and biphenyl powder. Bands 1 and 2 of Figure 6.3c correspond to the vibrations of the intermolecular biphenyl C=O bond, while bands 3 to 9 correspond to the triazine component. Bands 3 and 4 correspond to NH_2 stretching vibrations coupled with C-NH_2, and C-C ring vibrations. Lastly, band 10 corresponds to the vibration of unreacted methoxy groups arising from partially crosslinked biphenyl molecules. A more detailed assignment of the other HCP vibrational bands can be found in Table A3.6.

One should note that all the aforementioned experimental infrared spectra were acquired using ATR-IR spectroscopy. As each infrared technique uses different sampling configurations, they will display different surface and bulk sensitivities and certain spectral features might differ.[248] To achieve a precise band assignment, one must compare spectra that are measured using identical IR techniques and necessary precautions must be taken when comparing spectra acquired using different sampling configurations, e.g. ATR-IR and DRIFTS. As Figure A3.6 shows, in the 1800 to 1000 cm^{-1} spectral region, the vibrational bands observed by ATR-IR and DRIFT spectra of the HCP are similar. I can therefore unequivocally transpose the obtained HCP band assignment based on the ATR-IR studies to that of the DRIFT spectra.

So far, I focused the vibrational analysis on the 1800 to 1000 cm^{-1} region. Yet, the 3650 to 3275 cm^{-1} region is also of interest as it corresponds to the 'pure' amino region (i.e. not coupled with aromatic vibrations). Interestingly, as Figure 6.3d shows, the measured ATR-IR spectrum of the triazine-biphenyl HCP displays little amine vibrational bands. However, when performing DRIFTS analysis, reported below, I observe vibrational bands at 3530 and 3415 cm^{-1}, corresponding to the primary NH_2 asymmetric and symmetric stretching vibrations, respectively.[249] As mentioned above, this variance likely arises from the difference in measurement technique used. In ATR-IRS, the penetration depth of the infrared light depends on the incoming wavelength. At smaller wavelengths, the penetration depth decreases, resulting in a loss of sensitivity at higher wavenumbers. Such phenomenon could explain the apparent absence of the primary amine bands at 3530 and 3415 cm^{-1}.

Though tangentially relevant to the objective of the study, DRIFTS provided insights into the reaction mechanism linked to HCP formation. In brief, it supports the S_N1 route speculated in earlier studies, as shown in Figure A3.7.[221, 250] Upon protonation by the acid catalyst, a methoxy group of the biphenyl monomer leaves as methanol, forming a carbocation. The carbocation then undergoes nucleophilic attack from the triazine monomer and finally regeneration of the acid catalyst occurs by proton transfer. As I detected primary amine groups and no secondary amines, I conject that the phenyl ring of the triazine monomer, and not the primary amines, act as nucleophile. Overall, the stretching vibration of the primary amines observed using DRIFTS unveiled the synthesis mechanism of the triazine-biphenyl HCP.

3.4. Vibrational band analysis during CO_2 adsorption

Having assigned the HCP vibrational bands, I next evaluated those involved in CO_2 adsorption to identify the CO_2 adsorption sites. To do this, I conducted time-resolved in-situ DRIFTS measurements by alternatingly passing CO_2 and He through the DRIFTS cell. I carried out two CO_2-He cycles for each temperature studied (50, 100 and 150 °C). Prior to passing CO_2 through the DRIFTS cell, I collected the DRIFT spectrum of the HCP under He and used it as background spectrum. As Figure 6.4a shows, under CO_2 at 50 °C, the obtained difference spectra display negative and positive bands, while under He, these spectral features are not visible (Figure 6.4b).

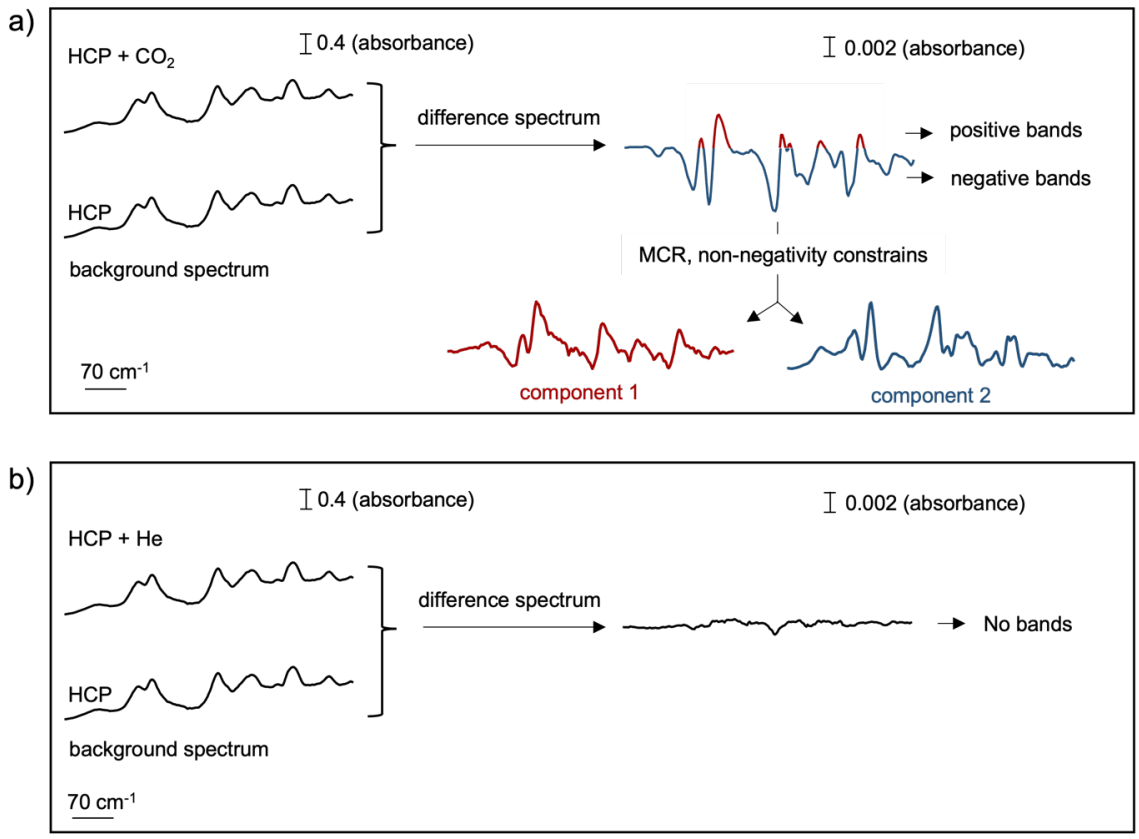


Figure 6.4 Representation of the spectral components obtained upon processing the difference spectrum using MCR. (a) The represented difference spectrum corresponds to the average of the difference spectra acquired under a CO_2 atmosphere at 50 °C, and (b) the represented difference spectrum corresponds to the average of the difference spectra acquired under a He atmosphere at 50 °C.

To understand the origin of these positive and negative bands, one must remember that the analysed data are obtained by subtracting the background spectrum (i.e. HCP spectrum in absence of CO_2) from the HCP spectrum acquired under a CO_2 atmosphere. If the background spectrum exhibits spectral features which are absent in the spectrum obtained under a CO_2 atmosphere, negative bands emerge due to the subtraction. Conversely, if the spectrum obtained under a CO_2 atmosphere exhibits spectral features absent in the background spectrum, positive bands emerge. Importantly in infrared spectroscopy, the concomitance of negative and positive bands in a difference spectrum is often the result of band shifts. As Figure 6.5a illustrates, when the vibrational band of a material shifts compared

to the background spectrum, the difference spectrum displays a negative band at the original band position and a positive band at the new band location. The relative positions of the negative and positive bands in the difference spectrum enable to determine the direction of the band shift.

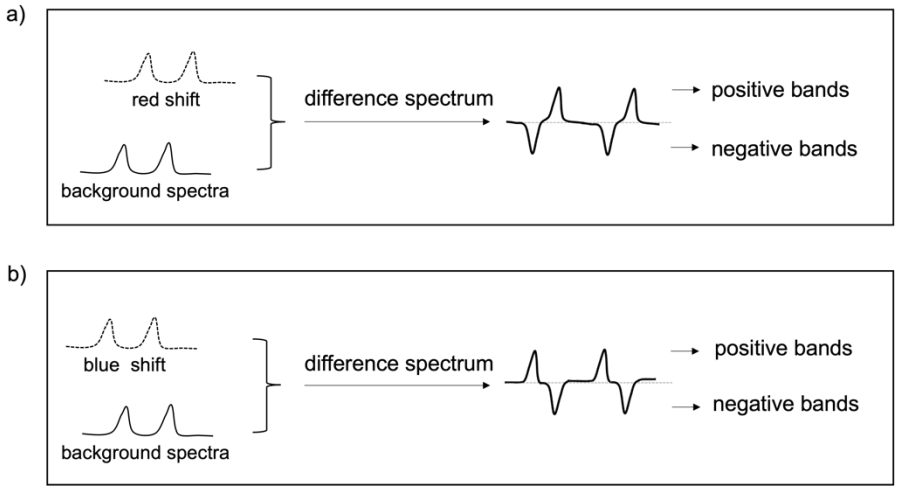


Figure 6.5 Representation of the origin of positive and negative bands in a difference spectrum. Panel (a) illustrates the type of difference spectrum obtained upon a red shift of the vibrational bands of a material compared to its background spectrum. Panel (b) illustrates the type of difference spectrum obtained upon a blue shift of the vibrational bands of a material compared to its background spectrum.

As illustrated in Figure 6.5a, if negative bands precede positive ones (left to right; higher to lower wavenumbers), it indicates that the vibrational bands are shifting towards lower wavenumbers. Conversely, if positive bands precede negative ones, it indicates that the vibrational bands are shifting towards higher wavenumbers (Figure 6.5b). In this study, as shown by the difference spectra in Figures 6.4a and A3.8, under CO_2, negative bands precede positive bands, indicating that some of the HCP vibrational bands shifted towards lower wavenumbers. This red shift results from CO_2 adsorption on the HCP surface. Yet, the complexity of the obtained difference spectrum prevents a precise identification of the HCP vibrational bands that are red-shifted.

To address this challenge, one can process the difference spectra using MCR. MCR is a mathematical method that extracts the individual sources of variations present in a signal (see Section 3.1.3.3 for more detail).[251] When applied to time-resolved DRIFTS, MCR can extract kinetic behaviours. It identifies

the vibrational bands' kinetics, i.e. the speed at which bands shift or appear or disappear. Based on the vibrational bands' kinetics, MCR separates them into kinetically pure spectral components. Vibrational bands that have identical kinetic behaviours, i.e. (dis)appearing at the same time, are associated to the same component. The relative intensity of those kinetically pure components to the global signal are also determined and are referred to as a concentration profile. When processing the data using MCR in this study, a non-negativity constraint is applied, i.e. vibrational bands cannot be negative. As Figure 6.4a illustrates, this constraint converts the negative spectral features of the difference spectrum into positive ones and describes their "negative" intensity by assigning them negative concentrations. After applying the non-negativity constraint, negative and positive spectral features respectively exhibit negative and positive concentration profiles, thereby behaving kinetically differently. Hence, MCR separates them into two different components (Figure 6.4). The first component represented in red (Figure 6.6a) corresponds to the positive spectral features of the difference spectra, and the second component in blue (Figure 6.6b) to the negative ones.

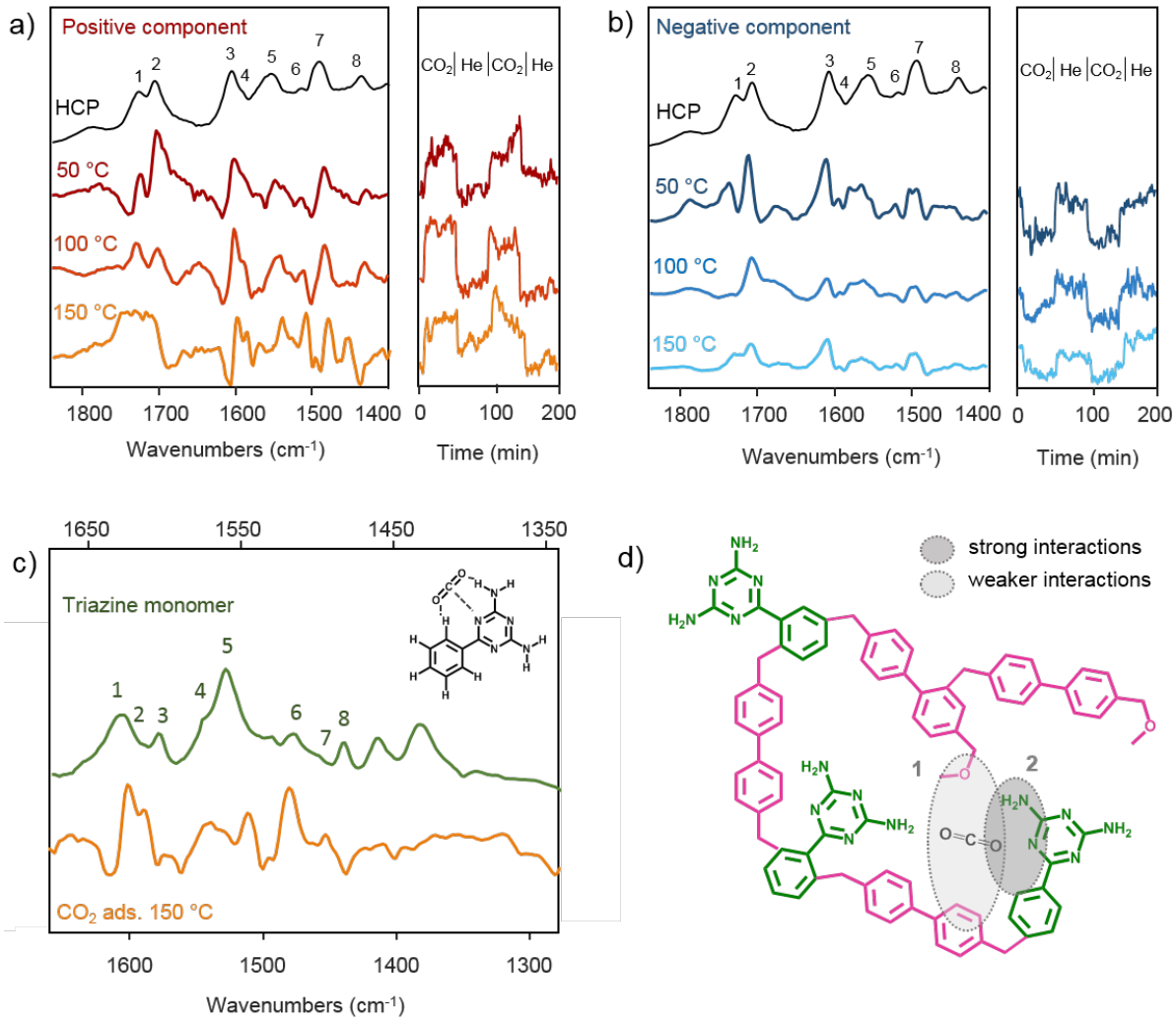


Figure 6.6 DRIFTS study of CO_2 adsorption on HCP. Left panels of (a) and (b): comparison between the DRIFT infrared spectrum of the triazine-biphenyl HCP sample with the positive (a) and negative (b) spectral components obtained for CO_2 adsorption measurements at 50 °C, 100 °C and 150 °C after performing MCR analysis. The right panels of (a) and (b) represent the component concentration profiles obtained by MCR, which illustrate the contribution of the spectral component to the overall spectra over time. (c) Comparison between the ATR infrared spectrum of the triazine monomer with the positive spectral components obtained for CO_2 adsorption measurements at 150 °C after MCR analysis. (d) Illustration of the CO_2 adsorption sites in triazine-biphenyl HCP.

As shown by the concentration profiles, at 50 °C, both positive and negative components dynamically appear or disappear in the presence or absence of CO_2, respectively (Figures 6.6a and 6.6b, right panels). This finding corroborates the observation made using unprocessed difference spectra

suggesting the presence of both positive and negative bands due to CO_2 adsorption on the HCP surface. After MCR analysis, an exact determination of the HCP vibrational bands red-shifted upon CO_2 adsorption is now possible. As shown in Figures 6.6a and 6.6b, at 50 °C, both negative and positive components display vibrational bands at 1726, 1704, 1605, 1551 and 1490 cm^{-1} (bands 1, 2, 3, 5 and 7 of Figures 6.6a - b). These bands are the ones shifted upon CO_2 adsorption on HCP. They correspond to the intermolecular biphenyl C=O bond vibrations, NH_2 scissoring vibrations coupled with different C-NH_2 vibrations modes, and N-C=N stretching vibrations of the triazine monomer. Comparing the position of the vibrational bands present in the positive component with the corresponding unshifted HCP vibrational bands, I estimate that upon interaction with CO_2, the HCP vibrational bands located at 1726, 1704, 1605, 1551 and 1490 cm^{-1} are shifted by -2, -6, -6, -11, and -8 cm^{-1}, respectively (Figure A3.9). To verify that these bands are indeed the ones shifting under a CO_2 atmosphere, I simulated the difference spectrum obtained when the above-mentioned bands are red-shifted by 8 cm^{-1}. As shown in Figure A3.10, the simulated difference spectrum is almost identical to the one measured, corroborating our hypothesis. The small differences I observe are expected as each vibrational band interacts differently with CO_2, and therefore not all bands will shift to the same extent, as in our simulation.

Another aspect to study using MCR analysis is the kinetic behaviour of the positive and negative vibrational bands present in the difference spectra. As determined by MCR, all the positive vibrational bands belong to the same kinetically pure component and therefore dynamically appear or disappear at the same rate in the presence or absence of CO_2. A similar reasoning applies to the negative vibrational bands. Following this analysis, the HCP's vibrational bands located 1726, 1704, 1605, 1551 and 1490 cm^{-1} are all shifting at the same rate under a CO_2 atmosphere. This observation can only occur if, upon CO_2 adsorption, CO_2 molecules interact with all five vibrational bands at the same time, within the time-resolution of our measurements. Thereby, as Figures 6.6a - b illustrate, at 50 °C, CO_2 concurrently interacts with the intermolecular biphenyl C=O bond, the primary amines and the triazine groups of the triazine monomer. While I anticipated the interactions between CO_2 and the primary amines and the triazine groups, I did not foresee CO_2 interaction with the intermolecular biphenyl C=O bond. It is interesting to see that residual oxygen from the incomplete conversion of methoxy groups to crosslinks, an a priori undesired feature, plays a role in CO_2 adsorption.

To investigate the strength of CO_2 adsorption with the above-mentioned functional groups, I conducted additional CO_2 adsorption measurements at 100 °C and 150 °C. At higher temperatures, weakly bound CO_2 desorbs and only the spectral features promoted by strongly adsorbed CO_2 are observed. As Figure 6.6a shows, when increasing the temperature to 100 °C and 150 °C, the vibrational bands of the positive component corresponding to the intermolecular biphenyl C=O bond gradually disappear (bands 1 and 2), while the ones corresponding to the triazine monomer remain unchanged (bands 3, 5 and 7). A similar behaviour is observed for the negative component: the negative vibrational bands of the intermolecular biphenyl C=O bond disappear faster than those of the triazine monomer. Such observations indicate that CO_2 adsorbs more strongly to the triazine groups than to the biphenyl sites (Figure 6.6d). At 150 °C, one only observes the vibrational bands corresponding to the triazine monomer (Figure 6.6c), suggesting that at 150 °C, CO_2 mainly adsorbs on the triazine monomer. I illustrate how CO_2 interacts with the triazine component of the HCP in Figure 6.6c. As the temperature increases from 50 to 150 °C, some of the positive triazine vibrational bands become sharper (Figure 6.6a) as strong CO_2 interactions with HCP restrict vibrational motion. At 150 °C, the broad HCP band at 1605 cm^{-1} originates from two narrower bands at 1605 and 1593 cm^{-1} (bands 3 and 4, Figure 6.6a). Both bands correspond to NH_2 stretching vibrations coupled with N-C=N vibrations, respectively. The positive bands at 1551 and 1490 cm^{-1} (bands 5 and 7, Figure 6.6a) also become shaper and come from primary amine vibrations, specifically NH_2 stretching vibrations coupled with C-N and C-NH_2 vibrations, respectively. As all the positive bands which become sharper involve NH_2 vibrations, one can conclude that the primary amine groups of the triazine monomers are strongly involved in CO_2 adsorption.

6.3.2 Vibrational analysis during H_2O adsorption

I then investigated the HCP vibrational bands involved in H_2O adsorption. For H_2O adsorption measurements, I performed time-resolved DRIFTS measurements by alternatingly passing water-saturated He and He through the DRIFT cell. I carried out two H_2O-He cycles for each temperature studied (50, 100 and 150 °C). Prior to passing water vapour through the DRIFTS cell, I collected a DRIFT spectrum of the HCP under He and used it as background spectrum to produce the difference spectra.

As Figure 6.7a shows, in the presence of H_2O at 50 °C, the difference spectrum displays negative and positive bands, suggesting that some of the HCP vibrational bands are shifted due to interactions between HCP and H_2O. Following the same reasoning as for CO_2 adsorption, as negative bands precede positive ones, I infer that some of the HCP vibrational bands are red shifted. I then processed the time-resolved DRIFT spectra using MCR to determine which HCP vibrational bands shifted upon interactions with H_2O. As water vapour absorbs infrared light, it creates an undesirable background noise in the 2000 - 1300 cm^{-1} region and one should separate this effect from that of water adsorption. Thanks to the different kinetic behaviour of water vapour and that of adsorbed water, MCR can resolve the water vapour contribution and separate it from the other spectral components (Figure 6.7a).

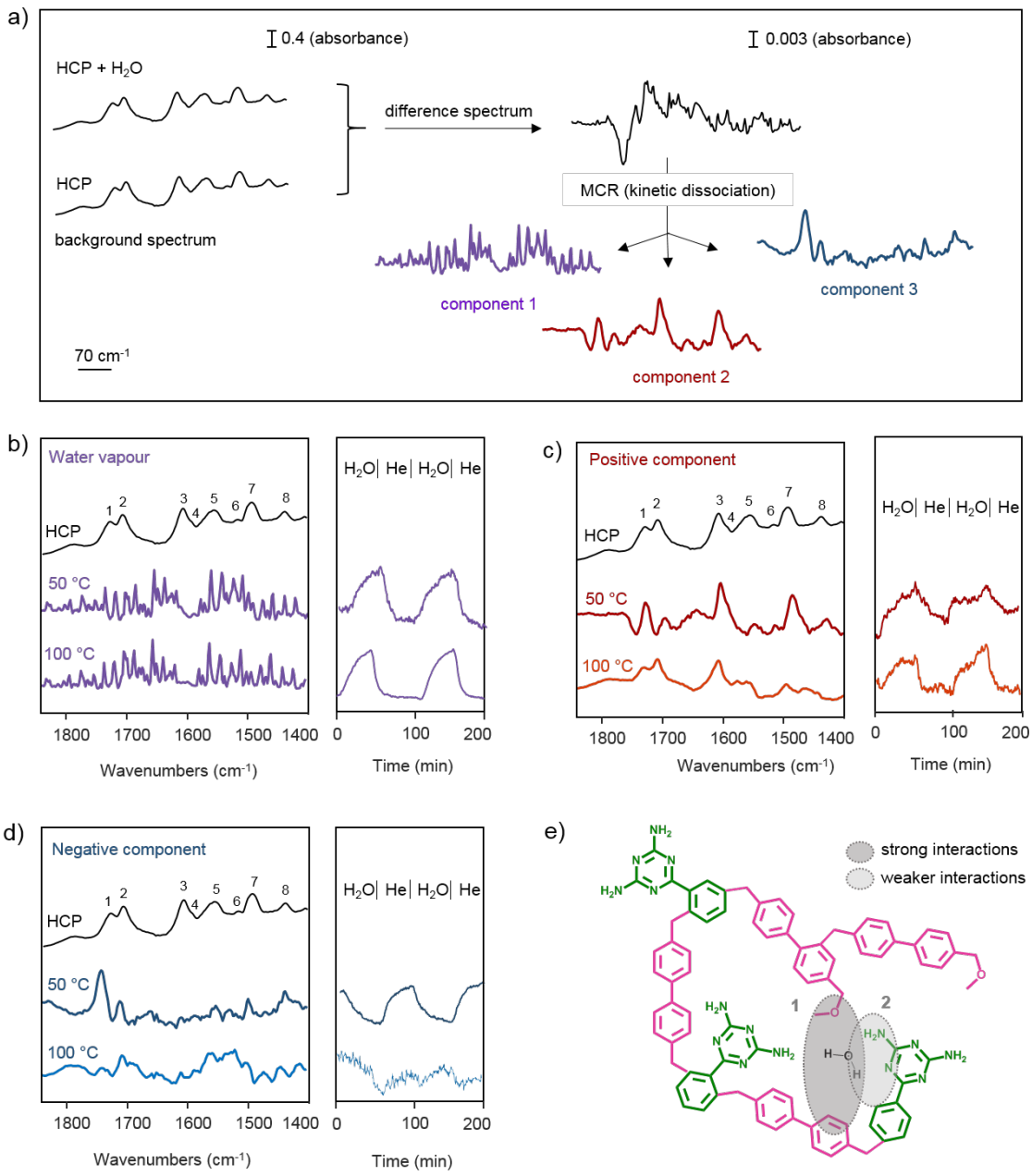


Figure 6.7 DRIFTS study of H_2O adsorption on HCP. (a) Schematic illustration of the spectral components obtained after processing the difference spectrum using MCR. The difference spectrum corresponds to the average of the difference spectrum acquired under a H_2O atmosphere at 50 °C. Left panels of (b), (c) and (d): comparison between the DRIFT spectrum of the triazine-biphenyl HCP sample with: water vapour (b), the positive (c) and negative (d) spectral components obtained for H_2O adsorption measurements at 50 °C and 100 °C after performing MCR analysis. Right panels of (b), (c) and (d): component concentration profiles obtained by MCR. (e) Illustration of the H_2O adsorption sites in HCP.

As Figure 6.7a shows, when processing the difference spectrum obtained under a H_2O atmosphere using MCR, I extract three spectrally significant and kinetically pure components. The first component (purple, Figure 6.7b) corresponds to the water vapour present in the DRIFTS cell, the second component (red, Figure 6.7c) to the positive spectral features of the difference spectrum, and the third component (blue, Figure 6.7d) to the negative spectral features of the difference spectrum. As shown in Figure 6.7c, at 50 °C, the positive component displays vibrational bands at around 1726, 1704, 1605, 1551 and 1490 cm^{-1} (bands 1, 2, 3, and 7) and the negative component display vibrational bands at around 1726, and 1704 cm^{-1} (bands 1 and 2 of Figure 6.7d). The HCP vibrational bands located at those wavenumbers are the ones shifted upon H_2O adsorption. Interestingly, the shifted HCP vibrational bands in presence of H_2O are identical to those shifted in presence of CO_2. At 50 °C, as for CO_2, H_2O interacts with the intermolecular C=O bond of the biphenyl component, the primary amines and the triazine groups of the triazine monomer. Additionally, all the positive vibrational bands belong to the same kinetically pure components and therefore dynamically appear or disappear at the same time in presence or absence of H_2O. A similar reasoning can be made for the negative vibrational bands. As for CO_2 adsorption, these observations indicate that the HCPs vibrational bands located at those wavenumbers are all shifting at the same rate in the presence of H_2O and suggest that H_2O interacts simultaneously with all five functional groups. In short, at 50 °C, H_2O and CO_2 adsorb in a similar manner on the HCP.

To investigate the strength of H_2O adsorption, I conducted additional H_2O adsorption measurements at 100 °C and 150 °C. As Figures 6.7c shows, at 100 °C, the positive vibrational bands linked to the triazine monomer (bands 3 and 7 and of Figures 6.7c), decrease faster than those of the intermolecular biphenyl C=O bond (bands 1 and 2). Hence, unlike CO_2, H_2O adsorbs more strongly to the biphenyl site than to the triazine one (Figure 6.7e). This phenomenon likely results from strong hydrogen bonds between the water molecules and the intermolecular biphenyl C=O bonds. At 150 °C, due to very low H_2O adsorption, I did not extract meaningful data.

6.3.3 Vibrational band analysis in the presence of CO_2 and H_2O under irradiation

Finally, I investigated CO_2 and H_2O co-adsorption on HCP under transient light irradiation. During transient irradiation, I exposed the sample to a water-saturated CO_2 atmosphere at 50 °C with UV-Vis light turned on and off every 5 min. Prior to passing water-saturated CO_2 through the DRIFTS cell, I collected a DRIFT spectrum of the HCP under He as background spectrum. I then processed the difference spectrum obtained during the transient DRIFTS measurement using MCR.

As Figure 6.8a shows, I extracted five different kinetically pure components with spectral significance. The first one (purple, component A) corresponds to water vapour present in the DRIFTS cell, while the others (component B-E) correspond to four different positive spectral components. As shown by the concentration profiles of the extracted components in Figure 6.8b, components B and C exhibit an amplitude change between light on and off similar to that of water vapour, while components D and E display more pronounced amplitude changes. Such signal difference likely arises from the different adsorption strengths between CO_2 and H_2O on the HCP. As the signal amplitude of components B and C is like that of water vapour, I assign these changes to water adsorption, while components D and E correspond to changes in CO_2 adsorption. Compared to the CO_2 components D and E, the smaller signal changes observed for H_2O possibly arise from strong hydrogen bonds between the water molecules and the HCP, favouring strong interactions.

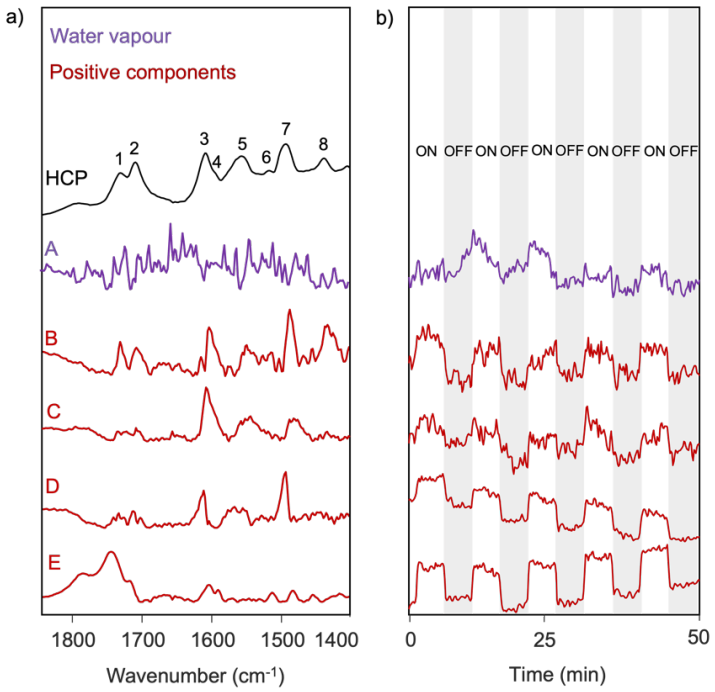


Figure 6.8 MCR components extracted from DRIFTS measurements during CO_2 and H_2O co-adsorption HCP under intermittent light irradiation. (a) Comparison between the DRIFT spectrum of the triazine-biphenyl HCP sample with that of water vapour (A), and the positive (B, C, D, E) spectral components obtained under a CO_2/H_2O atmosphere and transient UV-Vis irradiation at 50 °C. (b) Component concentration profiles were obtained by MCR.

The concentration profile of the water vapour component suggests an increase of water vapour in the DRIFTS cell under light irradiation. This phenomenon likely results from water desorption caused by an increase of temperature at the HCP surface during irradiation. I also note that all the vibrational bands belonging to components B and C are red-shifted compared to that present in the background spectrum and dynamically appear and disappear under light on and off, respectively. Such behaviour suggests an increase of substrate-HCP interactions upon light irradiation. Thus, despite partial H_2O desorption, an increase in the number of interactions between the H_2O molecules that are still adsorbed on the HCP occurs. As two components (B and C) can be extracted, I conject that the H_2O molecules that are still adsorbed interact with the newly available adsorption sites in two different manners. The first one (component B) suggests that some of the adsorbed H_2O molecules interact with both newly available biphenyl C=O bond (bands 1 and 2, Figure 6.8a) and the triazine groups (bands 3 and 7), while the

second component (component C) suggests that part of the adsorbed H_2O only interacts with the newly available triazine groups as only bands 3 and 7 are visible.

Regarding the CO_2 components, the vibrational bands belonging to component E are blue-shifted compared to those in the background spectrum and dynamically appear and disappear under light on and off, respectively (Figure 6.8 and Figure A3.11). As blue-shifted bands result from a decrease of substrate interactions and component E is mainly constituted of two vibrational bands corresponding to the biphenyl C=O bond vibrations (bands 1 and 2 of Figure 6.8a), I suggest that under light irradiation, adsorbed CO_2, which originally interacts with both C=O and the triazine component, desorbs from the bridging C=O biphenyl site. In addition, the vibrational bands of component D, which correspond to the triazine group vibrations (bands 3 and 7, Figure 6.8a) are red-shifted compared to the one present in the background spectrum and dynamically appear and disappear under light on and off, respectively, suggesting that upon light irradiation, the number of CO_2-triazine interactions increases. As under irradiation some H_2O molecules desorb, partial CO_2 desorption will also likely occur, generating newly available adsorption sites. Thus, I conject that upon light irradiation, CO_2 molecules that are still adsorbed will interact with the newly available triazine adsorption sites. In summary, upon light irradiation, I observe partial H_2O and CO_2 desorption followed by a redistribution of the number of interactions between the H_2O and CO_2 molecules that are still adsorbed on the HCP adsorption sites. I illustrate the impact of light irradiation upon CO_2 and H_2O interactions with the HCP in Figure 6.9.

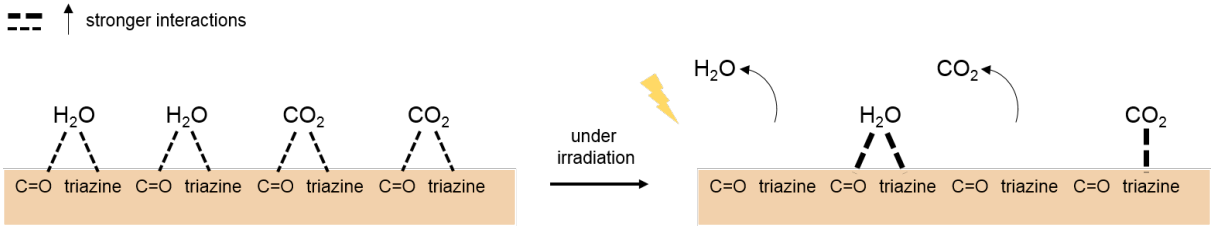


Figure 6.9 Schematic illustration of the impact of light irradiation upon CO_2 and H_2O interactions with the HCP. It highlights the changes in the number of interactions between the HCP and the substrates. The latter is relative to the number of interactions detected under light off.

Finally, I did not detect any intermediate species during the transient DRIFTS measurement. To confirm this, I conducted a transient isotopic $^{13}CO_2$ measurement and exposed the HCP to a water-saturated

$^{13}CO_2$ atmosphere instead of a water-saturated $^{12}CO_2$ atmosphere and irradiated the sample with a UV-Vis light 5 min intermittently. Compared to $^{12}CO_2$, the vibrational bands of $^{13}CO_2$ should be red-shifted. As Figure A3.12a shows, under irradiation, when switching from a $^{12}CO_2/H_2O$ to a $^{13}CO_2/H_2O$ atmosphere, the spectroscopic signature of CO_2 shifted. Such shift is clearly visible for the combination bands located at 3725, 3700, 3627, and 3600 cm^{-1}, and the symmetric and asymmetric CO_2 stretching bands located at ~ 2350 and 2330 cm^{-1}, respectively. Yet, in the 2000 - 1400 cm^{-1} spectral region, where one expects the vibrational bands of intermediate species such as carboxylate, the difference spectra obtained under a $^{13}CO_2/H_2O$ atmosphere resemble that obtained under a $^{12}CO_2/H_2O$ atmosphere (Figure A3.12b). These observations suggest that no intermediate species are observed under irradiation. At an early stage of our transient DRIFTS data analysis, I assigned component E of Figure 6.8a to be a carboxylate species due to its bands' locations at around 1750 cm^{-1}. Thanks to the isotopic measurement, I can conclude that component E is not an intermediate species. One should note that isotopic experiments like this one, though rarely performed, remain important to unambiguously confirm the presence or absence of intermediate species.

6.4 Conclusion

In this chapter, I show how to probe gas (CO_2) and vapour (H_2O) interactions with hypercosslinked polymers. This was done by combining DFT calculations, in-situ DRIFTS and MCR. DRIFTS measurements were undertaken at varying temperatures and with or without light irradiation. At 50 °C, CO_2 adsorbs on both the triazine and biphenyl components of the HCP, albeit more strongly on the triazine one. The primary amine groups of triazine promoted strong interactions with CO_2. On the other hand, H_2O adsorbed on the same sites but more strongly on the biphenyl component. Under transient light irradiation, I observed partial H_2O and CO_2 desorption and a redistribution of interactions between the H_2O and CO_2 molecules that are still adsorbed on the HCP adsorption sites. Finally, the stretching vibrations of the primary amines, undetectable under ATR-IRS, are observed when using DRIFTS, enabling to unveil the synthesis mechanism of the triazine-biphenyl HCP. Overall, this study helps gain a better understanding of the relationship between CO_2/H_2O adsorption and the HCPs structure. I foresee that enhanced photoactivity can be archived by increasing and/or decreasing the number of

CO_2 and H_2O adsorption sites, respectively. These findings can be used to develop improved HCP photocatalysts for CO_2 conversion and for other CO_2 management processes such as gas separation.

Chapter 7

Conclusions and Future plans

7.1 Findings and achievements

This thesis investigated the potential of porous organic-based photocatalysts for CO_2 photoreduction. To do so, I focused on two different routes: 1) investigating the key factors influencing electron-hole flow across MOF-based heterojunctions and 2) exploring the potential of HCPs as CO_2 photoreduction catalysts.

In Chapter 4, I demonstrated the importance of considering band bending when developing a MOF-based heterojunction, an aspect that is not commonly investigated for MOF-based heterojunctions. Using XPS, valence band, work function and bang gap measurements, I showed how to construct a simple band model that can predict the positive or negative impact of band bending on the heterojunction photoactivity. These findings were instrumental to develop a Ti-MOF-based heterojunction with favourable band bending, from which I measured a ~2-fold improvement in CO_2 photoreduction activity compared to the physical mixture. Overall, this study offers a better understanding of the semiconductor/MOF interface and highlights the factors that influence electron flow across such interface. As a result, this study supports the rational design of efficient MOF-based heterojunctions.

In Chapter 5, I investigated for the first time HCPs as active photocatalysts for CO_2 reduction under both UV and visible light irradiation. The lead material significantly outperformed the benchmark material TiO_2 P25, using only sacrificial H_2O under visible light irradiation; a remarkable feature for an organic photocatalyst requiring no co-catalyst or doping. In addition, I showed the impact of using H_2O vs H_2 as sacrificial agent on the HCPs photoactivity. The improved activity when using H_2O was hypothesised to arise from superior H_2O adsorption capacities which facilitate access of the sacrificial

agent to photoactive sites, enhancing photocatalytic conversion rates when compared to sacrificial H_2. The stability of the HCPs under operating conditions was also investigated. As determined by po-irradiation XPS measurements, the degradation likely arises from decomposition of the aliphatic crosslinkers and partially crosslinked methoxy groups. Yet, to confirm the source of degradation and the degradation mechanism, further studies are required. To summarise, this study comes at a time when the field of organic-based photocatalysts is emerging, and presents HCPs as an exciting and versatile new photocatalytic platform for solar-energy conversion.

In Chapter 6, I investigated the sorption mechanism of CO_2 and H_2O on a triazine-biphenyl HCP. This was done by combining DFT calculations, in-situ DRIFTS and MCR analysis. Using this approach, I identified the adsorption sites of CO_2 and H_2O, determined unambiguously with which HCP functional group they interact with, and assessed the strength of adsorption with respect to the functional group. I found that both CO_2 and H_2O interact with the triazine and biphenyl HCP components, however, CO_2 interacted more strongly with the triazine component, while H_2O interacted more strongly with the biphenyl component. In addition, the amino groups of the triazines were found to promote strong CO_2 interactions. Given the ability of HCPs to photoreduce CO_2, I also investigated CO_2 and H_2O adsorption under transient light irradiation. Under transient light irradiation, I observed partial H_2O and CO_2 desorption and a redistribution of interactions between the H_2O and CO_2 molecules that are still adsorbed on the HCP adsorption sites. This study opens new research avenues towards the rational design of optimised HCP adsorbents and photocatalysts for CO_2 management.

In summary, this thesis opens new doors to tailor the physicochemical properties of porous organic-based photocatalysts for improved CO_2 conversion by seeking to answer the following significant questions: How do the chemical, structural and optoelectronic properties of porous organic-based photocatalysts influence CO_2 photoreduction? What is the extent (if any) of degradation? How does CO_2 and H_2O adsorb at the surface of porous organic-based photocatalysts? This research contributes to making this class of versatile photocatalysts a competitive alternative to traditional ones and contributes to the implementation of photocatalysis as a promising method to mitigate climate change and the global energy crisis.

7.2 Future plans

The design of high-performing and robust photocatalysts is key to the success of solar fuel production via CO_2 conversion. In that regards numerous efforts still need to be made.

To design efficient photocatalysts, one must establish the relationship between the photocatalyst activity/selectivity and its structure, which can be achieved via in-situ characterisation techniques. Regarding HCPs, it would be of interest to further investigate how different functional groups affect CO_2 coordination at the HCPs surface and how they influence the strength of CO_2 binding interactions. When more than one functional group is present, is CO_2 synergistically interacting with all the functional groups? If yes, how does this impact CO_2 adsorption? A deeper understanding of the aforementioned adsorption mechanisms is needed to develop more effective HCPs adsorbents and CO_2 photoreduction catalysts. This aspect could be investigated by synthesising a library of HCPs with different functional groups and use the approach explained in Chapter 6, which combines DFT and in-situ DRIFTS. One could explore the effect of hydroxyl, diphenylamine, and triazine functional groups alone, as well as their synergic effects on CO_2 adsorption. These functional groups have been repeatedly employed to improve CO_2 adsorption, but their synergic effect on CO_2 adsorption is much less understood.[252, 253] The obtained results could be applied not only to the design of new HCPs but to other porous adsorbents and photocatalysts such as conjugated polymers, MOFs, COFs and their derivatives (e.g. MOF-based heterojunctions).

In terms of material robustness, porous organic-based materials are more prone to degradation than traditional inorganic photocatalysts. A better understanding of the degradation process is needed as this could hinder the development of promising photocatalysts. By coupling distinct in-situ characterisation techniques (e.g. EPR and XPS), one could monitor in real-time degradation, which would support the design of more robust photocatalysts by limiting/preventing degradation. In the case of HCPs, such a study would confirm our hypothesis that degradation arises from the deterioration of methoxy groups initiated by H_2O_2 formation, and would enable the development of new strategies towards increased stability.

Overall, to bridge the gap between the currently achieved activity of photocatalysts and the one needed for real-world application, a deeper understanding of the photocatalytic, adsorption, and degradation

processes is required. I believe that combining in-situ analyses and advanced processing/computational techniques can provide unparalleled insights into these processes and help address such objective.

References

1. IEA, Renewable Energy Market Update. **2021**.

2. Kahn, A., Fermi level, work function and vacuum level. *Mater Horiz* **2016,** *3* (1), 7-10.

3. Helander, M. G.; Greiner, M. T.; Wang, Z. B.; Lu, Z. H., Pitfalls in measuring work function using photoelectron spectroscopy. *Appl Surf Sci* **2010,** *256* (8), 2602-2605.

4. Maarisetty, D.; Baral, S. S., Defect engineering in photocatalysis: formation, chemistry, optoelectronics, and interface studies. *J Mater Chem A* **2020,** *8* (36), 18560-18604.

5. Crake, A., Metal-organic frameworks based materials for photocatalytic CO2 reduction. *Mater Sci Tech-Lond* **2017,** *33* (15), 1737-1749.

6. Tu, W. G.; Zhou, Y.; Zou, Z. G., Photocatalytic Conversion of CO2 into Renewable Hydrocarbon Fuels: State-of-the-Art Accomplishment, Challenges, and Prospects. *Adv Mater* **2014,** *26* (27), 4607-4626.

7. Zhang, L. W.; Mohamed, H. H.; Dillert, R.; Bahnemann, D., Kinetics and mechanisms of charge transfer processes in photocatalytic systems: A review. *J Photoch Photobio C* **2012,** *13* (4), 263-276.

8. Marszewski, M.; Cao, S. W.; Yu, J. G.; Jaroniec, M., Semiconductor-based photocatalytic CO2 conversion. *Mater Horiz* **2015,** *2* (3), 261-278.

9. Melchionna, M.; Fornasiero, P., Updates on the Roadmap for Photocatalysis. *Acs Catal* **2020,** *10* (10), 5493-5501.

10. Kisch, H.; Bahnemann, D., Best Practice in Photocatalysis: Comparing Rates or Apparent Quantum Yields? *J Phys Chem Lett* **2015,** *6* (10), 1907-1910.

11. Qureshi, M.; Takanabe, K., Insights on Measuring and Reporting Heterogeneous Photocatalysis: Efficiency Definitions and Setup Examples. *Chem Mater* **2017,** *29* (1), 158-167.

12. Reddy, M. S. B.; Ponnamma, D.; Sadasivuni, K. K.; Kumar, B.; Abdullah, A. M., Carbon dioxide adsorption based on porous materials. *Rsc Adv* **2021,** *11* (21), 12658-12681.

13. Morales, E. M. C.; Kharisov, B. I.; Mendez-Rojas, M. A., CO2 photoreduction by MOF-derived carbon nanomaterials: A review. *Mater Today-Proc* **2021,** *46*, 2982-2997.

14. Thompson, W. A.; Fernandez, E. S.; Maroto-Valer, M. M., Review and Analysis of CO2 Photoreduction Kinetics. *Acs Sustain Chem Eng* **2020,** *8* (12), 4677-4692.

15. Schneider, D.; Mehlhorn, D.; Zeigermann, P.; Karger, J.; Valiullin, R., Transport properties of hierarchical micro-mesoporous materials. *Chem Soc Rev* **2016,** *45* (12), 3439-3467.

16. Fu, J. W.; Jiang, K. X.; Qiu, X. Q.; Yu, J. G.; Liu, M., Product selectivity of photocatalytic CO2 reduction reactions. *Mater Today* **2020,** *32*, 222-243.

17. Valenti, M.; Prasad, N. P.; Kas, R.; Bohra, D.; Ma, M.; Balasubramanian, V.; Chu, L.; Gimenez, S.; Bisquert, J.; Dam, B.; Smith, W. A., Suppressing H2 Evolution and Promoting Selective CO2 Electroreduction to CO at Low Overpotentials by Alloying Au with Pd. *Acs Catal* **2019,** *9* (4), 3527-3536.

18. Olivo, A.; Ghedini, E.; Signoretto, M.; Compagnoni, M.; Rossetti, I., Liquid vs. Gas Phase CO2 Photoreduction Process: Which Is the Effect of the Reaction Medium? *Energies* **2017,** *10* (9), 1394.

19. Schreck, M.; Niederberger, M., Photocatalytic Gas Phase Reactions. *Chem Mater* **2019,** *31* (3), 597-618.

20. Nitopi, S.; Bertheussen, E.; Scott, S. B.; Liu, X. Y.; Engstfeld, A. K.; Horch, S.; Seger, B.; Stephens, I. E. L.; Chan, K.; Hahn, C.; Norskov, J. K.; Jaramillo, T. F.; Chorkendorff, I., Progress and Perspectives of Electrochemical CO2 Reduction on Copper in Aqueous Electrolyte. *Chem Rev* **2019,** *119* (12), 7610-7672.

21. Wey Yang Teoh, A. U., Yun Hau Ng, Patrick Sit *Heterogeneous Catalysts: Advanced Design, Characterization, and Applications*. Wiely: 2021; p 768.

22. Bobadilla, L. F.; Santos, J. L.; Ivanova, S.; Odriozola, J. A.; Urakawa, A., Unravelling the Role of Oxygen Vacancies in the Mechanism of the Reverse Water-Gas Shift Reaction by Operando DRIFTS and Ultraviolet-Visible Spectroscopy. *Acs Catal* **2018,** *8* (8), 7455-7467.

23. Martensson, N.; Soderstrom, J.; Svensson, S.; Travnikova, O.; Patanen, M.; Miron, C.; Saethre, L. J.; Borve, K. J.; Thomas, T. D.; Kas, J. J.; Vila, F. D.; Rehr, J. J., On the relation between X-ray Photoelectron Spectroscopy and XAFS. *J Phys Conf Ser* **2013,** *430*.

24. Zhong, L. P.; Chen, D. K.; Zafeiratos, S., A mini review of in situ near-ambient pressure XPS studies on non-noble, late transition metal catalysts. *Catal Sci Technol* **2019,** *9* (15), 3851-3867.

25. Li, X. D.; Wang, S. M.; Li, L.; Sun, Y. F.; Xie, Y., Progress and Perspective for In Situ Studies of CO2 Reduction. *Journal of the American Chemical Society* **2020,** *142* (21), 9567-9581.

26. Tasbihi, M.; Fresno, F.; Simon, U.; Villar-Garcia, I. J.; Perez-Dieste, V.; Escudero, C.; O'Shea, V. A. D., On the selectivity of CO2 photoreduction towards CH4 using Pt/TiO2 catalysts supported on mesoporous silica. *Appl Catal B-Environ* **2018,** *239*, 68-76.

27. Chang, C.-J.; Zhu, Y.; Wang, J.; Chen, H.-C.; Tung, C.-W.; Chu, Y.-C.; Chen, H. M., In situ X-ray diffraction and X-ray absorption spectroscopy of electrocatalysts for energy conversion reactions. *J Mater Chem A* **2020,** *8* (37), 19079-19112.

28. Yuan, L.; Hung, S. F.; Tang, Z. R.; Chen, H. M.; Xiong, Y. J.; Xu, Y. J., Dynamic Evolution of Atomically Dispersed Cu Species for CO2 Photoreduction to Solar Fuels. *Acs Catal* **2019,** *9* (6), 4824-4833.

29. Park, H. R.; Pawar, A. U.; Pal, U.; Zhang, T. R.; Kang, Y. S., Enhanced solar photoreduction of CO2 to liquid fuel over rGO grafted NiO-CeO2 heterostructure nanocomposite. *Nano Energy* **2021,** *79*.

30. Wang, Z. L.; Cheng, B.; Zhang, L. Y.; Yu, J. G.; Tan, H. Y., BiOBr/NiO S-Scheme Heterojunction Photocatalyst for CO2 Photoreduction. *Sol Rrl* **2022,** *6* (1).

31. Sharma, N.; Das, T.; Kumar, S.; Bhosale, R.; Kabir, M.; Ogale, S., Photocatalytic Activation and Reduction of CO2 to CH4 over Single Phase Nano Cu3SnS4: A Combined Experimental and Theoretical Study. *Acs Appl Energ Mater* **2019,** *2* (8), 5677-5685.

32. Pang, H.; Meng, X. G.; Li, P.; Chang, K.; Zhou, W.; Wang, X.; Zhang, X. L.; Jevasuwan, W.; Fukata, N.; Wang, D. F.; Ye, J. H., Cation Vacancy-Initiated CO2 Photoreduction over ZnS for Efficient Formate Production. *Acs Energy Lett* **2019,** *4* (6), 1387-1393.

33. Wang, J. P.; Yu, Y.; Cui, J. Y.; Li, X. N.; Zhang, Y. L.; Wang, C.; Yu, X. L.; Ye, J. H., Defective g-C3N4/covalent organic framework van der Waals heterojunction toward highly efficient S-scheme CO2 photoreduction. *Appl Catal B-Environ* **2022,** *301*.

34. Wilfong, W. C.; Srikanth, C. S.; Chuang, S. S. C., In Situ ATR and DRIFTS Studies of the Nature of Adsorbed CO2 on Tetraethylenepentamine Films. *Acs Appl Mater Inter* **2014,** *6* (16), 13617-13626.

35. Ordono, M. B.; Urakawa, A., Active Surface Species Ruling Product Selectivity in Photocatalytic CO2 Reduction over Pt- or Co-Promoted TiO2. *J Phys Chem C* **2019,** *123* (7), 4140-4147.

36. Wang, L. B.; Cheng, B.; Zhang, L. Y.; Yu, J. G., In situ Irradiated XPS Investigation on S-Scheme TiO2@ZnIn2S4 Photocatalyst for Efficient Photocatalytic CO2 Reduction. *Small* **2021,** *17* (41).

37. Liu, L. J.; Zhao, C. Y.; Li, Y., Spontaneous Dissociation of CO2 to CO on Defective Surface of Cu(I)/TiO2-x Nanoparticles at Room Temperature. *J Phys Chem C* **2012,** *116* (14), 7904-7912.

38. Monakhova, Y. B.; Astakhov, S. A.; Mushtakova, S. P.; Gribov, L. A., Methods of the decomposition of spectra of various origin in the analysis of complex mixtures. *J Anal Chem+* **2011,** *66* (4), 351-362.

39. Jaumot, J.; de Juan, A.; Tauler, R., MCR-ALS GUI 2.0: New features and applications. *Chemometr Intell Lab* **2015,** *140*, 1-12.

40. Yaashikaa, P. R.; Kumar, P. S.; Varjani, S. J.; Saravanan, A., A review on photochemical, biochemical and electrochemical transformation of CO2 into value-added products. *J Co2 Util* **2019,** *33*, 131-147.

41. Pei, Y. H.; Zhong, H.; Jin, F. M., A brief review of electrocatalytic reduction of CO2-Materials, reaction conditions, and devices. *Energy Sci Eng* **2021,** *9* (7), 1012-1032.

42. Garg, S.; Li, M. R.; Weber, A. Z.; Ge, L.; Li, L. Y.; Rudolph, V.; Wang, G. X.; Rufford, T. E., Advances and challenges in electrochemical CO2 reduction processes: an engineering and design perspective looking beyond new catalyst materials. *J Mater Chem A* **2020,** *8* (4), 1511-1544.

43. Xu, L.; Xiu, Y.; Liu, F.; Liang, Y.; Wang, S., Research Progress in Conversion of CO2 to Valuable Fuels. *Molecules* **2020,** *25* (16).

44. Saravanan, A.; Kumar, P. S.; Vo, D. V. N.; Jeevanantham, S.; Bhuvaneswari, V.; Narayanan, V. A.; Yaashikaa, P. R.; Swetha, S.; Reshma, B., A comprehensive review on different approaches for CO2 utilization and conversion pathways. *Chem Eng Sci* **2021,** *236*.

45. Nguyen, T. P.; Nguyen, D. L. T.; Nguyen, V. H.; Le, T. H.; Vo, D. V. N.; Trinh, Q. T.; Bae, S. R.; Chae, S. Y.; Kim, S. Y.; Le, Q. V., Recent Advances in TiO2-Based Photocatalysts for Reduction of CO2 to Fuels. *Nanomaterials-Basel* **2020,** *10* (2).

46. Crake, A.; Christoforidis, K. C.; Kafizas, A.; Zafeiratos, S.; Petit, C., CO2 capture and photocatalytic reduction using bifunctional TiO2/MOF nanocomposites under UV-vis irradiation. *Appl Catal B-Environ* **2017,** *210*, 131-140.

47. Maity, P.; Mohammed, O. F.; Katsiev, K.; Idriss, H., Study of the Bulk Charge Carrier Dynamics in Anatase and Rutile TiO2 Single Crystals by Femtosecond Time-Resolved Spectroscopy. *J Phys Chem C* **2018,** *122* (16), 8925-8932.

48. Wang, T.; Meng, X. G.; Liu, G. G.; Chang, K.; Li, P.; Kang, Q.; Liu, L. Q.; Li, M.; Ouyang, S. X.; Ye, J. H., In situ synthesis of ordered mesoporous Co-doped TiO2 and its enhanced photocatalytic activity and selectivity for the reduction of CO2. *J Mater Chem A* **2015,** *3* (18), 9491-9501.

49. Crake, A.; Christoforidis, K. C.; Godin, R.; Moss, B.; Kafizas, A.; Zafeiratos, S.; Durrant, J. R.; Petit, C., Titanium dioxide/carbon nitride nanosheet nanocomposites for gas phase CO2 photoreduction under UV-visible irradiation. *Appl Catal B-Environ* **2019,** *242*, 369-378.

50. Ola, O.; Maroto-Valer, M. M., Review of material design and reactor engineering on TiO2 photocatalysis for CO2 reduction. *J Photoch Photobio C* **2015,** *24*, 16-42.

51. Liu, L. J.; Jiang, Y. Q.; Zhao, H. L.; Chen, J. T.; Cheng, J. L.; Yang, K. S.; Li, Y., Engineering Coexposed {001} and {101} Facets in Oxygen-Deficient TiO2 Nanocrystals for Enhanced CO2 Photoreduction under Visible Light. *Acs Catal* **2016,** *6* (2), 1097-1108.

52. Wang, S. B.; Han, X.; Zhang, Y. H.; Tian, N.; Ma, T. Y.; Huang, H. W., Inside-and-Out Semiconductor Engineering for CO2 Photoreduction: From Recent Advances to New Trends. *Small Struct* **2021,** *2* (1).

53. Nunez, J.; O'Shea, V. A. D.; Jana, P.; Coronado, J. M.; Serrano, D. P., Effect of copper on the performance of ZnO and ZnO1-xNx oxides as CO2 photoreduction catalysts. *Catal Today* **2013,** *209*, 21-27.

54. Wang, S. B.; Wang, X. C., Photocatalytic CO2 reduction by CdS promoted with a zeolitic imidazolate framework. *Appl Catal B-Environ* **2015,** *162*, 494-500.

55. Yang, K. H.; Yang, Z. Z.; Zhang, C.; Gu, Y. L.; Wei, J. J.; Li, Z. H.; Ma, C.; Yang, X.; Song, K. X.; Li, Y. M.; Fang, Q. Z.; Zhou, J. W., Recent advances in CdS-based photocatalysts for CO2 photocatalytic conversion. *Chem Eng J* **2021,** *418*, 129344.

56. Navalon, S.; Dhakshinamoorthy, A.; Alvaro, M.; Garcia, H., Photocatalytic CO2 Reduction using Non-Titanium Metal Oxides and Sulfides. *Chemsuschem* **2013,** *6* (4), 562-577.

57. Chen, S. S.; Ma, G. J.; Wang, Q.; Sun, S.; Hisatomi, T.; Higashi, T.; Wang, Z.; Nakabayashi, M.; Shibata, N.; Pan, Z. H.; Hayashi, T.; Minegishi, T.; Takata, T.; Domen, K.,

Metal selenide photocatalysts for visible-light-driven Z-scheme pure water splitting. *J Mater Chem A* **2019,** *7* (13), 7415-7422.

58. Guo, J. H.; Dao, X. Y.; Sun, W. Y., An iron-nitrogen doped carbon and CdS hybrid catalytic system for efficient CO2 photochemical reduction. *Chem Commun* **2021,** *57* (16), 2033-2036.

59. Ismael, M.; Wu, Y., A mini-review on the synthesis and structural modification of g-C3N4-based materials, and their applications in solar energy conversion and environmental remediation. *Sustain Energ Fuels* **2019,** *3* (11), 2907-2925.

60. Thomas, A.; Fischer, A.; Goettmann, F.; Antonietti, M.; Muller, J. O.; Schlogl, R.; Carlsson, J. M., Graphitic carbon nitride materials: variation of structure and morphology and their use as metal-free catalysts. *J Mater Chem* **2008,** *18* (41), 4893-4908.

61. Yang, S.; Gong, Y.; Zhang, J.; Zhan, L.; Ma, L.; Fang, Z.; Vajtai, R.; Wang, X.; Ajayan, P. M., Exfoliated graphitic carbon nitride nanosheets as efficient catalysts for hydrogen evolution under visible light. *Adv Mater* **2013,** *25* (17), 2452-6.

62. Ping Niu, L. Z., Gang Liu, Hui-Ming Cheng, Graphene-Like Carbon Nitride Nanosheets for Improved Photocatalytic Activities. *Advanced functional materials* **2012,** *22* (22), 4763-4770.

63. Zhang, X.; Xie, X.; Wang, H.; Zhang, J.; Pan, B.; Xie, Y., Enhanced photoresponsive ultrathin graphitic-phase C3N4 nanosheets for bioimaging. *J Am Chem Soc* **2013,** *135* (1), 18-21.

64. Li, J. Y.; Wang, X. H.; Huang, L.; Tian, L.; Shalom, M.; Xiong, C. Y.; Zhang, H. J.; Jia, Q. L.; Zhang, S. W.; Liang, F., Ultrathin mesoporous graphitic carbon nitride nanosheets with functional cyano group decoration and nitrogen-vacancy defects for an efficient selective CO2 photoreduction. *Nanoscale* **2021,** *13* (29), 12634-12641.

65. Wang, Y. L.; Tian, Y.; Yan, L. K.; Su, Z. M., DFT Study on Sulfur-Doped g-C3N4 Nanosheets as a Photocatalyst for CO2 Reduction Reaction. *J Phys Chem C* **2018,** *122* (14), 7712-7719.

66. Shen, M.; Zhang, L. X.; Wang, M.; Tian, J. J.; Jin, X. X.; Guo, L. M.; Wang, L. Z.; Shi, J. L., Carbon-vacancy modified graphitic carbon nitride: enhanced CO2 photocatalytic reduction performance and mechanism probing. *J Mater Chem A* **2019,** *7* (4), 1556-1563.

67. Tu, W. G.; Xu, Y.; Wang, J. J.; Zhang, B. W.; Zhou, T. H.; Yin, S. M.; Wu, S. Y.; Li, C. M.; Huang, Y. Z.; Zhou, Y.; Zou, Z. G.; Robertson, J.; Kraft, M.; Xu, R., Investigating the Role of Tunable Nitrogen Vacancies in Graphitic Carbon Nitride Nanosheets for Efficient Visible-Light-Driven H-2 Evolution and CO2 Reduction. *Acs Sustain Chem Eng* **2017,** *5* (8), 7260-7268.

68. Eddaoudi, M.; Moler, D. B.; Li, H. L.; Chen, B. L.; Reineke, T. M.; O'Keeffe, M.; Yaghi, O. M., Modular chemistry: Secondary building units as a basis for the design of highly porous and robust metal-organic carboxylate frameworks. *Accounts Chem Res* **2001,** *34* (4), 319-330.

69. Nemiwal, M.; Subbaramaiah, V.; Zhang, T. C.; Kumar, D., Recent advances in visible-light-driven carbon dioxide reduction by metal-organic frameworks. *Sci Total Environ* **2021,** *762*.

70. Liu, B. T.; Vikrant, V.; Kim, K. H.; Kumar, V.; Kailasa, S. K., Critical role of water stability in metal-organic frameworks and advanced modification strategies for the extension of their applicability. *Environ Sci-Nano* **2020,** *7* (5), 1319-1347.

71. Park, H.; Reddy, D. A.; Kim, Y.; Ma, R.; Choi, J.; Kim, T. K.; Lee, K. S., Zeolitic imidazolate framework-67 (ZIF-67) rhombic dodecahedrons as full-spectrum light harvesting photocatalyst for environmental remediation. *Solid State Sci* **2016,** *62*, 82-89.

72. Subudhi, S.; Rath, D.; Parida, K. M., A mechanistic approach towards the photocatalytic organic transformations over functionalised metal organic frameworks: a review. *Catal Sci Technol* **2018,** *8* (3), 679-696.

73. Shen, L. J.; Liang, R. W.; Wu, L., Strategies for engineering metal-organic frameworks as efficient photocatalysts. *Chinese J Catal* **2015,** *36* (12), 2071-2088.

74. Hendon, C. H.; Tiana, D.; Fontecave, M.; Sanchez, C.; D'arras, L.; Sassoye, C.; Rozes, L.; Mellot-Draznieks, C.; Walsh, A., Engineering the Optical Response of the Titanium-MIL-125 Metal-Organic Framework through Ligand Functionalization. *Journal of the American Chemical Society* **2013,** *135* (30), 10942-10945.

75. Logan, M. W.; Ayad, S.; Adamson, J. D.; Dilbeck, T.; Kenneth, H. B.; Uribe-Romo, F. J., Systematic variation of the optical bandgap in titanium based isoreticular metal-organic frameworks for photocatalytic reduction of CO2 under blue light. *J Mater Chem A* **2017,** *5* (23), 11854-11863.

76. Xu, H. Q.; Hu, J. H.; Wang, D. K.; Li, Z. H.; Zhang, Q.; Luo, Y.; Yu, S. H.; Jiang, H. L., Visible-Light Photoreduction of CO2 in a Metal-Organic Framework: Boosting Electron-Hole Separation via Electron Trap States. *Journal of the American Chemical Society* **2015,** *137* (42), 13440-13443.

77. Wang, M.; Liu, J. X.; Guo, C. M.; Gao, X. S.; Gong, C. H.; Wang, Y.; Liu, B.; Li, X. X.; Gurzadyan, G. G.; Sun, L. C., Metal-organic frameworks (ZIF-67) as efficient cocatalysts for photocatalytic reduction of CO2: the role of the morphology effect. *J Mater Chem A* **2018,** *6* (11), 4768-4775.

78. Sun, D. R.; Liu, W. J.; Qiu, M.; Zhang, Y. F.; Li, Z. H., Introduction of a mediator for enhancing photocatalytic performance via post-synthetic metal exchange in metal-organic frameworks (MOFs) (vol 51, pg 2056, 2015). *Chem Commun* **2015,** *51* (53), 10765-10765.

79. Cheng, Y. Z.; Ding, X. S.; Han, B. H., Porous Organic Polymers for Photocatalytic Carbon Dioxide Reduction. *Chemphotochem* **2021,** *5* (5), 406-417.

80. You, J. H.; Zhao, Y.; Wang, L.; Bao, W. T., Recent developments in the photocatalytic applications of covalent organic frameworks: A review. *J Clean Prod* **2021,** *291*.

81. Li, H.; Wang, L. P.; Yu, G., Covalent organic frameworks: Design, synthesis, and performance for photocatalytic applications. *Nano Today* **2021,** *40*, 101247.

82. Li, Z. P.; Feng, X.; Zou, Y. C.; Zhang, Y. W.; Xia, H.; Liu, X. M.; Mu, Y., A 2D azine-linked covalent organic framework for gas storage applications. *Chem Commun* **2014,** *50* (89), 13825-13828.

83. Xu, R.; Wang, X. S.; Zhao, H.; Lin, H.; Huang, Y. B.; Cao, R., Rhenium-modified porous covalent triazine framework for highly efficient photocatalytic carbon dioxide reduction in a solid-gas system. *Catal Sci Technol* **2018,** *8* (8), 2224-2230.

84. Lei, K.; Wang, D.; Ye, L. Q.; Kou, M. P.; Deng, Y.; Ma, Z. Y.; Wang, L.; Kong, Y., A Metal-Free Donor-Acceptor Covalent Organic Framework Photocatalyst for Visible-Light-Driven Reduction of CO2 with H2O. *Chemsuschem* **2020,** *13* (7), 1725-1729.

85. Barawi, M.; Collado, L.; Gomez-Mendoza, M.; Oropeza, F. E.; Liras, M.; O'Shea, V. A. P., Conjugated Porous Polymers: Ground-Breaking Materials for Solar Energy Conversion. *Adv Energy Mater* **2021,** *11* (43).

86. Sprick, R. S.; Jiang, J. X.; Bonillo, B.; Ren, S. J.; Ratvijitvech, T.; Guiglion, P.; Zwijnenburg, M. A.; Adams, D. J.; Cooper, A. I., Tunable Organic Photocatalysts for Visible-Light-Driven Hydrogen Evolution. *Journal of the American Chemical Society* **2015,** *137* (9), 3265-3270.

87. Yang, C.; Huang, W.; da Silva, L. C.; Zhang, K. A. I.; Wang, X. C., Functional Conjugated Polymers for CO2 Reduction Using Visible Light. *Chem-Eur J* **2018,** *24* (66), 17454-17458.

88. Dai, C. H.; Zhong, L. X.; Gong, X. Z.; Zeng, L.; Xue, C.; Li, S. Z.; Liu, B., Triphenylamine based conjugated microporous polymers for selective photoreduction of CO2 to CO under visible light. *Green Chem* **2019,** *21* (24), 6606-6610.

89. Liang, H. P.; Acharjya, A.; Anito, D. A.; Vogl, S.; Wang, T. X.; Thomas, A.; Han, B. H., Rhenium-Metalated Polypyridine-Based Porous Polycarbazoles for Visible-Light CO2 Photoreduction. *Acs Catal* **2019,** *9* (5), 3959.

90. Dawson, R.; Ratvijitvech, T.; Corker, M.; Laybourn, A.; Khimyak, Y. Z.; Cooper, A. I.; Adams, D. J., Microporous copolymers for increased gas selectivity. *Polym Chem-Uk* **2012,** *3* (8), 2034-2038.

91. Ramezanipour Penchah, H.; Ghanadzadeh Gilani, H.; Ghaemi, A., CO2, N2, and H2 Adsorption by Hyper-Cross-Linked Polymers and Their Selectivity Evaluation by Gas–Solid Equilibrium. *Journal of Chemical & Engineering Data* **2020,** *65* (10), 4905-4913.

92. Wang, S. L.; Xu, M.; Peng, T. Y.; Zhang, C. X.; Li, T.; Hussain, I.; Wang, J. Y.; Tan, B. E., Porous hypercrosslinked polymer-TiO2-graphene composite photocatalysts for visible-light-driven CO2 conversion. *Nat Commun* **2019,** *10*.

93. Sun, Z. X.; Wang, H. Q.; Wu, Z. B. A.; Wang, L. Z., g-C3N4 based composite photocatalysts for photocatalytic CO2 reduction. *Catal Today* **2018,** *300*, 160-172.

94. Li, R.; Zhang, W.; Zhou, K., Metal-Organic-Framework-Based Catalysts for Photoreduction of CO2. *Adv Mater* **2018,** *30* (35), 1705512.

95. Lin, H. X.; Chen, C. P.; Zhou, T. H.; Zhang, J., Two-Dimensional Covalent-Organic Frameworks for Photocatalysis: The Critical Roles of Building Block and Linkage. *Sol Rrl* **2021,** *5* (6).

96. Gopalakrishnan, V. N.; Nguyen, D. T.; Becerra, J.; Sakar, M.; Ahad, J. M. E.; Jautzy, J. J.; Mindorlf, L. M.; Beland, F.; Do, T. O., Manifestation of an Enhanced Photoreduction of

CO2 to CO over the In Situ Synthesized rGO-Covalent Organic Framework under Visible Light Irradiation. *Acs Appl Energ Mater* **2021,** *4* (6), 6005-6014.

97. Wang, S.; Hai, X.; Ding, X.; Jin, S.; Xiang, Y.; Wang, P.; Jiang, B.; Ichihara, F.; Oshikiri, M.; Meng, X.; Li, Y.; Matsuda, W.; Ma, J.; Seki, S.; Wang, X.; Huang, H.; Wada, Y.; Chen, H.; Ye, J., Intermolecular cascaded π-conjugation channels for electron delivery powering CO2 photoreduction. *Nat Commun* **2020,** *11* (1), 1149.

98. Low, J. X.; Jiang, C.; Cheng, B.; Wageh, S.; Al-Ghamdi, A. A.; Yu, J. G., A Review of Direct Z-Scheme Photocatalysts. *Small Methods* **2017,** *1* (5).

99. Ikreedeegh, R. R.; Tahir, M., A critical review in recent developments of metal-organic-frameworks (MOFs) with band engineering alteration for photocatalytic CO2 reduction to solar fuels. *J Co2 Util* **2021,** *43*, 101381.

100. Taraka, T. P. Y.; Gautam, A.; Jain, S. L.; Bojja, S.; Pal, U., Controlled addition of Cu/Zn in hierarchical CuO/ZnO p-n heterojunction photocatalyst for high photoreduction of CO2 to MeOH. *J Co2 Util* **2019,** *31*, 207-214.

101. Jin, J.; Yu, J. G.; Guo, D. P.; Cui, C.; Ho, W. K., A Hierarchical Z-Scheme CdS-WO3 Photocatalyst with Enhanced CO2 Reduction Activity. *Small* **2015,** *11* (39), 5262-5271.

102. Zhang, L.; Zhang, L. J.; Chen, Y. M.; Zheng, Y. K.; Guo, J.; Wan, S. L.; Wang, S.; Ngaw, C. K.; Lin, J. D.; Wang, Y., CdS/ZnO: A Multipronged Approach for Efficient Reduction of Carbon Dioxide under Visible Light Irradiation. *Acs Sustain Chem Eng* **2020,** *8* (13), 5270-5277.

103. Aguirre, M. E.; Zhou, R. X.; Eugene, A. J.; Guzman, M. I.; Grela, M. A., Cu2O/TiO2 heterostructures for CO2 reduction through a direct Z-scheme: Protecting Cu2O from photocorrosion. *Appl Catal B-Environ* **2017,** *217*, 485-493.

104. Beigi, A. A.; Fatemi, S.; Salehi, Z., Synthesis of nanocomposite CdS/TiO2 and investigation of its photocatalytic activity for CO2 reduction to CO and CH4 under visible light irradiation. *J Co2 Util* **2014,** *7*, 23-29.

105. Qin, S. Y.; Xin, F.; Liu, Y. D.; Yin, X. H.; Ma, W., Photocatalytic reduction of CO2 in methanol to methyl formate over CuO-TiO2 composite catalysts. *J Colloid Interf Sci* **2011,** *356* (1), 257-261.

106. Wen, J. Q.; Xie, J.; Chen, X. B.; Li, X., A review on g-C3N4-based photocatalysts. *Appl Surf Sci* **2017,** *391*, 72-123.

107. Ong, W. J., 2D/2D Graphitic Carbon Nitride (g-C3N4) Heterojunction Nanocomposites for Photocatalysis: Why Does Face-to-Face Interface Matter? *Front Mater* **2017,** *4*.

108. Zhang, M.; Lu, M.; Lang, Z. L.; Liu, J.; Liu, M.; Chang, J. N.; Li, L. Y.; Shang, L. J.; Wang, M.; Li, S. L.; Lan, Y. Q., Semiconductor/Covalent-Organic-Framework Z-Scheme Heterojunctions for Artificial Photosynthesis. *Angew Chem Int Edit* **2020,** *59* (16), 6500-6506.

109. Vu, N. N.; Kaliaguine, S.; Do, T. O., Synthesis of the g-C3N4/CdS Nanocomposite with a Chemically Bonded Interface for Enhanced Sunlight-Driven CO2 Photoreduction. *Acs Appl Energ Mater* **2020,** *3* (7), 6422-6433.

110. Ohno, T.; Murakami, N.; Koyanagi, T.; Yang, Y., Photocatalytic reduction of CO2 over a hybrid photocatalyst composed of WO3 and graphitic carbon nitride (g-C3N4) under visible light. *J Co2 Util* **2014,** *6*, 17-25.

111. He, Y. M.; Wang, Y.; Zhang, L. H.; Teng, B. T.; Fan, M. H., High-efficiency conversion of CO2 to fuel over ZnO/g-C3N4 photocatalyst. *Appl Catal B-Environ* **2015,** *168*, 1-8.

112. Ong, W. J.; Tan, L. L.; Chai, S. P.; Yong, S. T.; Mohamed, A. R., Surface charge modification via protonation of graphitic carbon nitride (g-C3N4) for electrostatic self-assembly construction of 2D/2D reduced graphene oxide (rGO)/g-C3N4 nanostructures toward enhanced photocatalytic reduction of carbon dioxide to methane. *Nano Energy* **2015,** *13*, 757-770.

113. Wang, M.; Shen, M.; Zhang, L. X.; Tian, J. J.; Jin, X. X.; Zhou, Y. J.; Shi, J. L., 2D-2D MnO2/g-C3N4 heterojunction photocatalyst: In-situ synthesis and enhanced CO2 reduction activity. *Carbon* **2017,** *120*, 23-31.

114. Guo, S.; Yang, P.; Zhao, Y. F.; Yu, X. X.; Wu, Y. Y.; Zhang, H. Y.; Yu, B.; Han, B. X.; George, M. W.; Liu, Z. M., Direct Z-Scheme Heterojunction of SnS2/Sulfur-Bridged Covalent Triazine Frameworks for Visible-Light-Driven CO2 Photoreduction. *Chemsuschem* **2020,** *13* (23), 6278-6283.

115. Qian, Y. T.; Zhang, F. F.; Pang, H., A Review of MOFs and Their Composites-Based Photocatalysts: Synthesis and Applications. *Adv Funct Mater* **2021,** *31* (37).

116. Hong, J. D.; Chen, C. P.; Bedoya, F. E.; Kelsall, G. H.; O'Hare, D.; Petit, C., Carbon nitride nanosheet/metal-organic framework nanocomposites with synergistic photocatalytic activities. *Catal Sci Technol* **2016,** *6* (13), 5042-5051.

117. Wang, Y. N.; Guo, L. N.; Zeng, Y. Q.; Guo, H. W.; Wan, S. P.; Ou, M.; Zhang, S. L.; Zhong, Q., Amino-Assisted NH2-UiO-66 Anchored on Porous g-C3N4 for Enhanced Visible-Light-Driven CO2 Reduction. *Acs Appl Mater Inter* **2019,** *11* (34), 30673-30681.

118. Mu, Q. Q.; Zhu, W.; Li, X.; Zhang, C. F.; Su, Y. H.; Lian, Y. B.; Qi, P. W.; Deng, Z.; Zhang, D.; Wang, S.; Zhu, X.; Peng, Y., Electrostatic charge transfer for boosting the photocatalytic CO2 reduction on metal centers of 2D MOF/rGO heterostructure. *Appl Catal B-Environ* **2020,** *262*.

119. Peng, H. J.; Zhu, L.; Wang, Y. L.; Chao, H. Y.; Jiang, L.; Qiao, Z. P., CdS/ZIF-67 nanocomposites with enhanced performance for visible light CO2 photoreduction *Inorg Chem Commun* **2020,** *117*.

120. Wang, H. J.; Wu, D. P.; Yang, C.; Lu, H.; Gao, Z. Y.; Xu, F.; Jiang, K., Multi-functional amorphous TiO2 layer on ZIF-67 for enhanced CO2 photoreduction performances under visible light. *J Co2 Util* **2019,** *34*, 411-421.

121. Wang, S. B.; Lin, J. L.; Wang, X. C., Semiconductor-redox catalysis promoted by metal-organic frameworks for CO2 reduction. *Phys Chem Chem Phys* **2014,** *16* (28), 14656-14660.

122. Xu, G. L.; Zhang, H. B.; Wei, J.; Zhang, H. X.; Wu, X.; Li, Y.; Li, C. S.; Zhang, J.; Ye, J. H., Integrating the g-C3N4 Nanosheet with B-H Bonding Decorated Metal-Organic Framework for CO2 Activation and Photoreduction. *Acs Nano* **2018,** *12* (6), 5333-5340.

123. Dao, X. Y.; Xie, X. F.; Guo, J. H.; Zhang, X. Y.; Kang, Y. S.; Sun, W. Y., Boosting Photocatalytic CO2 Reduction Efficiency by Heterostructures of NH2-MIL-101(Fe)/g-C3N4. *Acs Appl Energ Mater* **2020,** *3* (4), 3946-3954.

124. Li, R.; Hu, J. H.; Deng, M. S.; Wang, H. L.; Wang, X. J.; Hu, Y. L.; Jiang, H. L.; Jiang, J.; Zhang, Q.; Xie, Y.; Xiong, Y. J., Integration of an Inorganic Semiconductor with a Metal-Organic Framework: A Platform for Enhanced Gaseous Photocatalytic Reactions. *Adv Mater* **2014,** *26* (28), 4783-+.

125. Wang, M. T.; Wang, D. K.; Li, Z. H., Self-assembly of CPO-27-Mg/TiO2 nanocomposite with enhanced performance for photocatalytic CO2 reduction. *Appl Catal B-Environ* **2016,** *183*, 47-52.

126. Yan, S. S.; Ouyang, S. X.; Xu, H.; Zhao, M.; Zhang, X. L.; Ye, J. H., Co-ZIF-9/TiO2 nanostructure for superior CO2 photoreduction activity. *J Mater Chem A* **2016,** *4* (39), 15126-15133.

127. Hu, J. M.; Ding, J.; Zhong, Q., In situ fabrication of amorphous TiO2/NH2-MIL-125(Ti) for enhanced photocatalytic CO2 into CH4 with H2O under visible-light irradiation. *J Colloid Interf Sci* **2020,** *560*, 857-865.

128. Bunaciu, A. A.; Udristioiu, E. G.; Aboul-Enein, H. Y., X-Ray Diffraction: Instrumentation and Applications. *Crit Rev Anal Chem* **2015,** *45* (4), 289-299.

129. Schukraft, G. E. M.; Woodward, R. T.; Kumar, S.; Sachs, M.; Eslava, S.; Petit, C., Hypercrosslinked Polymers as a Photocatalytic Platform for Visible-Light-Driven CO2 Photoreduction Using H2O. *Chemsuschem* **2021,** *14* (7), 1720-1727.

130. Ul-Hamid, A., *A Beginners' Guide to Scanning Electron Microscopy*. Springer International Publishing: 2018.

131. Crake, A.; Christoforidis, K. C.; Gregg, A.; Moss, B.; Kafizas, A.; Petit, C., The Effect of Materials Architecture in TiO2/MOF Composites on CO2 Photoreduction and Charge Transfer. *Small* **2019,** *15* (11), 1805473.

132. Joseph D. Menczel, R. B. P., *Thermal Analysis of Polymers: Fundamentals and Applications*. John Wiley & Sons: 2008.

133. Duer, M. J., *Solid-State NMR Spectroscopy Principles and Applications*. Wiely: 2001; p 567.

134. Armenta, M. d. l. G. S., *Green analytical chemistry : theory & practice*. Elsevier: 2011.

135. van der Heide, P., *X-ray Photoelectron Spectroscopy: An introduction to Principles and Practices*. Wiley: 2011.

136. L'Hermitte, A.; Dawson, D. M.; Ferrer, P.; Roy, K.; Held, G.; Tian, T.; Ashbrook, S. E.; Petit, C., Formation Mechanism and Porosity Development in Porous Boron Nitride. *J Phys Chem C* **2021,** *125* (49), 27429-27439.

137. Shankar R, L.-P. D., Mistry E, Nevjestić I, Heutz S, Petit C., Water-Stable Boron-Doped Boron Nitride Photocatalyst for Visible Light-Driven H2 Evolution and CO2 Photoreduction. *ChemRxiv* **2020**

138. Wang, Y.; Wang, X. C.; Antonietti, M., Polymeric Graphitic Carbon Nitride as a Heterogeneous Organocatalyst: From Photochemistry to Multipurpose Catalysis to Sustainable Chemistry. *Angew Chem Int Edit* **2012,** *51* (1), 68-89.

139. Smith, B. C., *Fundamentals of Fourier Transform Infrared Spectroscopy*. CRC Press: 2011.

140. Schukraft, G. E. M.; Moss, B.; Kafizas, A. G.; Petit, C., Effect of Band Bending in Photoactive MOF-Based Heterojunctions. *Acs Appl Mater Inter* **2022,** *14* (17), 19342–19352.

141. Carter, D. B. W. B., *Transmission Electron Microscopy*. Springer: 2009.

142. Sing, K., The use of nitrogen adsorption for the characterisation of porous materials. *Colloid Surface A* **2001,** *187*, 3-9.

143. Walton, K. S.; Snurr, R. Q., Applicability of the BET method for determining surface areas of microporous metal-organic frameworks. *Journal of the American Chemical Society* **2007,** *129* (27), 8552-8556.

144. Brunauer, S. E., P. H.; Teller, E, Adsorption of Gases in Multimolecular Layers. *Journal of the American Chemical Society* **1938,** *60* (2), 309-319.

145. Françoise Rouquerol, J. R. a. K. S., *Adsorption by Powders and Porous Solids*. Elsevier: 1999.

146. Chen, S. G.; Yang, R. T., Theoretical Basis for the Potential-Theory Adsorption-Isotherms - the Dubinin-Radushkevich and Dubinin-Astakhov Equations. *Langmuir* **1994,** *10* (11), 4244-4249.

147. Mirabella, F. M., *Modern Techniques in Applied Molecular Spectroscopy*. Wiely: 1998.

148. Mirabella, F. M., Diffuse Reflectance Spectroscopy. In *Modern Techniques in Applied Molecular Spectroscopy*, Wiley: 1998.

149. kubelka, P. M., F.Z, Ein Beitrag zur Optik der Farbanstriche (Contribution to the optic of paint). *Zeitschrift fur Technische Physik* **1931,** *12*, 593-601.

150. Dzimbeg-Malcic, V.; Barbaric-Mikocevic, Z.; Itric, K., Kubelka-Munk Theory in Describing Optical Properties of Paper (I). *Teh Vjesn* **2011,** *18* (1), 117-124.

151. Dzimbeg-Malcic, V.; Barbaric-Mikocevic, Z.; Itric, K., Kubelka-Munk Theory in Describing Optical Properties of Paper (Ii). *Teh Vjesn* **2012,** *19* (1), 191-196.

152. de Juan, A.; Jaumot, J.; Tauler, R. A., Multivariate Curve Resolution (MCR). Solving the mixture analysis problem. *Anal Methods-Uk* **2014,** *6* (14), 4964-4976.

153. Ruckebusch, C.; Blanchet, L., Multivariate curve resolution: A review of advanced and tailored applications and challenges. *Anal Chim Acta* **2013,** *765*, 28-36.

154. Voronov, A.; Urakawa, A.; van Beek, W.; Tsakoumis, N. E.; Emerich, H.; Ronning, M., Multivariate curve resolution applied to in situ X-ray absorption spectroscopy data: An efficient tool for data processing and analysis. *Anal Chim Acta* **2014,** *840*, 20-27.

155. Shankar R, H. A., Kerherve G, Petit C, Band Positioning in Boron Nitride and Metal-Free Photocatalysts via Photoelectron- and UV-Vis Diffuse Reflectance Spectroscopy. *ChemRxiv* **2020**.

156. Becker, W., Fluorescence lifetime imaging by multi-dimensional time correlated single photon counting. *Medical Photonics* **2015,** *27*, 41-61.

157. Wei, L. P.; Yan, W. R.; Ho, D., Recent Advances in Fluorescence Lifetime Analytical Microsystems: Contact Optics and CMOS Time-Resolved Electronics. *Sensors-Basel* **2017,** *17* (12).

158. Dias, E. M.; Christoforidis, K. C.; Francas, L.; Petit, C., Tuning Thermally Treated Graphitic Carbon Nitride for H-2 Evolution and CO2 Photoreduction: The Effects of Material Properties and Mid Gap States. *Acs Appl Energ Mater* **2018,** *1* (11), 6524-6534.

159. Wang, C. C.; Zhang, Y. Q.; Li, J.; Wang, P., Photocatalytic CO2 reduction in metal-organic frameworks: A mini review. *J Mol Struct* **2015,** *1083*, 127-136.

160. White, J. L.; Baruch, M. F.; Pander, J. E.; Hu, Y.; Fortmeyer, I. C.; Park, J. E.; Zhang, T.; Liao, K.; Gu, J.; Yan, Y.; Shaw, T. W.; Abelev, E.; Bocarsly, A. B., Light-Driven Heterogeneous Reduction of Carbon Dioxide: Photocatalysts and Photoelectrodes. *Chem Rev* **2015,** *115* (23), 12888-12935.

161. Izumi, Y., Recent advances in the photocatalytic conversion of carbon dioxide to fuels with water and/or hydrogen using solar energy and beyond. *Coordin Chem Rev* **2013,** *257* (1), 171-186.

162. Xu, H.; Ouyang, S. X.; Liu, L. Q.; Reunchan, P.; Umezawa, N.; Ye, J. H., Recent advances in TiO2-based photocatalysis. *J Mater Chem A* **2014,** *2* (32), 12642-12661.

163. Xiong, Z.; Lei, Z.; Xu, Z. W.; Chen, X. X.; Gong, B. G.; Zhao, Y. C.; Zhao, H. B.; Zhang, J. Y.; Zheng, C. G., Flame spray pyrolysis synthesized ZnO/CeO2 nanocomposites for enhanced CO2 photocatalytic reduction under UV-Vis light irradiation. *J Co2 Util* **2017,** *18*, 53-61.

164. Yang, Y. H.; Zhan, F. Q.; Li, H.; Liu, W. H.; Yu, S., In situ Sn-doped WO3 films with enhanced photoelectrochemical performance for reducing CO2 into formic acid. *J Solid State Electr* **2017,** *21* (8), 2231-2240.

165. Reli, M.; Kobielusz, M.; Matejova, L.; Danis, S.; Macyk, W.; Obalova, L.; Kustrowski, P.; Rokicinska, A.; Koci, K., TiO2 Processed by pressurized hot solvents as a novel photocatalyst for photocatalytic reduction of carbon dioxide. *Appl Surf Sci* **2017,** *391*, 282-287.

166. Koci, K.; Praus, P.; Edelmannova, M.; Ambrozova, N.; Troppova, I.; Fridrichova, D.; Slowik, G.; Ryczkowski, J., Photocatalytic Reduction of CO2 Over CdS, ZnS and Core/Shell CdS/ZnS Nanoparticles Deposited on Montmorillonite. *J Nanosci Nanotechno* **2017,** *17* (6), 4041-4047.

167. Schneider, J.; Matsuoka, M.; Takeuchi, M.; Zhang, J. L.; Horiuchi, Y.; Anpo, M.; Bahnemann, D. W., Understanding TiO2 Photocatalysis: Mechanisms and Materials. *Chem Rev* **2014,** *114* (19), 9919-9986.

168. Ong, W. J.; Tan, L. L.; Ng, Y. H.; Yong, S. T.; Chai, S. P., Graphitic Carbon Nitride (g-C3N4)-Based Photocatalysts for Artificial Photosynthesis and Environmental Remediation: Are We a Step Closer To Achieving Sustainability? *Chem Rev* **2016,** *116* (12), 7159-7329.

169. Liu, Q.; Low, Z. X.; Li, L. X.; Razmjou, A.; Wang, K.; Yao, J. F.; Wang, H. T., ZIF-8/Zn2GeO4 nanorods with an enhanced CO2 adsorption property in an aqueous medium for photocatalytic synthesis of liquid fuel. *J Mater Chem A* **2013,** *1* (38), 11563-11569.

170. Kampouri, S.; Ebrahim, F. M.; Fumanal, M.; Nord, M.; Schouwink, P. A.; Elzein, R.; Addou, R.; Herman, G. S.; Smit, B.; Ireland, C. P.; Stylianou, K. C., Enhanced Visible-Light-Driven Hydrogen Production through MOF/MOF Heterojunctions. *Acs Appl Mater Inter* **2021,** *13* (12), 14239-14247.

171. Xu, M.-L.; Jiang, X.-J.; Li, J.-R.; Wang, F.-J.; Li, K.; Cheng, X., Self-Assembly of a 3D Hollow BiOBr@Bi-MOF Heterostructure with Enhanced Photocatalytic Degradation of Dyes. *Acs Appl Mater Inter* **2021,** *13* (47), 56171–56180.

172. Zhu, C.; He, Q.; Yao, H.; Le, S.; Chen, W.; Chen, C.; Wang, S.; Duan, X., Amino-functionalized NH2-MIL-125(Ti)-decorated hierarchical flowerlike Znln2S4 for boosted visible-light photocatalytic degradation. *Environ Res* **2021,** *204*, 112368.

173. Kampouri, S.; Ireland, C. P.; Valizadeh, B.; Oveisi, E.; Schouwink, P. A.; Mensi, M.; Stylianou, K. C., Mixed-Phase MOF-Derived Titanium Dioxide for Photocatalytic Hydrogen Evolution: The Impact of the Templated Morphology. *Acs Appl Energ Mater* **2018,** *1* (11), 6541-6548.

174. Gong, H. M.; Zhang, X. J.; Wang, G. R.; Liu, Y.; Li, Y. B.; Jin, Z. L., Dodecahedron ZIF-67 anchoring ZnCdS particles for photocatalytic hydrogen evolution. *Mol Catal* **2020,** *485*, 110832.

175. Cao, Y.; Wang, G. R.; Liu, H.; Li, Y. B.; Jin, Z. L.; Ma, Q. X., Regular octahedron Cu-MOFs modifies Mn0.05Cd0.95S nanoparticles to form a S-scheme heterojunction for photocatalytic hydrogen evolution. *Int J Hydrogen Energ* **2021,** *46* (10), 7230-7240.

176. Zhou, A. W.; Dou, Y. B.; Zhao, C.; Zhou, J.; Wu, X. Q.; Li, J. R., A leaf-branch TiO2/carbon@MOF composite for selective CO2 photoreduction. *Appl Catal B-Environ* **2020,** *264*, 118519.

177. Zhang, J. C.; Zhang, T. C.; Yu, D. B.; Xiao, K. S.; Hong, Y., Transition from ZIF-L-Co to ZIF-67: a new insight into the structural evolution of zeolitic imidazolate frameworks (ZIFs) in aqueous systems. *Crystengcomm* **2015,** *17* (43), 8212-8215.

178. Xiao, X. F.; He, C. T.; Zhao, S. L.; Li, J.; Lin, W. S.; Yuan, Z. K.; Zhang, Q.; Wang, S. Y.; Dai, L. M.; Yu, D. S., A general approach to cobalt-based homobimetallic phosphide ultrathin nanosheets for highly efficient oxygen evolution in alkaline media. *Energ Environ Sci* **2017,** *10* (4), 893-899.

179. Kim, S. N.; Kim, J.; Kim, H. Y.; Cho, H. Y.; Ahn, W. S., Adsorption/catalytic properties of MIL-125 and NH2-MIL-125. *Catal Today* **2013,** *204*, 85-93.

180. Wang, X. C.; Maeda, K.; Thomas, A.; Takanabe, K.; Xin, G.; Carlsson, J. M.; Domen, K.; Antonietti, M., A metal-free polymeric photocatalyst for hydrogen production from water under visible light. *Nat Mater* **2009,** *8* (1), 76-80.

181. Yang, S. B.; Gong, Y. J.; Zhang, J. S.; Zhan, L.; Ma, L. L.; Fang, Z. Y.; Vajtai, R.; Wang, X. C.; Ajayan, P. M., Exfoliated Graphitic Carbon Nitride Nanosheets as Efficient Catalysts for Hydrogen Evolution Under Visible Light. *Adv Mater* **2013,** *25* (17), 2452-2456.

182. Xu, J.; Zhang, L. W.; Shi, R.; Zhu, Y. F., Chemical exfoliation of graphitic carbon nitride for efficient heterogeneous photocatalysis. *J Mater Chem A* **2013,** *1* (46), 14766-14772.

183. Zhu, J. Y.; Li, H.; Hou, J. W.; Liu, J. D.; Zhang, Y. T.; Van der Bruggen, B., Heteroepitaxial growth of vertically orientated zeolitic imidazolate framework-L (Co/Zn-ZIF-L) molecular sieve membranes. *Aiche Journal* **2020,** *66* (5), e16935.

184. Crake, A.; Christoforidis, K. C.; Gregg, A.; Moss, B.; Kafizas, A.; Petit, C., The Effect of Materials Architecture in TiO2/MOF Composites on CO2 Photoreduction and Charge Transfer. *Small* **2019,** *15* (11), e1805473.

185. Shi, L.; Wang, T.; Zhang, H. B.; Chang, K.; Ye, J. H., Electrostatic Self-Assembly of Nanosized Carbon Nitride Nanosheet onto a Zirconium Metal-Organic Framework for Enhanced Photocatalytic CO2 Reduction. *Adv Funct Mater* **2015,** *25* (33), 5360-5367.

186. Liu, S. W.; Chen, F.; Li, S. T.; Peng, X. X.; Xiong, Y., Enhanced photocatalytic conversion of greenhouse gas CO2 into solar fuels over g-C3N4 nanotubes with decorated transparent ZIF-8 nanoclusters. *Appl Catal B-Environ* **2017,** *211*, 1-10.

187. Devarayapalli, K. C.; Vattikuti, S. V. P.; Sreekanth, V. M.; Yoo, K. S.; Nagajyothi, P. C.; Shim, J., Hydrogen production and photocatalytic activity of g-C3N4/Co-MOF (ZIF-67) nanocomposite under visible light irradiation. *Appl Organomet Chem* **2020,** *34* (3), e5376.

188. Cao, A. H.; Zhang, L. J.; Wang, Y.; Zhao, H. J.; Deng, H.; Liu, X. M.; Lin, Z.; Su, X. T.; Yue, F., 2D-2D Heterostructured UNiMOF/g-C3N4 for Enhanced Photocatalytic H-2 Production under Visible-Light Irradiation. *Acs Sustain Chem Eng* **2019,** *7* (2), 2492-2499.

189. Zhang, Z.; Yates, J. T., Band Bending in Semiconductors: Chemical and Physical Consequences at Surfaces and Interfaces. *Chem Rev* **2012,** *112* (10), 5520-5551.

190. Francis, M. N., The theory of crystal rectifiers. *The royal society* **1939,** *171* (944).

191. Francis, M. N., Note on the contact between a metal and an insulator or semi-conductor. *Mathematical Proceedings of the Cambridge Philosophical Society* **1938,** *4*, 568-572.

192. Moss, B.; Wang, Q.; Butler, K. T.; Grau-Crespo, R.; Selim, S.; Regoutz, A.; Hisatomi, T.; Godin, R.; Payne, D. J.; Kafizas, A.; Domen, K.; Steier, L.; Durrant, J. R., Linking in situ charge accumulation to electronic structure in doped SrTiO3 reveals design principles for hydrogen-evolving photocatalysts. *Nat Mater* **2021,** *20* (4), 511-517.

193. Bessegato, G. G.; Guaraldo, T. T.; de Brito, J. F.; Brugnera, M. F.; Zanoni, M. V. B., Achievements and Trends in Photoelectrocatalysis: from Environmental to Energy Applications. *Electrocatalysis-Us* **2015,** *6* (5), 415-441.

194. Rhimi, B.; Wang, C. Y.; Bahnemann, D. W., Latest progress in g-C(3)N(4)based heterojunctions for hydrogen production via photocatalytic water splitting: a mini review. *J Phys-Energy* **2020,** *2* (4), 042003.

195. Zhong, S. X.; Xi, Y. M.; Chen, Q.; Chen, J. R.; Bai, S., Bridge engineering in photocatalysis and photoelectrocatalysis. *Nanoscale* **2020,** *12* (10), 5764-5791.

196. Li, Y.; Xia, Y.; Liu, K. L.; Ye, K. H.; Wang, Q. S.; Zhang, S. Q.; Huang, Y. C.; Liu, H., Constructing Fe-MOF-Derived Z-Scheme Photocatalysts with Enhanced Charge Transport: Nanointerface and Carbon Sheath Synergistic Effect. *Acs Appl Mater Inter* **2020,** *12* (22), 25494-25502.

197. Christoforidis, K. C.; Melchionna, M.; Montini, T.; Papoulis, D.; Stathatos, E.; Zafeiratos, S.; Kordouli, E.; Fornasiero, P., Solar and visible light photocatalytic enhancement of halloysite nanotubes/g-C3N4 heteroarchitectures. *Rsc Adv* **2016,** *6* (89), 86617-86626.

198. Miller, T. S.; Jorge, A. B.; Suter, T. M.; Sella, A.; Cora, F.; McMillan, P. F., Carbon nitrides: synthesis and characterization of a new class of functional materials. *Phys Chem Chem Phys* **2017,** *19* (24), 15613-15638.

199. Chen, H.; Wu, X. X.; Zhao, R.; Zheng, Z.; Yuan, Q. H.; Dong, Z. J.; Gan, W., Preparation of reduced graphite oxide loaded with cobalt(II) and nitrogen co-doped carbon polyhedrons from a metal-organic framework (type ZIF-67), and its application to electrochemical determination of metronidazole. *Microchimica Acta* **2019,** *186* (9).

200. Glover, E. N. K.; Ellington, S. G.; Sankar, G.; Palgrave, R. G., The nature and effects of rhodium and antimony dopants on the electronic structure of TiO2: towards design of Z-scheme photocatalysts. *J Mater Chem A* **2016,** *4* (18), 6946-6954.

201. Oropeza, F. E.; Egdell, R. G., Control of valence states in Rh-doped TiO2 by Sb co-doping: A study by high resolution X-ray photoemission spectroscopy. *Chem Phys Lett* **2011,** *515* (4-6), 249-253.

202. Wang, S. J.; Xu, D. P.; Ma, L.; Qiu, J. X.; Wang, X.; Dong, Q. L.; Zhang, Q.; Pan, J.; Liu, Q., Ultrathin ZIF-67 nanosheets as a colorimetric biosensing platform for peroxidase-like catalysis. *Anal Bioanal Chem* **2018,** *410* (27), 7145-7152.

203. Li, X.; Li, Z. H.; Lu, L.; Huang, L. M.; Xiang, L.; Shen, J.; Liu, S. Y.; Xiao, D. R., The Solvent Induced Inter-Dimensional Phase Transformations of Cobalt Zeolitic-Imidazolate Frameworks. *Chem-Eur J* **2017,** *23* (44), 10638-10643.

204. Dong, L. Z.; Zhang, L.; Liu, J.; Huang, Q.; Lu, M.; Ji, W. X.; Lan, Y. Q., Stable Heterometallic Cluster-Based Organic Framework Catalysts for Artificial Photosynthesis. *Angew Chem Int Edit* **2020,** *59* (7), 2659-2663.

205. Wang, M. H.; Yang, L. Y.; Yuan, J. Y.; He, L. H.; Song, Y. P.; Zhang, H. Z.; Zhang, Z. H.; Fang, S. M., Heterostructured Bi2S3@NH2-MIL-125(Ti) nanocomposite as a bifunctional photocatalyst for Cr(VI) reduction and rhodamine B degradation under visible light. *Rsc Adv* **2018,** *8* (22), 12459-12470.

206. Liu, H.; Zhang, J.; Ao, D., Construction of heterostructured ZnIn2S4@NH2-MIL-125(Ti) nanocomposites for visible-light-driven H-2 production. *Appl Catal B-Environ* **2018,** *221*, 433-442.

207. Holder, C. F.; Schaak, R. E., Tutorial on Powder X-ray Diffraction for Characterizing Nanoscale Materials. *Acs Nano* **2019,** *13* (7), 7359-7365.

208. Ma, L. F.; Zhang, X. Y.; Ikram, M.; Ullah, M.; Wu, H. Y.; Shi, K. Y., Controllable synthesis of an intercalated ZIF-67/EG structure for the detection of ultratrace Cd2+, Cu2+, Hg2+ and Pb2+ ions. *Chem Eng J* **2020,** *395*, 125216.

209. Zhang, X. M.; Wang, J. Y.; Fan, Y.; Ren, H. D.; Liu, Z. Y.; Wang, Y. F.; Liu, Y.; Bai, H. C.; Kong, L. B., NiCo alloy/C nanocomposites derived from a Ni-doped ZIF-67 for lightweight microwave absorbers. *Nanotechnology* **2021,** *32* (38), 385602.

210. Ao, D.; Zhang, J.; Liu, H., Visible-light-driven photocatalytic degradation of pollutants over Cu-doped NH2 -MIL-125(Ti). *J Photoch Photobio A* **2018,** *364*, 524-533.

211. Zhang, B. X.; Zhang, J. L.; Tan, X. N.; Shao, D.; Shi, J. B.; Zheng, L. R.; Zhang, J.; Yang, G. Y.; Han, B. X., MIL-125-NH2@TiO2 Core-Shell Particles Produced by a Post-Solvothermal Route for High-Performance Photocatalytic H-2 Production. *Acs Appl Mater Inter* **2018,** *10* (19), 16418-16423.

212. Huang, Q. Q.; Hu, Y.; Pei, Y.; Zhang, J. H.; Fu, M. L., In situ synthesis of TiO2@NH2-MIL-125 composites for use in combined adsorption and photocatalytic degradation of formaldehyde. *Appl Catal B-Environ* **2019,** *259*, 118106.

213. Choudhury, B.; Giri, P. K., Isotype heterostructure of bulk and nanosheets of graphitic carbon nitride for efficient visible light photodegradation of methylene blue. *Rsc Adv* **2016,** *6* (30), 24976-24984.

214. Luo, S. H.; Zeng, Z. T.; Zeng, G. M.; Liu, Z. F.; Xiao, R.; Xu, P.; Wang, H.; Huang, D. L.; Liu, Y.; Shao, B. B.; Liang, Q. H.; Wang, D. B.; He, Q. Y.; Qin, L.; Fu, Y. K., Recent advances in conjugated microporous polymers for photocatalysis: designs, applications, and prospects. *J Mater Chem A* **2020,** *8* (14), 6434-6470.

215. Xu, C.; Zhang, W. J.; Tang, J. T.; Pan, C. Y.; Yu, G. P., Porous Organic Polymers: An Emerged Platform for Photocatalytic Water Splitting. *Front Chem* **2018,** *6*.

216. Xiao, J. D.; Jiang, H. L., Metal-Organic Frameworks for Photocatalysis and Photothermal Catalysis. *Accounts Chem Res* **2019,** *52* (2), 356-366.

217. Wang, T. X.; Liang, H. P.; Anito, D. A.; Ding, X. S.; Han, B. H., Emerging applications of porous organic polymers in visible-light photocatalysis. *J Mater Chem A* **2020,** *8* (15), 7003-7034.

218. Fu, Z. W.; Wang, X. Y.; Gardner, A.; Wang, X.; Chong, S. Y.; Neri, G.; Cowan, A. J.; Liu, L. J.; Li, X. B.; Vogel, A.; Clowes, R.; Bilton, M.; Chen, L. J.; Sprick, R. S.; Cooper, A. I., A stable covalent organic framework for photocatalytic carbon dioxide reduction. *Chem Sci* **2020,** *11* (2), 543-550.

219. Huang, J.; Turner, S. R., Hypercrosslinked Polymers: A Review. *Polym Rev* **2018,** *58* (1), 1-41.

220. Tan, L. X.; Tan, B., Hypercrosslinked porous polymer materials: design, synthesis, and applications (vol 42, pg 3322, 2017). *Chem Soc Rev* **2017,** *46* (11), 3481-3481.

221. Woodward, R. T., The design of hypercrosslinked polymers from benzyl ether self-condensing compounds and external crosslinkers. *Chem Commun* **2020,** *56* (36), 4938-4941.

222. Woodward, R. T.; Stevens, L. A.; Dawson, R.; Vijayaraghavan, M.; Hasell, T.; Silverwood, I. P.; Ewing, A. V.; Ratvijitvech, T.; Exley, J. D.; Chong, S. Y.; Blanc, F.; Adams, D. J.; Kazarian, S. G.; Snape, C. E.; Drage, T. C.; Cooper, A. I., Swellable, Water- and Acid-Tolerant Polymer Sponges for Chemoselective Carbon Dioxide Capture. *Journal of the American Chemical Society* **2014,** *136* (25), 9028-9035.

223. Lu, X.; Shi, S.; Zhu, G. Z.; Zhao, L.; Wang, M.; Gao, J.; Du, Z. T.; Xu, J., Generation of Strong Basic Site on Hypercrosslinked Porous Polymers as Catalyst for the Catalytic Oxidation of Methylene Compounds. *Chemistryselect* **2020,** *5* (2), 549-553.

224. Li, B.; Gong, R.; Wang, W.; Huang, X.; Zhang, W.; Li, H.; Hu, C.; Tan, B., A new strategy to microporous polymers: knitting rigid aromatic building blocks by external cross-linker. *Macromolecules* **2011,** *44* (8), 2410-2414.

225. Woodward, R. T., The design of hypercrosslinked polymers from benzyl ether self-condensing compounds and external crosslinkers. *Chem Commun (Camb)* **2020**, 4938-4941.

226. Thommes, M.; Kaneko, K.; Neimark, A. V.; Olivier, J. P.; Rodriguez-Reinoso, F.; Rouquerol, J.; Sing, K. S. W., Physisorption of gases, with special reference to the evaluation of surface area and pore size distribution (IUPAC Technical Report). *Pure Appl Chem* **2015,** *87* (9-10), 1051-1069.

227. Varghese, A. M.; Karanikolos, G. N., CO2 capture adsorbents functionalized by amine ? bearing polymers: A review. *Int J Greenh Gas Con* **2020,** *96*, 103005.

228. Dawson, R.; Stevens, L. A.; Drage, T. C.; Snape, C. E.; Smith, M. W.; Adams, D. J.; Cooper, A. I., Impact of Water Coadsorption for Carbon Dioxide Capture in Microporous Polymer Sorbents. *Journal of the American Chemical Society* **2012,** *134* (26), 10741-10744.

229. Kosco, J.; Sachs, M.; Godin, R.; Kirkus, M.; Francas, L.; Bidwell, M.; Qureshi, M.; Anjum, D.; Durrant, J. R.; McCulloch, I., The Effect of Residual Palladium Catalyst Contamination on the Photocatalytic Hydrogen Evolution Activity of Conjugated Polymers. *Advanced Energy Materials* **2018,** *8* (34).

230. Sachs, M.; Cha, H.; Kosco, J.; Aitchison, C. M.; Francàs, L.; Corby, S.; Chiang, C.-L.; Wilson, A.; Godin, R.; Fahey-Williams, A.; Cooper, A.; Sprick, S.; McCulloch, I.; Durrant, J. R., Tracking Charge Transfer to Residual Metal Clusters in Conjugated Polymers for Photocatalytic Hydrogen Evolution. *Journal of the American Chemical Society* **2020**, 14574–14587.

231. Yu, X. X.; Yang, Z. Z.; Qiu, B.; Guo, S. E.; Yang, P.; Yu, B.; Zhang, H. Y.; Zhao, Y. F.; Yang, X. Z.; Han, B. X.; Liu, Z. M., Eosin Y-Functionalized Conjugated Organic Polymers for

Visible-Light-Driven CO2 Reduction with H2O to CO with High Efficiency. *Angew Chem Int Edit* **2019,** *58* (2), 632-636.

232. Lee, H. M.; Youn, I. S.; Saleh, M.; Lee, J. W.; Kim, K. S., Interactions of CO2 with various functional molecules. *Phys Chem Chem Phys* **2015,** *17* (16), 10925-10933.

233. Che, W.; Cheng, W. R.; Yao, T.; Tang, F. M.; Liu, W.; Su, H.; Huang, Y. Y.; Liu, Q. H.; Liu, J. K.; Hu, F. C.; Pan, Z. Y.; Sun, Z. H.; Wei, S. Q., Fast Photoelectron Transfer in (C-ring)-C3N4 Plane Heterostructural Nanosheets for Overall Water Splitting. *Journal of the American Chemical Society* **2017,** *139* (8), 3021-3026.

234. Zhong, H.; Hong, Z. X.; Yang, C.; Li, L. Y.; Xu, Y. S.; Wang, X. C.; Wang, R. H., A Covalent Triazine-Based Framework Consisting of Donor-Acceptor Dyads for Visible-Light-Driven Photocatalytic CO2 Reduction. *Chemsuschem* **2019,** *12* (19), 4493-4499.

235. Ning, H. L.; Yang, Z. Y.; Yin, Z. Q.; Wang, D. C.; Meng, Z. Y.; Wang, C. G.; Zhang, Y. T.; Chen, Z. P., A Novel Strategy to Enhance the Performance of CO2 Adsorption Separation: Grafting Hyper-cross-linked Polyimide onto Composites of UiO-66-NH2 and GO. *Acs Appl Mater Inter* **2021,** *13* (15), 17781-17790.

236. Stevens, R. W.; Siriwardane, R. V.; Logan, J., In Situ Fourier Transform Infrared (FTIR) Investigation of CO2 Adsorption onto Zeolite Materials. *Energ Fuel* **2008,** *22* (5), 3070-3079.

237. Proano, L.; Tello, E.; Arellano-Trevino, M. A.; Wang, S. X.; Farrauto, R. J.; Cobo, M., In-situ DRIFTS study of two-step CO2 capture and catalytic methanation over Ru,"Na2O"/Al2O3 Dual Functional Material. *Appl Surf Sci* **2019,** *479*, 25-30.

238. Rege, S. U.; Yang, R. T., A novel FTIR method for studying mixed gas adsorption at low concentrations: H2O and CO2 on NaX zeolite and gamma-alumina. *Chem Eng Sci* **2001,** *56* (12), 3781-3796.

239. Mino, L.; Spoto, G.; Ferrari, A. M., CO2 Capture by TiO2 Anatase Surfaces: A Combined DFT and FTIR Study. *J Phys Chem C* **2014,** *118* (43), 25016-25026.

240. Kock, E. M.; Kogler, M.; Bielz, T.; Klotzer, B.; Penner, S., In Situ FT-IR Spectroscopic Study of CO2 and CO Adsorption on Y2O3, ZrO2, and Yttria-Stabilized ZrO2. *J Phys Chem C* **2013,** *117* (34), 17666-17673.

241. Law, R. V.; Sherrington, D. C.; Snape, C. E.; Ando, I.; Kurosu, H., Solid-State 13C MAS NMR Studies of Hyper-Cross-Linked Polystyrene Resins. *Macromolecules* **1996,** *29* (19), 6284-6293.

242. Mohamed, M. G.; Zhang, X.; Mansoure, T. H.; El-Mahdy, A. F. M.; Huang, C. F.; Danko, M.; Xin, Z.; Kuo, S. W., Hypercrosslinked porous organic polymers based on tetraphenylanthraquinone for CO2 uptake and high-performance supercapacitor. *Polymer* **2020,** *205*, 122857.

243. Chen, L. Y.; Rong, M.; Yang, L. R.; Yu, J. M.; Qu, H. N.; Meng, Q. Y.; Ni, S.; Xu, Z. H.; Zhu, X. Y.; Wang, L.; Xing, H. F.; Liu, H. Z., Construction of super-hydrophobic hypercrosslinked porous polymers for selectively removing aromatic diamines from the polyurethane bio-hydrolysate. *Chem Eng J* **2022,** *428*, 132509.

244. Alwin, E.; Nowicki, W.; Wojcieszak, R.; Zielinski, M.; Pietrowski, M., Elucidating the structure of the graphitic carbon nitride nanomaterials via X-ray photoelectron spectroscopy and X-ray powder diffraction techniques. *Dalton T* **2020,** *49* (36), 12805-12813.

245. Hauchhum, L.; Mahanta, P., Carbon dioxide adsorption on zeolites and activated carbon by pressure swing adsorption in a fixed bed. *International Journal of Energy and Environmental Engineering* **2014,** *5* (4), 349-356.

246. Martin, C. F.; Stockel, E.; Clowes, R.; Adams, D. J.; Cooper, A. I.; Pis, J. J.; Rubiera, F.; Pevida, C., Hypercrosslinked organic polymer networks as potential adsorbents for pre-combustion CO2 capture. *J Mater Chem* **2011,** *21* (14), 5475-5483.

247. Son, K. N.; Richardson, T. M. J.; Cmarik, G. E., Equilibrium Adsorption Isotherms for H2O on Zeolite 13X. *J Chem Eng Data* **2019,** *64* (3), 1063-1071.

248. Roedel, E.; Urakawa, A.; Kureti, S.; Baiker, A., On the local sensitivity of different IR techniques: Ba species relevant in NOx storage-reduction. *Phys Chem Chem Phys* **2008,** *10* (40), 6190-6198.

249. Yuan, X. H.; Luo, K.; Zhang, K. Q.; He, J. L.; Zhao, Y. C.; Yu, D. L., Combinatorial Vibration-Mode Assignment for the FTIR Spectrum of Crystalline Melamine: A Strategic Approach toward Theoretical IR Vibrational Calculations of Triazine-Based Compounds. *J Phys Chem A* **2016,** *120* (38), 7427-7433.

250. Zafar, M. S.; Liaqat, S.; Najeeb, S.; Khurshid, Z.; Alrahabi, M.; Zohaib, S. In *Polymer science : research advances , practical applications and educational aspects*, 2015.

251. de Juan, A.; Tauler, R., Multivariate Curve Resolution: 50 years addressing the mixture analysis problem-A review. *Anal Chim Acta* **2021,** *1145*, 59-78.

252. Petrovic, B.; Gorbounov, M.; Soltani, S. M., Influence of surface modification on selective CO2 adsorption: A technical review on mechanisms and methods. *Micropor Mesopor Mat* **2021,** *312*, 110751.

253. Petrovic, B.; Gorbounov, M.; Masoudi Soltani, S., Impact of Surface Functional Groups and Their Introduction Methods on the Mechanisms of CO2 Adsorption on Porous Carbonaceous Adsorbents. *Carbon Capture Science & Technology* **2022,** *3*, 100045.

Appendix 1

Table A1.1 Composition of the samples as derived by the thermogravimetric analysis of CNNS-1, Co-ZIF-L and CNNS-1/ZIF-L-X heterojunctions. The numbers in parenthesis correspond to approximations to the nearest unit.

Samples	Final mass (% mass)	Mass loss[a] (% mass)	X_{CNNS-1}[b] (% mass)	$X_{Co-ZIF-L}$[c] (% mass)
Co-ZIF-L	48.57		0	100
CNNS-1/ZIF-L-96	46.78	1.79	3.68 (4)	96
CNNS-1/ZIF-L-88	42.76	5.81	11.96 (12)	88
CNNS-1/ZIF-L-22	10.79	37.78	77.78 (78)	22
CNNS-1/ZIF-L-8	3.68	44.71	92.42 (92)	8
CNNS-1	0.08		100	0

[a] $\text{Mass loss} = \text{Co-ZIF-L}_{\text{Final mass}} - \text{CNNS-1/ZIF-L-X}_{\text{Final mass}}$

[b] Calculated: $X_{\text{CNNS}-1} = \frac{\Delta\text{mass loss}}{\text{Co}-\text{ZIF}-\text{L}_{\text{Final mass}}}$

[c] $X_{\text{Co}-\text{ZIF}-\text{L}} = 1 - X_{\text{CNNS}-1}$

Table A1.2 Composition analysis of CNNS-2, Ti-MIL-125-NH_2 and CNNS-2/MIL-25 derived from thermogravimetric analyses. The number in parenthesis correspond to approximations to the nearest unit.

Samples	Final mass (% mass)	Mass loss[a] (% mass)	x_{CNNS-2}[b] (% mass)	$x_{MIL-125-NH2}$[c] (% mass)
Ti-MIL-125-NH_2	53.69		0	100
CNNS-2/MIL-25	13.71	39.98	74.45 (75)	25
CNNS-2	0.2		100	0

[a] Calculated: $\text{Mass loss} = \text{MIL-125-NH}_{2\,\text{Final mass}} - \text{CNNS-2/MIL-25}_{\text{Final mass}}$

[b] Calculated: $X_{\text{CNNS}-2} = \frac{\Delta\text{mass loss}}{\text{MIL}-125-NH_{2\,\text{Final mass}}}$

[c] $X_{\text{MIL}-125-\text{N}H_2} = 1 - X_{\text{CNNS}-2}$

Table A1.3 Summary of textural properties derived from N_2 sorption isotherms at 77 K and CO_2 adsorption capacity at 298 K and 1 bar of CNNS-1, Co-ZIF-L and CNNS-1/ZIF-L-22.

Sample	V_{MICRO} ($cm^3.g^{-1}$)	V_{TOT} ($cm^3.g^{-1}$)	S_{BET} ($m^2.g^{-1}$)	CO_2 ads. ($mmol.g^{-1}$)
CNNS-1	nil	0.049	33	0.15
Co-ZIF-L	nil	0.053	41	1.28
CNNS-1/ZIF-L-22	nil	0.051	37 (35)[a]	0.27 (0.4)[b]

[a] Expected value $= (S_{\text{BET CNNS-1}} \times 0.78) + (S_{\text{BET Co-ZIF-L}} \times 0.22)$

[b] Expected value $= (CO_2 \text{ ads.}_{\text{CNNS-1}} \times 0.78) + CO_2 \text{ ads.}_{\text{Co-ZIF-L}} \times 0.22)$

Table A1.4 CO evolution rates for CNNS-1, Co-ZIF-L and CNNS-1/ZIF-L-X photocatalysts under UV-Vis irradiation using H_2 as reducing agent.

Samples	CO produced ($\mu mol.cm^{-2}.h^{-1}$)	CO produced ($\mu mol.g^{-1}.h^{-1}$)	Expected photoactivity[a] ($\mu mol.g^{-1}.h^{-1}$)
Co-ZIF-L		0.057 ± 0.008 0.023 (λ > 495nm)	
CNNS-1		0.22 ± 0.01	
CNNS-1/ZIF-L-96		0.066 ± 0.005	0.064
CNNS-1/ZIF-L-88		0.060 ± 0.003	0.09
CNNS-1/ZIF-L-22		0.018 ± 0.01	0.188
CNNS-1/ZIF-L-22 physical mixture		0.189	0.188
CNNS-1/ZIF-L-8		0.075 ± 0.009	0.21

[a] Expected value $= (\text{activity}_{\text{CNNS}} \times X_{\text{CNNS}}) + (\text{activity}_{\text{MOF}} \times X_{\text{MOF}})$, where X represents the weight percent of CNNS or MOF in the sample.

Table A1.5 Comparison of the measured band edge position of CNNS, Ti-MIL-125-NH_2 and ZIF-67 with those reported in literature.

Photocatalyst	CB position vs NHE pH=0 (V)	VB position vs NHE pH=0 (V)	Method used	Ref
CNNS	-0.78	2.07	Mott–Schottky	[1]
CNNS	-0.67	2.0	Mott–Schottky	[2]
CNNS	-0.75	2.05	XPS	[3]
CNNS-1	-0.85	2.0	XPS	This work
CNNS-2	-0.79	1.96	XPS	This work
Ti-MIL-125-NH_2	-0.59	2.09	Mott–Schottky	[4]
Ti-MIL-125-NH_2	-0.72	2.02	Mott–Schottky	[5]
Ti-MIL-125-NH_2	-0.64	2.28	XPS	This work
ZIF-67	-0.45	1.39	Mott–Schottky	[6]
ZIF-67	-0.74	1.18	Mott–Schottky	[7]
Co-ZIF-L	-0.72	1.23	XPS	This work
Co-ZIF-67 NS	-0.55	1.20	XPS	This work
CoNi-ZIF-67 NS	-0.65	1.19	XPS	This work
Ni-ZIF-67 NS	-1.94	1.15	XPS	This work

Table A1.6 Summary of textural properties derived from the N_2 sorption isotherms at -196 °C and CO_2 adsorption capacity at 25 °C and 1 bar of CNNS-2, Ti-MIL-125-NH_2 and CNNS-2/MIL-25.

Sample	V_{MICRO} ($cm^3.g^{-1}$)	V_{TOT} ($cm^3.g^{-1}$)	S_{BET} ($m^2.g^{-1}$)	CO_2 ads. ($mmol.g^{-1}$)
CNNS-2	nil	0.16	32	0.13
Ti-MIL-125-NH_2	0.55	0.67	1635	3.64
CNNS-2/MIL-25	0.13	0.37	462 (433 expected)[a]	1.07 (1.00 expected)[b]
CNNS-2/MIL-25 after irradiation	0.11	0.34	403	0.98

[a] $\text{Expected value} = (S_{\text{BET CNNS}-2} \times 0.25) + (S_{\text{BET MIL}-125-\text{NH2}} \times 0.75)$

[b] $\text{Expected value} = (CO_2 \text{ ads.}_{\text{CNNS-2}} \times 0.25) + CO_2 \text{ ads.}_{\text{MIL}-125-\text{NH2}} \times 0.75)$

Table A1.7 CO evolution rates for CNNS-2, Ti-MIL-125-NH_2, CNNS-2/MIL and P25 TiO2 photocatalysts under UV-Vis irradiation using H_2 as reducing agent.

Samples	CO produced ($\mu mol.cm^{-2}.h^{-1}$)	CO produced ($\mu mol.g^{-1}.h^{-1}$)	Expected photoactivity[a] ($\mu mol.g^{-1}.h^{-1}$)
Ti-MIL-125-NH_2		0.68 ± 0.03	
CNNS-2		0.23± 0.009	
CNNS-2/MIL-25		0.60 ± 0.025	0.34
CNNS-2/MIL-25 physical mixture		0.35	0.34
TiO_2 P25		1.64 ± 0.058	

[a] Expected value= (activity $_{CNNS}$ × X_{CNNS}) + (activity $_{MOF}$ × X_{MOF}), where X represents the weight percent of CNNS or MOF in the sample.

Table A1.8 CO_2 photocatalytic control experiments. The former two tests were performed on CNNS-2/MIL-25, the leading material of this study using H_2 as reducing agent. UV-Vis irradiation was used when needed.

Samples	CO produced ($\mu mol.g^{-1}.h^{-1}$)
N_2/H_2 (catalyst + irradiation)	0.17 ± 0.013
N_2/H_2 (catalyst + no irradiation)	nil
N_2/H_2 (no catalyst + irradiation)	nil

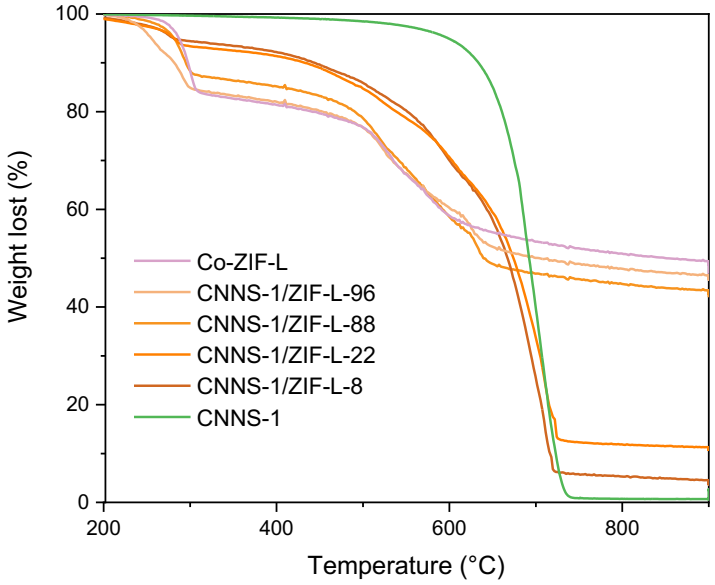


Figure A1.1 Thermogravimetric analyses of CNNS-1, Co-ZIF-L and CNNS-1/ZIF-L-X heterojunctions under N_2 atmosphere.

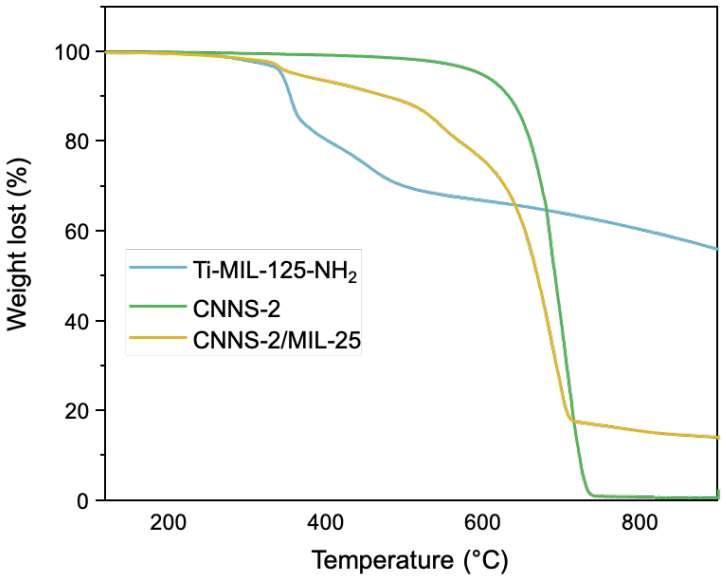


Figure A1.2 Thermogravimetric analysis of CNNS-2, Ti-MIL-125-NH_2 and CNNS-2/MIL-25 under N_2 atmosphere.

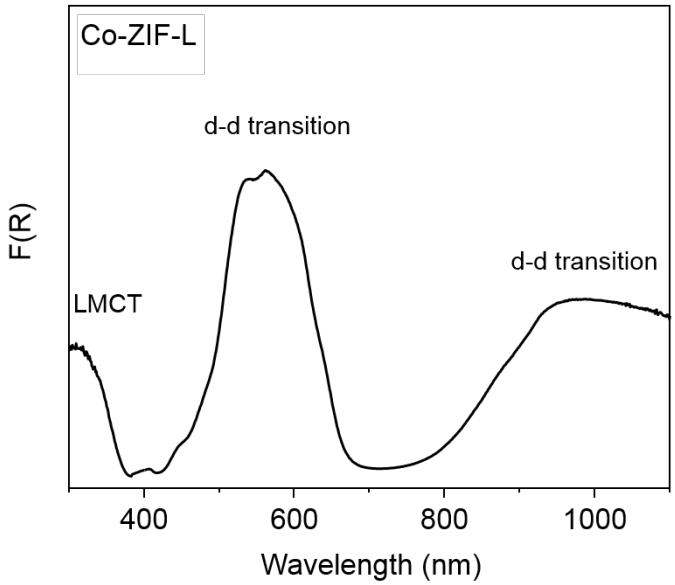


Figure A1.3 UV-Vis absorption spectra of Co-ZIF-L showing the absorption bands of the ligand-to-metal charge-transfer (LMCT) and two Co d-d absorptions bands.

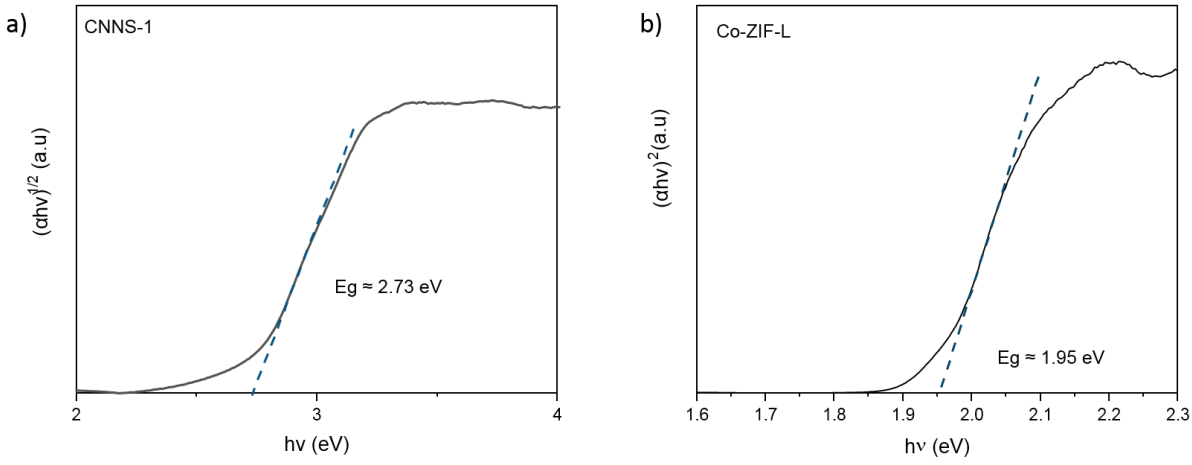


Figure A1.4 Tauc plots of a) CNNS-1 and b) Co-ZIF-L. The UV-Vis reflectance spectra were converted to Tauc plots using the transformed Kubelka-Munk function.

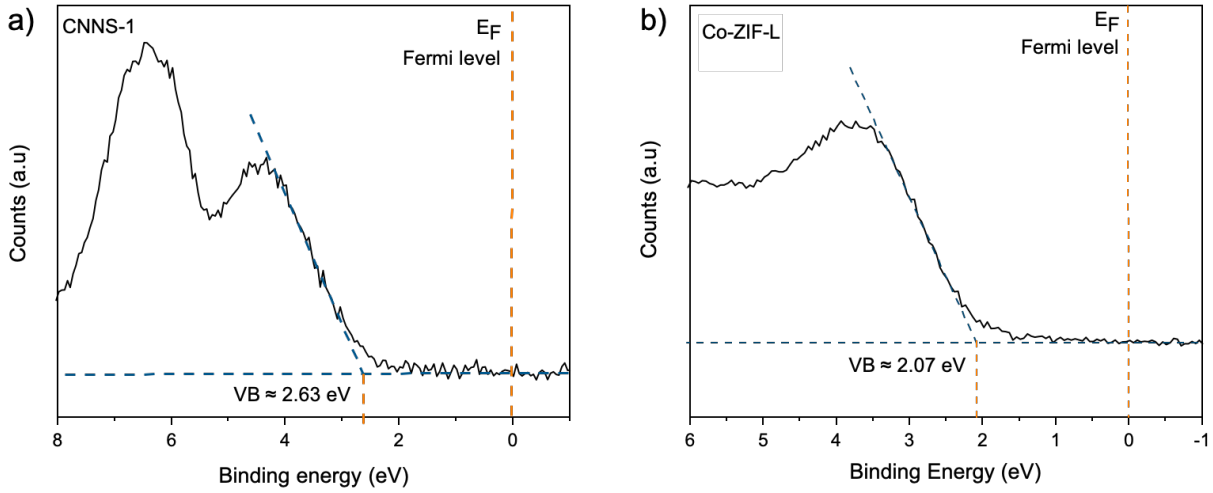


Figure A1.5 Valence band measurements of a) CNNS-1 and b) Co-ZIF-L.

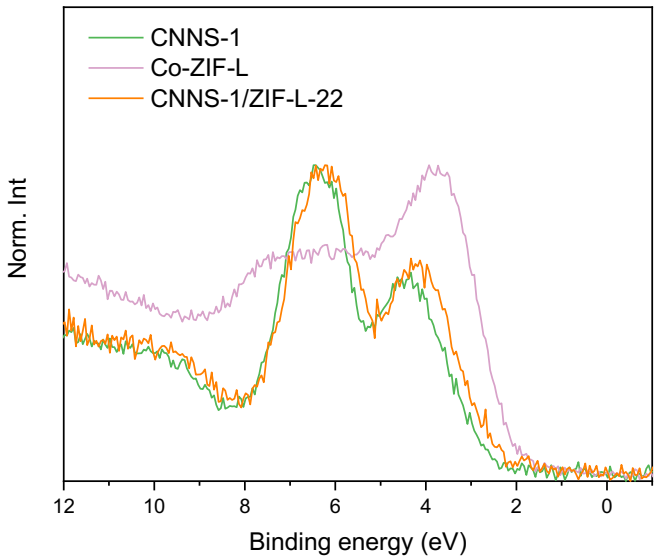


Figure A1.6 Valence band measurements of CNNS-1, Co-ZIF-L and CNNS-1/ZIF-L-22.

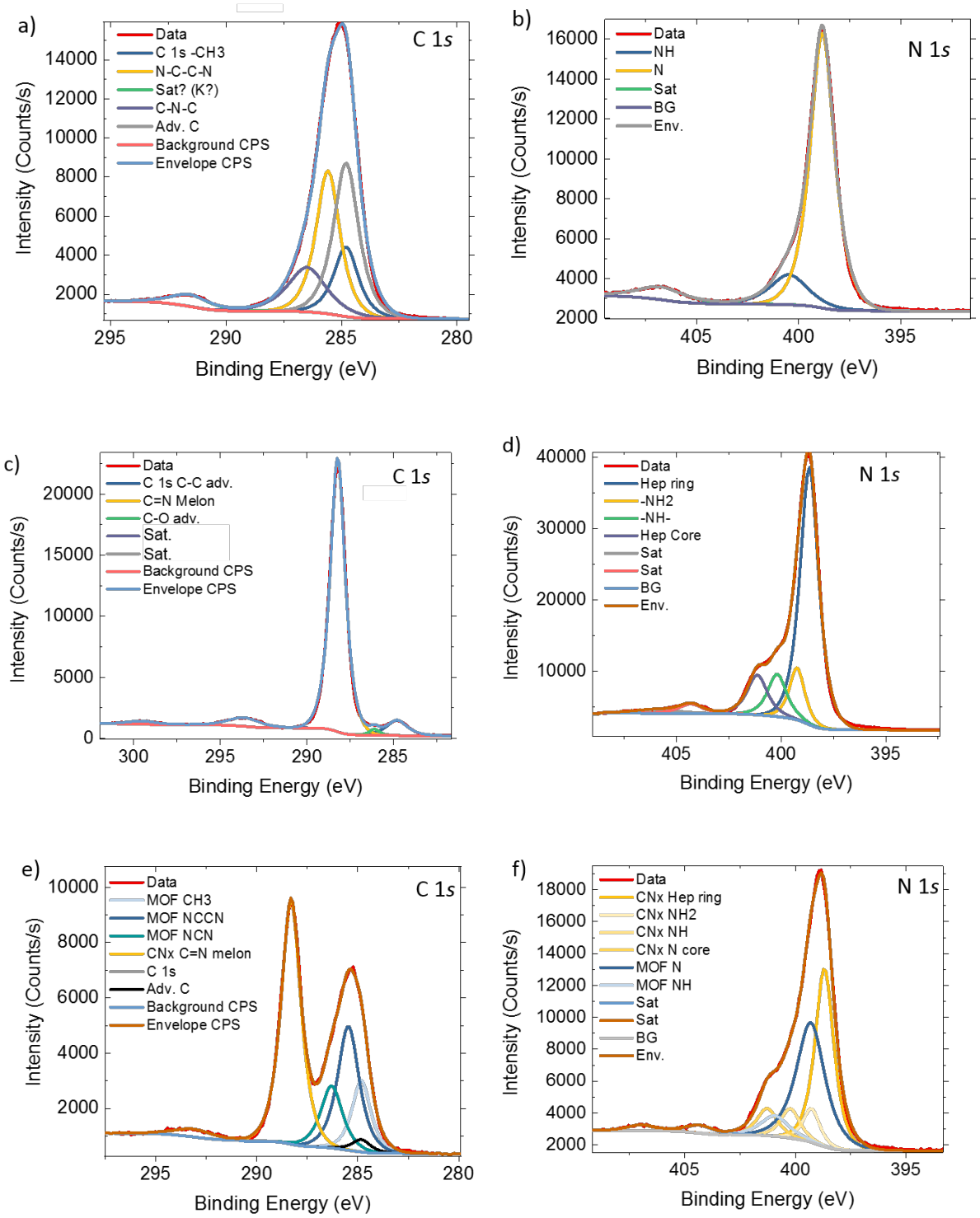


Figure A1.7 High resolution XPS and peak fittings of the C 1*s* and N 1*s* core levels in: (a - b) Co-ZIF-L, (c - d) CNNS-1 and (e - f) CNNS-1/ZIF-L-22.

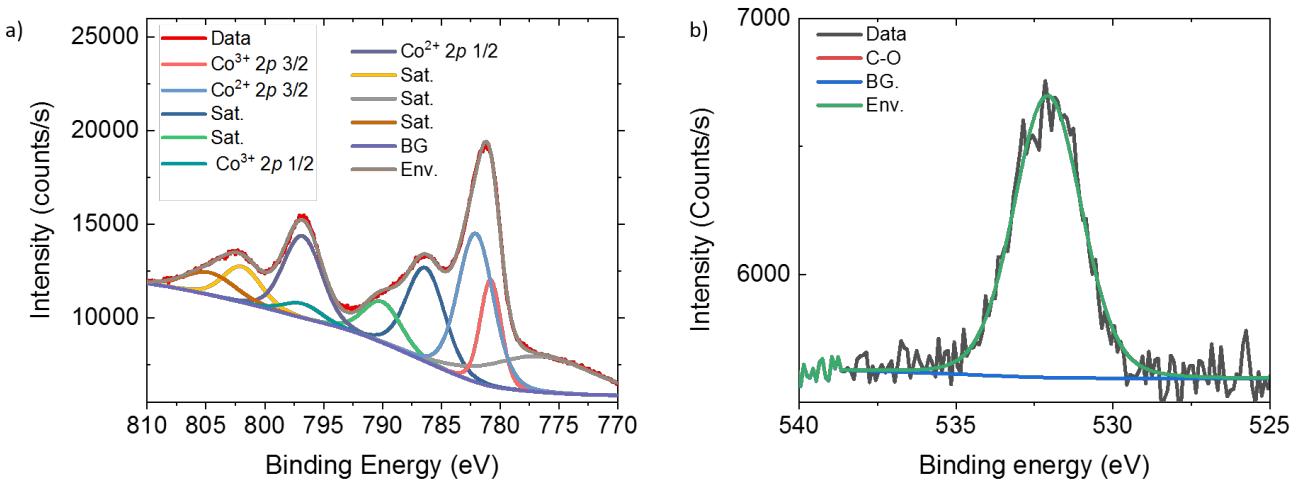


Figure A1.8 High resolution XPS and peak fittings of Co-ZIF-L in the (a) Co *2p* and (b) O 1*s* core level regions.

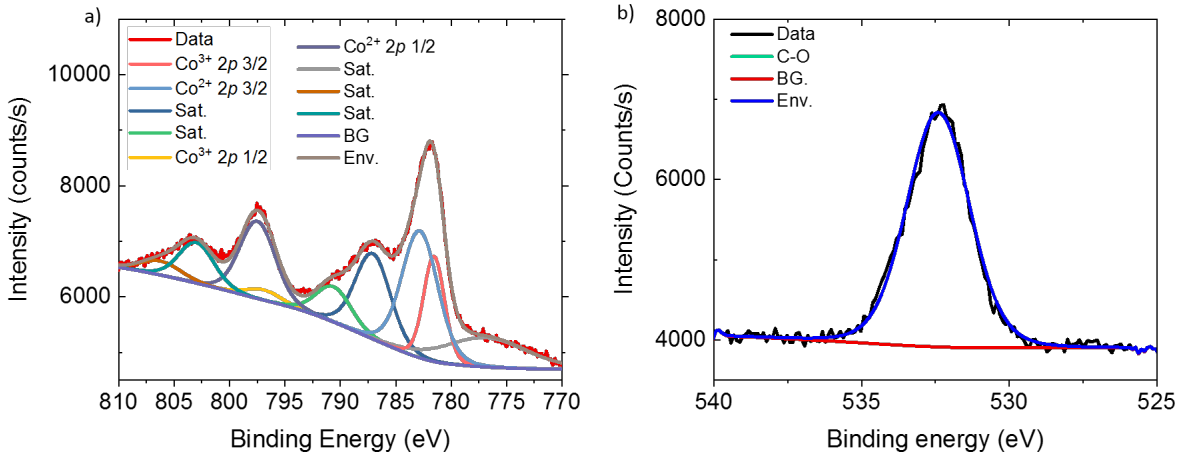


Figure A1.9 High resolution XPS and peak fittings of CNNS-1/ZIF-L-22 in the (a) Co *2p* and (b) O 1*s* core level regions.

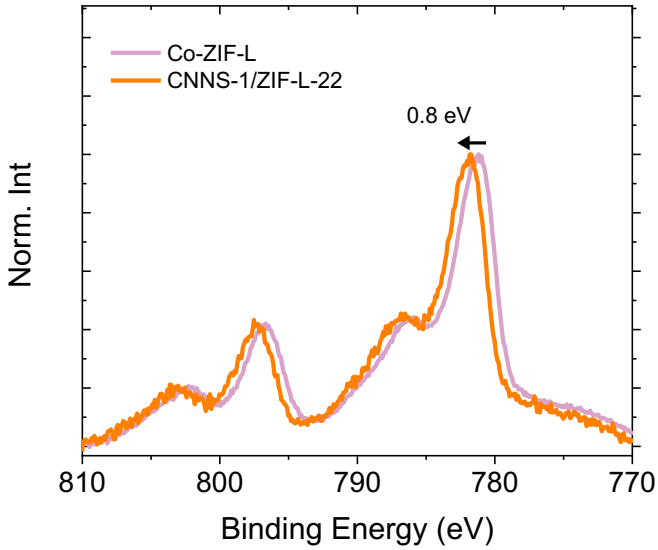


Figure A1.10 High resolution XPS of Co-ZIF-L and CNNS-1/ZIF-L-22 in the Co 2*p* core level region illustrating the Fermi level shift.

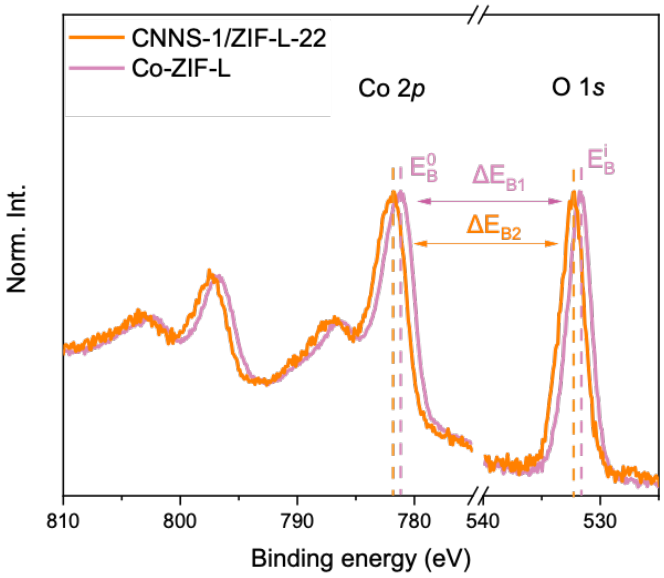


Figure A1.11 High resolution XPS of Co-ZIF-L and CNNS-1/ZIF-L-22 Co 2*p* and O 1*s* core level spectra showing an identical shift towards lower binding energies upon heterojunction formation. Consequently, the Co 2*p* - O 1*s* peak separation (Δ) is invariant upon heterojunction formation. This observation can be explained by the Equations below (A1.1 - A1.2).[8,9] For a given material, referencing the binding energy of one core line against another produces a property that is not sensitive to the position of the Fermi level.

$$\Delta E_B = E_B^o - E_B^i = (E_f - E_{core}^o) - (E_f - E_{core}^i) \quad \text{(A1.1)}$$

$$\Delta E_B = E_{core}^i - E_{core}^o \quad \text{(A1.2)}$$

E_B^i: binding energy of a peak of interest (here O 1*s*); E_B^o: binding energy of the second peak of interest (Co 2*p*); E_{core}^i and E_{core}^o correspond to the absolute energy of these states.

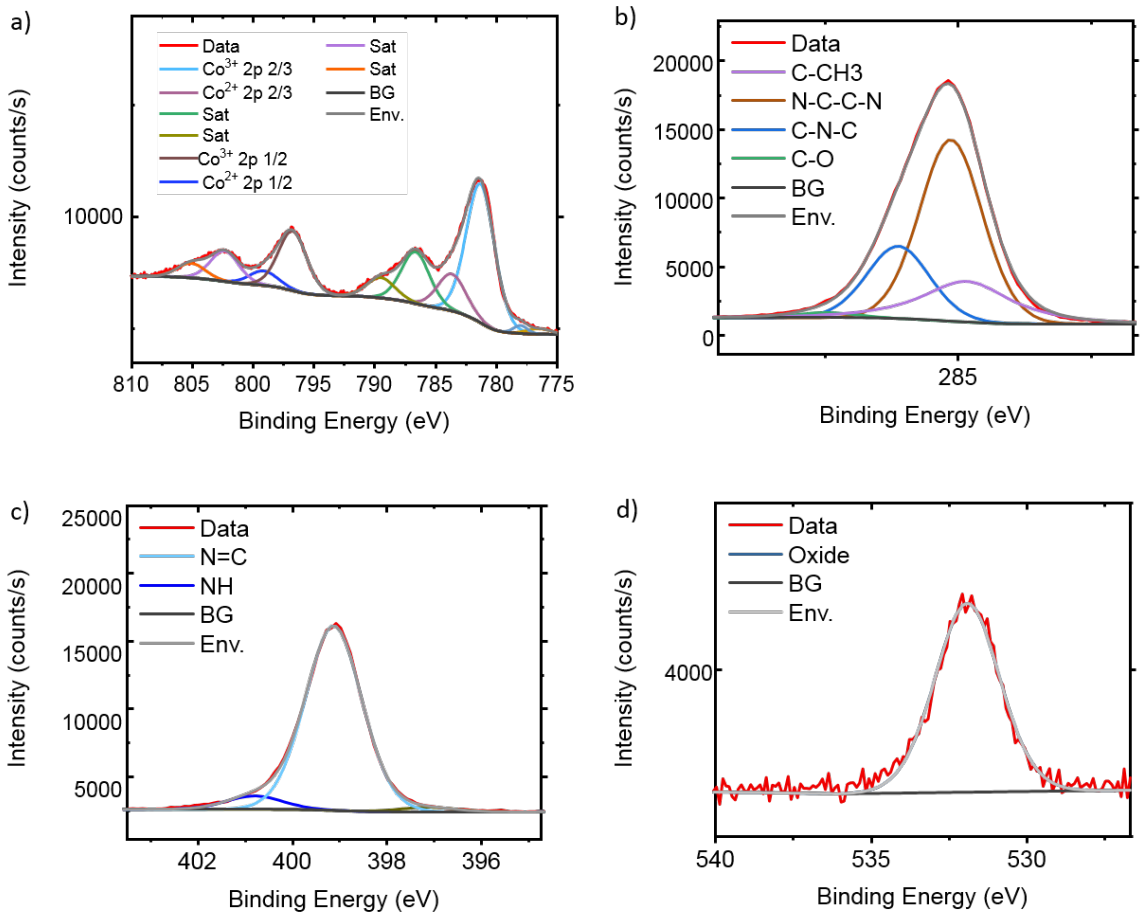


Figure A1.12 High resolution XPS and peak fittings of Co-ZIF-67 Ns in the (a) Co *2p*, (b) C 1*s*, (c) N 1*s* and (d) O 1*s* core level regions.

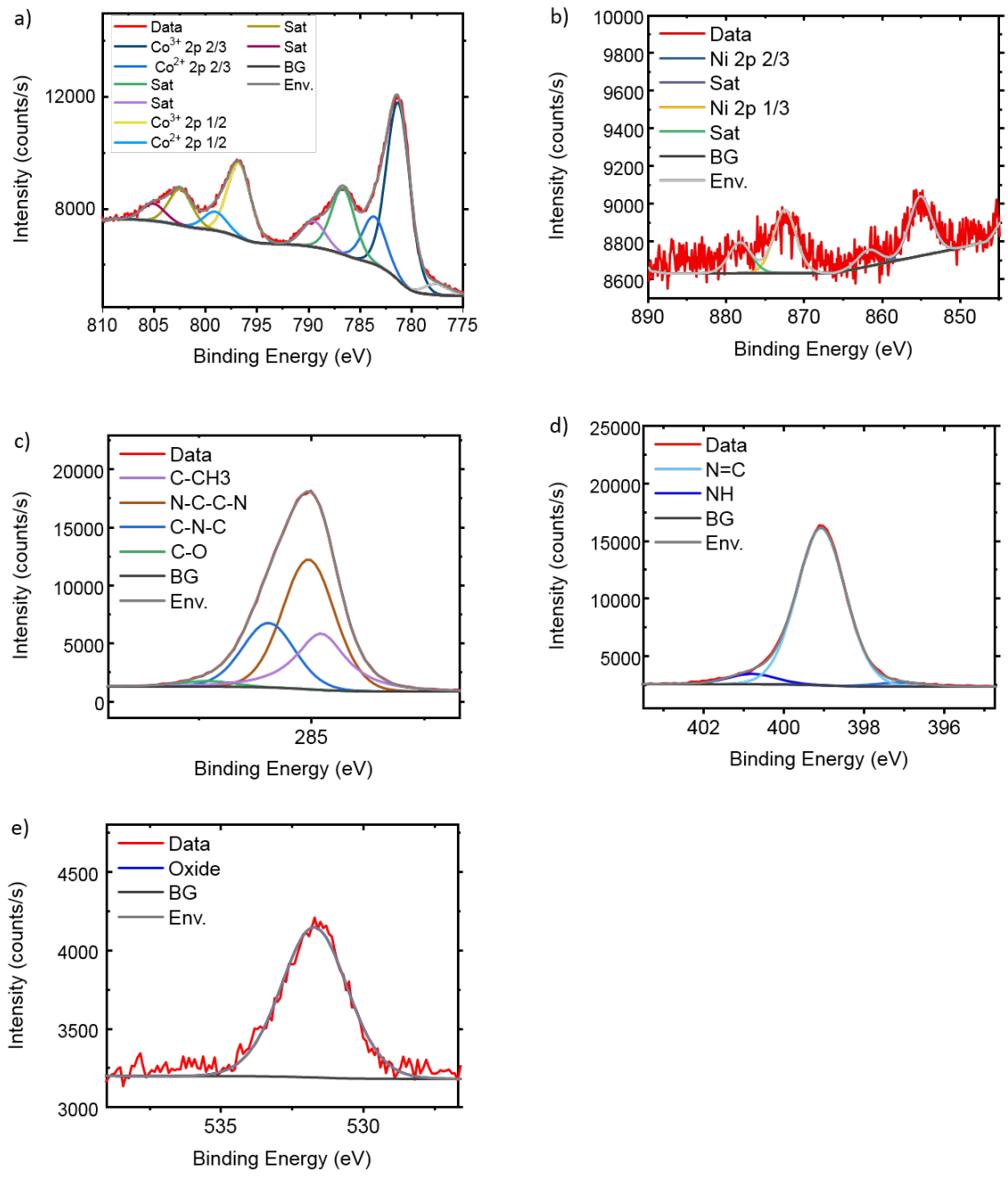


Figure A1.13 High resolution XPS and peak fittings of CoNi-ZIF-67 Ns in the (a) Co *2p*, (b) Ni 2*p*, (c) C 1*s*, (d) N 1*s* and (e) O 1*s* core level regions.

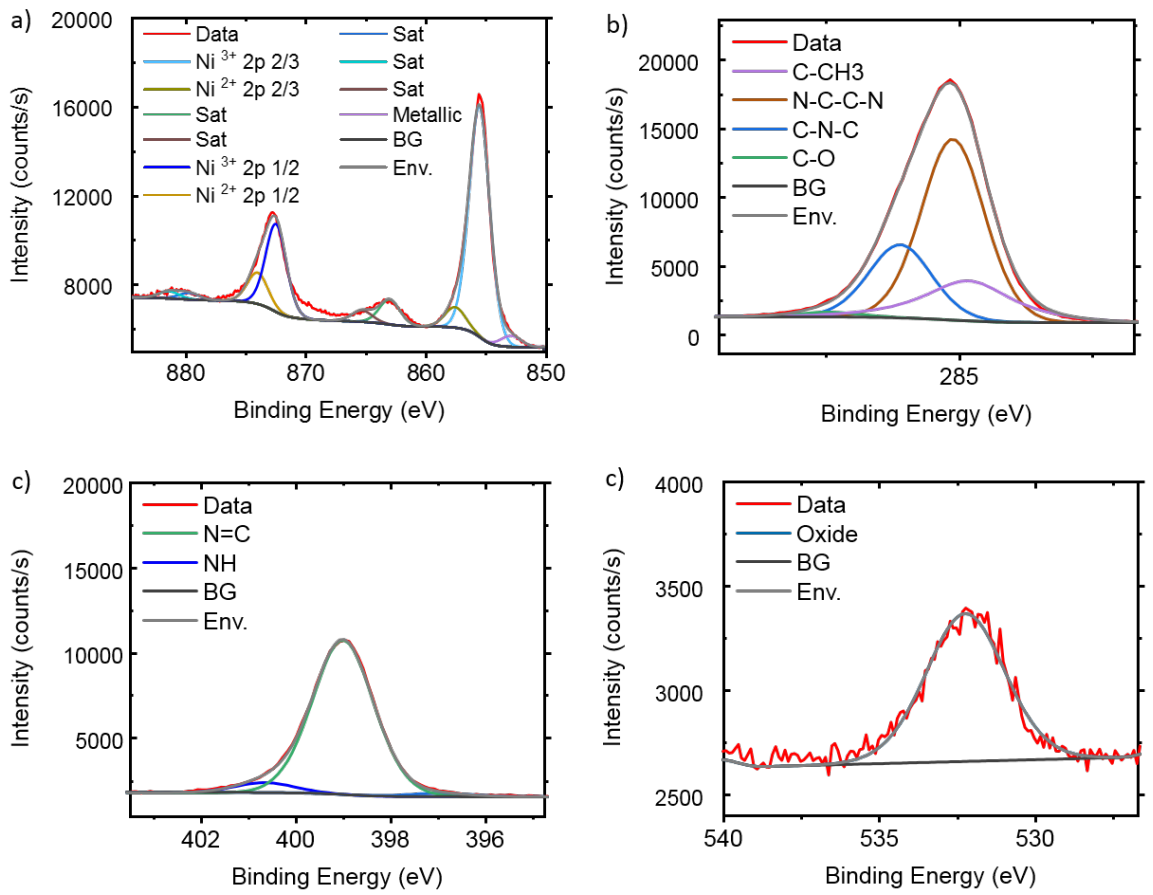


Figure A1.14 High resolution XPS and peak fittings of Ni-ZIF-67 NS in the (a) Ni 2*p*, (b) C 1*s*, (c) N 1*s* and (d) O 1*s* core level regions.

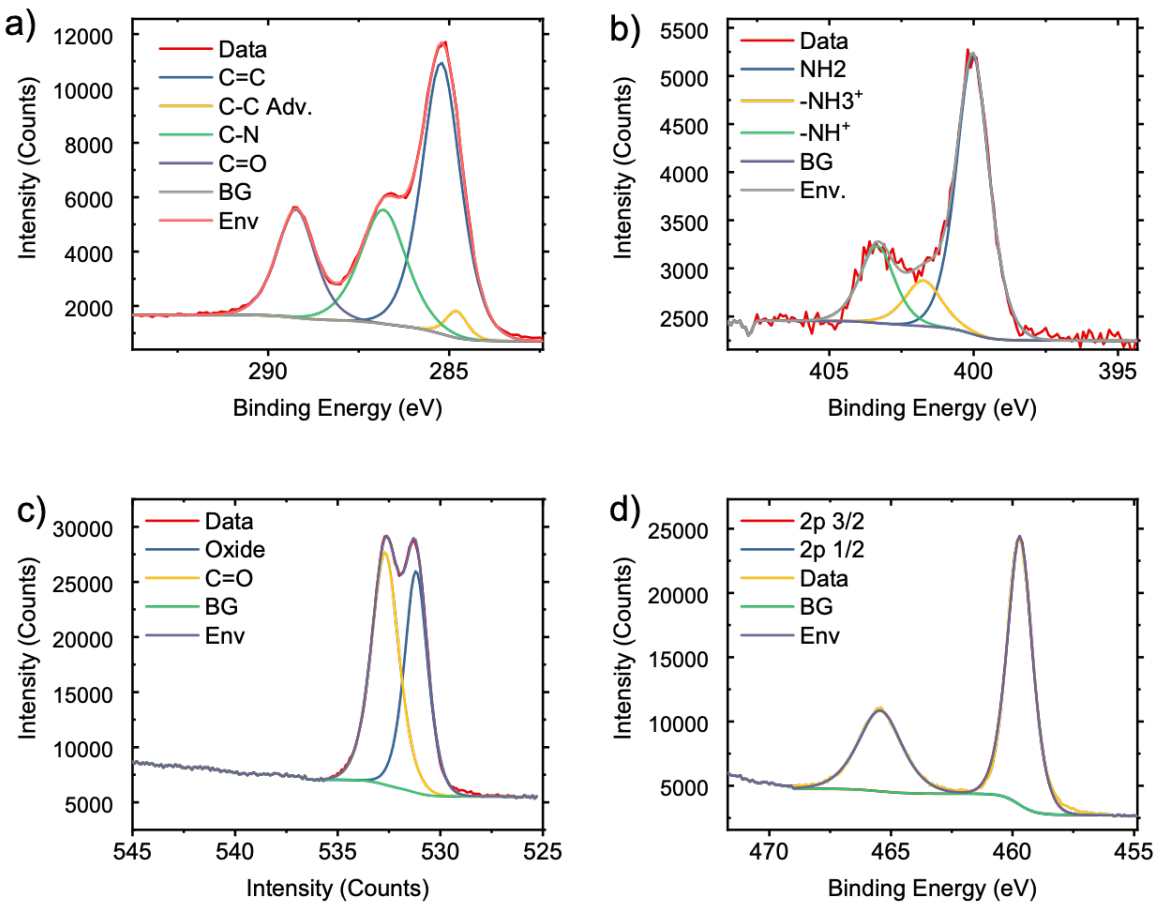


Figure A1.15 High resolution XPS and peak fittings of Ti-MIL-125-NH_2 in the: (a) C 1*s*, b) N 1*s*, (c) O 1*s* and (d) Ti 2*p* core level regions.

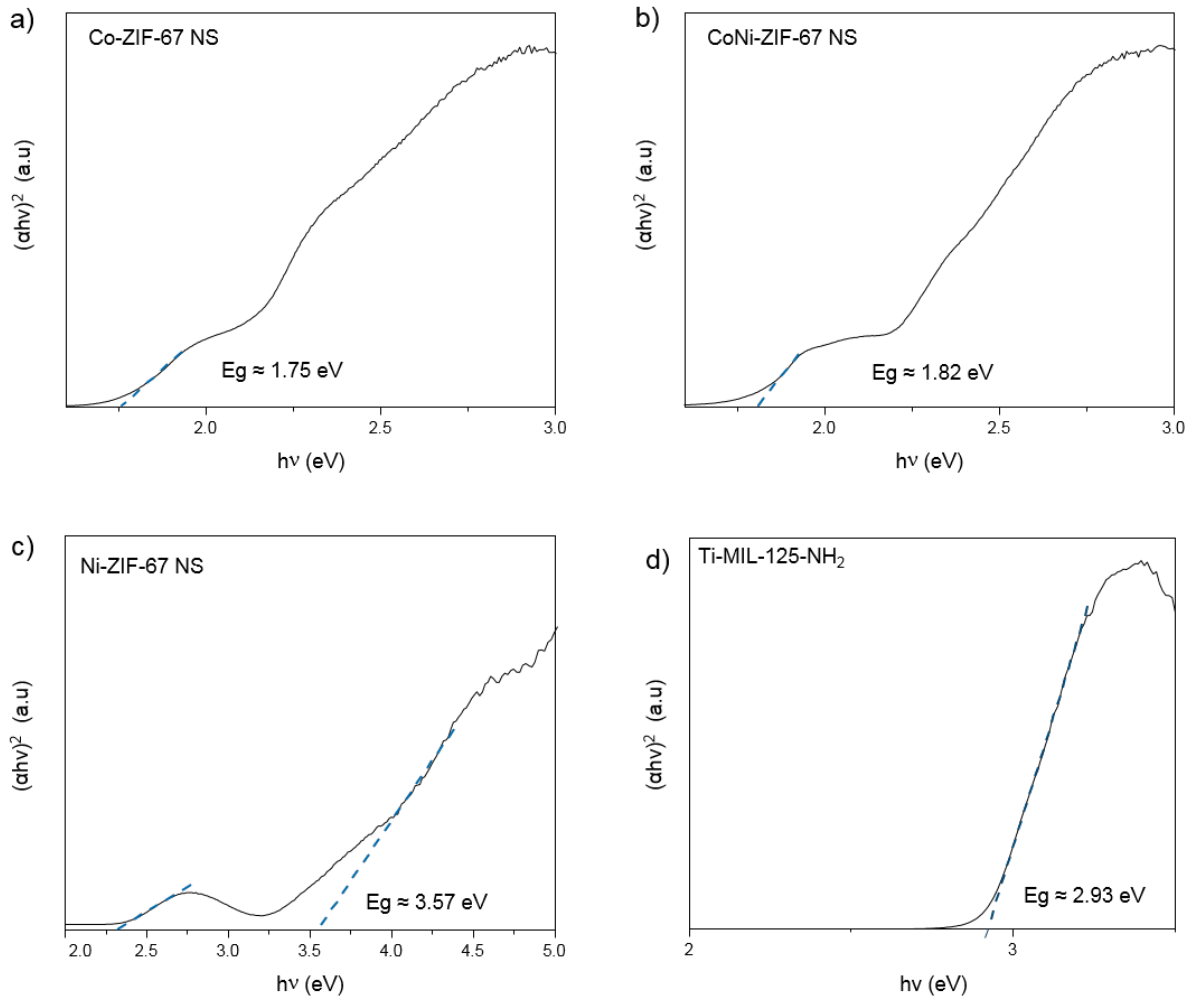


Figure A1.16. Tauc plots of (a) Co-ZIF-67 NS, (b) Co-ZIF-67 NS, (c) Ni-ZIF-67 NS and (d) Ti-MIL-125-NH_2

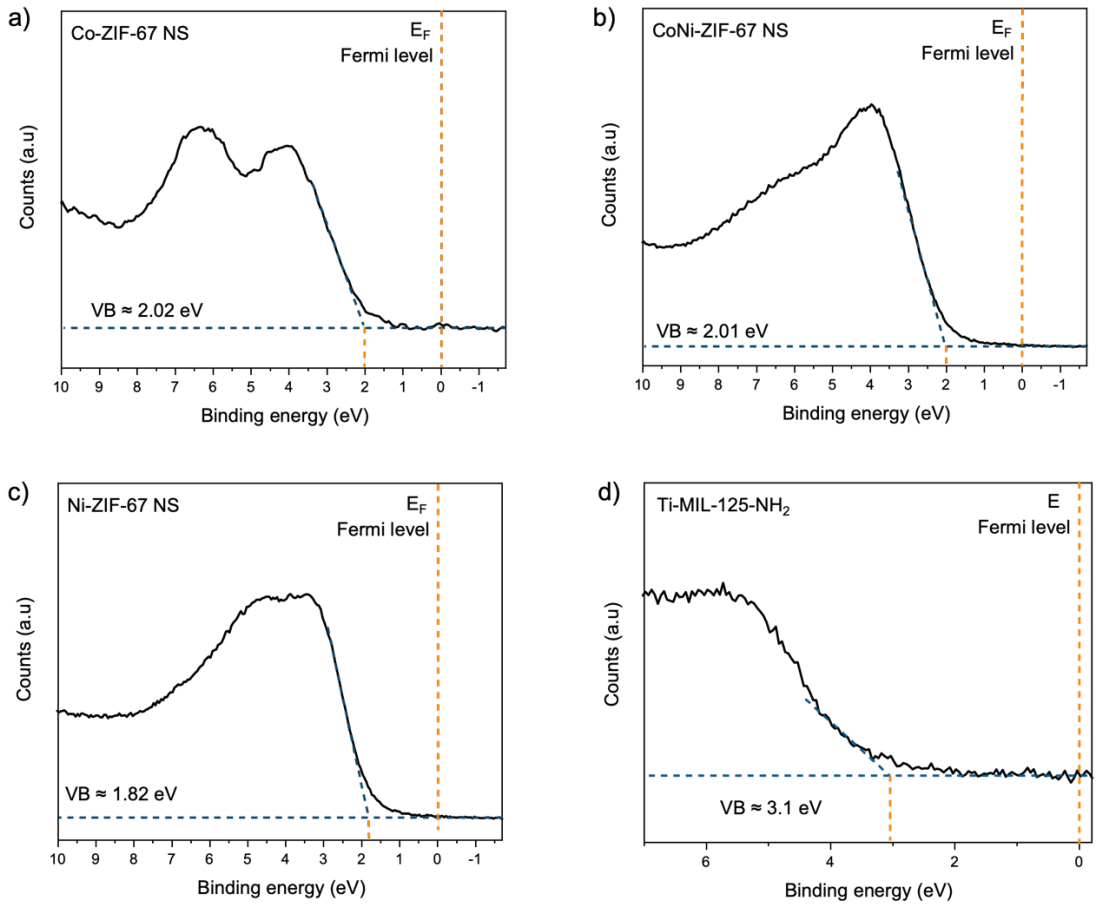


Figure A1.17 Valence band measurements of (a) Co-ZIF-67 NS, (b) CoNi-ZIF-67 NS, and (c) Ni-ZIF-67 NS.

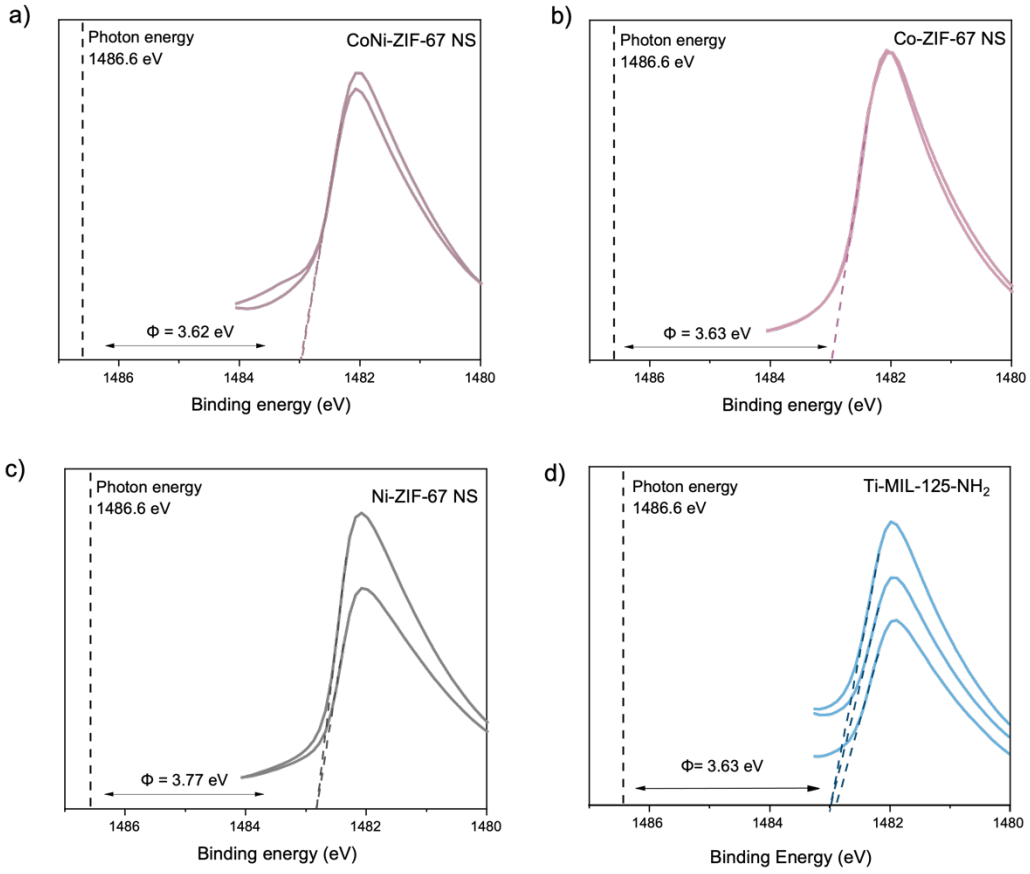


Figure A1.18 Work function measurements of (a) Co-ZIF-67 NS, (b) CoNi-ZIF-67 NS and (c) Ni-ZIF-67 NS.

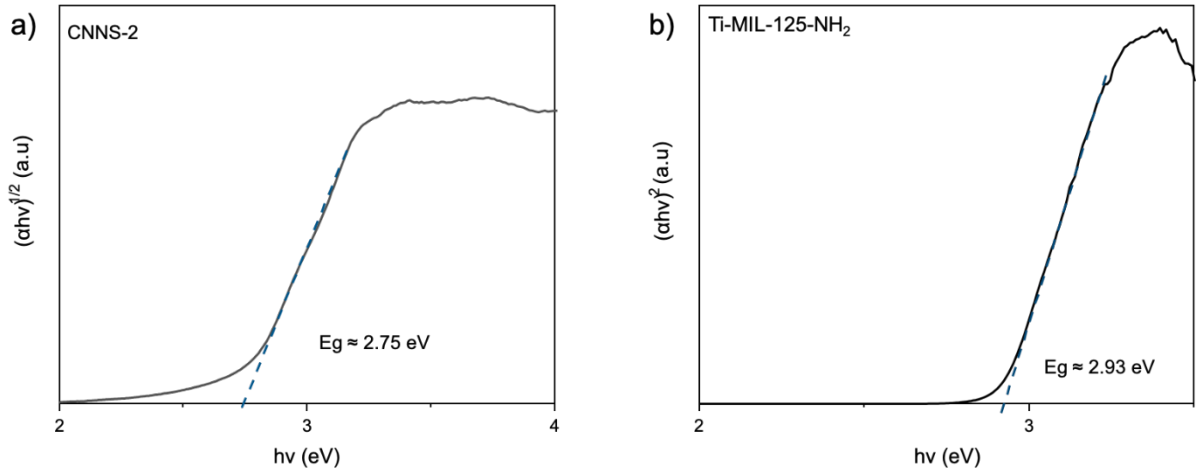


Figure A1.19 Tauc plots of (a) CNNS-2 and (b) Ti-MIL-125-NH_2.

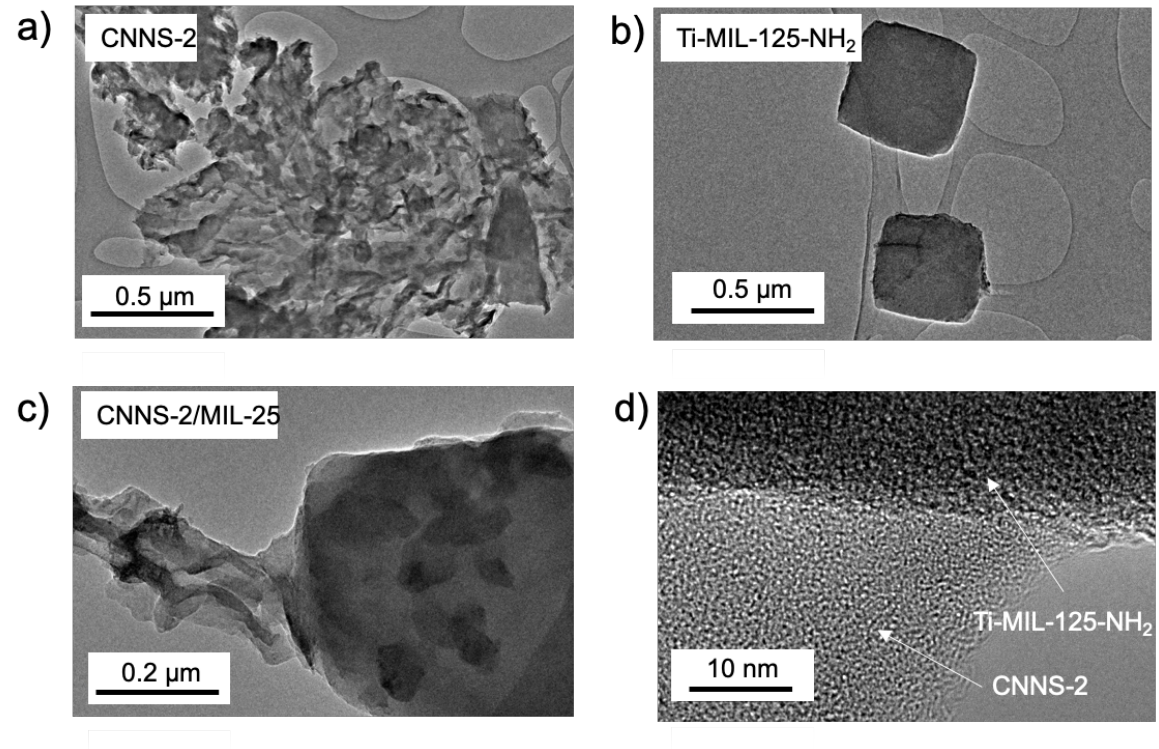


Figure A1.20 TEM images of: (a) CNNS-2, (b) Ti-MIL-125-NH_2 and (c), d) CNNS-2/MIL-25 (High resolution).

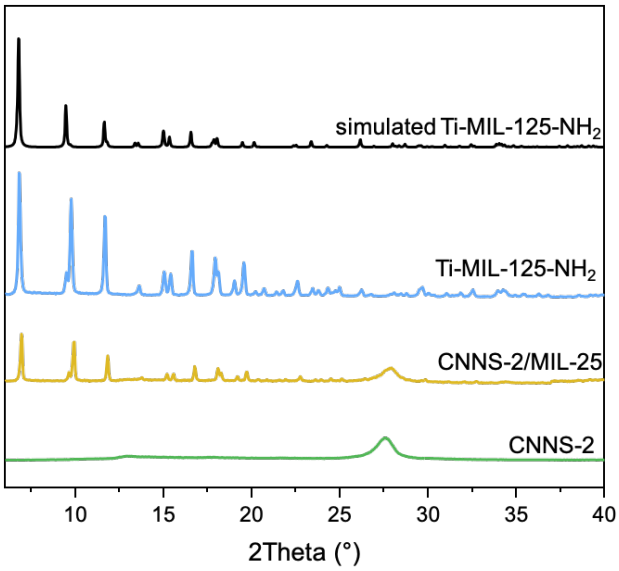


Figure A1.20 XRD patterns of CNNS-2, Ti-MIL-125-NH_2, CNNS-2/MIL-25 and the simulated Ti-MIL-125-NH_2. The measured XRD patterns of Ti-MIL-125-NH_2 are similar to the simulated one, confirming the successful synthesis of Ti-MIL-125-NH_2. In addition, CNNS-2/MIL-25 exhibits a combination of CNNS-2 and Ti-MIL-125-NH_2 patterns, indicating that both CNNS-2 and Ti-MIL-125-NH_2 have been successful incorporated in the heterojunction.

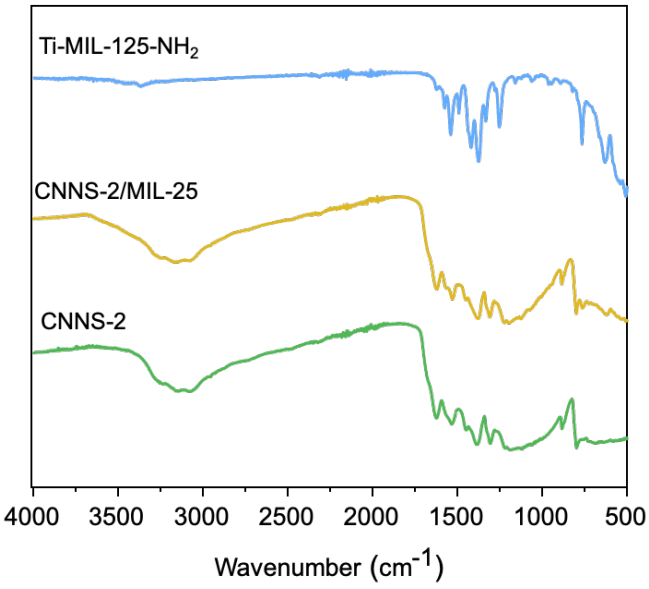


Figure A1.21 FTIR spectra of CNNS-2, Ti-MIL-125-NH_2 and CNNS-2/MIL-25.

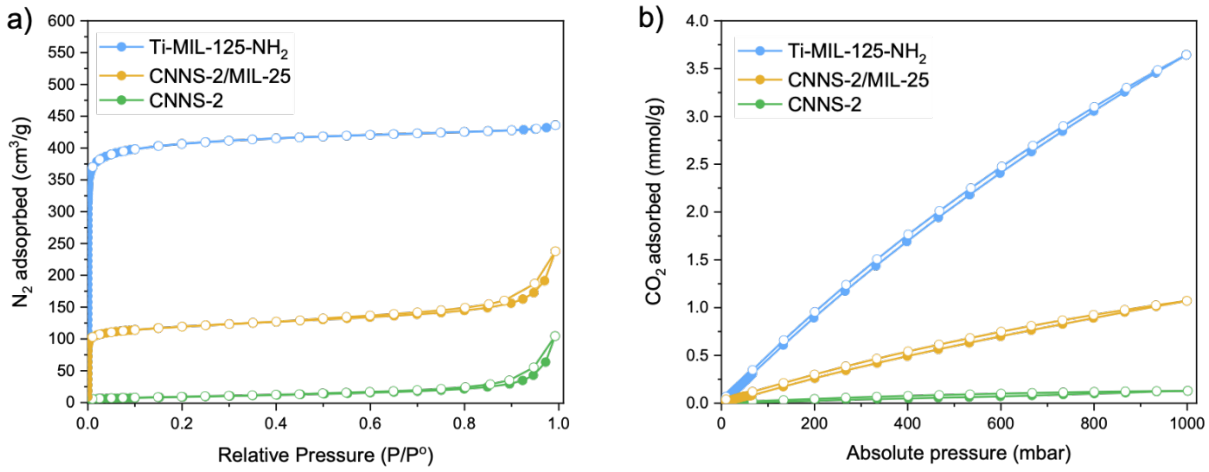


Figure A1.22 (a) N_2 sorption isotherms at -196 °C and **(**b) CO_2 sorption isotherms at 25 °C of Ti-MIL-125-NH_2, CNNS-2 and CNNS-2/MIL-25

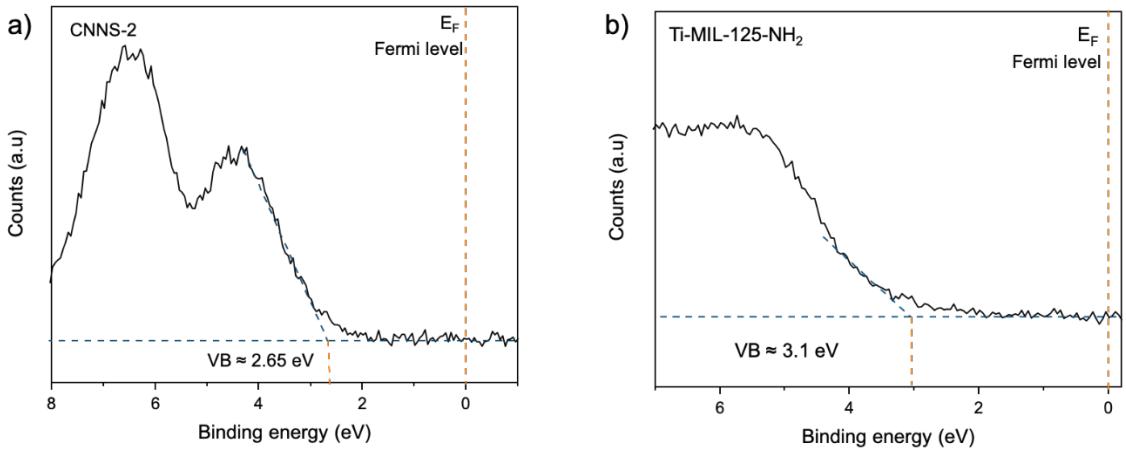


Figure A1.23 Valence band measurements of (a) CNNS-2 and (b) Ti-MIL-125-NH_2.

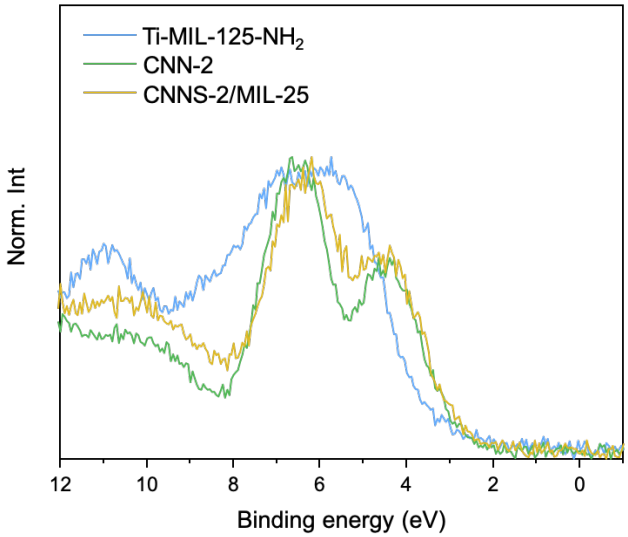


Figure A1.24 Valence band spectra of CNNS-2, Ti-MIL-125-NH_2 and CNNS-2/MIL-25.

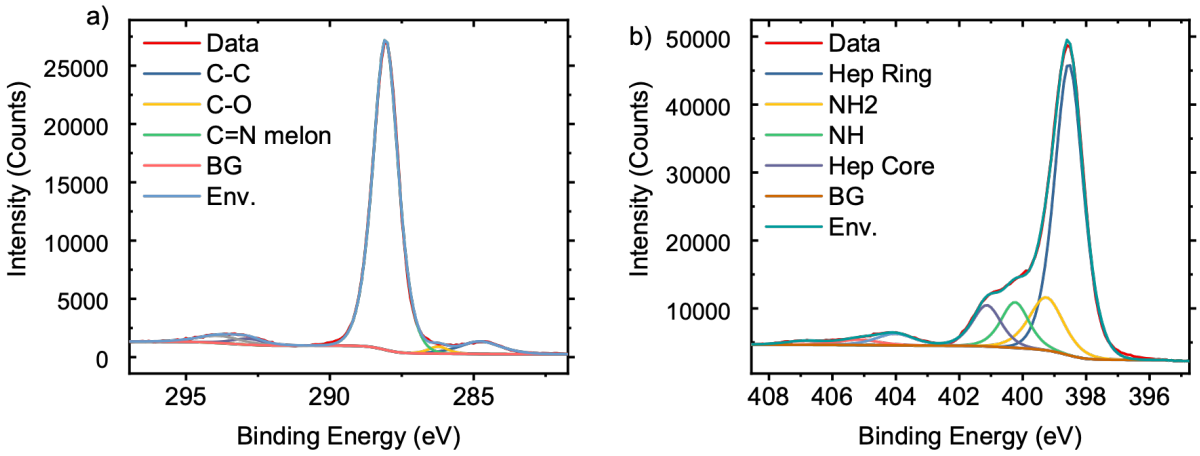


Figure A1.25 High resolution XPS and peak fittings of CNNS-2 in the (a) C 1*s* and (b) N 1*s* core level regions.

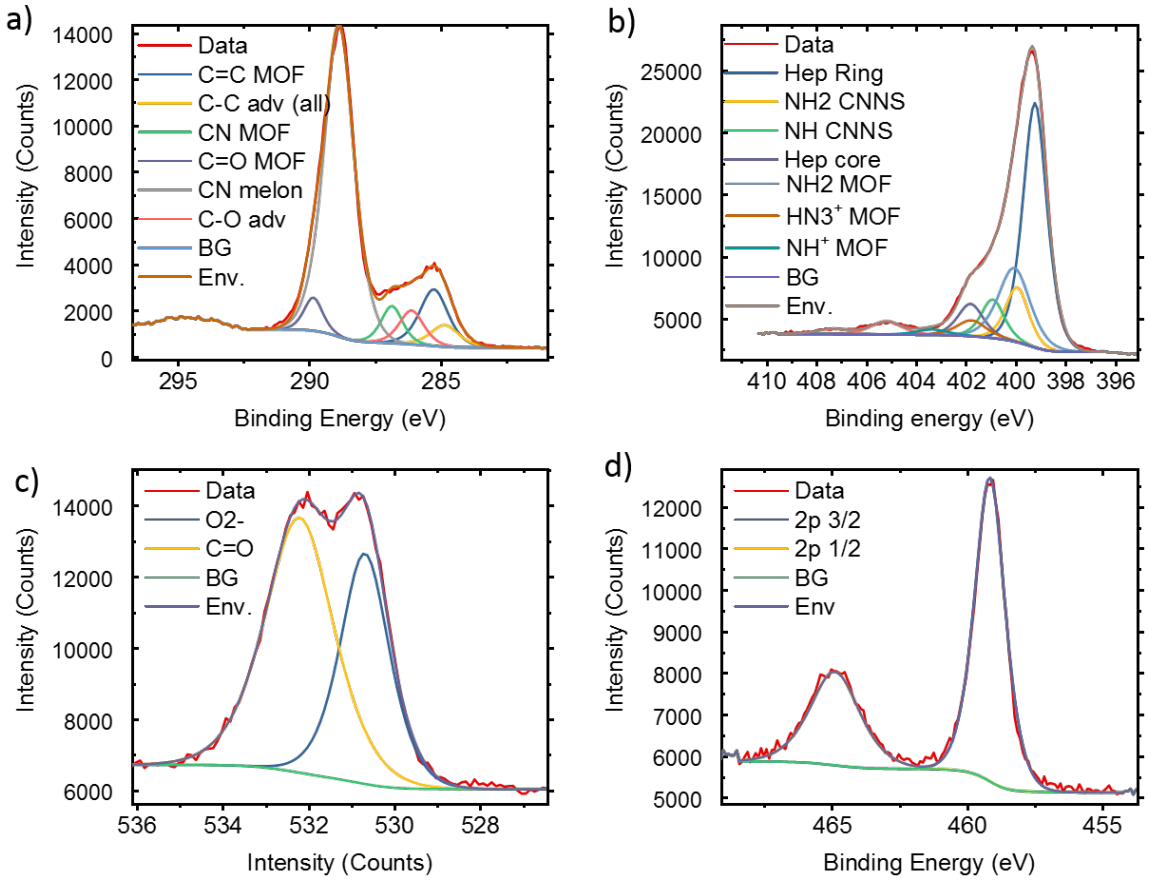


Figure A1.26 High resolution XPS and peak fittings of CNNS-2/MIL-25 in the: (a) C 1*s*, (b) N 1*s*, (c) O 1*s* and (d) Ti 2*p* core level regions.

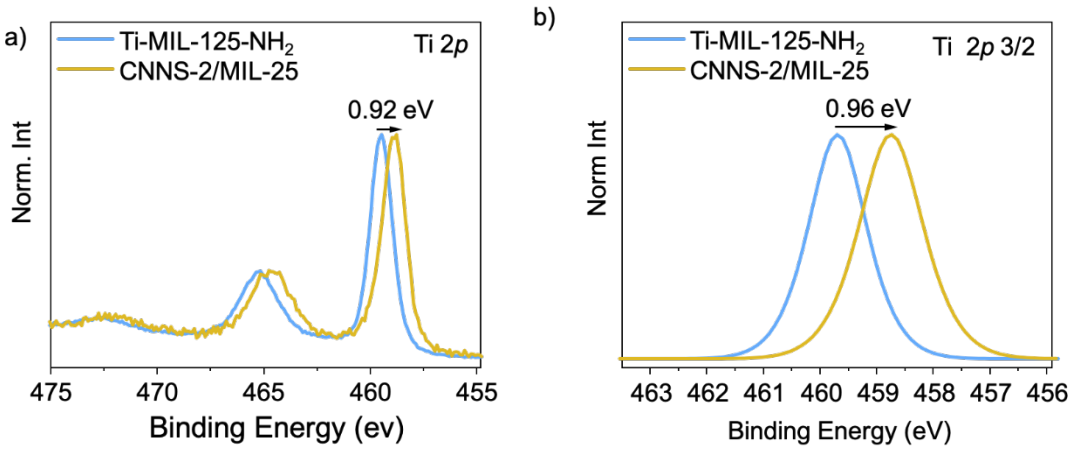


Figure A1.27 Comparison of Ti-MIL-125-NH_2 and CNNS-2/MIL-25 of the XPS in the: (a) Ti $2p_{3/2}$ (Ti^{4+}) and (b) O 1*s* (metal oxide; O^{2-}) deconvolution, illustrating the Fermi level shift.

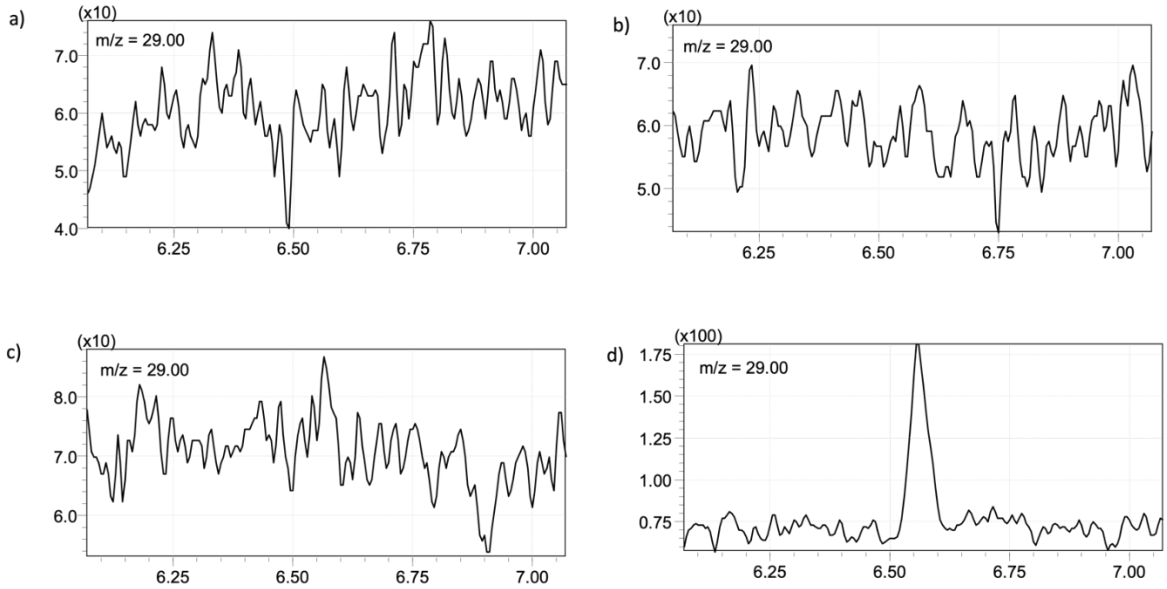


Figure A1.28 Mass spectrum chromatogram of CNNS-2/MIL-25 illustrating the ^{13}CO (m/z = 29) peak observed with $^{12}CO_2$ after (a) 0 min and (b) 5 h UV-Vis irradiation, and the ^{13}CO (m/z = 29) peak observed with $^{13}CO_2$ after (c) 0 min and (d) 5 h UV-Vis irradiation.

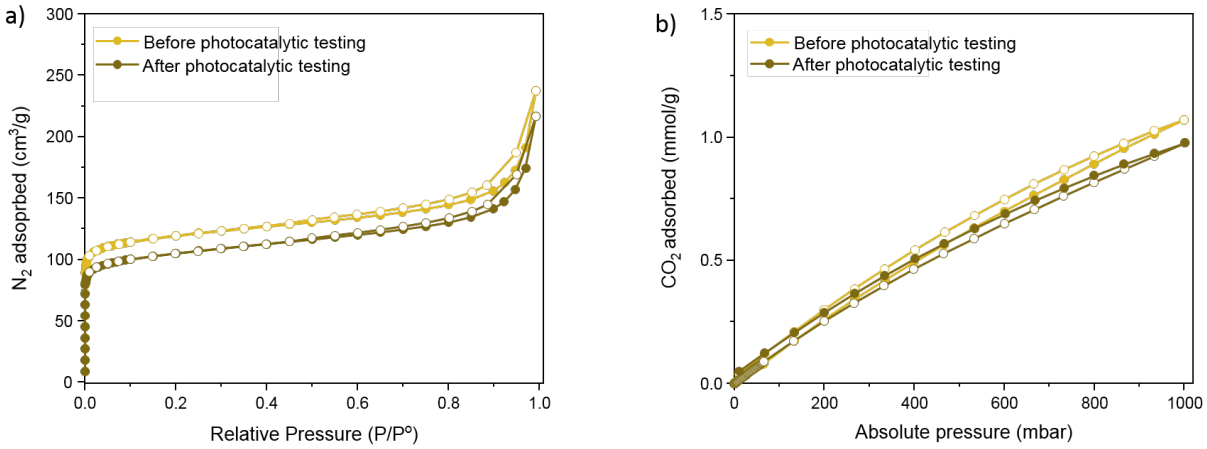


Figure A1.29 (a) N_2 adsorption isotherms at -196 °C and (b) CO_2 adsorption isotherms at 25 °C of CNNS-2/MIL-25 before and after CO_2 photoreduction tests.

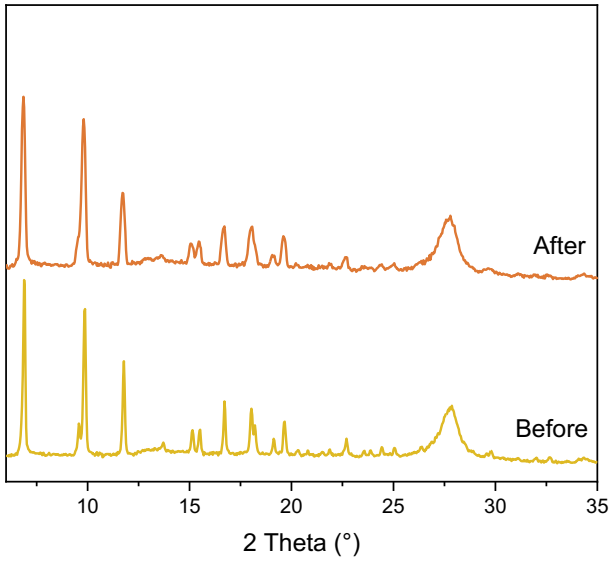


Figure A1.30 XRD patterns of CNNS-2/MIL-25 before and after CO_2 photoreduction tests.

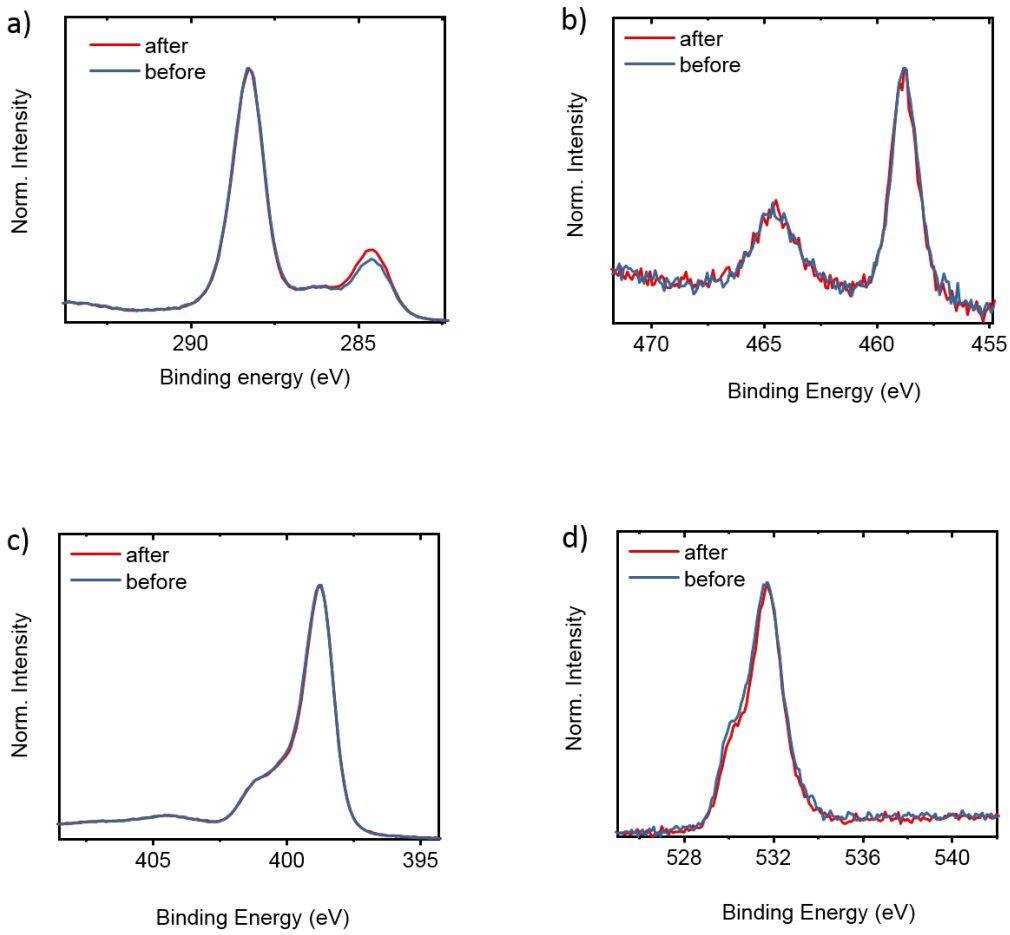


Figure A1.32 High resolution XPS of CNNS-2/MIL-25 before and after photocatalytic testing in the: (a) C 1*s*, (b) Ti 2*p* (c) O 1*s* and (d) N 1*s* core level regions.

References:

1. Xu, G. L.; Zhang, H. B.; Wei, J.; Zhang, H. X.; Wu, X.; Li, Y.; Li, C. S.; Zhang, J.; Ye, J. H., Integrating the g-C3N4 Nanosheet with B-H Bonding Decorated Metal-Organic Framework for CO2 Activation and Photoreduction. *Acs Nano* **2018,** *12* (6), 5333-5340.

2. Li, X.; Song, X. H.; Ma, C. C.; Cheng, Y. L.; Shen, D.; Zhang, S. M.; Liu, W. K.; Huo, P. W.; Wang, H. Q., Direct Z-Scheme WO3/Graphitic Carbon Nitride Nanocomposites for the Photoreduction of CO2. *Acs Appl Nano Mater* **2020,** *3* (2), 1298-1306.

3. Crake, A.; Christoforidis, K. C.; Godin, R.; Moss, B.; Kafizas, A.; Zafeiratos, S.; Durrant, J. R.; Petit, C., Titanium dioxide/carbon nitride nanosheet nanocomposites for gas phase CO2 photoreduction under UV-visible irradiation. *Appl Catal B-Environ* **2019,** *242*, 369-378.

4. Wang, M. H.; Yang, L. Y.; Yuan, J. Y.; He, L. H.; Song, Y. P.; Zhang, H. Z.; Zhang, Z. H.; Fang, S. M., Heterostructured Bi2S3@NH2-MIL-125(Ti) nanocomposite as a bifunctional photocatalyst for Cr(VI) reduction and rhodamine B degradation under visible light. *Rsc Adv* **2018,** *8* (22), 12459-12470.

5. Liu, H.; Zhang, J.; Ao, D., Construction of heterostructured ZnIn2S4@NH2-MIL-125(Ti) nanocomposites for visible-light-driven H-2 production. *Appl Catal B-Environ* **2018,** *221*, 433-442.

6. Wang, L.; Zhang, Z.; Han, Q.; Liu, Y.; Zhong, J.; Chen, J.; Huang, J.; She, H.; Wang, Q., Preparation of CdS-P25/ZIF-67 composite material and its photocatalytic CO2 reduction performance. *Appl Surf Sci* **2022,** *584*, 152645.

7. Shao, W.; Chen, Y. R.; Xie, F.; Zhang, H.; Wang, H. T.; Chang, N., Facile construction of a ZIF-67/AgCl/Ag heterojunction via chemical etching and surface ion exchange strategy for enhanced visible light driven photocatalysis. *Rsc Adv* **2020,** *10* (63), 38174-38183.

8. Moss, B.; Wang, Q.; Butler, K. T.; Grau-Crespo, R.; Selim, S.; Regoutz, A.; Hisatomi, T.; Godin, R.; Payne, D. J.; Kafizas, A.; Domen, K.; Steier, L.; Durrant, J. R., Linking in situ charge accumulation to electronic structure in doped SrTiO3 reveals design principles for hydrogen-evolving photocatalysts. *Nat Mater* **2021,** *20* (4), 511-517.

9. Glover, E. N. K.; Ellington, S. G.; Sankar, G.; Palgrave, R. G., The nature and effects of rhodium and antimony dopants on the electronic structure of TiO2: towards design of Z-scheme photocatalysts. *J Mater Chem A* **2016,** *4* (18), 6946-6954.

Appendix 2

Table A2.1 Atomic composition of HCP-1, HCP-2, and HCP-3 before and after irradiation as well as residual Fe content for all networks.

Samples	O [post-irradiation] (wt.%)[a]	N [post-irradiation] (wt.%)[a]	C [post-irradiation] (wt.%)[a]	Fe (ppm)[b]
HCP-1	11.38 [10.29]	- [-]	76.09 [78.81]	14500
HCP-2	4.12 [4.83]	1.34 [1.47]	88.82 [88.27]	487
HCP-3	3.55 [3.89]	7.05 [7.06]	81.47 [81.03]	31

[a] Determined using CHNS-O analysis.

[b] Determined using ICP-OES.

Figures in square brackets refer to data measured for polymers post-irradiation.

Table A2.2 Textural parameters derived from N_2 sorption isotherms at -196 °C and CO_2 adsorption capacities at 25 °C.

Sample	V_{MICRO} ($cm^3.g^{-1}$)[a]	V_{TOT} ($cm^3.g^{-1}$)[a]	SA_{BET} ($m^2.g^{-1}$)[a]	CO_2 ad. ($mmol.g^{-1}$)	
				Dry[b]	Wet[c]
HCP-1	0.46	1.07	951	1.25	0.99
HCP-2	0.13	0.21	311	0.78	0.82
HCP-3	0.16	0.25	357	0.92	0.89
HCP-3 after irradiation	0.11	-	300	0.77	-

[a] Derived from N_2 sorption isotherms at -196 °C .

[b] Capacity of degassed HCP at 25 °C and 1 bar.

[c] Capacity of non-degassed HCP at 25 °C and 1 bar after 48 h exposure to humid atmosphere.

Table A2.3. Photocatalytic evolution rates of HCP-1, HCP-2, HCP-3, and TiO_2 P25 and control experiments.

Sample	UV-vis (Sacrificial H_2)		UV-Vis (Sacrificial H_2O)		Visible (Sacrificial H_2O)	
	CO*	CH_4*	CO*	CH_4*	CO*	CH_4*
HCP-1	3.7 ± 0.1	0	8.6 ± 0.1	0.4 ± 0.1	4.2	0.1
HCP-2	1.6 ± 0.3	0.1 ± 0.1	4.6 ± 0.5	0.4 ± 0.2	1	0
HCP-3	6.3 ± 0.2	0.5 ± 0.1	15.6 ± 0.9	0.4 ± 0.1	5.2	0.1
P25 (TiO_2)	6.4 ± 0.4	0.3 ± 0.2	14.7 ± 0.9	0.3 ± 0.1	0.69	0.2
HCP-1[a] "dry condition"	-	-	2.87	-	-	-
HCP-2[a] "dry condition"	-	-	1.67	-	-	-
HCP-3[a] "dry condition"	-	-	6.0	-	-	-
N_2/H_2O, no catalyst	-	-	0	-	-	-
N_2/H_2O [b]	-	-	3.58 (23% [c])	-	-	-
N_2/H_2O repeat [b,c]	-	-	3.78 (24% [c])	-	-	-
N_2/H_2O b	-	-	-	-	0.82 (15% [c])	-
N_2/H_2O repeat [b,c]	-	-	-	-	1.06 (20% [c])	-
N_2/H_2 [b]	0.74 (12% [c])	-	-	-	-	-
N_2/H_2 repeat [b,c]	0.61 (10% [c])	-	-	-	-	-
CO_2/ H_2O, no light [b]	-	-	0.16 (1% [c])	-	-	-
CO_2/ H_2O, no catalyst	-	-	10 ppm	-	-	-

* All data are given in $\mu mol.g^{-1}.h^{-1}$.

[a] Samples were exposed to a humid environment (> 99% humidity) overnight before photocatalysis.

[b] Tests were performed on HCP-3, the leading material of this study.

[c] Repeat samples were done on the same sample as the first one, without opening the photo-reactor.

[d] Percentage compared to the total activity of HCP-3.

Table A2.4 Photocatalytic evolution rates of HCP-1, HCP-2, HCP-3 in μmol.cm^{-2}·h^{-1}.

Sample	UV-Vis (Sacrificial H_2O)	Visible (Sacrificial H_2O)
	CO*	**CO***
HCP-1	8.14*10^{-3}	4.68*10^{-3}
HCP-2	6.93*10^{-3}	2.18*10^{-3}
HCP-3	17.96 *10^{-3}	7.23*10^{-3}

* All data are given in μmol.cm^{-2}·h^{-1}

Table A2.5 Quantum efficiency calculation of HCP-3

Sample	UV-vis irradiation (sacrificial H_2O)	Visible irradiation (sacrificial H_2O)
HCP-3	0.002 %	0.0005 %

*The quantum efficiency was calculated from a polychromatic light source. The total number of absorbed photons across the wavelength range (200 - 900 nm for UV-Vis and 400 - 900 nm for visible irradiation) was taken into consideration.

Table A2.6 Apparent quantum yields (AQY) or quantum efficiencies (QE) and production rates of HCP-3 and a selection of organic photocatalysts.

Type of photocatalysts	**Phase**	**Irradiation conditions**	**Production rate ($umol.g^{-1}.h^{-1}$)**	**AQY**	**Ref.**
Triphenylamine based conjugated microporous polymers	Gas	300 W Xe lamp, > 420 nm	37	0.19% (420 nm)	188888 888888 788
Conjugated polymer (PEosinY-1)	Gas	300 W Xe lamp, > 420 nm	33	-	2
Triazine based 2D COF	Gas	300 W high pressure Xe lamp, > 420 nm	103	0.010% (full spectrum, QE)	3
Boron-doped carbon nitride	Gas	500 W Xe arc lamp, UV-Vis	1.23	-	4
HCP-3 (This study)	Gas	300 W Xe lamp, UV-Vis	15.6	0.002% (full spectrum, QE)	-
HCP-3 (This study)	Gas	300 W Xe lamp, > 420nm	5.2	0.0005% (full spectrum, QE)	-



Figure A2.1 Photographic images of: HCP-1, HCP-2 and HCP-3 (from left to right, respectively).

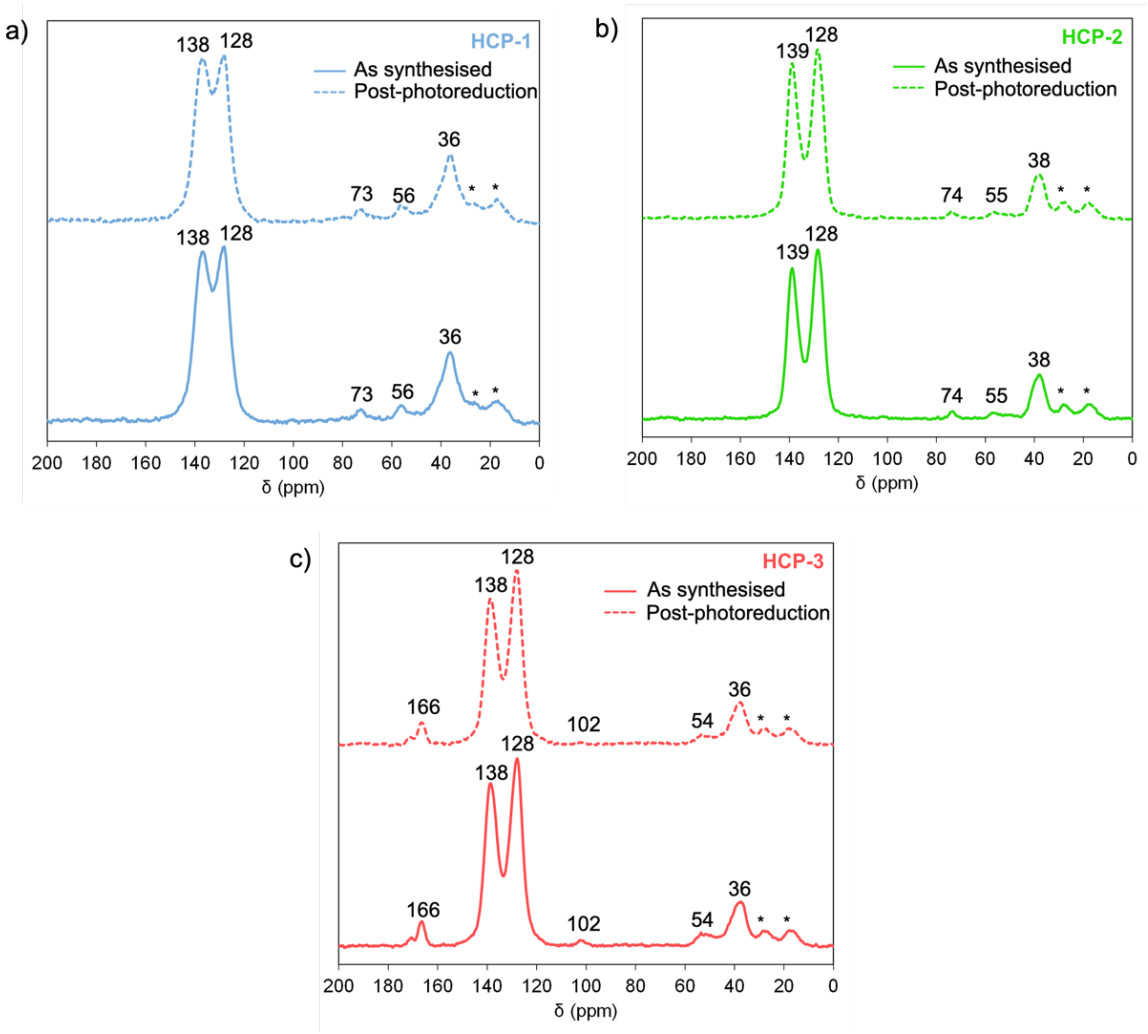


Figure A2.2 Solid-state NMR spectra of networks as synthesised and post CO_2 photoreduction, (a) HCP-1, (b) HCP-2, and (c) HCP-3. Spinning sidebands are labelled with an asterisks.

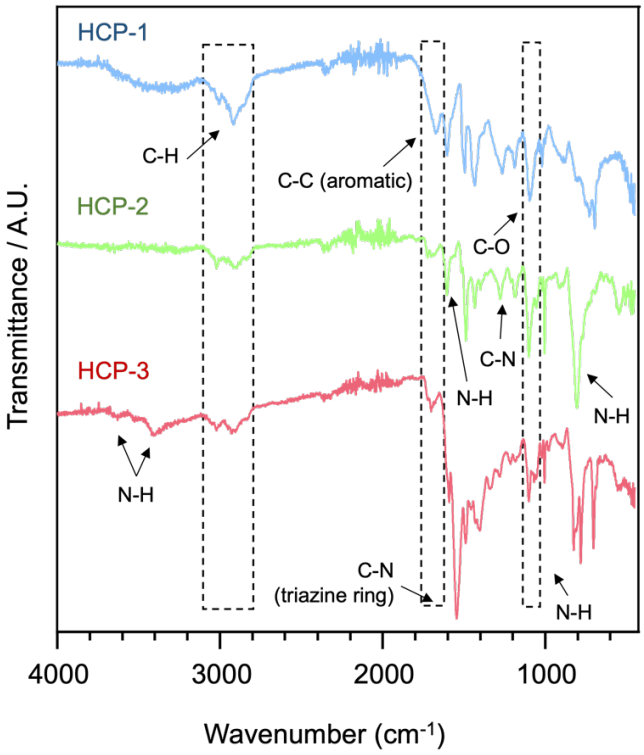


Figure A2.3 FTIR spectra of HCP-1 (blue), HCP-2 (green) and HCP-3 (red). Signals present in all spectra are highlighted by dashed lines.

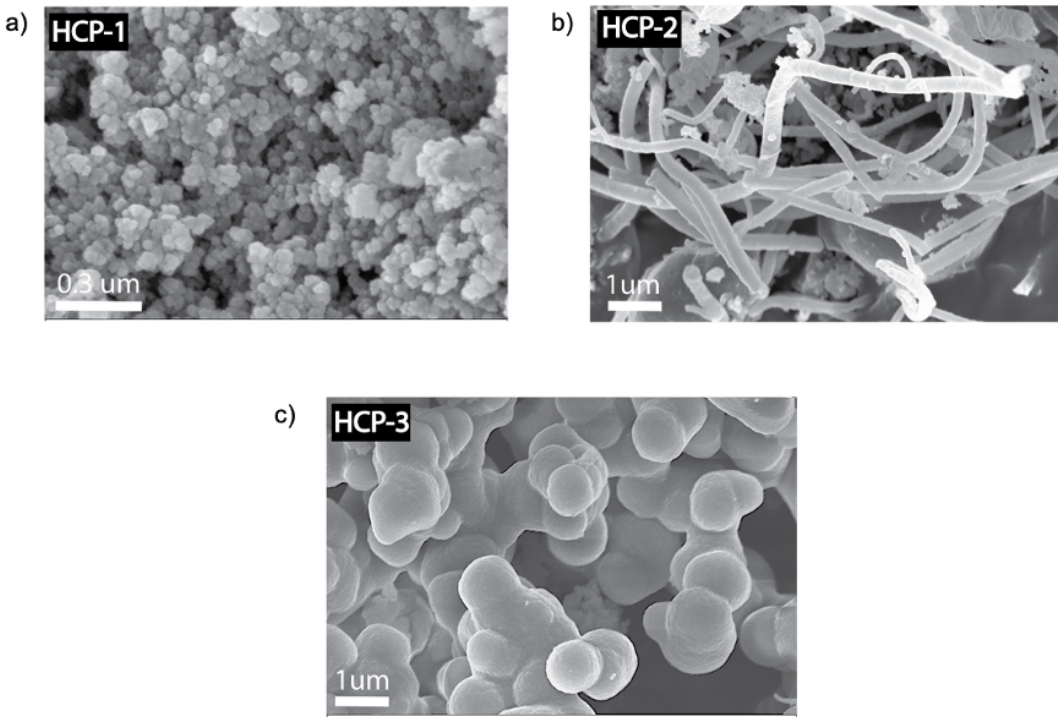


Figure A2.4 SEM images of (a) HCP-1, (b) HCP-2, and (c) HCP-3.

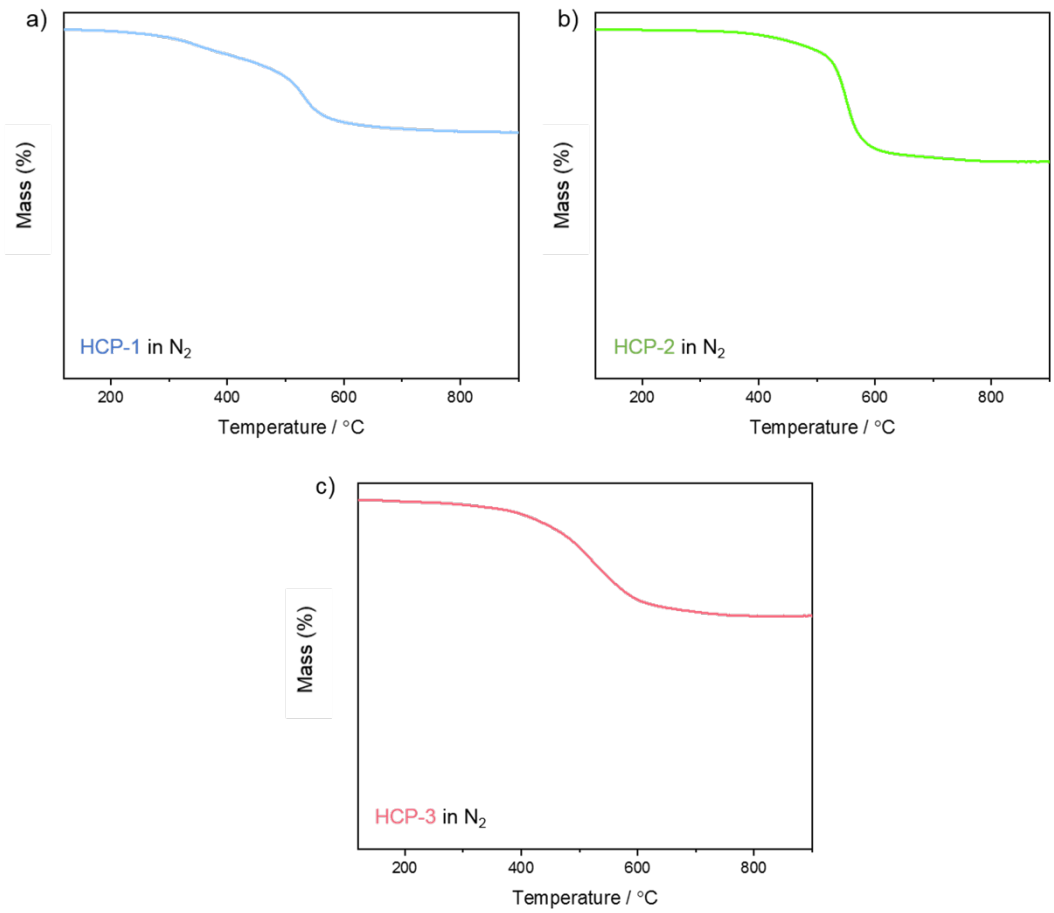


Figure A2.5 TGA thermograms up to 900 °C in a N_2 atmosphere, heated at a ramp rate of 10 °C.min^{-1} with a N_2 flow rate of 100 mL.min^{-1}. (a) HCP-1, (b) HCP-2, and (c) HCP-3.

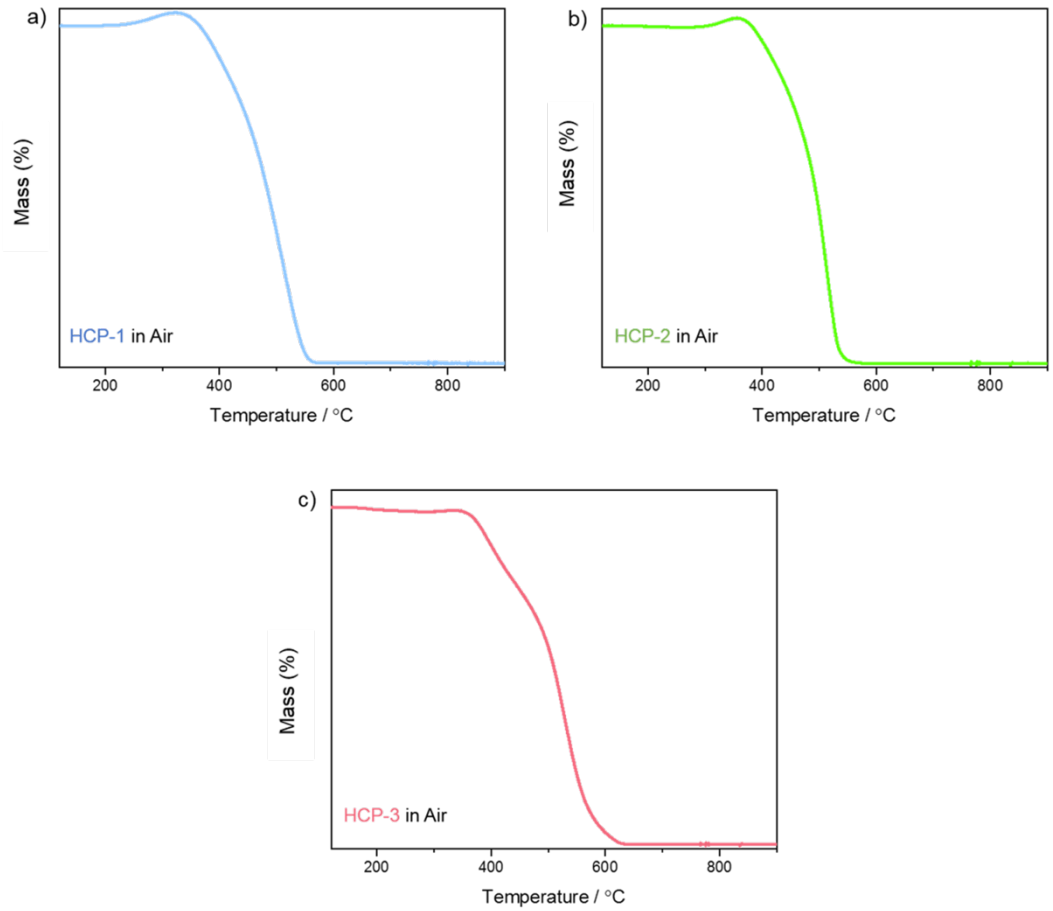


Figure A2.6 TGA thermograms up to 900 °C in air, heated at a ramp rate of 10 °C.min^{-1} with an air flow rate of 100 mL.min^{-1}. (a) HCP-1, (b) HCP-2, and (c) HCP-3.

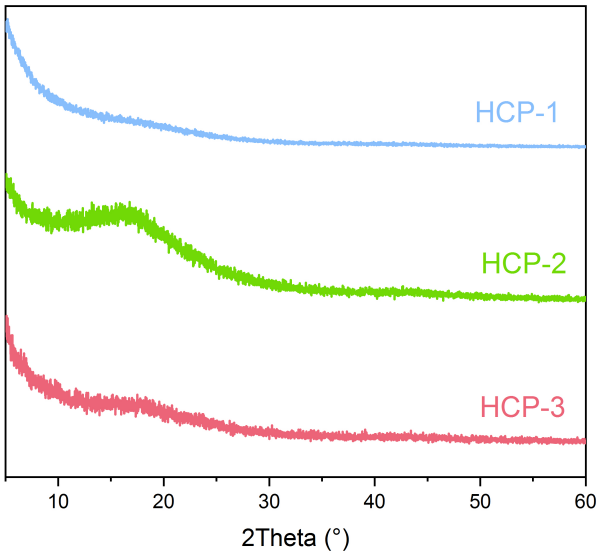


Figure A2.7 PXRD patterns of (a) HCP-1, (b) HCP-2, and (c) HCP-3.

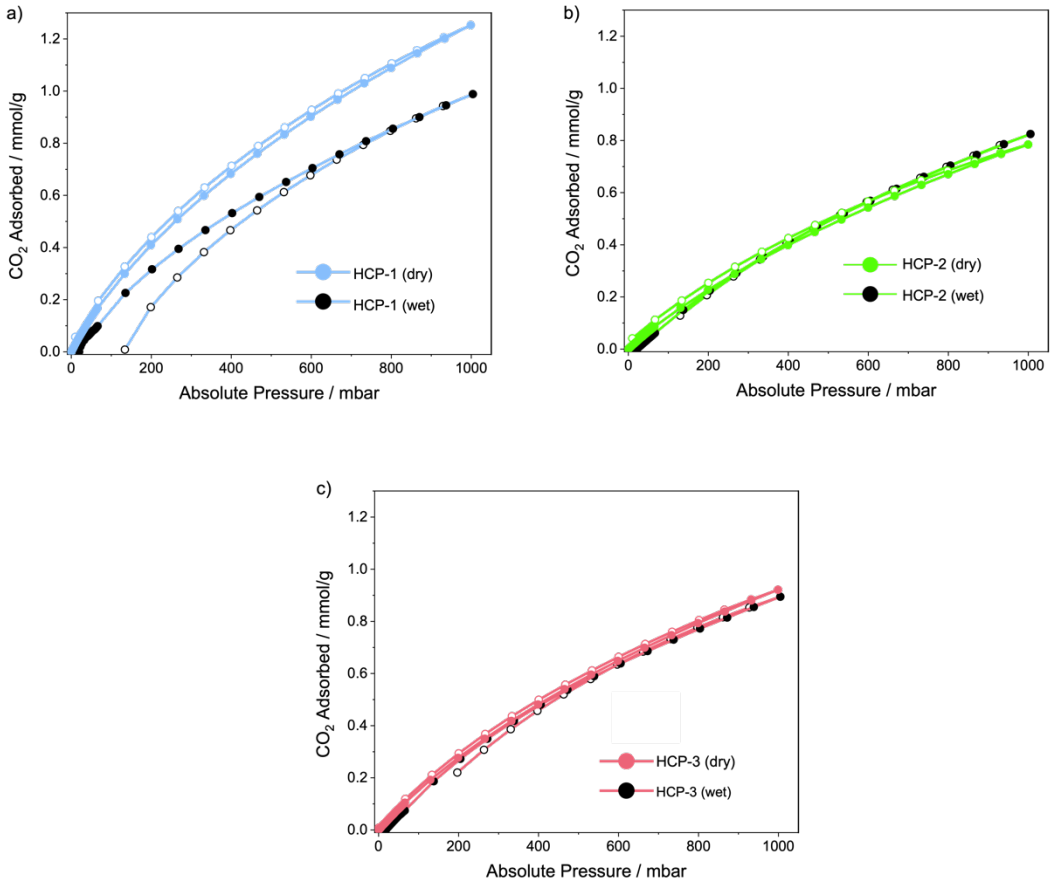


Figure A2.8 CO_2 adsorption isotherms at 25 °C of both dry and wet (i.e. exposed to humid air for at least 48 h before measurement, 99% humidity) networks. (a) HCP-1, (b) HCP-2, and (c) HCP-3. Filled symbols represent adsorption, empty symbols represent desorption.

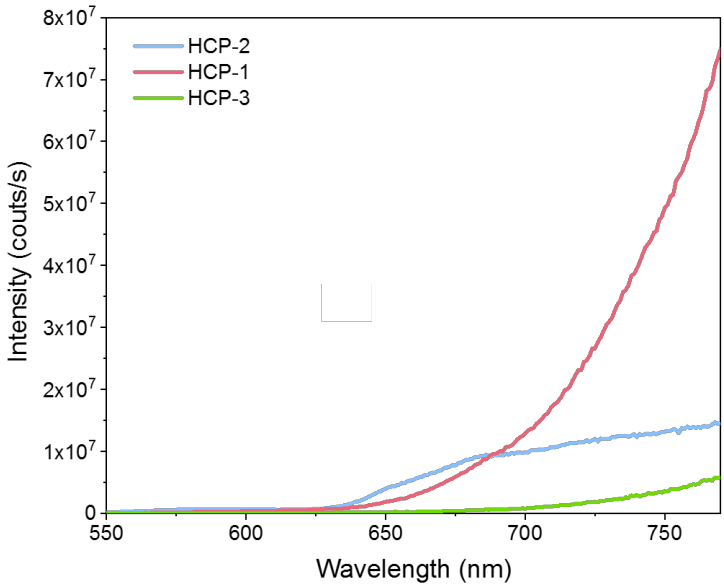


Figure A2.9 Photoluminescence emission spectra

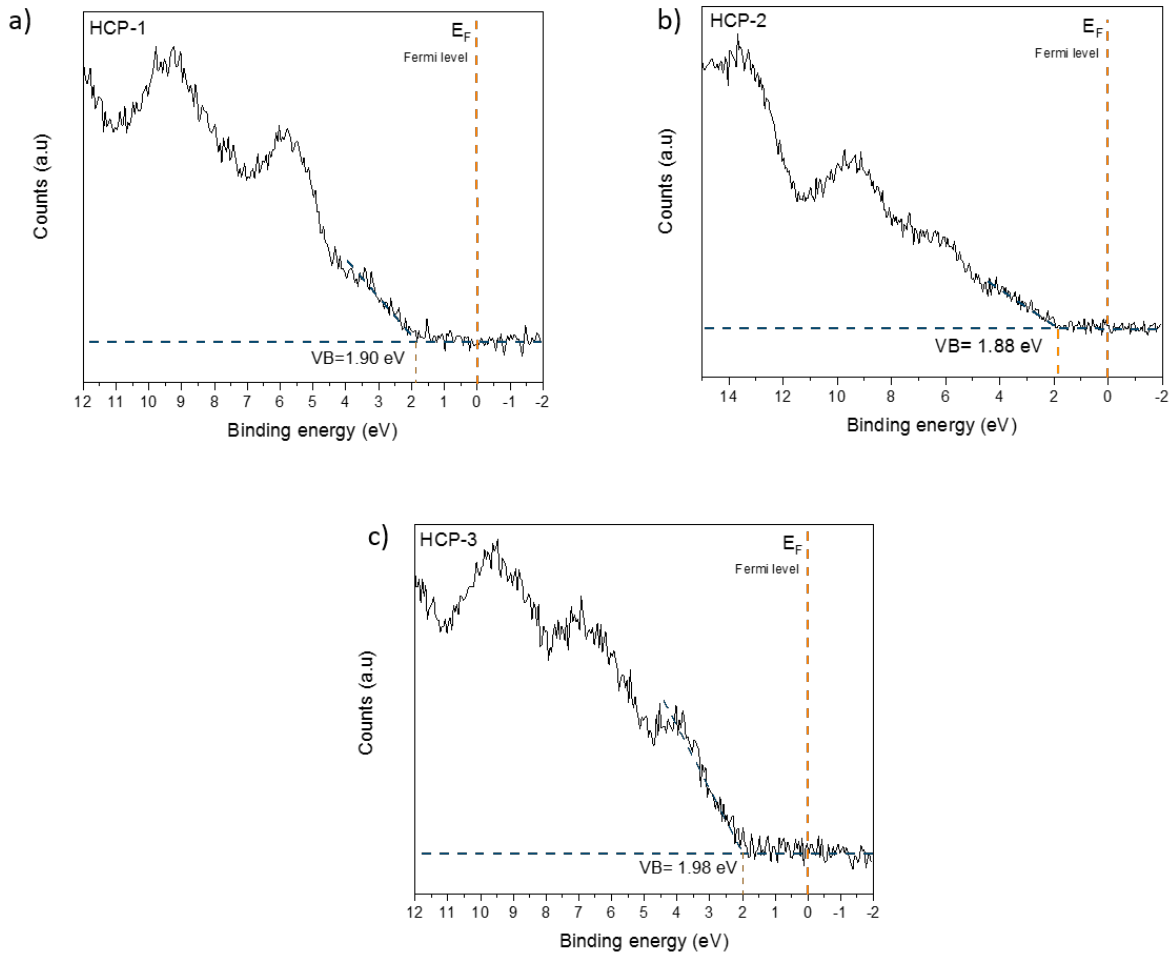


Figure A2.10 Valence band XPS spectra of (a) HCP-1, (b) HCP-2, and HCP-3. To account for potential variation on the surface valence band measurements were collected on an area of 4 different points.

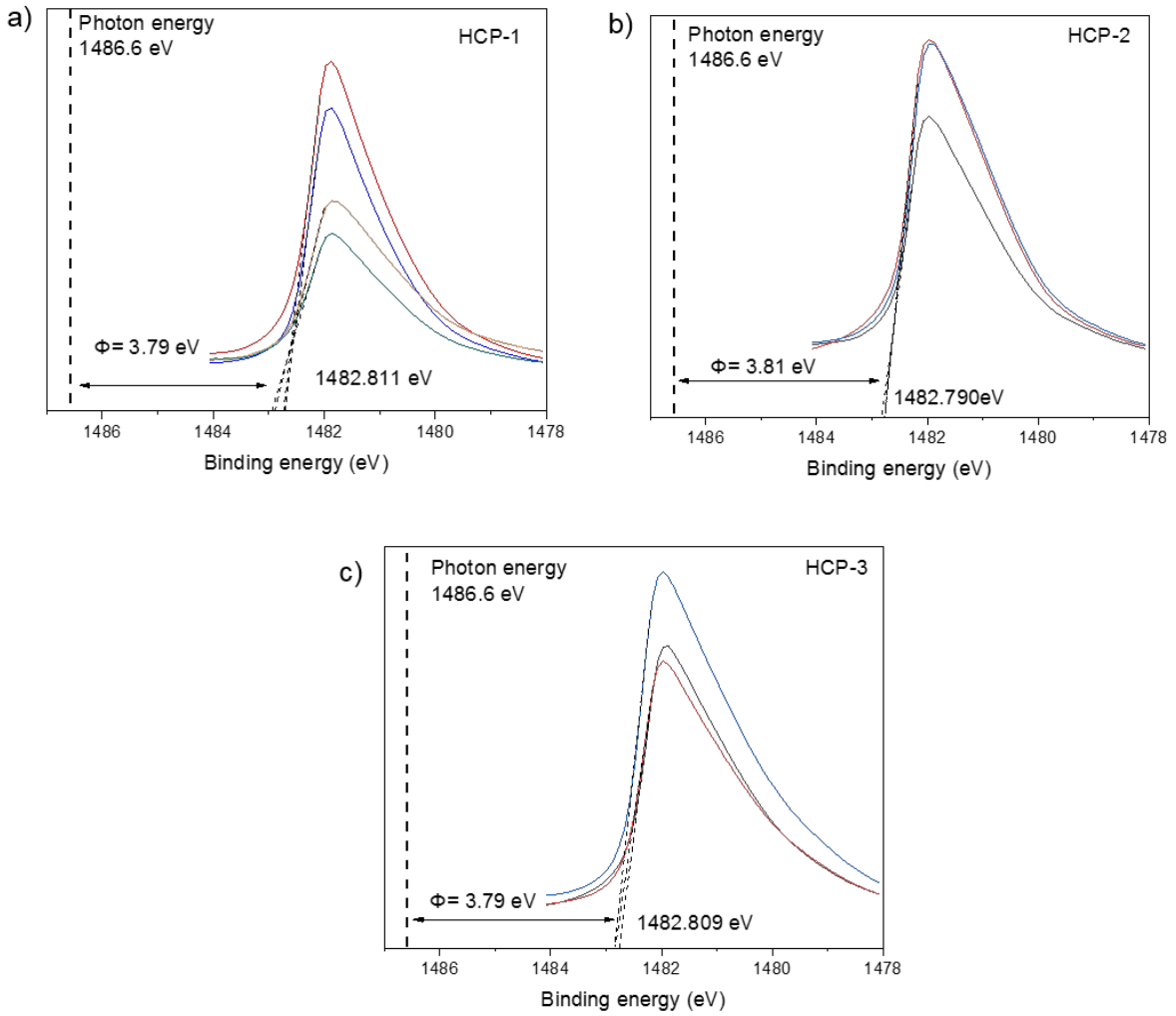


Figure A2.11 Work function measurements at different locations on a) HCP-1, b) HCP-2, and c) HCP-3 to account for potential variations across the surface.

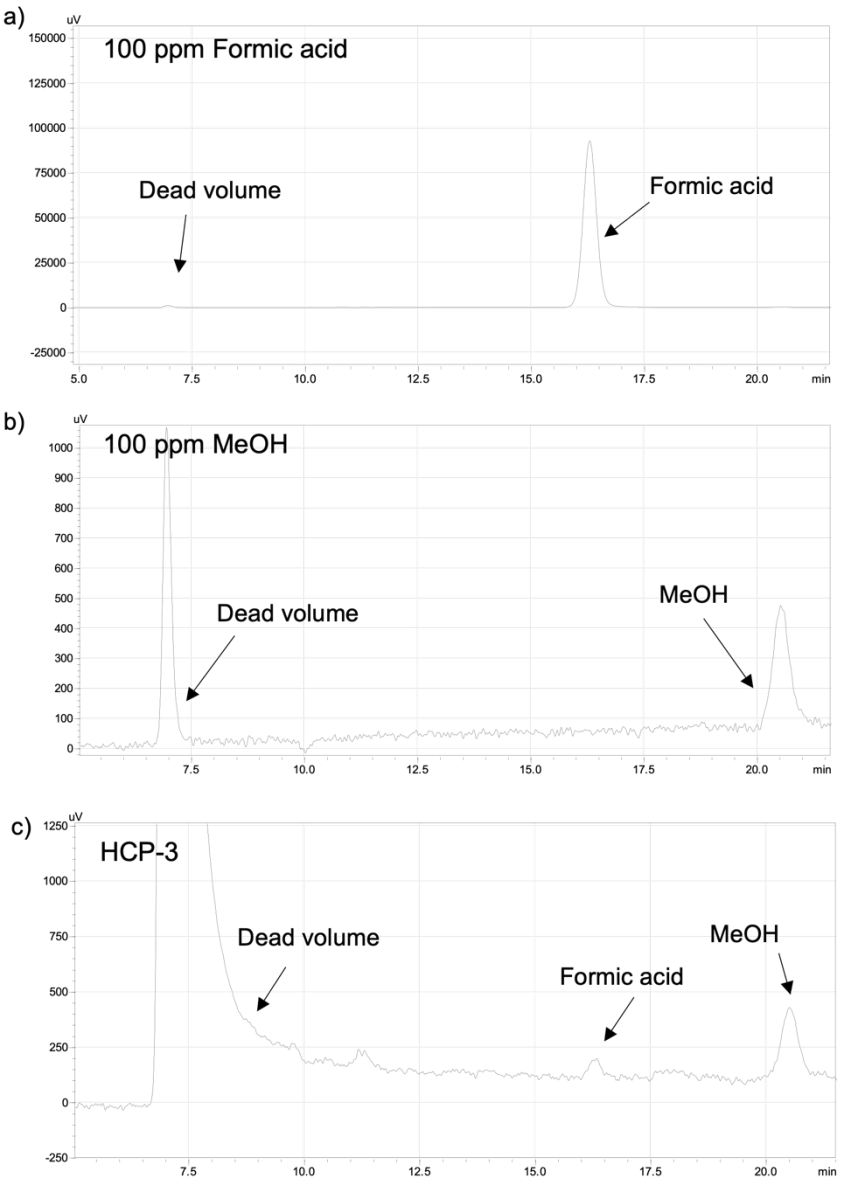


Figure A2.12 HPLC measurements of (a) a 100 ppm solution of formic acid, (b) a 100 ppm solution of MeOH and (c) an aqueous solution derived from washing with deionised water HCP-3 after 3 h UV-Vis irradiation under a CO_2 stream and using water as sacrificial agent.

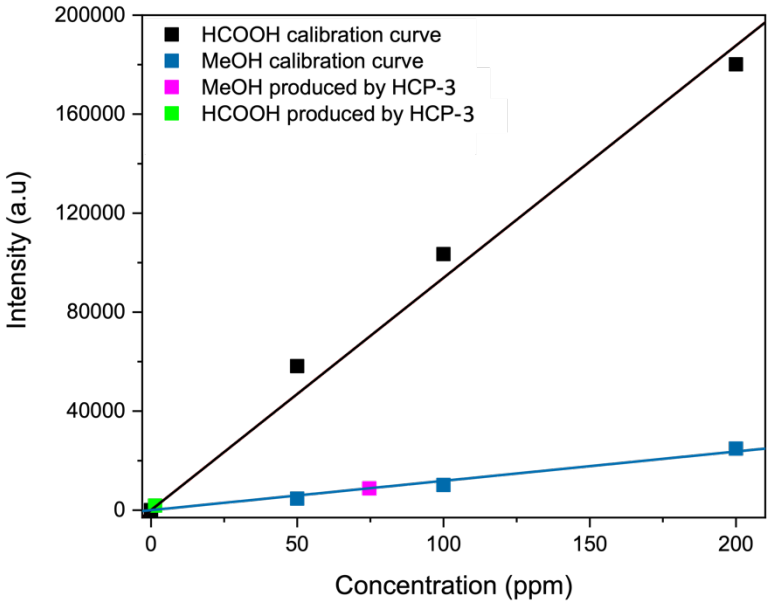


Figure A2.13 HPLC calibration curves to estimate the concentrations of formic acid and methanol produced during CO_2 photoreduction. The data points obtained when using HCP-3 are indicated on the graphs.

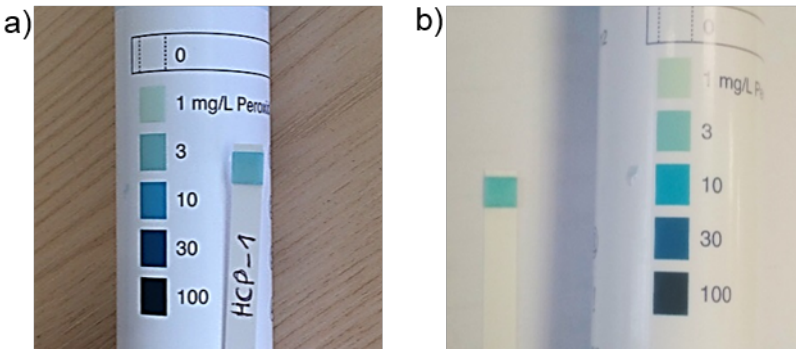


Figure A2.14 Results of the colorimetric test carried out to detect the presence of H_2O_2 as a result of the photocatalytic process. H_2O_2 was detected for both (a) and (b) HCP-3. A concentration of around 3 ppm was detected after 3 h of UV-Vis irradiation for HCP-1 and of around 7 ppm for HCP-3.

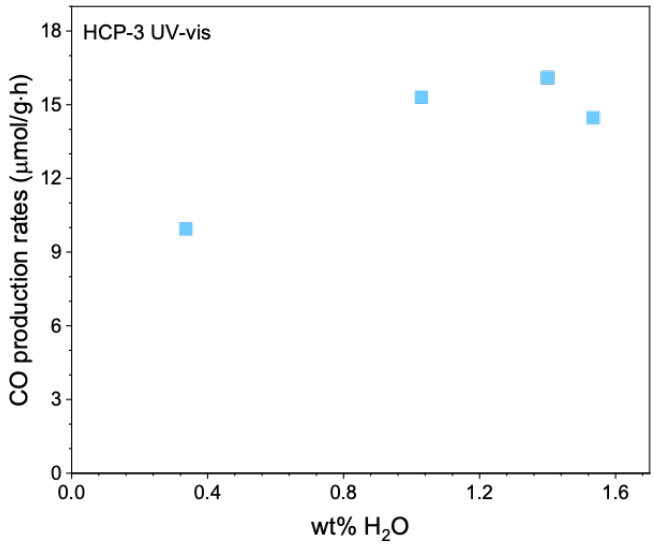


Figure A2.15 CO production rates of HCP-3 under UV-Vis irradiation using different water vapour contents.

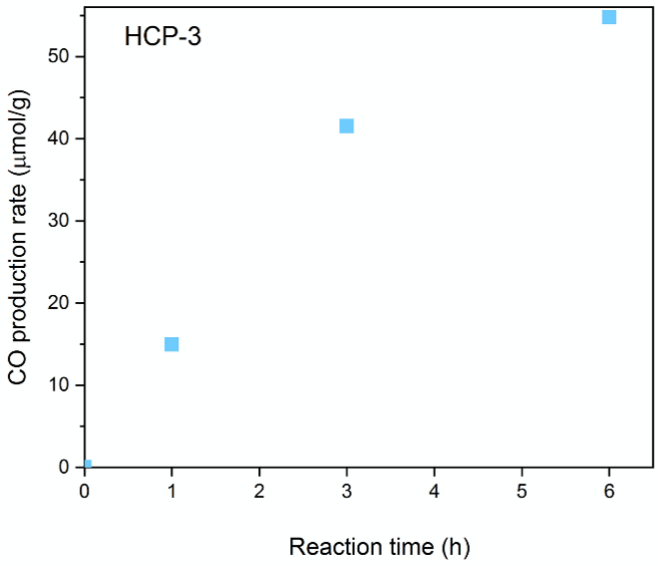


Figure A2.16 Photocatalytic CO evolution from HCP-3 under UV-Vis irradiation as a function of time.

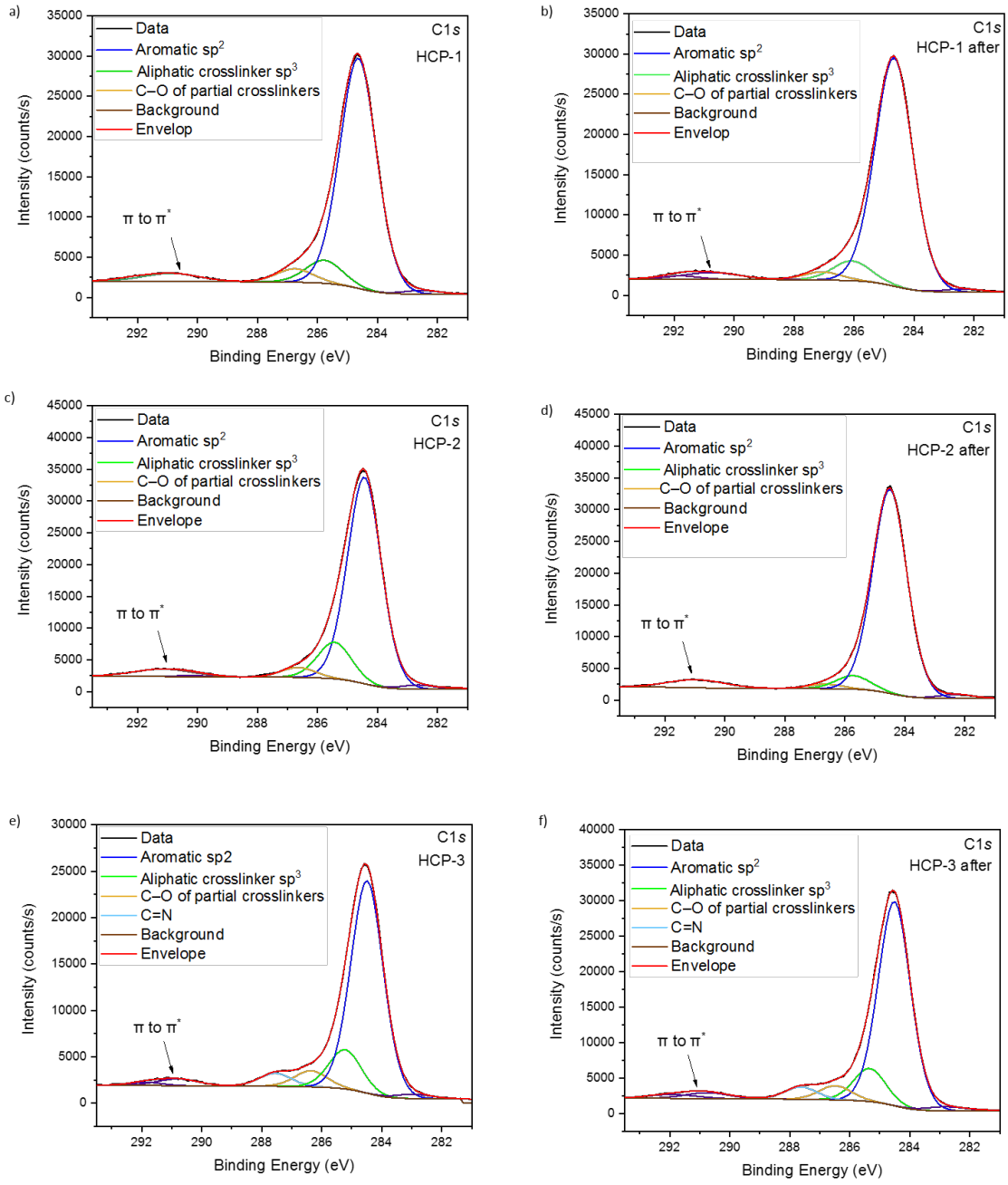


Figure A2.17. Comparison of C 1*s* core level spectra before and after the CO_2 photoreduction reaction of HCP-1, HCP-2, and HCP-3.

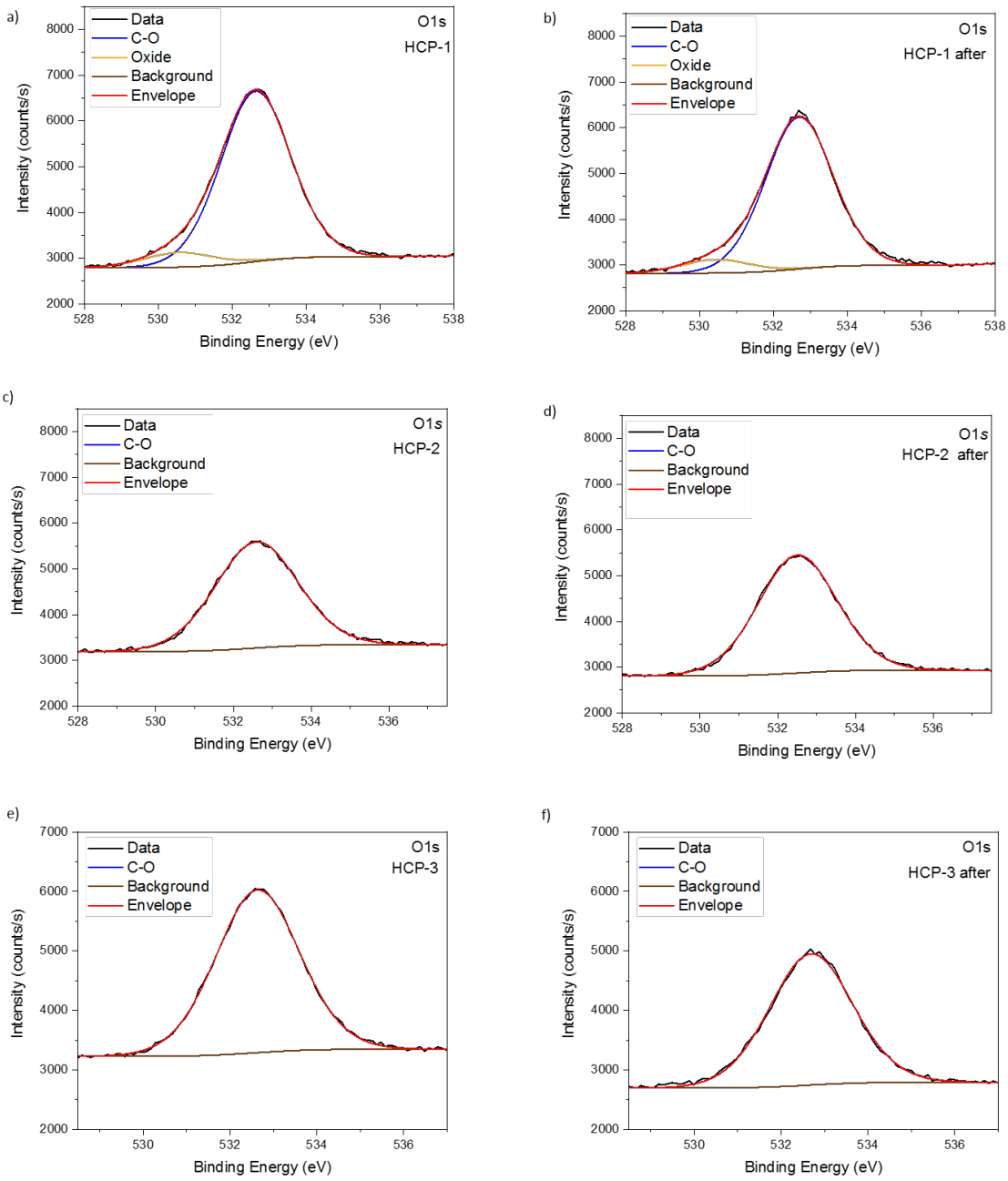


Figure A2.18 Comparison of O 1*s* core level spectra before and after the CO_2 photoreduction reaction of HCP-1, HCP-2, and HCP-3.

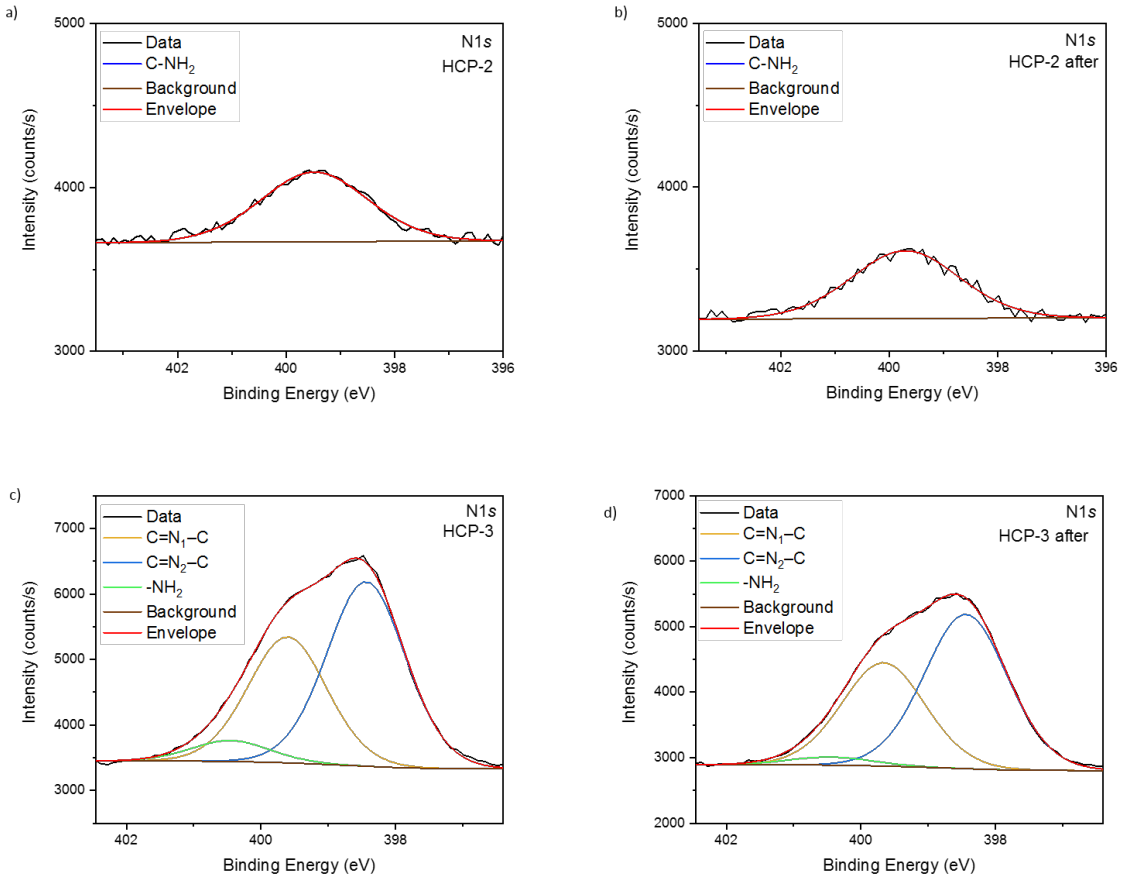


Figure A2.19 Comparison of N 1*s* core level spectra before and after the CO_2 photoreduction reaction of HCP-2 and HCP-3.

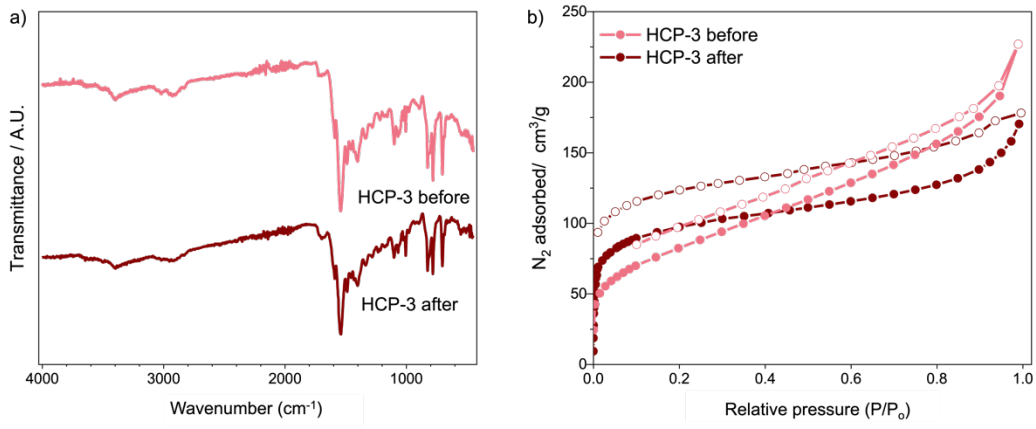


Figure A2.20 a) FTIR, and b) N_2 adsorption isotherms at 77 K of HCP-3 before and after the CO_2 photoreduction reaction.

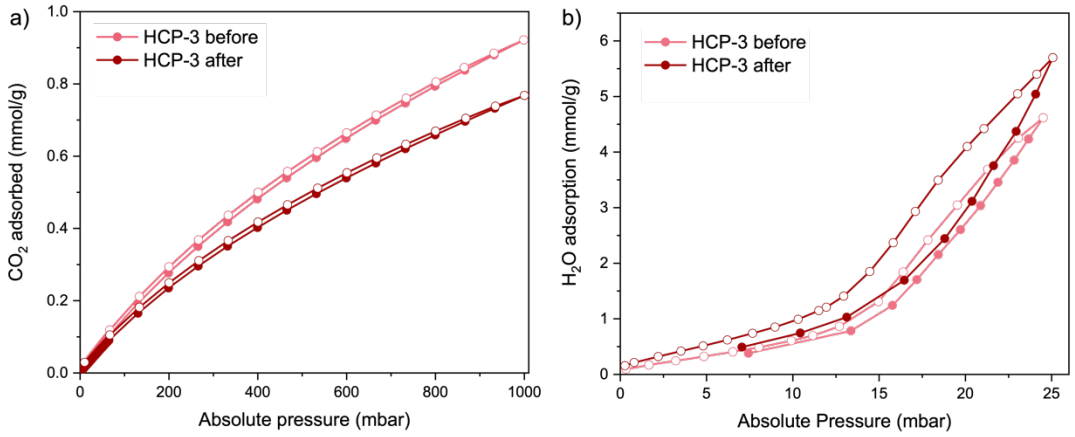


Figure A2.21 a) CO_2 adsorption isotherms and b) H_2O adsorption isotherms at 25 °C of HCP-3 before and after the CO_2 photoreduction reaction.

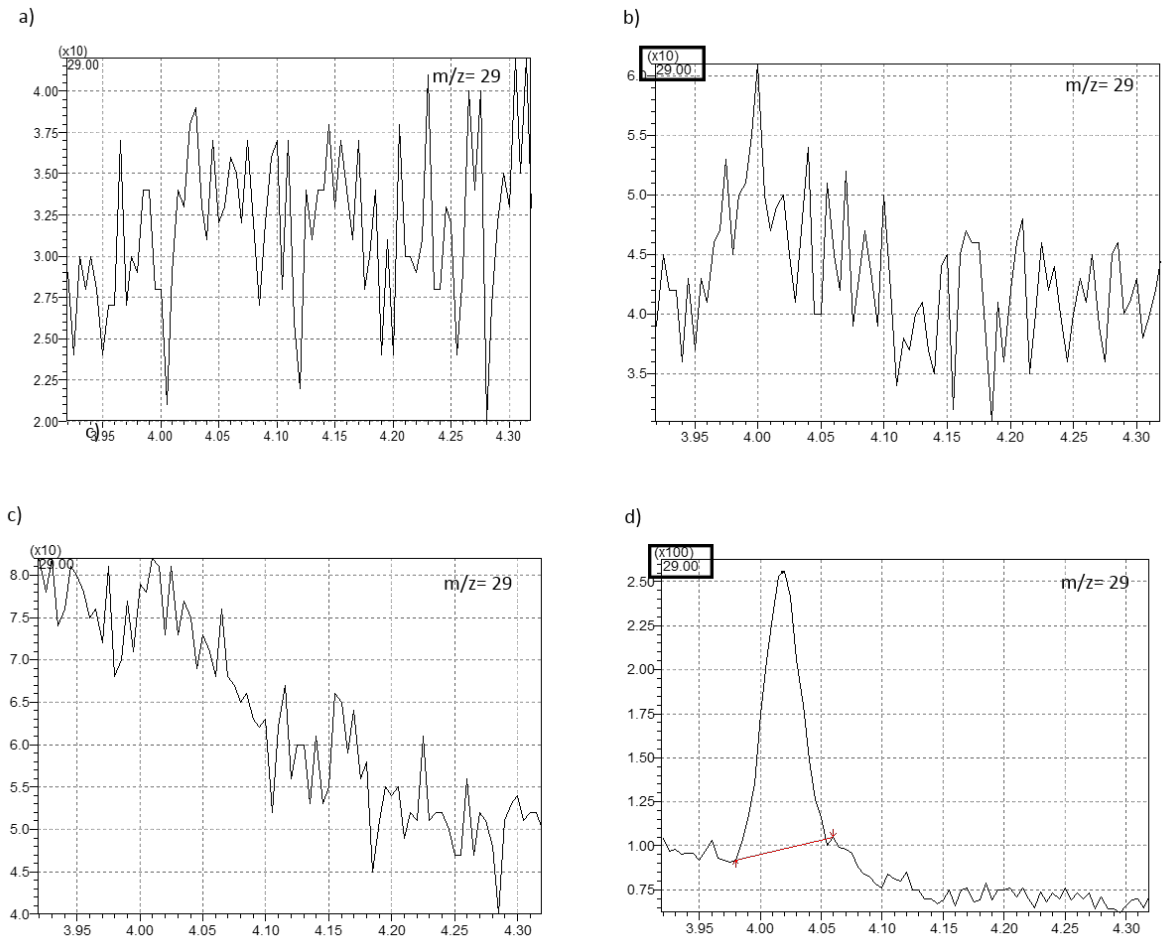


Figure A2.22 $^{12}CO_2$ and isotopic $^{13}CO_2$ measurements. Mass spectrum chromatogram of HCP-3 illustrating the ^{13}CO (m/z = 29) peak observed with $^{12}CO_2$ after a) 0 min and b) 4 h UV-Vis irradiation, and the ^{13}CO (m/z = 29) peak observed with $^{13}CO_2$ after c) 0 min irradiation and d) 4 h UV-Vis irradiation.

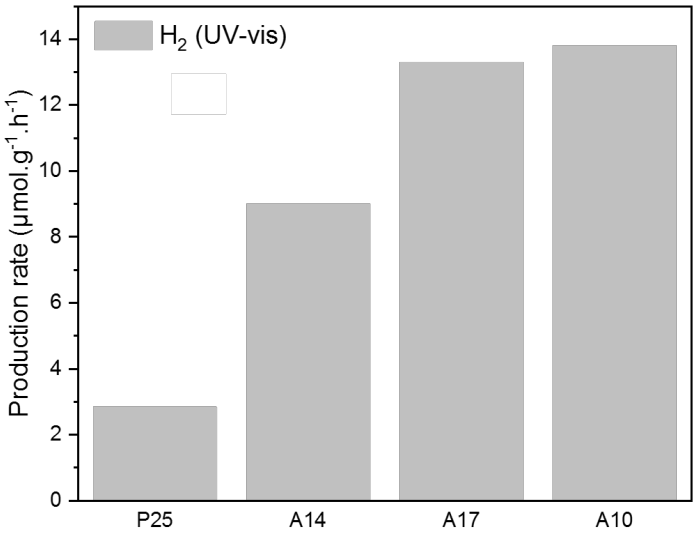


Figure A2.23 H_2 production rates of HCPs under UV-Viis irradiation using H_2O as sacrificial agent.

References:

1. Dai, C. H.; Zhong, L. X.; Gong, X. Z.; Zeng, L.; Xue, C.; Li, S. Z.; Liu, B., Triphenylamine based conjugated microporous polymers for selective photoreduction of CO2 to CO under visible light. *Green Chem* **2019,** *21* (24), 6606-6610.

2. Yu, X. X.; Yang, Z. Z.; Qiu, B.; Guo, S. E.; Yang, P.; Yu, B.; Zhang, H. Y.; Zhao, Y. F.; Yang, X. Z.; Han, B. X.; Liu, Z. M., Eosin Y-Functionalized Conjugated Organic Polymers for Visible-Light-Driven CO2 Reduction with H2O to CO with High Efficiency. *Angew Chem Int Edit* **2019,** *58* (2), 632-636.

3. Lei, K.; Wang, D.; Ye, L. Q.; Kou, M. P.; Deng, Y.; Ma, Z. Y.; Wang, L.; Kong, Y., A Metal-Free Donor-Acceptor Covalent Organic Framework Photocatalyst for Visible-Light-Driven Reduction of CO2 with H2O. *Chemsuschem* **2020,** *13* (7), 1725-1729.

4. Ojha, N.; Bajpai, A.; Kumar, S., Enhanced and selective photocatalytic reduction of CO2 by H2O over strategically doped Fe and Cr into porous boron carbon nitride. *Catal Sci Technol* **2020,** *10* (8), 2663-2680.

Appendix 3

Table A3.1 Elemental composition of the studied triazine-biphenyl HCP and the calculated atomic composition.

	C	N	O	H	S
w%	89.96	1.24	2.36	5.58	0.086
at%	56	0.62	1.1	42	0.02

The atomic composition was calculated using the following equation:

$$\text{C at\%} = \frac{\frac{\text{C w\%}}{\text{Cm}_a}}{\frac{\text{C w\%}}{\text{Cm}_a}+\frac{\text{Nw\%}}{\text{Nm}_a}+\frac{\text{Ow\%}}{\text{Om}_a}+\frac{\text{Hw\%}}{\text{Hm}_a}+\frac{\text{Sw\%}}{\text{Sm}_a}} \quad \text{(Equation A3.1)}$$

where m_a represent the atomic mass of an element.

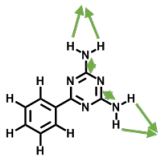
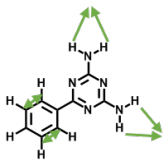
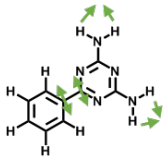
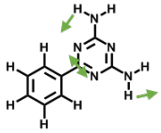
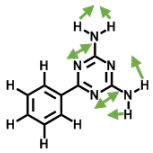
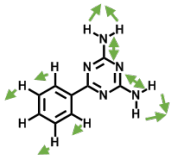
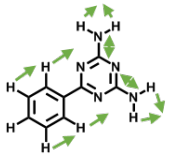
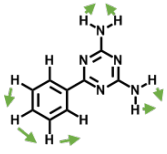
Table A3.2 Summary of textural properties derived from N_2 sorption isotherms at -196 °C, along with CO_2 adsorption capacities at 25 and 50 °C and 1 bar and H_2O adsorption capacities at 25 and 50 °C and 23 mbar for the studied HCP.

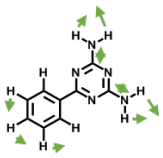
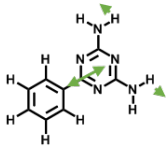
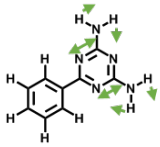
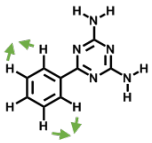
V_{MICRO} ($cm^3.g^{-1}$)	V_{TOT} ($cm^3.g^{-1}$)	S_{BET} ($m^2.g^{-1}$)	CO_2 ads. at 25 °C ($mmol.g^{-1}$)	CO_2 ads. At 50 °C ($mmol.g^{-1}$)	H_2O ads. at 25 °C (mmol.g-1)	H_2O ads. at 50 °C ($mmol.g^{-1}$)
0.136	0.978	1247	1.38	0.70	1.5	0.17

Table A3.3 CO_2 uptake capacity of different hypercrosslinked polymers reported in the literature.

Adsorbent	Surface area ($m^2.g^{-1}$)	V_{Tot} ($cm^3.g^{-1}$)	V_{micro} ($cm^3.g^{-1}$)	CO_2 adsorption at 1 bar and 25 °C ($mmol.g^{-1}$)	Ref.
Xylene-biphenyl HCP	1970	-	-	1.7	[1]
Biphenyl HCP	1260	1.15	0.55	1.25	[2]
Benzene based HCP	950	1.07	0.46	1.25	[3]
Benzene based HCP	857	-	0.151	2.8	[4]
NH_2 functionalized HCP	77	-	-	0.63	[5]
Triazine-quinone based HCP	1130	1.02	-	1.40	[6]
Triazine-biphenyl HCP	1247	0.9789	0.14	1.38	This work

Table A3.4 Comparison between the experimental ATR infrared spectrum of triazine powder and the simulated infrared spectrum of one triazine molecule, enabling assignment of the triazine monomer vibrational bands. To allow comparison between the simulated and the measured infrared spectra, a scaling factor of 0.973 was applied to the simulated one.

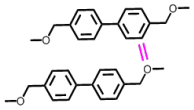
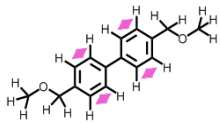
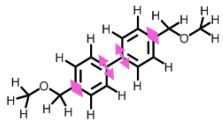
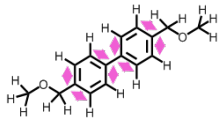
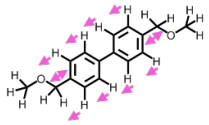
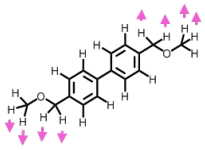
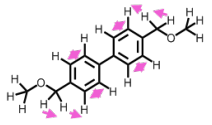
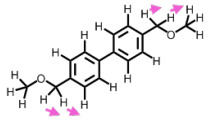
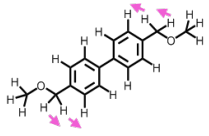
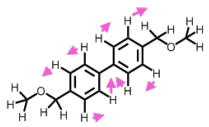
Band number as labeled in Figure 6.3a	**Experimental vibrational frequency of triazine powder (cm^{-1})**	**Calculated vibrational frequency (cm^{-1})***	**Assignment**	**Graphical illustration of the displacement vector**
1	1616	1615	s(NH_2) + v(C-NH_2)	
2	1603	1609	s(NH_2) + v(C-C)	
3	1590	1603	s(NH_2) +N-C=N + C-C=C	
4	1557	1563	v(NH) +N-C=N	
5	1531	1557	v(C-N) + v(NH)	
6	1506	1493	s(NH_2) + v(C-NH_2) + benzene ring vibrations	
7	1487	1472	s(NH_2) + v(C-NH_2) + benzene ring vibrations	
8	1450	1450	s(NH_2) + benzene ring vibrations	

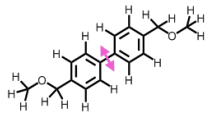
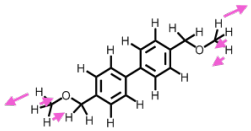
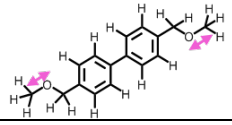
9	1425	1421	$s(NH_2)$ + $v(C\text{-}NH_2)$ + benzene ring vibrations	
-	1387	1394	v(C-C) between benzene and triazine ring	
-	1257	1264	v(C-N) + v(NH)	
-	1192	1153	benzene ring vibrations	

*Based on the simulated infrared spectra of 1 triazine molecule.

Definition: δ: bending vibration; v: stretching vibration; s: scissoring.

Table A3.5 Comparison between the experimental ATR infrared spectra of biphenyl powder and the simulated infrared spectra of one biphenyl molecule, enabling assignment of the biphenyl monomer vibrational bands. To allow comparison between the simulated and the measured infrared spectra a scaling factor of 0.975 was applied to the simulated one.

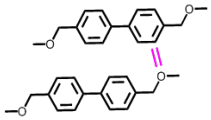
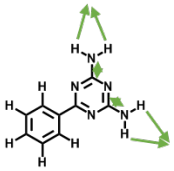
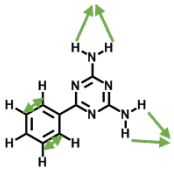
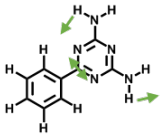
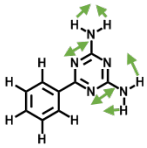
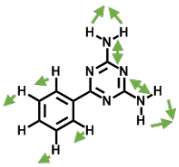
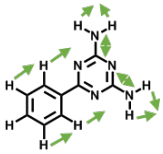
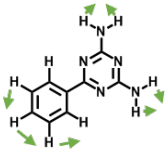
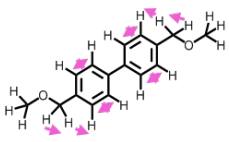
Band number as labeled in Figure 6.3b	Experimental vibrational frequency of biphenyl powder (cm^{-1})	Calculated vibrational frequency (cm^{-1})	Assignment	Graphical illustration of the displacement vector
1 2	1718 1697	-	intermolecular C=O vibrations	
3	1602	1623	v(C-C) of the benzene ring	
4	1579	1586	v(C-C) of the benzene ring	
5	1561	1566	v(C-C) of the benzene ring	
6	1498	1502	benzene ring vibrations	
7	1450	1446	benzene ring vibrations	
8	1399	1399	v(C-C) of the benzene ring	
9	1380	1371	δ(CH_2) of the methylene group	
10	1364	1369	benzene ring vibrations	
11	1312	1305	benzene ring vibrations	

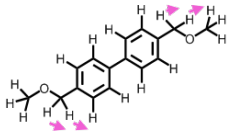
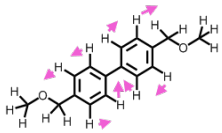
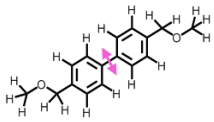
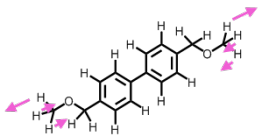
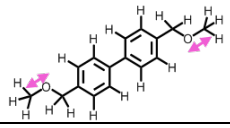
12	1275	1275	v(C-C)	
13	1208 1190	1208 1189	$\delta(CH_2)$ of the methylene group + $\delta(CH_3)$ of the methoxy group	
14	1088	1137	v(C-O)	

*Based on the simulated infrared spectra of 1 biphenyl molecule

Definition: δ: bending vibration; v: stretching vibration; s: scissoring.

Table A3.6 Vibrational analysis and assignment of the triazine-biphenyl HCP.

Band number as labeled in Figure 6.3c	Experimental vibrational frequency (cm^{-1})	Monomer contribution	Assignment	Graphical illustration of the displacement vector
1 2	1726 1704	biphenyl	Intermolecular C=O vibrations	
3	1605	triazine	s(NH_2) + v(C-NH_2)	
4	1593	triazine	s(NH_2) + v(C-C) benzene ring	
5	1551	triazine	v(N-H) + N-C=N stretching	
6	1515	triazine	v(C-N) + v(NH)	
7	1490	triazine	s(NH_2) + v(C-NH_2) + benzene ring vibrations	
8	1457	triazine	s(NH_2) + v(C-NH_2) + benzene ring vibrations	
9	1433	triazine	s(NH_2) + benzene ring vibrations	
-	1400	biphenyl	v(C-C) of the benzene ring	

-	1390	biphenyl	δ(CH_2) of the methylene group	
-	1332	biphenyl	benzene ring vibrations	
-	1246	biphenyl	v(C-C)	
-	1238 1211 1182	biphenyl	δ(CH_2) of the methylene group + δ(CH_3) of the methoxy group	
10	1110	biphenyl	v(C-O)	

Definition: δ: bending vibration; v: stretching vibration; s: scissoring.

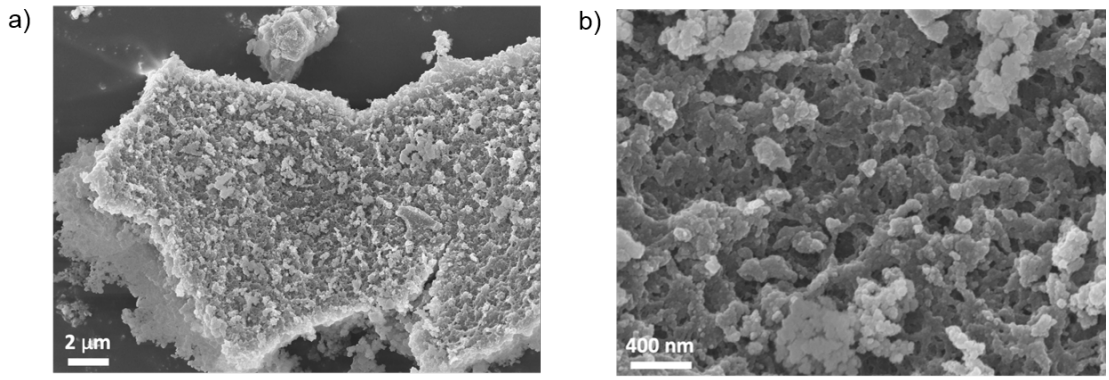


Figure A3.1 SEM images of the triazine-biphenyl HCP.

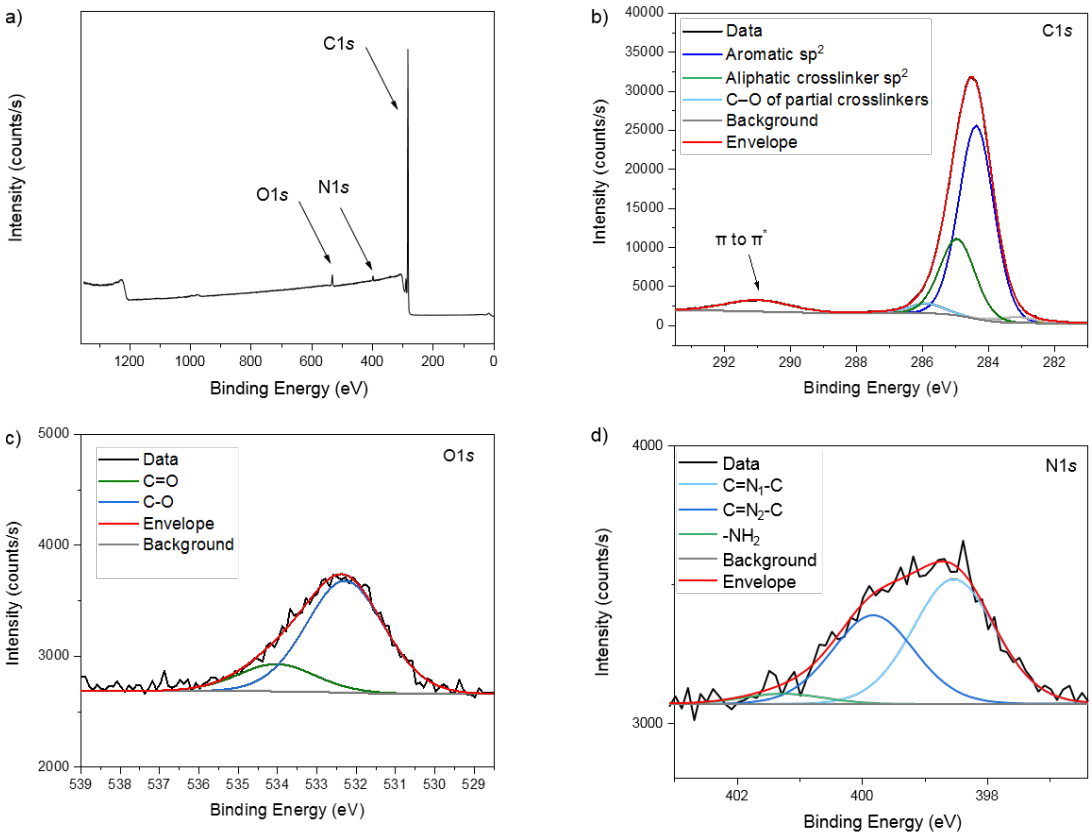


Figure A3.2 (a) XPS survey spectra, and high resolution XPS and peak fittings of the (b) C 1*s*, c) O 1*s* and d) N 1*s* core levels of the HCP.

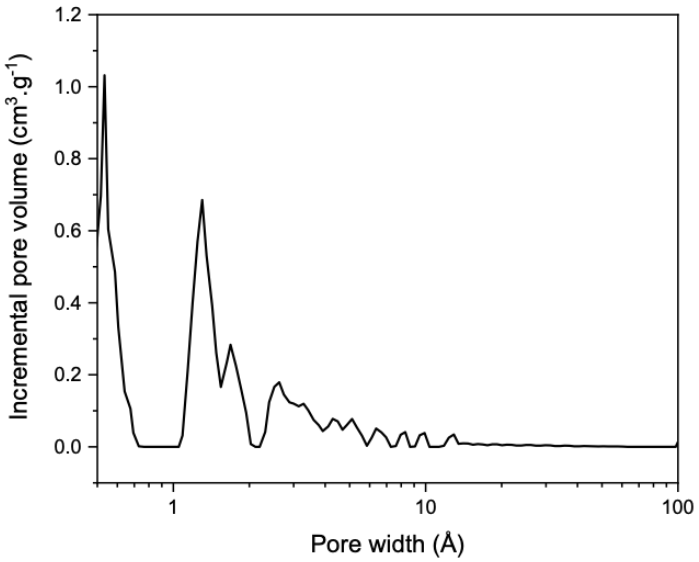


Figure A3.3 Pore size distribution of the triazine-biphenyl HCP.

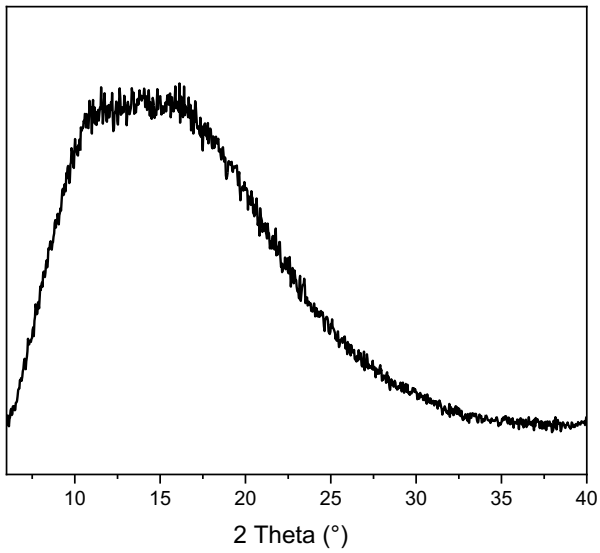


Figure A3.4 PXRD patterns of the triazine-biphenyl HCP.

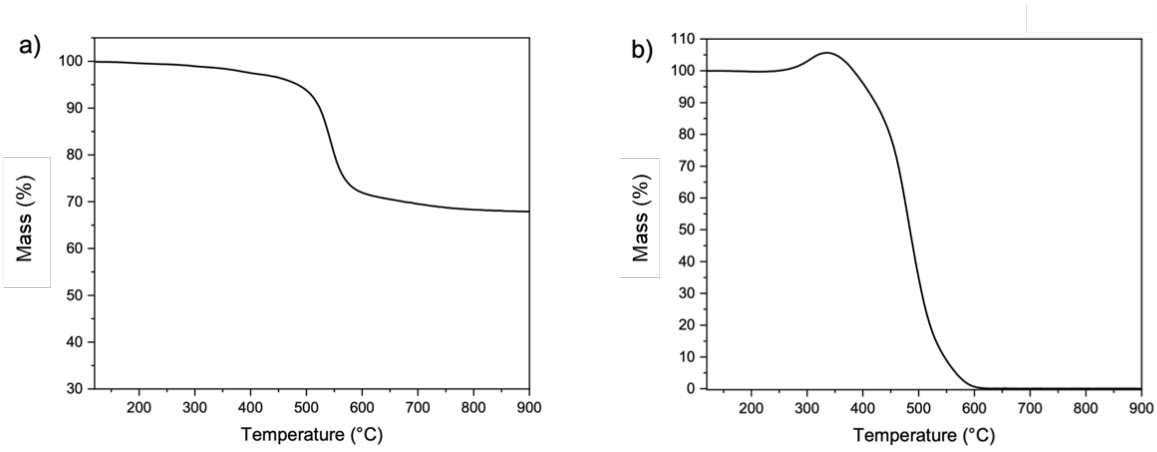


Figure A3.5 Thermogravimetric curves of the triazine-biphenyl HCP obtained under:

(a) N_2 and (b) air.

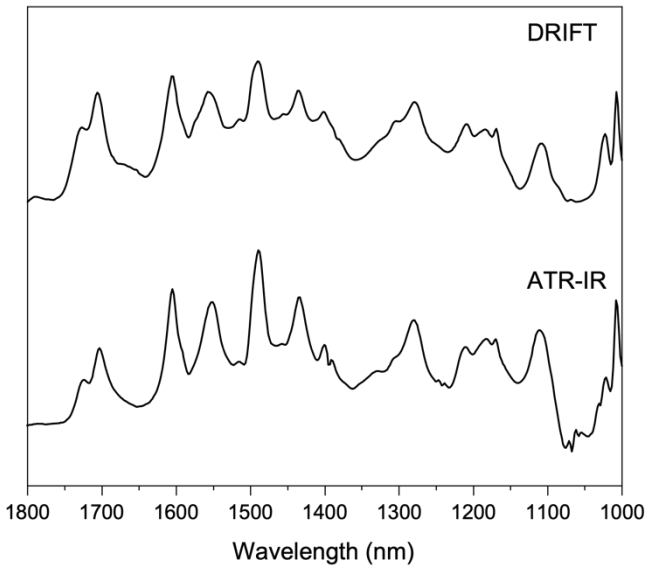


Figure A3.6 Comparison of the DRIFT and ATR-IR spectra of the triazine-biphenyl HCP.

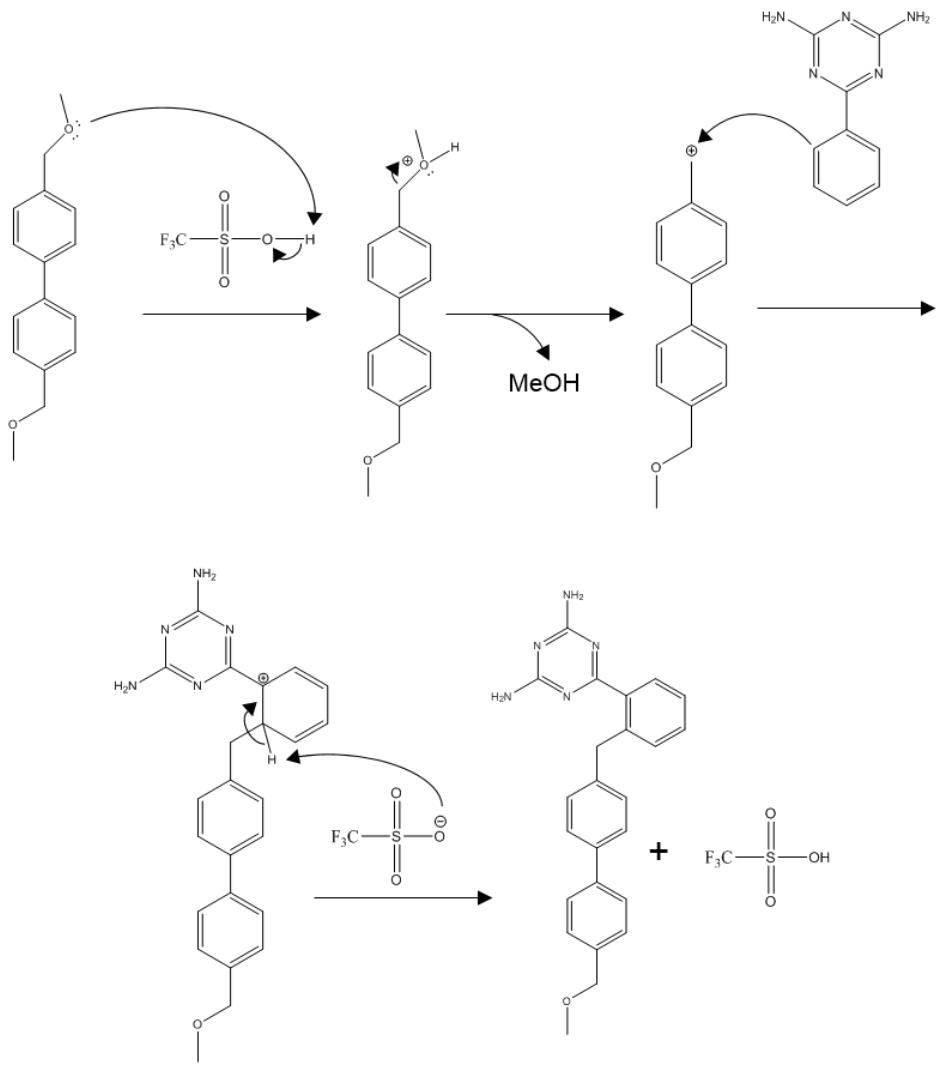


Figure A3.7 Proposed reaction synthesis of the triazine-biphenyl HCP when using triflic acid as polymerization catalyst.

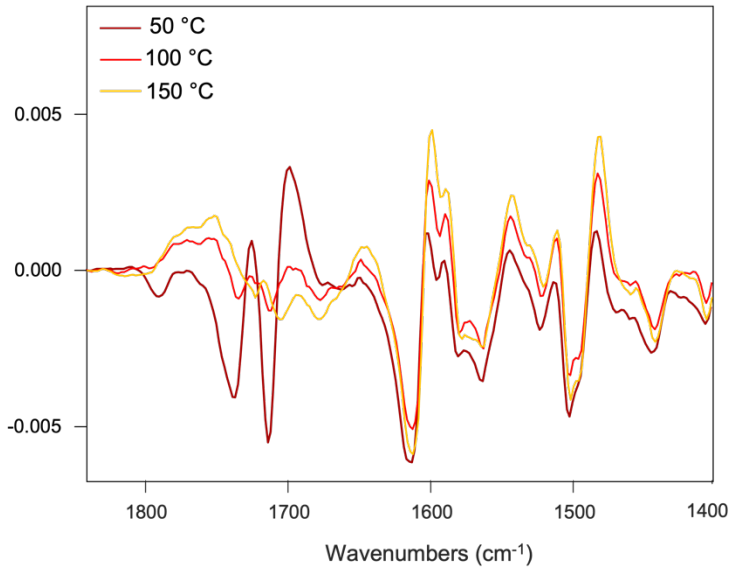


Figure A3.8 Average of the difference spectra obtained under a CO_2 atmosphere at 50, 100, 150 °C.

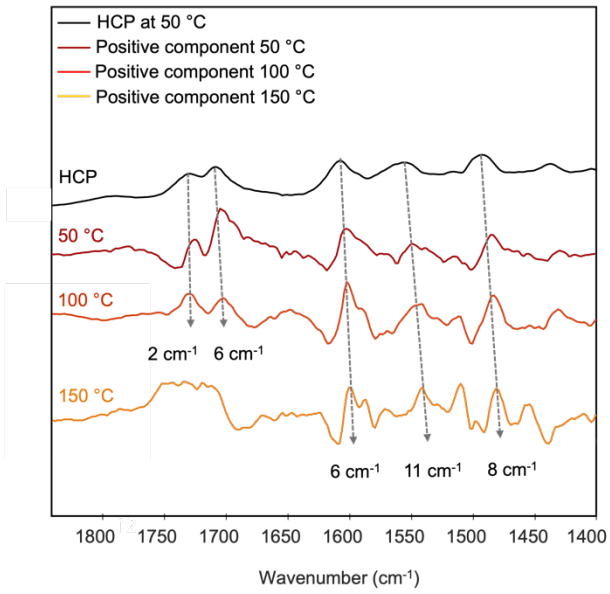


Figure A3.9 Comparison between the vibrational band positions of the positive components extracted by MCR at 50, 100 and 150 °C and the corresponding unshifted HCP vibrational bands.

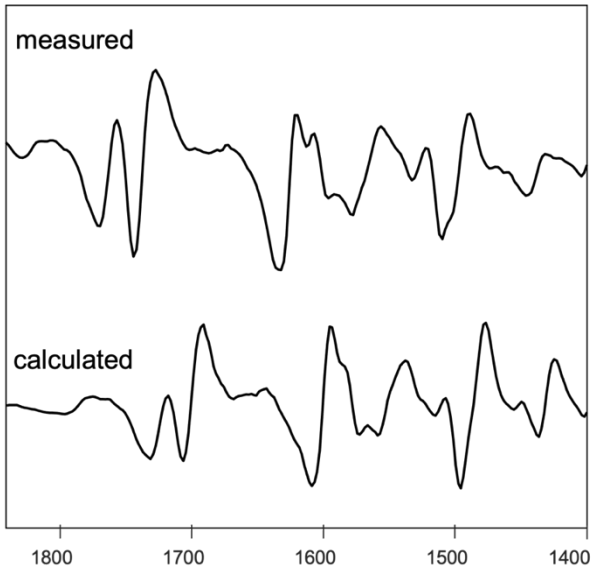


Figure A3.10 Comparison between the measured difference spectrum under a CO_2 atmosphere at 50 °C and the calculated one. The calculated difference spectrum is obtained by mathematically shifting the background spectrum by -8 cm^{-1}, and the latter is subtracted to the original background spectra

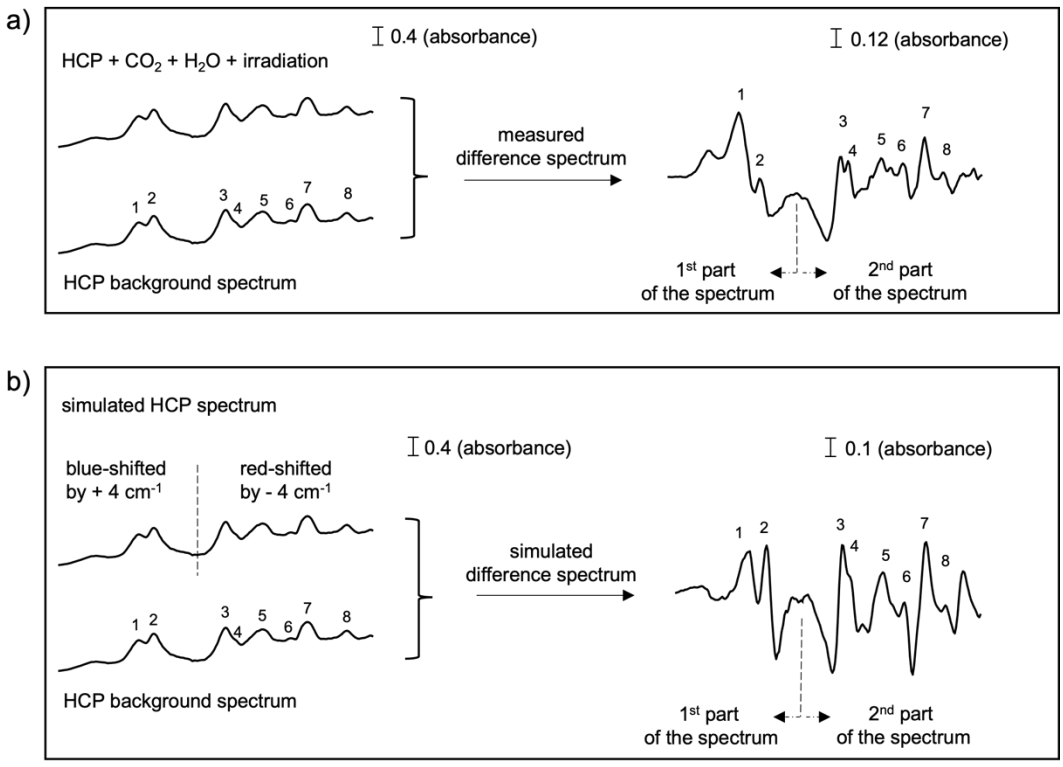


Figure A3.11 DRIFT study of CO_2 and H_2O co-adsorption on HCP under light irradiation. (a) schematic illustration of the spectral components obtained after processing the difference spectrum by MCR. The difference spectrum corresponds to the average of the difference spectra acquired at 50 °C under a CO_2/H_2O atmosphere and UV-vis irradiation. (b) Schematic illustration of the simulated difference spectrum. The spectral region of bands 1 and 2 is blue-shifted compared to the vibrational bands of the background spectrum, while the spectral region of the other bands is red-shifted.

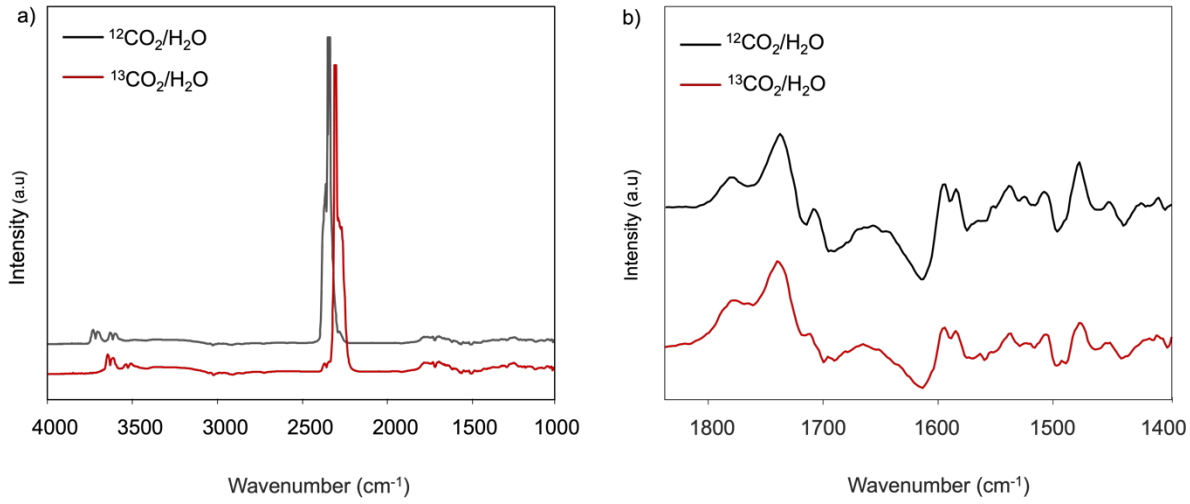


Figure A3.12 Comparison between the difference spectra obtained under light irradiation under a $^{12}CO_2/H_2O$ and a $^{13}CO_2/H_2O$ in the (a) 4000 - 1000 cm^{-1} and (b) 1840 - 1400 cm^{-1} regions.

References:

1. Martin, C. F.; Stockel, E.; Clowes, R.; Adams, D. J.; Cooper, A. I.; Pis, J. J.; Rubiera, F.; Pevida, C., Hypercrosslinked organic polymer networks as potential adsorbents for pre-combustion CO2 capture. *J Mater Chem* **2011,** *21* (14), 5475-5483.

2. Woodward, R. T., The design of hypercrosslinked polymers from benzyl ether self-condensing compounds and external crosslinkers. *Chem Commun* **2020,** *56* (36), 4938-4941.

3. Schukraft, G. E. M.; Woodward, R. T.; Kumar, S.; Sachs, M.; Eslava, S.; Petit, C., Hypercrosslinked Polymers as a Photocatalytic Platform for Visible-Light-Driven CO2 Photoreduction Using H2O. *Chemsuschem* **2021,** *14* (7), 1720-1727.

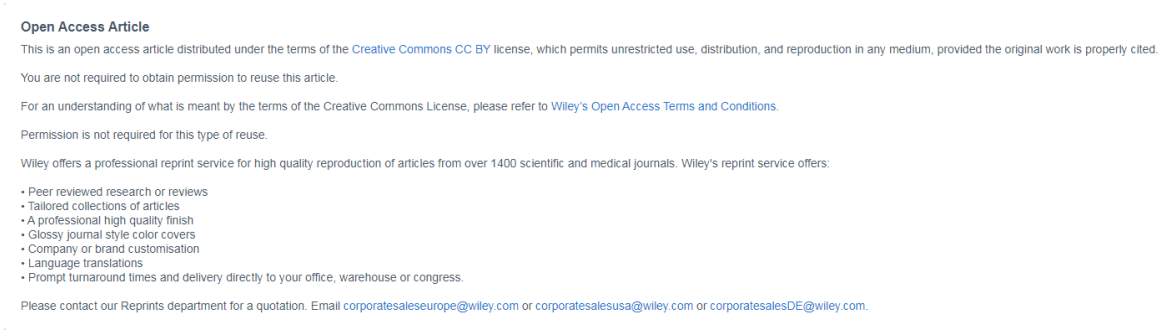
4. Ramezanipour Penchah, H.; Ghanadzadeh Gilani, H.; Ghaemi, A., CO2, N2, and H2 Adsorption by Hyper-Cross-Linked Polymers and Their Selectivity Evaluation by Gas–Solid Equilibrium. *Journal of Chemical & Engineering Data* **2020,** *65* (10), 4905-4913.

5. Su, P.; Zhang, X.; Xu, Z.; Zhang, G.; Shen, C.; Meng, Q., Amino-functionalized hypercrosslinked polymers for highly selective anionic dye removal and CO2/N2 separation. *New J Chem* **2019,** *43* (44), 17267-17274.

6. Mohamed, M. G.; Zhang, X.; Mansoure, T. H.; El-Mahdy, A. F. M.; Huang, C. F.; Danko, M.; Xin, Z.; Kuo, S. W., Hypercrosslinked porous organic polymers based on tetraphenylanthraquinone for CO2 uptake and high-performance supercapacitor. *Polymer* **2020,** *205*, 122857.

Rights and permissions

(1) Schukraft, G. E. M.; Woodward, R. T.; Kumar, S.; Sachs, M.; Eslava, S.; Petit, C., Hypercrosslinked Polymers as a Photocatalytic Platform for Visible-Light-Driven CO2 Photoreduction Using H2O. Chemsuschem 2021, 14 (7), 1720-1727.



Open Access Article

This is an open access article distributed under the terms of the Creative Commons CC BY license, which permits unrestricted use, distribution, and reproduction in any medium, provided the original work is properly cited.

You are not required to obtain permission to reuse this article.

For an understanding of what is meant by the terms of the Creative Commons License, please refer to Wiley's Open Access Terms and Conditions.

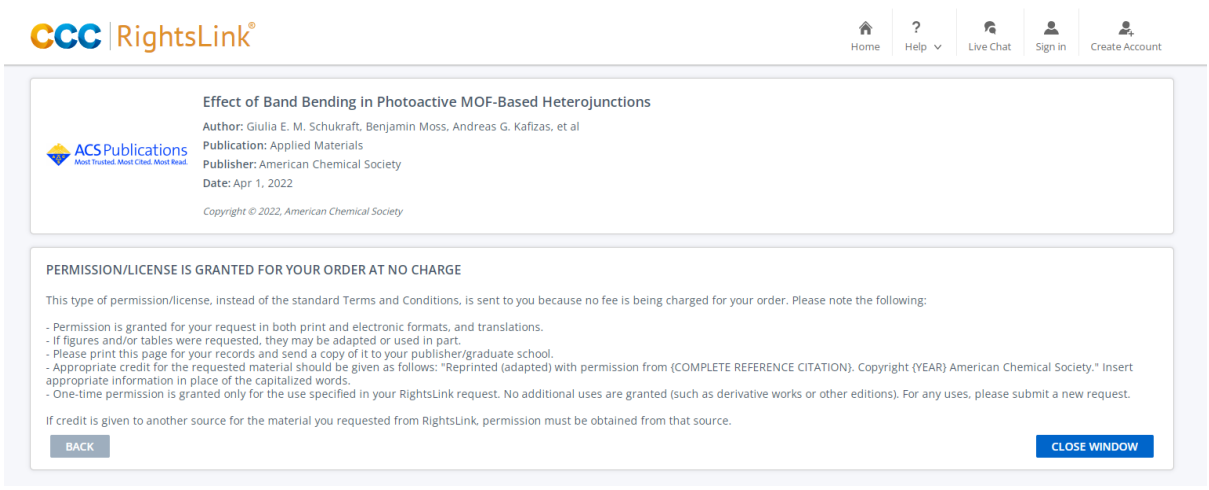
Permission is not required for this type of reuse.

Wiley offers a professional reprint service for high quality reproduction of articles from over 1400 scientific and medical journals. Wiley's reprint service offers:

- Peer reviewed research or reviews
- Tailored collections of articles
- A professional high quality finish
- Glossy journal style color covers
- Company or brand customisation
- Language translations
- Prompt turnaround times and delivery directly to your office, warehouse or congress.

Please contact our Reprints department for a quotation. Email corporatesaleseurope@wiley.com or corporatesalesusa@wiley.com or corporatesalesDE@wiley.com.

(2) Schukraft, G. E. M.; Moss, B.; Kafizas, A. G.; Petit, C., Effect of Band Bending in Photoactive MOF-Based Heterojunctions. Acs Appl Mater Inter **2022**.



CCC RightsLink®

Home | Help | Live Chat | Sign in | Create Account

ACS Publications
Most Trusted. Most Cited. Most Read.

Effect of Band Bending in Photoactive MOF-Based Heterojunctions

Author: Giulia E. M. Schukraft, Benjamin Moss, Andreas G. Kafizas, et al
Publication: Applied Materials
Publisher: American Chemical Society
Date: Apr 1, 2022

Copyright © 2022, American Chemical Society

PERMISSION/LICENSE IS GRANTED FOR YOUR ORDER AT NO CHARGE

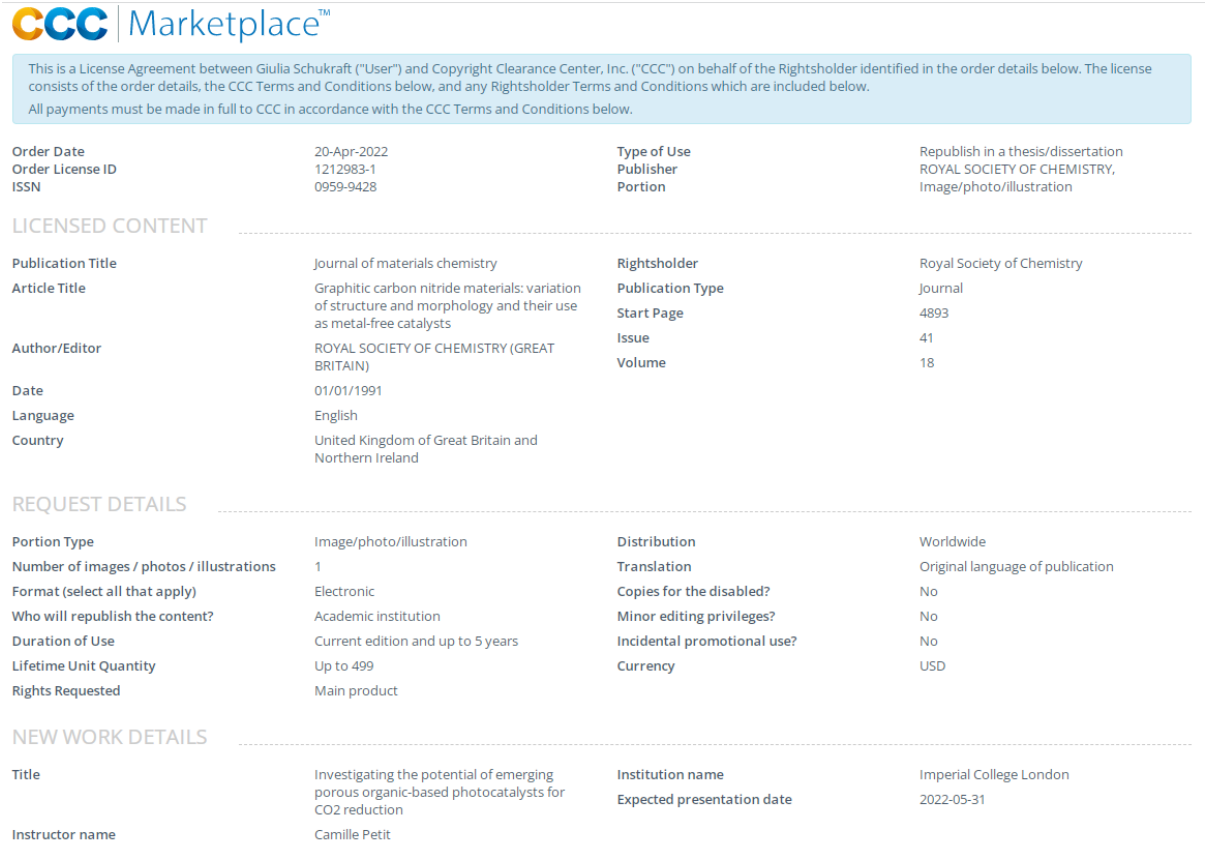
This type of permission/license, instead of the standard Terms and Conditions, is sent to you because no fee is being charged for your order. Please note the following:

- Permission is granted for your request in both print and electronic formats, and translations.
- If figures and/or tables were requested, they may be adapted or used in part.
- Please print this page for your records and send a copy of it to your publisher/graduate school.
- Appropriate credit for the requested material should be given as follows: "Reprinted (adapted) with permission from {COMPLETE REFERENCE CITATION}. Copyright {YEAR} American Chemical Society." Insert appropriate information in place of the capitalized words.
- One-time permission is granted only for the use specified in your RightsLink request. No additional uses are granted (such as derivative works or other editions). For any uses, please submit a new request.

If credit is given to another source for the material you requested from RightsLink, permission must be obtained from that source.

BACK | CLOSE WINDOW

(3) Thomas, A.; Fischer, A.; Goettmann, F.; Antonietti, M.; Muller, J. O.; Schlogl, R.; Carlsson, J. M., Graphitic carbon nitride materials: variation of structure and morphology and their use as metal-free catalysts. J Mater Chem 2008, 18 (41), 4893-490.



CCC Marketplace™

This is a License Agreement between Giulia Schukraft ("User") and Copyright Clearance Center, Inc. ("CCC") on behalf of the Rightsholder identified in the order details below. The license consists of the order details, the CCC Terms and Conditions below, and any Rightsholder Terms and Conditions which are included below.

All payments must be made in full to CCC in accordance with the CCC Terms and Conditions below.

Order Date	20-Apr-2022	Type of Use	Republish in a thesis/dissertation
Order License ID	1212983-1	Publisher	ROYAL SOCIETY OF CHEMISTRY,
ISSN	0959-9428	Portion	Image/photo/illustration

LICENSED CONTENT

Publication Title	Journal of materials chemistry	Rightsholder	Royal Society of Chemistry
Article Title	Graphitic carbon nitride materials: variation of structure and morphology and their use as metal-free catalysts	Publication Type	Journal
		Start Page	4893
Author/Editor	ROYAL SOCIETY OF CHEMISTRY (GREAT BRITAIN)	Issue	41
		Volume	18
Date	01/01/1991		
Language	English		
Country	United Kingdom of Great Britain and Northern Ireland		

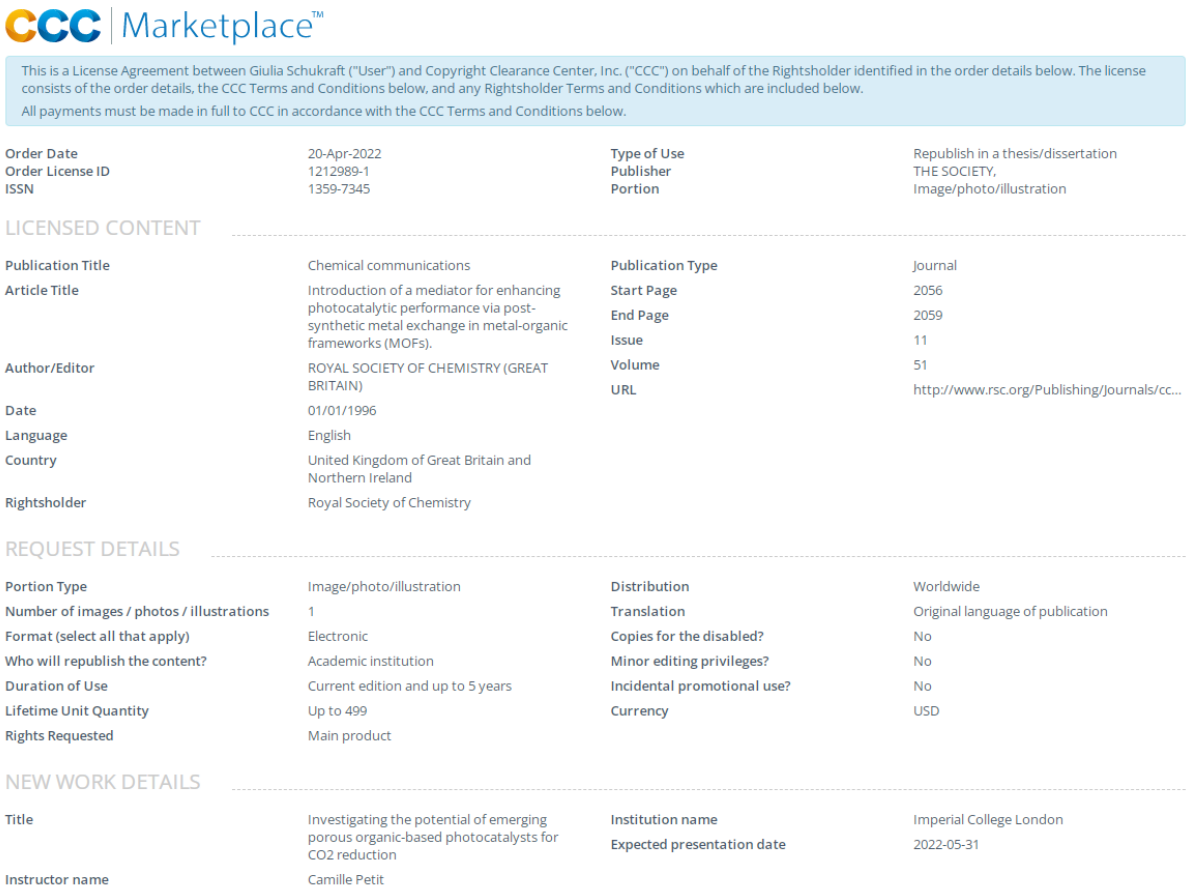
REQUEST DETAILS

Portion Type	Image/photo/illustration	Distribution	Worldwide
Number of images / photos / illustrations	1	Translation	Original language of publication
Format (select all that apply)	Electronic	Copies for the disabled?	No
Who will republish the content?	Academic institution	Minor editing privileges?	No
Duration of Use	Current edition and up to 5 years	Incidental promotional use?	No
Lifetime Unit Quantity	Up to 499	Currency	USD
Rights Requested	Main product		

NEW WORK DETAILS

Title	Investigating the potential of emerging porous organic-based photocatalysts for CO2 reduction	Institution name	Imperial College London
		Expected presentation date	2022-05-31
Instructor name	Camille Petit		

(4) Sun, D. R.; Liu, W. J.; Qiu, M.; Zhang, Y. F.; Li, Z. H., Introduction of a mediator for enhancing photocatalytic performance via post-synthetic metal exchange in metal-organic frameworks (MOFs) (vol 51, pg 2056, 2015). Chem Commun 2015, 51 (53), 10765-10765.



CCC Marketplace™

This is a License Agreement between Giulia Schukraft ("User") and Copyright Clearance Center, Inc. ("CCC") on behalf of the Rightsholder identified in the order details below. The license consists of the order details, the CCC Terms and Conditions below, and any Rightsholder Terms and Conditions which are included below.

All payments must be made in full to CCC in accordance with the CCC Terms and Conditions below.

Order Date	20-Apr-2022	Type of Use	Republish in a thesis/dissertation
Order License ID	1212989-1	Publisher	THE SOCIETY,
ISSN	1359-7345	Portion	Image/photo/illustration

LICENSED CONTENT

Publication Title	Chemical communications	Publication Type	Journal
Article Title	Introduction of a mediator for enhancing photocatalytic performance via post-synthetic metal exchange in metal-organic frameworks (MOFs).	Start Page	2056
		End Page	2059
		Issue	11
Author/Editor	ROYAL SOCIETY OF CHEMISTRY (GREAT BRITAIN)	Volume	51
		URL	http://www.rsc.org/Publishing/Journals/cc...
Date	01/01/1996		
Language	English		
Country	United Kingdom of Great Britain and Northern Ireland		
Rightsholder	Royal Society of Chemistry		

REQUEST DETAILS

Portion Type	Image/photo/illustration	Distribution	Worldwide
Number of images / photos / illustrations	1	Translation	Original language of publication
Format (select all that apply)	Electronic	Copies for the disabled?	No
Who will republish the content?	Academic institution	Minor editing privileges?	No
Duration of Use	Current edition and up to 5 years	Incidental promotional use?	No
Lifetime Unit Quantity	Up to 499	Currency	USD
Rights Requested	Main product		

NEW WORK DETAILS

Title	Investigating the potential of emerging porous organic-based photocatalysts for CO2 reduction	Institution name	Imperial College London
		Expected presentation date	2022-05-31
Instructor name	Camille Petit		

(5) You, J. H.; Zhao, Y.; Wang, L.; Bao, W. T., Recent developments in the photocatalytic applications of covalent organic frameworks: A review. J Clean Prod 2021, 291.

License Details

This Agreement between Giulia Schukraft ("You") and Elsevier ("Elsevier") consists of your license details and the terms and conditions provided by Elsevier and Copyright Clearance Center.

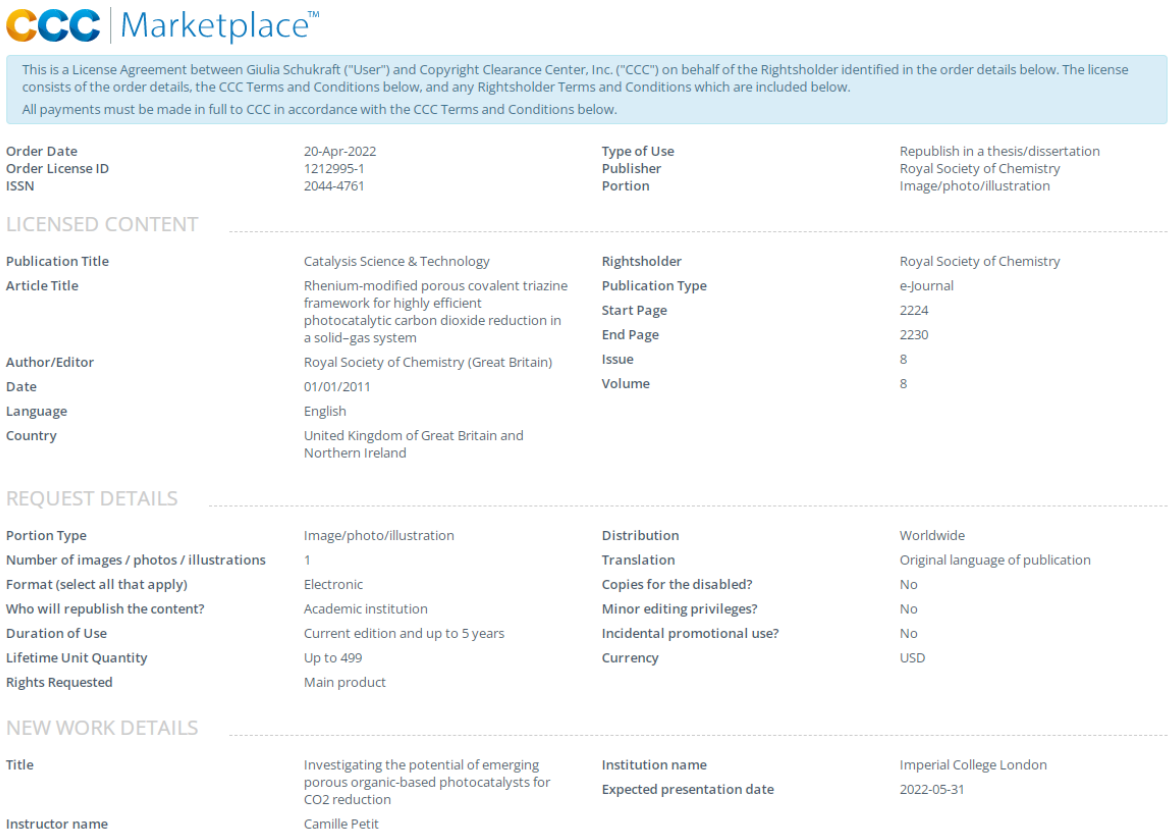
Print Copy

License Number	5293131331576
License date	Apr 20, 2022
Licensed Content Publisher	Elsevier
Licensed Content Publication	Journal of Cleaner Production
Licensed Content Title	Recent developments in the photocatalytic applications of covalent organic frameworks: A review
Licensed Content Author	Junhua You,Yao Zhao,Lu Wang,Wanting Bao
Licensed Content Date	Apr 1, 2021
Licensed Content Volume	291
Licensed Content Issue	n/a
Licensed Content Pages	1
Type of Use	reuse in a thesis/dissertation
Portion	figures/tables/illustrations
Number of figures/tables/illustrations	1
Format	both print and electronic
Are you the author of this Elsevier article?	No
Will you be translating?	No
Title	Investigating the potential of emerging porous organic-based photocatalysts for CO2 reduction
Institution name	Imperial College London
Expected presentation date	Jun 2022
Portions	Figure 2
Requestor Location	Giulia Schukraft 298 St paul's raod London, other United Kingdom Attn: Miss Giulia Schukraft
Publisher Tax ID	GB 494 6272 12
Total	**0.00 USD**

BACK

Copyright © 2022 Copyright Clearance Center, Inc. All Rights Reserved. Privacy statement . Terms and Conditions . Comments? We would like to hear from you. E-mail us at customercare@copyright.com

(6) Xu, R.; Wang, X. S.; Zhao, H.; Lin, H.; Huang, Y. B.; Cao, R., Rhenium-modified porous covalent triazine framework for highly efficient photocatalytic carbon dioxide reduction in a solid-gas system. Catal Sci Technol 2018, 8 (8), 2224-2230.



CCC Marketplace™

This is a License Agreement between Giulia Schukraft ("User") and Copyright Clearance Center, Inc. ("CCC") on behalf of the Rightsholder identified in the order details below. The license consists of the order details, the CCC Terms and Conditions below, and any Rightsholder Terms and Conditions which are included below.

All payments must be made in full to CCC in accordance with the CCC Terms and Conditions below.

Order Date	20-Apr-2022	Type of Use	Republish in a thesis/dissertation
Order License ID	1212995-1	Publisher	Royal Society of Chemistry
ISSN	2044-4761	Portion	Image/photo/illustration

LICENSED CONTENT

Publication Title	Catalysis Science & Technology	Rightsholder	Royal Society of Chemistry
Article Title	Rhenium-modified porous covalent triazine framework for highly efficient photocatalytic carbon dioxide reduction in a solid–gas system	Publication Type	e-Journal
		Start Page	2224
		End Page	2230
Author/Editor	Royal Society of Chemistry (Great Britain)	Issue	8
Date	01/01/2011	Volume	8
Language	English		
Country	United Kingdom of Great Britain and Northern Ireland		

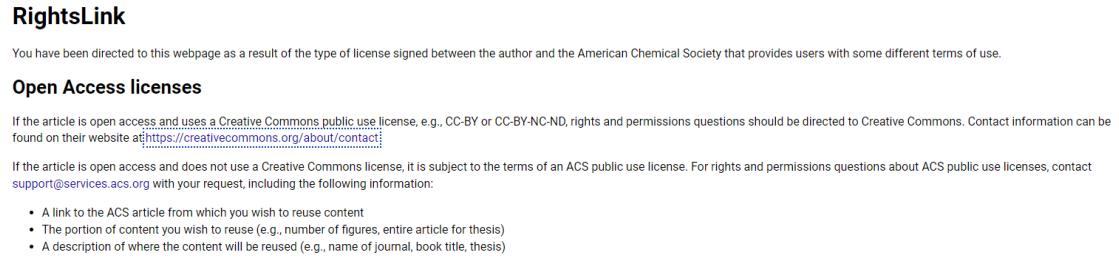
REQUEST DETAILS

Portion Type	Image/photo/illustration	Distribution	Worldwide
Number of images / photos / illustrations	1	Translation	Original language of publication
Format (select all that apply)	Electronic	Copies for the disabled?	No
Who will republish the content?	Academic institution	Minor editing privileges?	No
Duration of Use	Current edition and up to 5 years	Incidental promotional use?	No
Lifetime Unit Quantity	Up to 499	Currency	USD
Rights Requested	Main product		

NEW WORK DETAILS

Title	Investigating the potential of emerging porous organic-based photocatalysts for CO2 reduction	Institution name	Imperial College London
		Expected presentation date	2022-05-31
Instructor name	Camille Petit		

(7) Sprick, R. S.; Jiang, J. X.; Bonillo, B.; Ren, S. J.; Ratvijitvech, T.; Guiglion, P.; Zwijnenburg, M. A.; Adams, D. J.; Cooper, A. I., Tunable Organic Photocatalysts for Visible-Light-Driven Hydrogen Evolution. Journal of the American Chemical Society 2015, 137 (9), 3265-3270.



RightsLink

You have been directed to this webpage as a result of the type of license signed between the author and the American Chemical Society that provides users with some different terms of use.

Open Access licenses

If the article is open access and uses a Creative Commons public use license, e.g., CC-BY or CC-BY-NC-ND, rights and permissions questions should be directed to Creative Commons. Contact information can be found on their website at https://creativecommons.org/about/contact.

If the article is open access and does not use a Creative Commons license, it is subject to the terms of an ACS public use license. For rights and permissions questions about ACS public use licenses, contact support@services.acs.org with your request, including the following information:

- A link to the ACS article from which you wish to reuse content
- The portion of content you wish to reuse (e.g., number of figures, entire article for thesis)
- A description of where the content will be reused (e.g., name of journal, book title, thesis)

(8) Crake, A.; Christoforidis, K. C.; Gregg, A.; Moss, B.; Kafizas, A.; Petit, C., The Effect of Materials Architecture in TiO2/MOF Composites on CO2 Photoreduction and Charge Transfer. Small 2019, 15 (11), 1805473.

License Details

This Agreement between Giulia Schukraft ("You") and John Wiley and Sons ("John Wiley and Sons") consists of your license details and the terms and conditions provided by John Wiley and Sons and Copyright Clearance Center.

Print Copy

License Number	5293131110800
License date	Apr 20, 2022
Licensed Content Publisher	John Wiley and Sons
Licensed Content Publication	Small
Licensed Content Title	The Effect of Materials Architecture in TiO2/MOF Composites on CO2 Photoreduction and Charge Transfer
Licensed Content Author	Camille Petit, Andreas Kafizas, Benjamin Moss, et al
Licensed Content Date	Feb 4, 2019
Licensed Content Volume	15
Licensed Content Issue	11
Licensed Content Pages	12
Type of Use	Dissertation/Thesis
Requestor type	University/Academic
Format	Print and electronic
Portion	Figure/table
Number of figures/tables	1
Will you be translating?	No
Title	Investigating the potential of emerging porous organic-based photocatalysts for CO2 reduction
Institution name	Imperial College London
Expected presentation date	Jun 2022
Portions	Figure S1
Requestor Location	Giulia Schukraft 298 St paul's raod London, other United Kingdom Attn: Miss Giulia Schukraft
Publisher Tax ID	EU826007151
Total	**0.00 USD**

BACK

Copyright © 2022 Copyright Clearance Center, Inc. All Rights Reserved. Privacy statement . Terms and Conditions . Comments? We would like to hear from you. E-mail us at customercare@copyright.com

(9) Voronov, A.; Urakawa, A.; van Beek, W.; Tsakoumis, N. E.; Emerich, H.; Ronning, M., Multivariate curve resolution applied to in situ X-ray absorption spectroscopy data: An efficient tool for data processing and analysis. Anal Chim Acta 2014, 840, 20-27.

License Details

This Agreement between Giulia Schukraft ("You") and Elsevier ("Elsevier") consists of your license details and the terms and conditions provided by Elsevier and Copyright Clearance Center.

Print Copy

License Number	5293131482785
License date	Apr 20, 2022
Licensed Content Publisher	Elsevier
Licensed Content Publication	Analytica Chimica Acta
Licensed Content Title	Multivariate curve resolution applied to in situ X-ray absorption spectroscopy data: An efficient tool for data processing and analysis
Licensed Content Author	Alexey Voronov,Atsushi Urakawa,Wouter van Beek,Nikolaos E. Tsakoumis,Hermann Emerich,Magnus Rønning
Licensed Content Date	Aug 20, 2014
Licensed Content Volume	840
Licensed Content Issue	n/a
Licensed Content Pages	8
Type of Use	reuse in a thesis/dissertation
Portion	figures/tables/illustrations
Number of figures/tables/illustrations	1
Format	both print and electronic
Are you the author of this Elsevier article?	No
Will you be translating?	No
Title	Investigating the potential of emerging porous organic-based photocatalysts for CO2 reduction
Institution name	Imperial College London
Expected presentation date	Jun 2022
Portions	Figure 4
Requestor Location	Giulia Schukraft 298 St paul's raod London, other United Kingdom Attn: Miss Giulia Schukraft
Publisher Tax ID	GB 494 6272 12
Total	**0.00 USD**

BACK

Copyright © 2022 Copyright Clearance Center, Inc. All Rights Reserved. Privacy statement . Terms and Conditions . Comments? We would like to hear from you. E-mail us at customercare@copyright.com

(10) Shankar R, H. A., Kerherve G, Petit C, Band Positioning in Boron Nitride and Metal-Free Photocatalysts via Photoelectron- and UV-Vis Diffuse Reflectance Spectroscopy. ChemRxiv 2020.



(11) Becker, W., Fluorescence lifetime imaging by multi-dimensional time correlated single photon counting. Medical Photonics 2015, 27, 41-61.

Submission ID: 1251058
Date: 21 Apr 2022 3:10pm

Name: Miss Giulia Schukraft
Institute/company: Imperial College London
Address: 298 St paul's raod
Post/Zip Code: N12LH
City: London
State/Territory: Not US or Canada
Country: United Kingdom
Telephone:
Email: giulia.schukraft@gmail.com

Type of Publication: Journal

Title: Medical photonics
Auhtors: Wolfgang Becker
Year: 2015
From page: 41
To page: 61
ISSN: 2213-8846
Volume: 27
Article title: Fluorescence lifetime imaging by multi-dimensional time correlated single photon counting

I would like to use: Figure(s)

Quantity of material: 1
I am the author of the Elsevier material: No
Elsevier author is involved in my project: No

In what format will you use the material: Print and Electronic
Translation: No

Proposed use: Reuse in a thesis/dissertation

Material can be extracted: No

Additional Comments / Information:

Rights and Permissions (ELS) <Permissions@elsevier.com>
to me

Fri, Apr 22, 4:32 PM (10 days ago)

Dear Giulia Schukraft,

We hereby grant you permission to reproduce the material detailed below in print and electronic format at no charge subject to the following conditions:

1. If any part of the material to be used (for example, figures) has appeared in our publication with credit or acknowledgement to another source, permission must also be sought from that source. If such permission is not obtained then that material may not be included in your publication/copies.

2. Suitable acknowledgement to the source must be made, either as a footnote or in a reference list at the end of your publication as follows:

"This article was published in Publication title, Vol number, Author(s), Title of article, Page Nos, Copyright Elsevier (or appropriate Society name) (Year)."

3. This permission is granted for non-exclusive world rights in all languages.

4. Reproduction of this material is granted for the purpose for which permission is hereby given, and includes use in any future editions.

Kind regards,

Kaveri Thakuria
Senior Copyrights Coordinator
ELSEVIER | HCM - Health Content Management

Visit Elsevier Permissions